State Estimation of the Labrador Sea with a Coupled Sea Ice-Ocean Adjoint Model

by

Ian Gouverneur Fenty

B.S., Worcester Polytechnic Institute (2001)

Submitted to the Department of Earth, Atmosphere, and Planetary Sciences
in partial fulfillment of the requirements for the degree of

Doctor of Philosophy

at the

MASSACHUSETTS INSTITUTE OF TECHNOLOGY

June 2010

Author .....
Department of Earth, Atmosphere, and Planetary Sciences
April 21, 2010

Certified by .....
Carl Wunsch
Cecil and Ida Green Professor of Physical Oceanography
Massachusetts Institute of Technology
Thesis Supervisor

Accepted by .....
Maria T. Zuber
E.A. Griswold Professor of Geophysics
Head, Department of Earth, Atmospheric & Planetary Sciences

State Estimation of the Labrador Sea with a Coupled Sea Ice-Ocean Adjoint Model

by

Ian Gouverneur Fenty

Submitted to the Department of Earth, Atmosphere, and Planetary Sciences
on April 21, 2010, in partial fulfillment of the
requirements for the degree of
Doctor of Philosophy

Abstract

Sea ice (SI) and ocean variability in marginal polar and subpolar seas are closely coupled. SI variability in the Labrador Sea is of climatic interest because of its relationship to deep convection/mode water formation, carbon sequestration, and Northern Hemisphere atmospheric patterns. Historically, quantifying the link between the region's observed SI and oceanic variability has been limited due to *in situ* observation paucity and technical challenges associated with synthesizing ocean and SI observations with a three-dimensional time-evolving dynamically consistent numerical model.

To elaborate upon the relationship between SI and ocean variability, a one year (1996-1997) state estimate of the ocean and sea ice state in Labrador Sea and Baffin Bay is constructed and analyzed. The estimate is a synthesis of a regional coupled 32 km ocean and sea ice model with a suite of contemporary *in situ* and satellite hydrographic and SI data. The synthesis of SI data is made possible with the (novel) adjoint of a thermodynamic SI model. Model and data are made consistent, in a least-squares sense, by iteratively adjusting several control variables, such as ocean initial and lateral open boundary conditions and the atmospheric state, to minimize an uncertainty-weighted model-data misfit cost function.

It is shown that the SI pack attains a state of quasi-equilibrium in mid-March during which net SI growth/melt approaches zero; newly-formed SI diverges from coastal areas and converges, via wind/ocean forcing, in the marginal ice zone (MIZ). It is further shown that SI converging in the MIZ is primarily ablated by turbulent ocean-SI enthalpy fluxes. The primary source of energy required for sustained MIZ ice ablation is revealed to be the sensible heat reservoir of the subtropical-origin subsurface waters. Enthalpy from the heat reservoir is entrained into the mixed layer via buoyancy loss-driven convective deepening and brought to the SI via vertical mixing.

An analysis of ocean surface buoyancy fluxes reveals a critical role of low-salinity upper ocean anomalies for the advancement of SI seaward of the Arctic Water/Irminger Water thermohaline front. Anomalous low-salinity waters slow the rate of buoyancy loss-driven mixed layer deepening, shielding an advancing SI pack from the subsurface heat reservoir, and are conducive to a positive surface stratification enhancement feedback from SI melt-water release, both of which extend SI lifetimes. Preliminary analysis of two additional one-year state estimates (1992-1993, 2003-2004) suggests that interannual hydrographic variability provides a first-order explanation for SI maximum extent anomalies. Additional research on the mechanisms controlling the origin and distribution of upper ocean salinity anomalies is required to further understand observed SI variability in the northwest North

Atlantic.

Thesis Supervisor: Carl Wunsch
Title: Cecil and Ida Green Professor of Physical Oceanography
Massachusetts Institute of Technology

Acknowledgments

I owe a debt of gratitude to my professors, colleagues, friends, and family who have supported and encouraged me during my graduate studies.

I sincerely thank my advisor, Carl Wunsch, for providing me the opportunity to pursue my research. I am deeply grateful for his scientific and professional guidance, high standards, and patience. I also thank him for providing helpful feedback on several drafts of this thesis.

I thank the other members of my Thesis Committee: Patrick Heimbach, Raffaele Ferrari, and Eli Tziperman. With their combined experience they helped me define a tractable project and kept me on a steady course over the years. In particular, I thank Patrick for showing me how state estimation works in practice and for inspiring me with his enthusiasm. I thank Raf for challenging me to think critically about my findings and helping me appreciate the limitations of numerical models and their parameterizations. I am grateful to Eli for providing me with insights and direction at several key junctures. They all have been generous with constructive ideas.

I would never have been able to complete my thesis goals if not for the assistance of the MIT ECCO group and MITgcm development team. I thank Constantinos for his help with setting up the model to run on multiple processors and Gael for being a great sounding board for new ideas. Chris Hill and Jean-Michel Campin were always ready to help me understand the model's inner workings.

My time at MIT would have been far less interesting without my classmates and officemates. Daniel, Kjetil, Shaoyu, Evgeny, and Jinbo helped create a fun work environment. I am fortunate to know Udaya Bhaskar Gunturu - truly a good friend!

For personal support outside of MIT, I am indebted to my friends, especially Matthew, Robert, Daniel, and Jesse, and family, especially my parents.

Above all, I thank my darling wife, Renée, for encouraging me and for being a source of constant joy in my life over the past 10 years.

This work was supported by NASA Award #NNX08AF09G (Studies of Ocean Bottom Pressure and Circulation Using Gravity Field Measurements from GRACE), NSF Award #OCE-0530867 (Collaborative Research: CMG: Uncertainty Quantification in Geophysical State Estimation), and NASA Award #NNG04GM55G (U.S. GODAE: Sustained Global Ocean State Estimation for Scientific and Practical Application).

Contents

List of Figures

List of Tables

Chapter 1

Sea Ice and Ocean Variability of the Labrador Sea and Baffin Bay

1.1 Introduction

Sea ice is a fundamental component in the climate system. Where sea ice is present, the exchanges of heat, moisture, and momentum between the atmosphere and ocean are dramatically modified. Having a much higher albedo than seawater, the fraction of incoming solar radiation absorbed by the ocean in the presence of ice is dramatically reduced (Perovich et al. 1998). By reducing the amount of the absorbed solar radiation at high latitudes, sea ice significantly influences the global radiation budget. The global radiation budget determines the radiative-convective equilibrium pole-equator temperature gradient (Manabe and Strickler 1964). The meridional temperature gradient, in turn, modulates the rate of poleward heat flux (Stone 1978). The balance of local radiative-convective equilibrium and poleward heat flux convergence set the spatial and temporal patterns of the Earth's climatological surface temperature.

Sea ice cover exhibits variability on annual and interannual time scales (Cavalieri et al. 2003). The annual cycle is paced by the cycle of solar insolation, caused by the Earth's axial inclination. In the modern climate, polar and subpolar oceans undergo an annual cycle of heat flux divergence which leads to the expansion of approximately 23 million square kilometers of seasonal ice. The patterns and magnitudes of the seasonal ice cycle are hemispherically asymmetric. The Northern Hemisphere forms approximately 38% of

the global seasonal ice: 9.2 compared to 13.8 million square kilometers for the Southern Hemisphere.[1] The surface area associated with global seasonal ice represents approximately 7.4% of the total ocean surface or 5.3% of the entire Earth surface, making the sea ice annual cycle one of the more striking global-scale climate phenomena. While the seasonal cycle in the Southern Hemisphere is significantly more expansive than the Northern, the Northern Hemisphere is home to approximately 2.5 times more perennial ice area: 5 compared to 2 million square kilometers in the Southern.

Inevitably, each annual sea ice cycle is unique; on an annual basis the climate system evolves along slightly different lines. The intrinsic variations of incoming solar insolation at the surface, the circulation and transports of the ocean and atmosphere, and the feedbacks to the circulation and transport induced by the sea ice itself all influence the details of the evolution of each seasonal cycle.

In recent years, seeming trends in the short, $\sim$ 30 year, high quality observational record of sea ice have been identified. One that has provoked considerable attention is a decrease in perennial ice cover in the Arctic Ocean (Serreze et al. 2007). By extrapolation, some researchers have predicted a complete loss of perennial sea ice sometime within the 21st century (Holland et al. 2006; Stroeve et al. 2007). Apparent trends in the maximum extent of seasonal ice cover have also been observed, a decade-long decrease in the maximum seasonal ice extent in the Labrador Sea, for example (Comiso and Nishio 2008).

Some open questions within the scientific community concerning the spatial and temporal patterns of interannual sea ice variability awaiting conclusive answers include: What are their origin? Do the observed trends include a discernible signal of anthropogenic climate change? Do these trends indicate a transition from one climate regime to another? Do they reveal a surprising, but inevitable, progression along a trajectory in phase space of an imperfectly understood and extremely complex dynamical system? Is it possible to ascribe responsibility for changes in sea ice to either a changing atmosphere or ocean? Are these apparent trends simply artifacts of incomplete sampling of an system-wide oscillation which develops over multi-decadal time scales?

Given the nature of these questions, it is clear that polar climate variability is far from fully understood. Indeed, it is sobering to realize that robust cause-and-effect explanations

[1] Seasonal ice signifies ice which melts during summer whereas perennial ice remains throughout the entire year.

for even year-to-year variations in the sea ice annual cycle are beyond our current capabilities. With such large gaps in our collective knowledge, what is our basis to claim that future changes to sea ice coverage can be accurately predicted?

Why have efforts towards establishing a causal link between ice signals and other components of the climate system remained incomplete? There is no simple answer to this question. However, one outstanding problem is the knowledge gap between 1) acknowledgment that ice signals are the result of mutual interactions between the components of the coupled sea ice-ocean-atmosphere system and 2) knowing how the interactions between the components *have actually evolved in time*. Especially lacking is an understanding of the role of hydrographic variability in driving some of the observed changes in sea ice (Serreze et al. 2007). Without detailed observations of these interactions and components of the climate system, our collective ability to refute hypotheses and reduce uncertainties is severely limited.

Without question, to reconcile observed sea ice variability, a dynamical reconstruction of the actual historical interactions of the ocean, sea ice, and atmosphere is needed. However, at present, there are no credible time-varying reconstructions of the three-dimensional state of the polar and subpolar seas.

Why are there no believable estimates of the state and variability of the polar and subpolar seas? The primary reason is that quantitatively relating ice trends and patterns with the comparatively more difficult to observe and data-sparse high-latitude ocean and atmosphere is not a straightforward task.

This thesis is motivated by this problem. My primary goal is to elucidate the role of the ocean in annual and interannual sea ice variability. To achieve this goal, I focus on a region with large annual and interannual sea ice variability which is comparatively well-observed and climatologically relevant: the Arctic's Baffin Bay and the North Atlantic's Labrador Sea.

A secondary goal is to demonstrate the feasibility of the adjoint method, or method of Lagrange multipliers, to simultaneously synthesize observations of sea ice and the ocean into a dynamic coupled numerical model. As attention moves towards making truly global ocean state estimates, the synthesis of sea ice observations will prove to be increasingly important if not essential. The synthesis of physical ocean observations into numerical models using the adjoint method is now routine (Wunsch and Heimbach 2007). In this

thesis, the synthesis of sea ice observations is made possible using a novel technological contribution: the adjoint of a thermodynamic sea ice model.

These two goals are related. The achievement of the secondary goal permits the construction of a time-varying three-dimensional estimate of the ocean state and its dynamically and thermodynamically coupled sea ice cover. It is from the state estimate that I draw the inferences required for the primary goal.

The rest of the introductory chapter is organized as follows. The reasoning behind the choice of the Labrador Sea and Baffin Bay as the region of focused study is presented first (Section 1.2). I then introduce the annual and interannual variability of sea ice in the Northern Hemisphere (Section 1.3) and Labrador Sea and Baffin Bay (Section 1.4). Several theories which have been postulated to explain the observed variability are introduced (Section 1.5). I then review the ocean and sea ice numerical modeling efforts which have simulated the northwest North Atlantic (Section 1.6). I emphasize modeling work which was specifically intended to advance the level of sea ice understanding in the Northern Hemisphere and study region. The chapter concludes with a synopsis of the remainder of the thesis (Section 1.7).

1.2 Why the Labrador Sea and Baffin Bay?

The choice of studying the interaction of the ocean and sea ice (sea ice-ocean interaction) in the Labrador Sea and Baffin Bay was made based on the climatological significance of its ice variability, and the large number of suitable oceanographic measurements. Both of these points are further elaborated upon in the next two sections. A map of the Labrador Sea and Baffin Bay is presented in Figure 1-1.

1.2.1 Sea ice variability in the Labrador Sea and climate

Variability of the sea ice-ocean-atmosphere system in the Labrador Sea has been hypothesized to have far-reaching impact on global climate through its influence on deep convection and the circulation patterns of both the atmosphere and ocean.

Sea ice variability in the Labrador Sea may influence deep convection (Visbeck et al. 1995). Wintertime turbulent sensible heat fluxes from the warm ocean to the intensely cold atmosphere warms the atmosphere and, accordingly, reduces seawater enthalpy. As

Figure 1-1: Map of study region. Below 1000 m, depths are solidly colored in 1000 m intervals.

seawater enthalpy decreases its density increases resulting in a loss of buoyancy. Seawater buoyancy, b, is defined as:

$$b = -g\frac{\delta\rho}{\rho_{ref}} \tag{1.1}$$

Where g is the acceleration due to gravity, ρ_{ref} is a constant reference value of seawater density, and $\delta\rho$ is related to seawater density, ρ, via:

$$\rho = \rho_{ref} + \rho_0(z) + \delta\rho(x, y, z, t) \tag{1.2}$$

Where $\rho_0(z)$ is the ambient vertical stratification associated with the fluid parcel being considered.

When the buoyancy of a parcel of seawater becomes sufficiently low so as to exceed its local ambient stratification ($\partial_z\rho > 0$), the parcel becomes hydrostatically unstable. A hydrostatically unstable parcel undergoes convective downwelling, sinking until achieving a depth of neutral buoyancy. The depth to which downwelling occurs depends sensitively on the ambient vertical stratification and effects stemming from Earth's rotation (Jones and Marshall 1993). With evidence of convection to 2300 m, the Labrador Sea is one of the few sites of deep convection in the World Ocean (Lazier et al. 2002).

Convective mixing establishes a pathway along which atmospheric gases, including greenhouse gases such as CO_2, are sequestered into the intermediate and deep ocean. Evidence of the importance of deep convection for vertical transport of atmospheric gases is provided in Figure 1-2, which shows the distribution of anthropogenic CO_2 throughout the World Ocean. High concentrations of anthropogenic CO_2 in the deep ocean are predominantly found in the the North Atlantic. At sites of deep convection in the Labrador Sea, air-sea fluxes of CO_2 have been estimated to be of the same order of magnitude as other North Atlantic and sub-Arctic Seas (DeGrandpre et al. 2006).

The formation, melting, and presence of sea ice can have an effect on ocean surface buoyancy and therefore its propensity to convect. Where present, the ocean surface is insulated from the cold atmosphere and corresponding intense heat/buoyancy loss. Whereas cold air flowing over the open ocean warms as it gains heat lost from the ocean, cold air flowing over ice remains cold. Consequently, the spatial pattern of ice cover determines the location where circulating cold air meets the open ocean (Bitz et al. 2005; Griffies et al. 2009). Whether the actual ocean buoyancy loss off the ice edge induces deep convection is

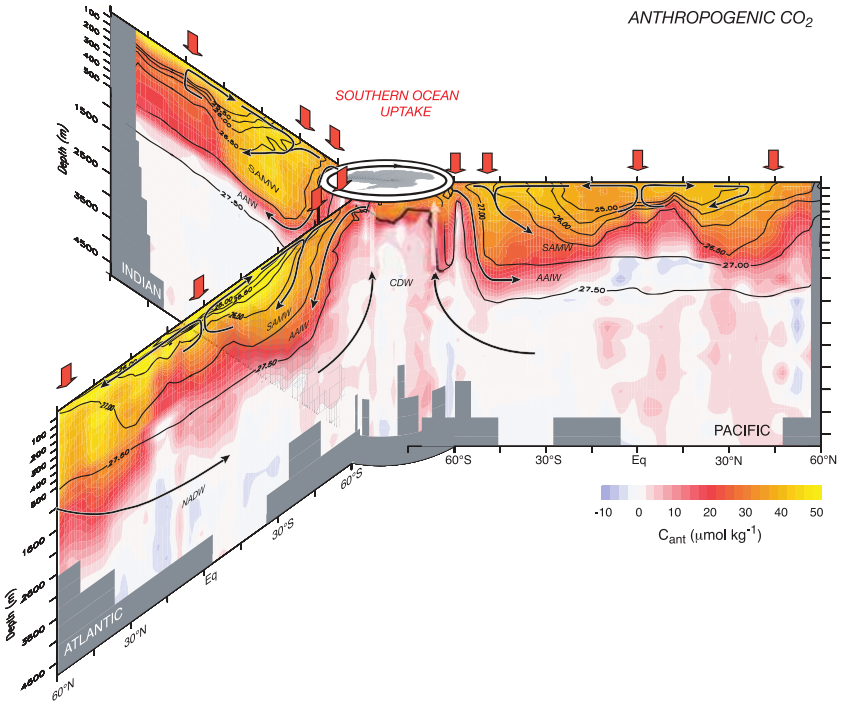

Figure 1-2: Contemporary distribution of anthropogenic CO_2 in the World Ocean as determined by inverse calculations. In the Atlantic Sector panel, high concentrations are found at depths exceeding 1000 m, owing to transport via deep convection in the Labrador and Greenland-Icelandic-Norwegian seas. The deep convection in the North Atlantic thus represents an important route for the sequestration of anthropogenic CO_2 into the deep ocean. Adapted from Gruber et al. (2009)

by no means assured; hydrographic conditions and ocean stratification set the maximum depth attainable at any given time and location.

The increase of buoyancy by sea ice melt near the ice edge may also influence the ability of the ocean to convect. Melting sea ice can either increase or decrease seawater buoyancy because of nonlinearities in the seawater equation of state. However, seawater density becomes more sensitive to salinity variations at low temperatures and (not surprisingly) seawater in the vicinity of sea ice tends to be cold. Consequently, during ocean sensible heat-induced sea ice melt, the buoyancy increase associated with the release of low-salinity ice meltwater exceeds the buoyancy decrease associated with the lowering of seawater temperature. Furthermore, the transport of sea ice into warmer and saltier surface waters by wind forcing and ocean currents is seen to be a common event.

Sea ice cover variability may also affect large-scale meteorological patterns on seasonal and longer time scales. The Labrador Sea lies along the northern edge of the North Atlantic storm track. The genesis and trajectories taken by synoptic weather systems are sensitive to the location of east-west surface temperature gradients. The modification of these gradients by sea ice cover anomalies has been hypothesized to influence the location and intensity of weather patterns in the North Atlantic, Europe, and east coast of North America (Deser et al. 2004; Magnusdottir et al. 2004).

Anomalies of sea ice cover persist for months, much longer than the the life cycle of individual storms. Understanding the mechanisms behind ice cover variability has implications for short-term and seasonal weather forecasting. Moreover, knowledge gleaned from studying contemporary sea ice-ocean interaction may provide insight into the sea ice state and large-scale atmospheric circulation of Earth's various climate epochs.[2]

1.2.2 Suitability of *in situ* ocean observations

To draw credible inferences about phenomena in the real world (in this thesis, basin-scale sea ice-ocean interaction) a state estimate must synthesize observations which *constrain the simulation of the phenomena*. In general, the greater the number of independent constraining data synthesized, the greater the likelihood that a dynamical reconstruction consistent with these data is an accurate reproduction of reality. Noting these two facts, the reason

[2]Although extremely interesting, the expression of sea ice in past climate epochs, such as the intensely-studied Last Glacial Maximum, is beyond the scope of this thesis.

behind the choice of study region in this thesis can be made clear.

Discussion of the suitability of *in situ* ocean observations must be restricted to the subset of observations which actually constrain the state estimate. Many *in situ* hydrographic measurements in the Labrador Sea sample from the energetic mesoscale eddy field (Lilly and Rhines 2002; Lilly et al. 2003; Hátún et al. 2007). For the purposes of ocean state estimation, these data are sparse and noisy and may not provide sufficient constraints.

Oceanographic data which provide constraints on the reproduction of sea ice in the model must be included. However, *in situ* hydrographic measurements near or beneath sea ice cover are some of the hardest to acquire (Morison et al. 1987; McPhee 2008). Moreover, proportionally more ship-based measurements are taken during the logistically easier to coordinate ice-free seasons. Even with the advent of autonomous profiling floats, the great majority of *in situ* ocean observations are offshore of the seasonal ice zone hundreds of meters below the sea surface.

Despite the above complications, several factors favor the possibility that at least a fraction of *in situ* oceanographic measurements from the Labrador Sea can be used to constrain the reproduction of sea ice: the general counter-clockwise tendency of its circulation, long residence time of observed water mass properties, and their relative abundance.

The general cyclonic tendency of circulation implies that many water parcels are transported towards, through, and, eventually away from the seasonal ice zone. The time evolution of sea ice depends on both the initial and subsequent ocean states. Consequently, depending on whether a Labrador Sea *in situ* ocean observation is made upstream or downstream of the seasonal ice zone, information about later or earlier ocean-sea ice interaction may be extracted. Such information can be used to constrain the sea ice-ocean state estimate.

Below the seasonal pycnocline and away from the swiftest parts of the boundary currents, the residence time of hydrographic properties in the Labrador Sea is on the order of one year or longer (Cuny et al. 2002). Thus, it is reasonable to expect that in this basin *in situ* ocean observations made within one year of a particular ice cycle may provide useful constraints of ice in a state estimate

The northwest North Atlantic Ocean and the Labrador Sea have long been the subject of investigation by meteorologists, oceanographers, and sea ice researchers. Since the mid-1990s, oceanographers have tremendously increased the number of *in situ* profiles made by

autonomous floats, surface drifters, ship-based CTDs, moored instruments, undersea gliders, and expendable bathythermographs (Marshall et al. 1998; Fratantoni 2001). Including the suite of regular ocean measurements from the satellite observation network, the Labrador Sea stands out as being one of Earth's best studied basins. Indeed, compared to other high-latitude seas with seasonal and perennial sea ice, the Labrador Sea may be the most well observed.[3].

Are the number and quality of the *in situ* observations in the Labrador Sea sufficient for a consistent and useful state estimate? In fact, there is no way to ascertain the answer definitively. An argument can be made that the basin is far too undersampled to adequately constrain an sea ice-ocean state estimate. With respect to mesoscale variability - the Rossby deformation radius in the basin is approximately 8 km - this is certainly true. Indeed, the existence of a large energetic turbulent eddy field which continually stirs and mixes water masses of quite distinct properties virtually guarantees that the Labrador Sea will remain undersampled for the foreseeable future. However, I assert that the question of whether it is possible to construct a *useful* state estimate using observations of the undersampled ocean is largely settled (*e.g.,* Wunsch and Heimbach 2006; Gebbie 2007; Mazloff 2008). Whether a useful state estimate can be constructed for the particular problem tackled in this thesis is impossible to know at the outset; past success does not assure future success. Bearing this in mind, I proceed.

1.3 The Context of Labrador Sea and Baffin Bay Sea Ice in the Northern Hemisphere

In this section, I introduce observations of the ice cover variability of the Labrador Sea and Baffin Bay. Variability of the Labrador Sea and Baffin Bay is best understood from the perspective of the entire Northern Hemisphere. I begin with a broad overview of the development of the annual cycle over the Northern Hemisphere (Section 1.3.1). In addition, I show the spatial distribution of ice extent and the interannual variability of the ice edge location (Section 1.3.2).

[3]A discussion of the hydrographic and sea ice data examined in this thesis is described in Sections 2.4.2 and 2.4.4

1.3.1 Development of sea ice in the Northern Hemisphere

Sea ice *concentration* is the most commonly derived sea ice variable, defined as the fraction of ice-covered surface per unit surface area. The ice *edge* is typically defined by the 15% concentration line. The radial southward expansion of sea ice cover permits the definition of a derived sea ice variable, sea ice *extent*, the total ice area inscribed by the seaward limit of the ice edge.

The analysis of Northern Hemisphere sea ice presented here is based on observations made during the satellite sea ice monitoring era, beginning with the 1978 launches of scanning multichannel microwave radiometers on board the SEASAT and Nimbus-7 satellites. Measurements taken with these instruments and their successors, namely a series of the special sensor microwave imagers (SSM/I), have been combined to provide a nearly unbroken record of daily global sea ice concentrations to the present (Comiso 1999, updated 2008). Ice concentration data are available with a minimum resolution of approximately 25×25 km for the majority of the satellite record.

From approximately the autumnal to the vernal equinoxes, net energy flux divergences are sufficient to extract enthalpy from seawater in some polar and sub-polar seas beyond the latent heat of fusion and trigger sea ice growth. The growing ice expands spatially, driven by a combination of heat exchange and advection. During the second half of the year, net energy convergence into the ice induces thinning. The combination of thermodynamic melt and dynamic transport reduces ice extent, eliminating all seasonal ice, by definition. The retreat of the ice edge is quite uneven owing to considerable heterogeneity in the magnitudes and sources of converging heat and momentum fluxes.

1.3.2 Northern Hemisphere sea ice interannual variability

It is instructive to establish a sense of the spatial extent of annual ice cycle and its interannual range; both of which are presented in Figure 1-3. With the loss of all seasonal ice in September, the perennial ice is almost completely confined to latitudes north of 70° N; the historical range lies between $4 - 10 \times 10^6$ km^2. At the seasonal maximum, typically in March, the ice front penetrates southward to approximately 40° N; the historical range lies between $13 - 18 \times 10^6$ km^2. The most southerly expression of ice cover is found primarily along continental western boundaries.

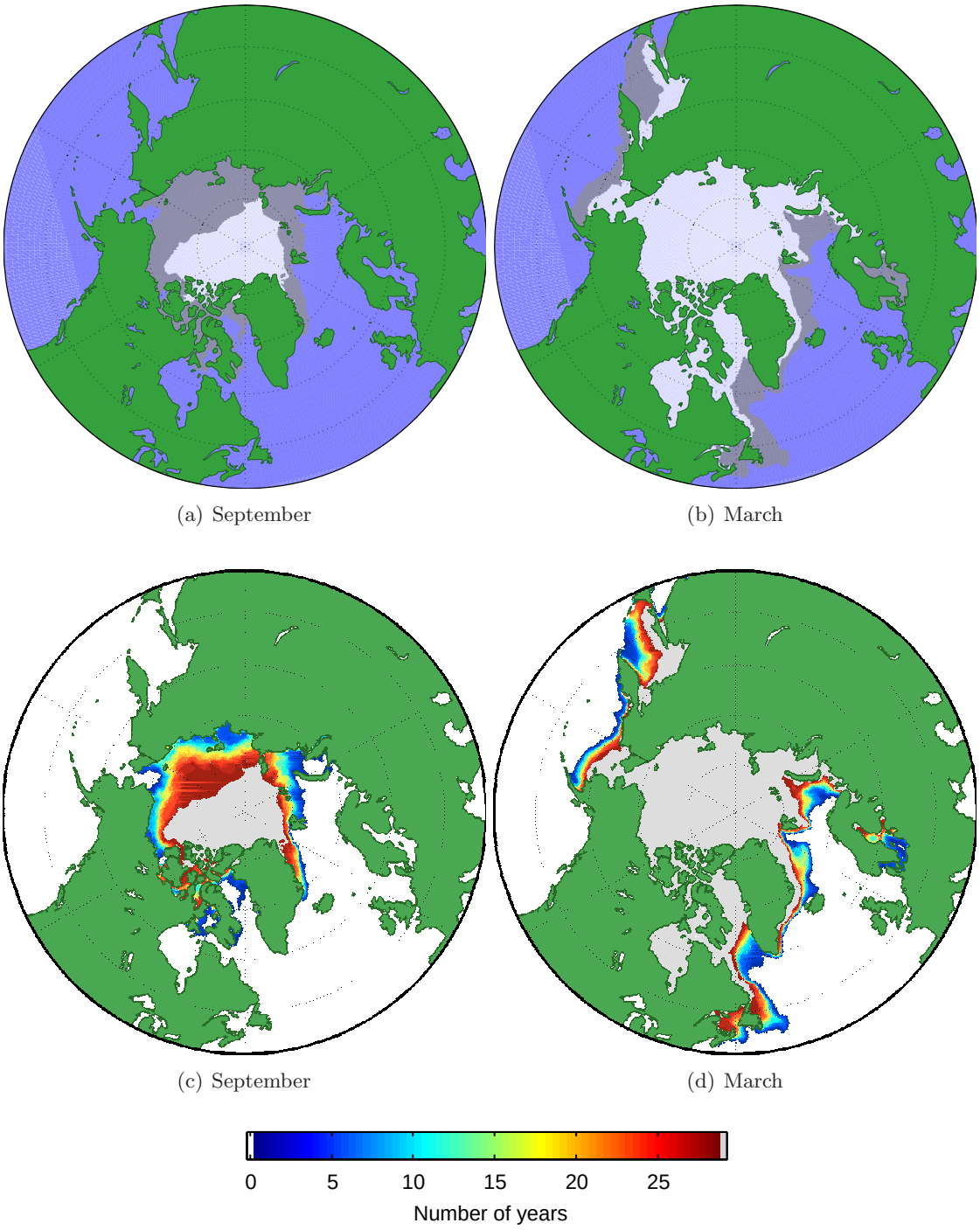

(a) September (b) March

(c) September (d) March

Figure 1-3: Sea ice extent extremes (a,b) and color histograms (c,d) from a composite of September (minimum) and March (maximum) mean sea ice extent over 1978-2008 SSM/I satellite record. White regions in (a,b) indicate where ice is present in each year. Colors in (c,d) indicate the number of years, out of 29, with ice in that location. Blue areas in (c,d) denote regions where ice is rarely observed. The large red area in (d) reveals the extreme rare minimum of 2008.

The distributions of September and March sea ice edge locations are not uniform across its range. As revealed in Figure 1-3, extremes of September minima and March maxima of seasonal ice are only rarely realized.

The magnitude and range of sea ice area in the Northern Hemisphere over the seasonal cycle is given in Fig. 1-4. It is interesting to note that for both extremes, March and September, the ranges of interannual variability are approximately equal.

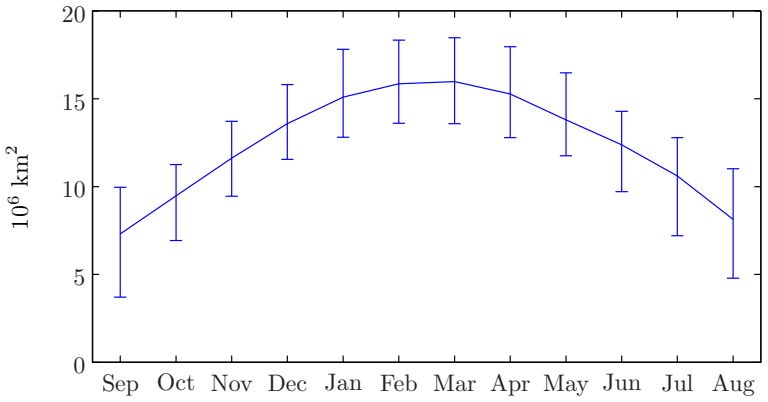

Figure 1-4: Average annual cycle of sea ice coverage in the Northern Hemisphere 1979-2008. Bars designate the extreme limits of the ice edge observed for each month.

The proportion of Northern Hemisphere seasonal sea ice found in the Labrador Sea and Baffin Bay can now be appreciated. Out of the total area of observed seasonal ice cover (the total surface area between the maximum March ice extent and the minimum September extent), approximately 20% is found within the study region. Out of the total surface area delimiting the extremes of March sea ice extent (the maximum March extent less the minimum March extent), 27% occurs within the confines of the Labrador Sea and Baffin Bay. Consequently, this thesis is concerned with a significant fraction of the entire Northern Hemisphere sea ice variability, despite excluding the central Arctic Ocean altogether.

Many authors have discussed the interannual variability of perennial and seasonal ice cover over the Arctic Ocean/Northern Hemisphere. For brevity, a review of that literature is not repeated here. Good starting points for the interested reader are the papers of Serreze et al. (2003), Cavalieri et al. (2003), Stroeve et al. (2005), and Stroeve et al. (2007). In this thesis, only the sea ice variability within the Labrador Sea and Baffin Bay is considered.

1.4 Labrador Sea and Baffin Bay Sea Ice Annual and Interannual Variability: Observations

Marshall et al. (1998) vividly describe the study region in their introduction to The Labrador Sea Deep Convection Experiment field campaign,

> The northwest corner of the Atlantic Ocean (the Labrador Sea ...) is a region of powerful physical forces, extremes of wind and cold, incursions of icebergs and sea ice, great contrasts in buoyancy of air and seawater, and a region of great biological activity.

The incursions of sea ice referred to in the above quotation evolve over an annual cycle with considerable interannual variability. This section provides an overview of the sea ice cycle and its variability so that the main thesis questions and my approach to answering them can be appreciated. A single realization of the cycle, subjectively deemed representative, is presented first (Section 1.4.1). A brief introduction to aspects of the observed interannual variability follows (Section 1.4.2).

1.4.1 The sea ice annual cycle in the Labrador Sea and Baffin Bay

Mean sea ice concentrations during four one-month periods of the ice annual cycle of 1994-1995 are shown in Figure 1-5. Sea ice is absent in September, the previous cycle's ice is completely melted. From October to December, ice rapidly extends across the Baffin Bay from northwest to southeast. By December, Baffin Bay is ice covered until Disko Island. Ice is found in the western Davis Strait and south along the northern half of the Labrador Coast. In a matter of a few weeks, the ice pack extends along the length of the Labrador Coast until the Newfoundland and the Grand Banks to the 2000 m isobath in the northern Labrador Sea. Between January and March there is little change in the maximum ice extent. After approximately the vernal equinox, ice begins to retreat, proceeding roughly in the reverse order of its expansion.[4] Between June and September, the ice remaining off the Baffin Island Coast retreats from east to west, leaving a mainly ice-free Baffin Bay for the onset of the next cycle.

[4] A major difference between the patterns of ice pack expansion/retreat is the springtime opening of the Northern Polynya at the mouth of Smith and Jones Sounds.

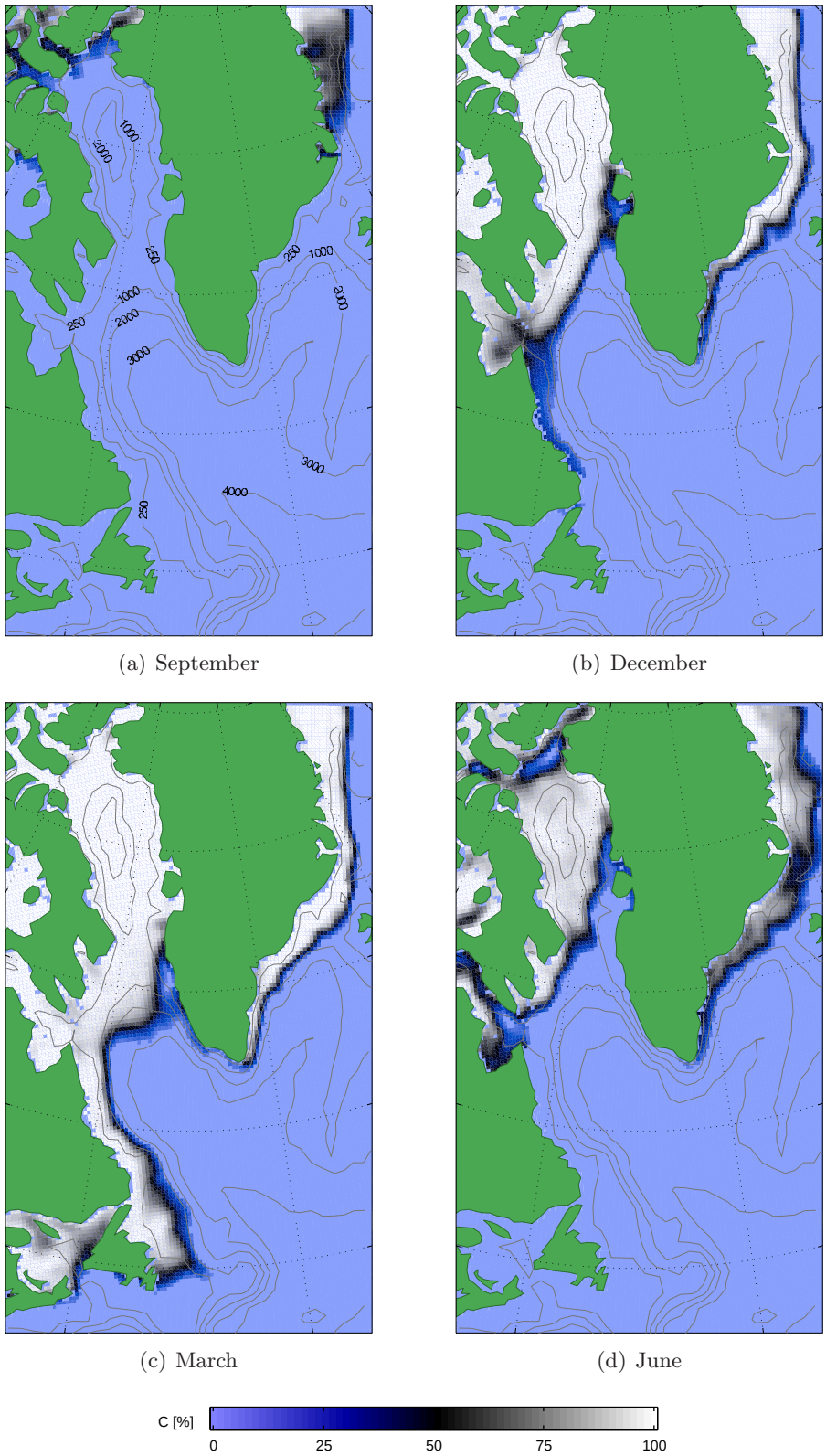

(a) September

(b) December

(c) March

(d) June

Figure 1-5: Monthly mean sea ice concentration for the annual cycle spanning September 1994-1995. For data details see Section 2.4.4.

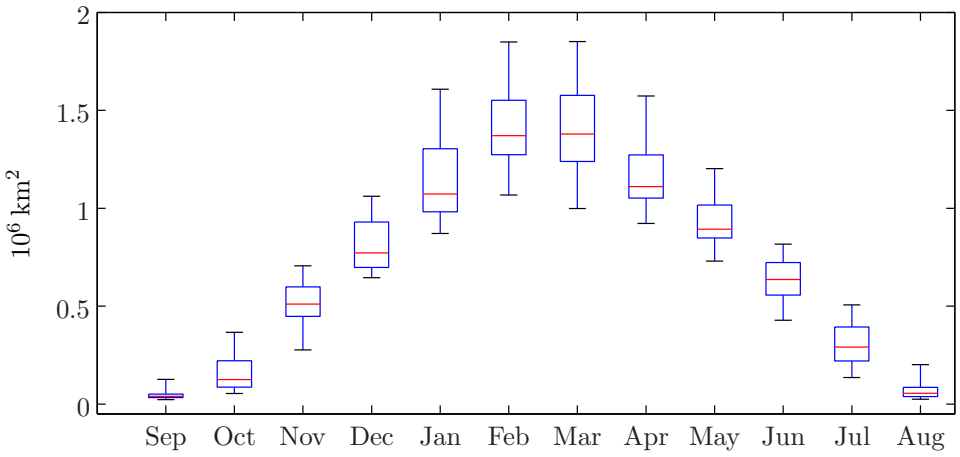

Figure 1-6: Annual cycle of sea ice extent, total area covered in sea ice with concentration above 15%, in the Labrador Sea and Baffin Bay, 1979 – 2008. Red lines within box designate median, box edges designate upper and lower quartiles, and whiskers extend to the observed limits. The total ice extent over the 1994 – 1995 ice cycle in the Labrador Sea and Baffin Bay described in Section 1.4.1 approximately follows the monthly medians.

1.4.2 Sea ice interannual variability in the Labrador Sea and Baffin Bay

Interannual sea ice variability in the study region is summarized by Figure 1-6. The range of of variability follows in accord with the total ice extent; one finds an increasing range between October and February, and a decreasing range between April and August. Consistent with the description of the annual cycle in the previous section, the beginning and end of the annual cycle is devoid of significant perennial ice with only few exceptions.

Ice extent variability is likely coupled to the interannual variability of the atmosphere and ocean. A tight linkage between ice extent variability and atmosphere-ocean variability can be deduced by examining the area between the limits of ice extent, the maximum extent less the minimum extent, for each month. During the first half of the cycle, sea ice ceases its expansion by reaching either a coastline or unfavorable atmospheric or oceanic conditions. When sea ice expansion is limited by coastal geometry, such as the coastal confines of the Arctic Ocean, the range of wintertime ice extent is small relative the median. However, in the Labrador Sea and Baffin Bay, the range of wintertime extent scales as roughly 50% of the median; the greatest deviation is during the peak month. Therefore, while coastal geometry provides obvious constraints, atmospheric and oceanic interannual variability must be the primary modulating factors.

The above analysis is useful but not sufficient to appreciate the existing explanations

of the observed sea ice interannual variability - to do so, one must be familiar with its spatial patterns. Examples of these temporally-variable patterns are presented in Figure 1-7. Two important features of winter and springtime sea ice variability are noted: 1) between December and June, interannual ice extent variability occurs primarily along the ice edge seaward of the Labrador Sea and 2) ice is found in the western Baffin Bay between December and June every year in $1979-2008$ record. It is perhaps useful to note that at least one reconstruction of pre-satellite era sea ice variability in the 20^{th} century ($1953-1977$) reveals essentially the same pattern (Walsh and Johnson 1979).

Consistent with Figure 1-6, in each month the total area associated with interannual ice variability rises and falls in tandem with the median ice extent. Finally, the spatial patterns of wintertime maximum ice variability indicate a correlation with bathymetric features. In the northern Labrador Sea, interannual ice variability is predominantly seaward of the 1000 m isobath. South of the Hamilton Bank, variability is predominantly seaward of the shelfbreak. Indeed, an imprint of the geography of the Grand Banks is obvious in these patterns.

The mechanisms responsible for these observed patterns of interannual variability have long been the subject of research. In the next section, these theories are summarized to expose the considerable (and persistent) uncertainty surrounding its underlying causes and modulating factors. With these theories in mind, the reader can appreciate the methodology used in this thesis for tackling the problem of understanding the relationship between ocean and sea ice variability in the Labrador Sea and Baffin Bay.

1.5 Labrador Sea and Baffin Bay Sea Ice Annual and Interannual Variability: Theories

The basic processes involved in sea ice formation, growth, and melt have been identified and are fairly well understood (Wadhams 2000, chap. 2-4). Consequently, it is relatively simple to postulate reasons for observed annual and interannual variability. The hypotheses proposed in the literature have evolved over a period of decades, reflecting an expanding observational record and ongoing developments in our basic understanding of the relevant physical processes involved.

Theories pertaining to annual sea ice variability are considered first (Section 1.5.1),

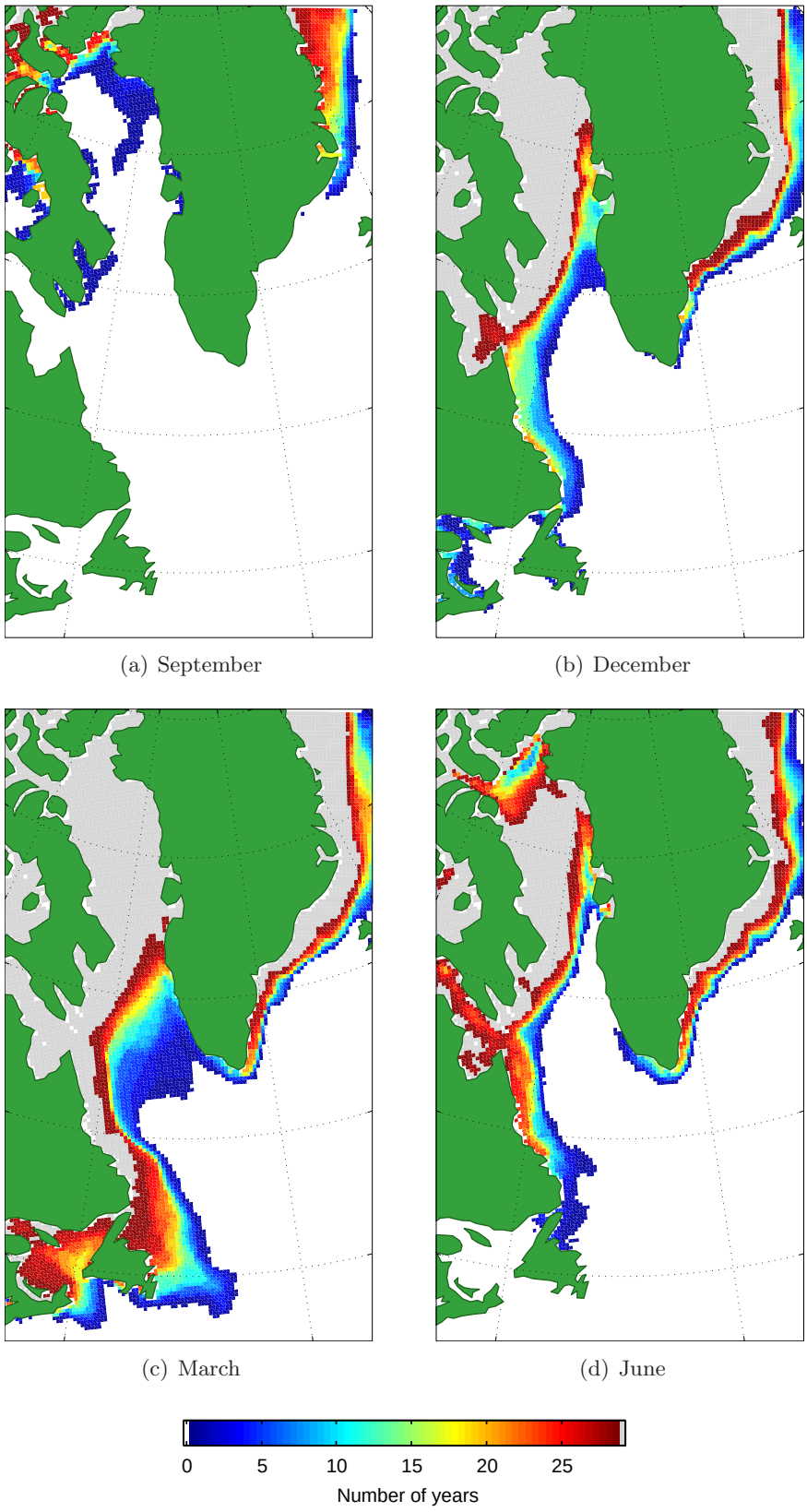

(a) September

(b) December

(c) March

(d) June

Figure 1-7: Color histograms of monthly mean sea ice extent in the study region.

followed by theories of interannual variability (Section 1.5.2). For the reader who is looking for an overview, a summary is also provided (Section 1.5.3).

1.5.1 Theories of annual sea ice variability

With respect to the annual cycle in the Labrador Sea and Baffin Bay, all authors either explicitly or implicitly attribute incoming solar radiation as the primary factor responsible for the sea ice annual cycle. The oscillation of solar radiation modulates the sign of the net ocean surface energy balance in the northwest North Atlantic leading to alternating periods of upper ocean warming and cooling. The time-varying downwelling radiative flux affects the local surface energy balance of the ocean directly, through the conversion of radiation to sensible heat, and indirectly, by modulating the sensible heat of air masses passing over the region.

Also, implicit in the literature is the notion that over much of the ice-covered domain, especially the Baffin Bay and inner Labrador Shelf, net ocean surface cooling is sufficient to induce *in situ* ice formation. Finally, it is widely accepted that any discrepancy between the actual sea ice coverage and that which is implied by considering only local air-sea heat fluxes can be accounted for by the transport of ice by winds or ocean currents. In the Labrador Sea and Baffin Bay, such locations are recognized as being mainly where the ice pack meets the warmer waters of the central Labrador Sea and along the southern extension of the Labrador Coast around the Grand Banks and Newfoundland (Symonds 1986; Yao et al. 2000).

1.5.2 Theories of interannual sea ice variability

Given that there is virtually no disagreement on the above, the existing Labrador Sea and Baffin Bay sea ice literature concentrates on ascribing causes for various aspects of variability on interannual time scales. However, despite general agreement on these theories, many details of the ice annual cycle are ignored and not well understood.

Of all possible aspects of ice interannual variability, attention is mainly paid to the most readily observable aspect of the ice pack: ice area concentration. Historically, the more difficult to observe aspects of the ice pack (such as the spatial and internal distributions of thickness, salt, enthalpy, and deformation) have largely been ignored.

With respect to ice area concentration, three aspects of its interannual variability tend

to be considered: the date at which ice appears and disappears in various locations, the horizontal motion of the ice pack, and the spatial extent or aggregate surface ice area through time.

In principle, the date of ice formation is predictable given information about the vertical distribution of heat and salt in the ocean, the time-varying surface atmospheric and radiative conditions, and the time-varying horizontal oceanic boundary conditions. The lateral presence of ice over an area which is not locally formed through ice motion is also predictable with sufficient information about forcing stresses from the ocean and wind and details of the ice pack's distribution in space.

Historically, knowledge of the initial hydrography for the Labrador Sea and Baffin Bay and its time-evolving horizontal and upper boundary conditions has been far from complete. Without being overly constrained by hydrographic or atmospheric measurements, researches have enjoyed a degree of creative freedom in postulating theories for the observed sea ice variability. However, as these theories are without much direct observational support, they must be recognized as speculative.

The proposed hypotheses for interannual sea ice variability in the Labrador Sea and Baffin Bay can be segregated into two categories based on whether their emphasis is placed on the role of variable atmospheric or oceanic conditions. Oceanic and atmospheric variability are obviously linked; variability in one medium drives variability in the other. The segregation of hypotheses into one or the other category reflects my interpretation of the emphasis placed on each particular theory.

For the sake of simplicity, I categorize a Labrador Sea and Baffin Bay sea ice hypothesis as being purely oceanographic in nature if it provides an explanation of interannual sea ice variability without reliance on interannual atmospheric variability in the study region.

Atmosphere-centric hypotheses are reviewed first, followed by ocean-centric theories.

Postulation of atmospheric causes

One of the earliest attempts at quantifying the relationship between the interannual variabilities of atmospheric conditions and sea ice in the Labrador Sea and Baffin Bay is by Crane (1978). In Crane's work, autumnal and vernal geostrophic wind anomalies were found to correlate with variations in the dates of initial seasonal ice advance and retreat. Specifically, in autumns associated with an above-average number of synoptic weather sys-

tems associated with northerly and westerly geostrophic winds over the Labrador Sea, ice was seen to advance across the Davis Strait and along the Labrador Coast earlier than normal. In those years with anomalous southerly and westerly springtime winds, ice retreat was seen to initiate earlier. In both cases, the advection of anomalously cold (warm) air over the open ocean (ice pack) was proposed as the mechanism responsible for anomalous movement of the ice edge.

Crane also noted that anomalous ice advance rates had little skill in predicting the subsequent tendencies of ice retreat within the same annual cycle. The lack of predictive skill of initial ice advance rates may be explained by a sub-seasonal auto-correlation time scale of meteorological variables in the North Atlantic (Walsh and Johnson 1979; Prinsenberg et al. 1997). (Or the large amount of high frequency noise inherent in synoptic weather systems during the short periods of ice advance and retreat.)

In contrast with Crane, later researches preferred to concentrate on relating sea ice and meteorological anomalies across longer time scales, from months to decades. With a lengthening of preferred anomaly time scales came a tendency to describe both the ice and atmospheric states using variables of reduced complexity.

Rogers and Van Loon (1979) were among the first to show a significant relationship between interannual large-scale atmospheric anomalies and ice conditions in the Labrador Sea. The authors found that ice cover anomalies were positive (negative) during years associated with an anomalously deep (shallow) Icelandic Low and shallow (deep) Azores High.[5] This sea level pressure (SLP) anomaly pattern has oppositely-signed centers of action, which is often referred to as a *seesaw* pattern.

Noting the far-reaching extent of the pattern's associated geostrophic wind anomalies, the authors rationalized the following:

> The severity of ice conditions during [these two classes of] winters therefore corresponds to that expected from the different circulation anomalies associated with the seesaw.

From an earlier work by the same authors, one may infer that their expectation of the effect of an anomalously deep Icelandic Low is an increase of the tendency for synoptic weather systems to advect cold air over the Labrador Sea and Baffin Bay (van Loon and

[5]The Icelandic Low and Azores High refer to climatological features of low and high mean sea level pressure, respectively.

Rogers 1978). The question of exactly how the severity of sea ice in the Davis Strait is related to anomalies in cold air flow was left conspicuously unanswered.

Two features of their work have been repeated in subsequent studies. The first is the use of a large-scale SLP anomaly pattern as the variable of reduced complexity to describe interannual atmospheric variability (*e.g.,* Mysak et al. 1996; Deser et al. 2002; Brauch and Gerdes 2005). The SLP anomaly pattern identified in Rogers and Van Loon (1979) closely resembles the SLP pattern associated with the North Atlantic Oscillation (NAO), the first eigenvector of North Atlantic SLP. Consequently, the NAO index, eigenvalues of the NAO eigenvector, became a popular time series against which to correlate sea ice anomalies.

The second feature is to leave as ambiguous or, more commonly, unquantified the mechanisms by which the meteorological conditions associated with NAO anomalies over the Labrador Sea and Baffin Bay influence sea ice conditions (*e.g.,* Prinsenberg et al. 1997; Deser et al. 2000; Krahmann and Visbeck 2003; Deser and Teng 2008). It is natural to wonder what proportion of the ice anomaly associated with changes to "cold air flow" is due to changes in sea ice advection versus enhanced local thermodynamic production or reduced local melting. It is also interesting that in the three decades since the work of Rogers and Van Loon there has been little progress in refining this explanation more quantitatively.

Many studies have suggested links between decadal time scale atmospheric variability in the North Atlantic and hydrographic variability in the Labrador Sea (Hakkinen and Rhines 2004; Yashayaev 2007). However, none have convincingly linked low frequency atmospheric variability, Labrador Sea hydrographic variability, and Labrador Sea sea ice variability. Attempts at explanations can be found with a small number of numerical model-based studies, (*e.g.,* Ikeda et al. 1988), but these invariably suffer from problems which will be elaborated upon in Section 1.6.

The shortcomings of the explanations offered by those who have focused on purely atmospheric causes to interannual sea ice variability are understandable. Given the coupled nature of the sea ice-ocean-atmosphere system, it is probably impossible to formulate a more quantitative explanation without incorporating further knowledge of concomitant ocean state variability.

Postulation of hydrographic causes

The ocean state is an important determinant of the locations of sea ice formation, transport, and melt. Therefore, hypotheses emphasizing oceanic variability have also been proposed.

For a given seasonal cycle of atmospheric and radiative conditions, the formation of sea ice is possible in only a particular range of hydrographic conditions. To drive the near-surface seawater to its freezing point, the specific quantity of enthalpy which must be removed depends sensitively on the vertical distribution and lateral transport of heat and salt in the underlying water column.

In short, for a given reduction of seawater enthalpy the propensity for sea ice formation is greater in an ocean column which has a shallow and cold surface layer which is well-stratified (and hence isolated) from the deeper ocean. A cold and shallow surface layer requires less atmospheric heat loss to drive the seawater enthalpy to its salinity-determined freezing point. Moreover, the isolation of a well-stratified upper ocean can be maintained in the presence of seawater density increase resulting from surface heat/buoyancy loss and the release of high-salinity brine during sea ice coalescence.[6]

The lateral transports of heat and salt are important insofar as transport can modify the stratification of the upper ocean (isolation from deeper waters) and therefore the necessary quantity of heat which must be removed for ice formation to occur. Noting the basic hydrographic features which make ice production more likely, the existing ocean-centered hypotheses can be easily understood.

Mysak and Manak (1989) postulated two oceanographic causes for interannual sea ice variability in the Labrador Sea and Baffin Bay: interannual sea surface temperature variability and the propagation of salinity anomalies into the region from upstream sources. Of these two, only the latter hypothesis is supported by observational evidence.

Mysak and Manak (1989) focused on the cyclonic transit of anomalously fresh seawater in the upper ocean through the subpolar gyre in the late 1960s, commonly referred to as the Great Salinity Anomaly. The authors recognized that over the course of several years large positive sea ice anomalies reappeared each winter in concurrence with the propagation of a low-salinity anomaly around the gyre. However, with a limited observational dataset with

[6] A positive correlation between expanding the area of a well-stratified upper ocean and sea ice extent in the northwest North Atlantic can be readily seen in so-called "hosing" numerical modeling experiments (*e.g.,* Hewitt et al. 2006).

which to work, the question of causality remained open. That is, did salinity anomalies induce sea ice anomalies or vice versa?

Observational support for the idea of upper ocean salinity anomalies inducing sea ice anomalies was soon provided by Marsden et al. (1991). In Marsden et al. (1991), measurements of July upper ocean salinity (50-600 m) from Fylla Bank on the west Greenland Coast over the period $1953 - 1986$ were compared with sea ice anomalies in the Baffin Bay and eastern Labrador Sea. The authors emphasized the role of salinity anomalies in enhancing the isolation of near surface waters from those at depth. To this point, salinity anomalies in the near surface (50-150 m), were found to have a statistically significant negative correlation with sea ice anomalies over the subsequent two winters. The temporally-lagged correlation was also found at greater depths (400-600 m) but of an opposite sign. The authors reasoned that a freshened buoyancy-isolated upper ocean will not mix down its low salinity waters to saltier subsurface waters as readily. Reduced mixing of fresh surface waters to depth disrupts the subsurface salt balance leading to an increase in subsurface salinity .

However, the interpreted link between salinity and sea ice anomalies is not without shortcomings. One complication is that the source of the near surface boundary current waters in the vicinity of Fylla Bank is the comparatively cold and fresh surface waters of the Arctic Ocean. Therefore, negative upper ocean salinity anomalies propagating into the Labrador Sea may arrive in tandem with negative upper ocean temperature anomalies. Thus, the observed positive sea ice anomalies may have been caused by the reduced seawater enthalpy extraction requirement (Reverdin et al. 1997). Without further observational support, no definitive determination of underlying cause could be made.

Additional empirical support for the notion of concurrent propagation of upper ocean hydrographic and sea ice anomalies through the Labrador Sea's branch of the subpolar gyre has accumulated in subsequent years (Deser et al. 2002). These additions to the observation record have not, however, resolved the issue of causality further. Indeed, some modeling work has suggested that enhanced upper ocean salinities of the magnitude observed during the Great Salinity Anomaly are insufficient to modify ice cover to the extent observed (Tang et al. 1999).

Not all sea ice-altering hydrographic anomalies in the Labrador Sea and Baffin Bay are inherited from sources upstream. Indeed, hydrographic anomalies can emerge from the dynamical interaction of the local sea ice-ocean-atmosphere system. The persistence of

hydrographic anomalies over multiple years in the Labrador Sea has motivated other sea ice interannual variability hypotheses.

During periods of reduced deep convective mixing in the Labrador Sea, the upper ocean may accumulate relatively fresh water from the Baffin Island/Labrador Current boundary current system (Houghton and Visbeck 2002). Enhancement of the sea ice cover might be expected from this surface freshening. Ice anomalies caused by anomalous surface freshening may continue until the recommencement of deep convection whereupon surface salinity anomalies are removed through vertical mixing with saltier waters below (Ikeda et al. 1996).

Sea ice anomalies can alter the hydrographic state in ways which affect ice propensity in successive years. Regardless of origin, positive (negative) ice extent anomalies leave less (more) ocean exposed to heat flux-driven buoyancy losses, which leads to shallower (deeper) mixed layers and reduced (enhanced) vertical transport of sensible heat and salt to the surface from depth. Therefore, by changing the amount of subsurface heat and salt brought to the surface, sea ice extent anomalies in one winter can alter the upper ocean hydrographic conditions for the next (Deser et al. 2002).

Finally, the seasonal ice melt following a winter with an unusually high sea ice volume or transport, independent of origin, can serve as the source of negative upper ocean salinity anomaly. Because sea ice in the Labrador Sea and Baffin Bay can be transported several hundred kilometers over the course of the annual cycle, ice may release its low-salinity meltwater far from its place of origin. The enhanced upper ocean stability associated with anomalous meltwater release may persist into succeeding winters with consequences for future sea ice development (Belkin et al. 1998).

1.5.3 Summary of interannual sea ice variability theories

The annual sea ice cycle in the Labrador Sea and Baffin Bay, is driven by solar insolation changes. With oscillation of solar insolation, ocean surface energy fluxes change sign, leading to the successive periods of ice formation and melt.

The leading hypotheses for interannual ice variability in the Labrador Sea and Baffin Bay invoke atmospheric variability. It is popular for proponents of atmospheric-centric hypotheses to use the wintertime NAO index to succinctly describe the atmospheric state because of its positive positively correlation with sea ice anomalies. This correlation is thought to be a result of the fact that during a positive (negative) NAO index, air-sea

ice/ocean heat fluxes and westerly-northwesterly wind forcings are greater (less), which leads to more (less) thermodynamic ice growth and offshore transport (*e.g.,* Deser and Teng 2008). Hypotheses of this type are attractive because of the statistically significant correlation and because they avoid consideration of hydrographic variability, which is very poorly understood.

Indeed, because it is so poorly understood, much less support is given hypotheses which explain interannual sea ice variability from an ocean-centric perspective. Studies have linked low-salinity upper ocean salinity anomalies in the Labrador Sea with positive ice extent anomalies. In theory, with low-salinity upper ocean anomalies, seawater buoyancy losses lead to shallower convective mixed layers, separating ice from the warm salty subsurface waters of the Labrador Sea. Moreover, in shallow stable mixed layers, seawater temperatures rapidly decrease becoming thereby more amenable to ice persistence.

Several sea ice-ocean feedbacks are possibly implicated with the generation of local hydrographic anomalies. Positive (negative) sea ice anomalies lead to negative (positive) upper ocean salinity anomalies, the implications of which have already been described. However, the extreme historical paucity of ocean observations has made it virtually impossible to demonstrate an unambiguous connection between hydrographic and sea ice anomalies.

1.6 Sea Ice Modeling in the Labrador Sea and Baffin Bay

The limitations of both atmosphere and ocean-centered hypotheses of sea ice variability which rely exclusively on the scarce observational record are plain. To understand the underlying causes of sea ice annual and interannual variability, several generations of dynamical computer models have been developed. This section reviews these efforts in roughly chronological order.

My review is confined to studies which specifically sought to understand the basin-scale evolution of sea ice in the study region.[7] The key insights gained from the reviewed work, both in terms of the relevant physical processes and modeling techniques, are emphasized. Such an emphasis is made so as to expose some outstanding scientific questions and to lend credibility to the technical design choices made during the formulation of my numerical model.

[7]Research into small-scale sea ice processes is outside of the scope of this thesis.

A discussion of modeling in the Labrador Sea would not be complete without mentioning that a great deal of effort has been directed to the simulation of its general circulation, transports, and small-scale features. The interested reader is directed toward the work of Spall and Pickart (2003), Treguier et al. (2005), Straneo (2006), Lu et al. (2007), Chanut et al. (2008), and references therein.

The reader who is uninterested in this review or already familiar with the literature detailing the historical progression of sea ice modeling work in the northwest North Atlantic should advance to the summary.

1.6.1 First generation: large-scale pan-Arctic experiments

The earliest geophysical sea ice models had a Northern Hemisphere or Arctic-North Atlantic Ocean focus; the simulation of sea ice in the Labrador Sea and Baffin Bay was merely incidental. Generally, sea ice in these early models could mechanically interact with wind and ocean stresses and exchange moisture and heat with the atmosphere and ocean.

Representation of the ocean was mainly restricted to slab mixed layer models without lateral tracer advection. A sea ice momemtum equation was solved, however, which was forced by prescribed ocean surface stress. The simulated mixed layer was supplied with a spatially and temporally constant vertical heat flux representing exchange with the deep ocean. The magnitude of the mixed layer basal heat flux was manually tuned so as to recreate sea ice observations in the Arctic Ocean. The representation of the atmosphere was limited to a prescribed non-interactive surface boundary layer. Horizontal spatial resolutions were coarse by contemporary standards; grid cells of $200 \times 200\,\mathrm{km}$ were typical.

Initially, the reproduction of a realistic annual sea ice cycle was sought. The models of Parkinson and Washington (1979), Hilber and Walsh (1982), and Walsh et al. (1985) were among the very first to simulate sea ice annual and interannual cycles. In general, these models failed to realistically recreate sea ice conditions in the sub-Arctic seas. Nevertheless, these early researchers recognized the first-order importance of including sea ice dynamics.

With respect to the Labrador Sea and Baffin Bay, the major shortcoming in these models was a gross excess of wintertime ice. Many possible reasons for excessive ice were proposed; most focused on model limitations. With respect to the ice models, the thermodynamical assumptions were considered incomplete. With respect to the ocean models, the mixed layer models were seen as unrealistic. Not unexpectedly, few suggestions were offered in

areas where little immediate improvement was anticipated - such as the atmospheric forcing fields and the parameterization of sea ice rheology - even though both also had large known errors.

Limited computational resources restricted modeling work to low grid resolutions and simple ocean models during this early period. Despite computational limitations, Hibler and Bryan (1984) examined the role of ocean circulation on sea ice extent in a groundbreaking study employing a thermodynamic-dynamic ice model coupled with a baroclinic ocean model. The simulated ice edge location in the Greenland-Iceland-Norwegian Seas was significantly improved with the northward transport of heat provided by the ocean model. Importantly, the magnitude of ocean heat flux convergence to the marginal ice zone was far greater than the prescribed mixed layer basal heat fluxes used in previous studies. Although the model domain excluded the Labrador Sea and Baffin Bay, the authors' key finding is general - the simulation of a realistic ice edge requires a three-dimensional ocean model capable of providing lateral ocean heat transport.

1.6.2 Second generation: exploring the Labrador Sea

Inspired by the results of Hibler and Bryan (1984) and others, Symonds (1986) sought to estimate the magnitude of wintertime ocean-sea ice heat fluxes and associated ice growth/melt rates on the southern Labrador Coast. By employing a thermodynamic sea ice model and a suite of observations of the time-varying atmospheric boundary layer, ocean mixed layer temperature, and sea ice cover, the magnitudes of sea ice-ocean fluxes were inferred as a residual.

Sea ice-ocean heat fluxes inferred by the author had magnitudes which far exceeded earlier assumptions. Furthermore, the analysis revealed that, from north to south along the Labrador Coast, thermodynamic ice growth rates gradually changed sign from positive to negative. Therefore, the existence of ice in regions with negative thermodynamic growth rates affirmed the important role of sea ice advection in the Labrador Sea. Too little was known about the ocean exchange processes in the region for the origin of the sensible heat responsible for ice melting to be conclusively identified.

Noting the findings of Symonds (1986), Ikeda et al. (1988) modeled sea ice on the Labrador Shelf using a sea ice-mixed layer model with an unprecedented horizontal resolution, 50×50 km. To compensate for a lack of lateral ocean heat transport to the ice edge, the

prescribed mixed layer basal heat flux was manually tuned to $35\,\mathrm{Wm}^{-2}$, an order of magnitude greater than earlier models. The enhanced mixed layer basal heat fluxes somewhat ameliorated the problem of excess ice extent encountered in earlier modeling studies.

The study of Ikeda et al. (1988) also considered the role of interannual atmospheric variability on sea ice in the region. The numerical simulations employed identical initial ocean conditions while varying the model's atmospheric forcing fields. Aspects of the observed interannual ice variability were recreated in the simulations which advanced an atmosphere-centric view of sea ice interannual variability.

The authors concluded that interannual ice variability in the southwest Labrador Sea could be traced to the thickness of ice formed on the northern Labrador Shelf. Unusually thick ice, associated with unusually high ocean-atmosphere heat fluxes, can be advected farther (persist longer before melting) along the Labrador Coast on the Labrador Current. The authors also noted that ocean-atmosphere fluxes across the Labrador Coast are spatially correlated. Consequently, high atmosphere-ocean heat fluxes were also suspected to increase the southerly ice extent by reducing the quantity of upper ocean sensible heat available to melt ice transported by the Labrador Current.

The simulations of the sea ice annual cycle also revealed discrepancies, most notably with respect to the timing of ice retreat and location of the offshore ice edge. Several causes were put forward including 1) inaccurate initial ocean conditions and northern ice open boundary conditions, 2) the magnitude of prescribed downwelling radiation, 3) missing lateral ocean tracer transport, and 4) missing thermodynamic sea ice processes.[8]

Yao and Ikeda (1990) extended the work of Ikeda et al. (1988) in a nearly identically parameterized model but with the important addition of a prescribed temporally constant lateral flow field for the advection of mixed layer properties. It was seen that with lateral tracer transport, the southernmost reach of sea ice on the Labrador Shelf was extended. Over the course of the simulation, waters cooled on the north Labrador Shelf were advected by the Labrador Current to the south, gradually displacing the warmer waters on the southern shelf. As a consequence, upon reaching the southern shelf, ice advected on the Labrador Current encountered less heat, melted more slowly, and therefore was advected farther than before.

[8] In this case, the missing ice model process was a representation of thermal inertia, liquid brine pockets within the interstitial ice matrix.

Interestingly, the offshore ice edge location was found to be largely insensitive to lateral ocean heat transport. The relative unimportance of lateral ocean heat transport led the authors to conclude that the offshore ice edge was maintained mainly by vertical mixing processes in the vicinity of the marginal ice zone (the sea ice-ocean boundary). That is, the seaward advection of ice is arrested by melting in warmer water brought to the surface via vertical mixing within the seasonally-deepened mixed layer. The authors further argued that vertical mixing processes were relatively unimportant on the southern Labrador Shelf because of the absence of warm subsurface waters there.

Finally, it was noted that substantial adjustments were required of the model's initial ocean state, originally derived from a climatology, to simulate the observed time evolution of a particular sea annual cycle. Thus these authors elucidated the critical importance of both lateral ocean tracer transport and an accurate initial ocean state for the realistic simulation of sea ice in the region.

1.6.3 Third generation: ocean mixed layers and the marginal ice zone

New appreciation for the role of sea ice-ocean mixed layer interaction in the region sparked several important lines of research. These aimed to elaborate details of the evolving mixed layer across the sea ice front, reproduce sea ice-mixed layer observations in numerical models, and ascertain the extent to which sea ice alters the development of the mixed layer near sites of deep convection (Tang 1991; Tang and DeTracey 1998; Tang et al. 1999). For the purposes of sea ice variability, the main finding of the above-cited line of research was a confirmation of the central role played by vertical and lateral ocean tracer transport for the maintenance of the sea ice edge.

Based on these studies, two requirements were established for realistic basin-scale sea ice simulations in the Labrador Sea and Baffin Bay. First, slab mixed layer ocean models are totally inadequate. At minimum, the ocean should be represented in three dimensions with a prognostic velocity field and tracer advection. Second, the ocean state must evolve in the model from initial conditions which have accurate spatial distributions of heat and salt.

1.6.4 Fourth generation: coupling to prognostic 3D ocean models

Ikeda et al. (1996) were probably the first to analyze the annual sea ice cycle in the Labrador

Sea with the aid of a three-dimensional prognostic ocean model coupled to a dynamic-thermodynamic sea ice model. The $1/3^\circ$ model (approximately 32 km in the North Atlantic) was parameterized for the Labrador Sea, initialized with a manually-tuned ocean climatology, and forced with various reconstructions of wintertime atmospheric conditions. These atmospheric reconstructions corresponded to three years associated with varying levels of sea ice cover. As before, the authors sought to determine how well sea ice conditions could be reproduced by varying interannual atmospheric conditions alone; initial ocean conditions were replicated for each model run.

In the subsequent analysis of the model-data discrepancies, the authors identified that the major factors limiting the fidelity of ice reproduction were uncertainties in the initial ocean conditions, atmospheric forcing fields, and the sea ice-ocean northern open boundary conditions.

As significant improvements in these areas were not expected, the acknowledgment of these conclusions led to the general abandonment of efforts to reproduce observed realizations of the sea ice annual cycle. Instead, later work mainly focused on understanding the effect of using incremental elaborations to both the sea ice and ocean model components. Yao et al. (2000) experimented with multiple ice thickness categories while the Zhang et al. (2004) allowed ice to have thermal inertia. The improvements realized with both features were minor. Finally, the impact of the explicit (partial) representation of mesoscale eddies in Labrador Sea in a $1/6^\circ$ coupled sea ice-ocean model was examined by Zhang et al. (1999). To date, there have been no additional insights gained with more sophisticated sea ice thermodynamical assumptions or by high-resolution coupled sea ice-ocean models towards understanding the role of basin-scale ocean variability on seasonal sea ice variability.

1.6.5 Other modeling work of note

With respect to sea ice modeling in the Labrador Sea and Baffin Bay, two important insights come from modeling work that did not focus on understanding basin-scale sea ice annual or interannual variability.

The first insight is that the use of monthly mean wind fields is inappropriate for recreating realistic annual sea ice cycles. Tang and Yao (1992) and Tang and Gui (1996) sought to improve sub-seasonal ice motion forecasts off the western Labrador Sea in coupled ocean-sea ice models. In both studies, ice motion forecasts were improved when the ice was dynam-

ically coupled to an ocean which responded to high-frequency wind forcing as opposed to an ocean with steady currents. A wind forcing field which captures the variability in magnitude and direction associated with passing synoptic weather systems drives more realistic short time scale fluctuations in ocean currents. As ice motion in the Labrador Sea is very sensitive to ocean stresses, an ocean forced with more realistic wind stresses reduced the misfit between the simulate and observed of ice motion.

It cannot escape attention of the astute reader that the overwhelming focus of these studies is limited geographically to the western Labrador Sea. Existing modeling work has revealed little about the importance of various physical processes associated with sea ice in the Baffin Bay, Davis Strait, and Northern Slope of the Labrador Sea. However, the second insight is that lessons learned in the western Labrador Sea may be applicable to historically neglected regions to the north.

Using a highly idealized steady-state approach, Mysak et al. (1991) concluded that the wintertime maximum sea ice edge could be approximately determined by lateral ocean heat fluxes. The magnitudes of lateral ocean heat fluxes were related to the position of a particular ocean surface isotherm. The isotherm position was determined by considering prescribed fields of mean wind stress and air-sea heat fluxes. By tuning several parameters, the authors approximately recreated the ice edge position observed during two anomalous years.

Finally, Bitz et al. (2005) calculated ocean energy convergence rates to estimate the sea ice-ocean enthalpy fluxes required to maintain the sea ice at its maximum wintertime position using an unconstrained coupled sea ice-ocean-atmosphere climate model. Ocean heat flux convergence rates in the simulation were shown to be high in the vicinity of the (unrealistic) climatological position of the Labrador Sea sea ice edge.[9]

If ocean heat flux convergence does indeed set the ice edge position in the northern Labrador Sea, as the findings of Mysak et al. (1991) and Bitz et al. (2005) suggest, then the technical requirements established for simulating sea ice on the western Labrador Sea are likely applicable across the entire domain.

[9]Notably, no attempt was made to relate the variabilities of ocean heat flux convergence and sea ice extent.

1.6.6 Summary of modeling work

To summarize, sea ice modeling efforts for the Labrador Sea have significantly advanced our understanding of the basin-scale physical process important for the annual sea ice cycle. Moreover, experience with these models has revealed a set of processes requiring representation, either explicitly or through parameterizations, for essential features of the coupled system to be captured.

Physically, we now understand that wintertime sea ice grows on the relatively fresh well-stratified northern Labrador shelves and is subsequently transported by winds and ocean currents southward and seaward. The offshore advancement of the sea ice pack is limited by sea ice-ocean enthalpy fluxes. Variability in atmospheric heat fluxes affect the amount of ice production on the northern shelves. Enhanced ice production on the northern shelves, associated with unusual seawater enthalpy loss from air-sea heat fluxes, extends the southernmost ice edge position.

Seaward of the Labrador shelfbreak, sensible heat is added to the mixed layer by entrainment in the convectively-deepened wintertime mixed layer. Newly entrained sensible heat may then be laterally advected towards ice, melting it. The combination of offshore ice transport and onshore heat transport maintains the ice edge position near the confluence of the Labrador Current and the central Labrador Sea.

With respect to the technical issues concerning coupled sea ice-ocean modeling in the Labrador Sea, several key issues must be addressed:

- The sea ice model must be able to dynamically respond to wind, ocean, and internal stresses.
- Sea ice must be able to grow and melt thermodynamically depending on the net divergence of energy at the air-ice/snow and ocean-ice interfaces.
- Ocean models must explicitly represent or parameterize convective and advective transport of heat and salt.
- Ocean velocities should be prognostically coupled to ice and wind stresses.
- Atmospheric forcing fields should be as accurate as possible. Surface winds should have variability on synoptic time scales to drive realistic ice motion.
- The northernmost model boundary should be set far to the north of Davis Strait or great care must be given with the specification of northern open boundary conditions.

- Initial conditions taken from the ocean temperature and salinity climatologies should be regarded as inadequate for simulations which attempt to recreate ice conditions observed during particular years.

Finally, as far as can be determined, a sea ice thermodynamic model must include parameterizations of internal sensible heat conduction and surface energy fluxes and the provision to increase/decrease the sea ice/open water fraction within a model grid cell as a function of thermodynamic growth/melt. Beyond these requirements, there is little evidence that added complexity to sea ice thermodynamic submodels significantly improves simulations of the sea ice annual cycle.

All of the aforementioned requirements, issues, and lessons have been incorporated into the modeling aspect of this thesis. For a realistic representation of basin-scale sea ice-ocean-atmosphere interaction in the Labrador Sea and Baffin Bay, the coupled sea ice-ocean model used in this work has the minimum permissible level of complexity.

1.7 Synopsis of Thesis

The purpose of this thesis is to advance understanding of sea ice annual and interannual variability in the Labrador Sea and Baffin Bay. Presently, understanding ice variability in the Labrador Sea and Baffin Bay is constrained by incomplete knowledge of the co-evolving ocean state to which sea ice is coupled. In this thesis, I attempt to remove this impediment by creating credible reconstructions of the sea ice-ocean state. Using these reconstructions, I make inferences concerning the role of hydrography on sea ice annual and interannual variability.

Three one-year (1992-1993, 1996-1997, 2003-2004) estimates of the three-dimensional time-evolving coupled ocean and sea ice state in Labrador Sea and Baffin Bay are constructed. Each state estimate is a synthesis of a regional coupled ocean and sea ice model with 32 km horizontal resolution and a suite of contemporary *in situ* and satellite hydrographic and sea ice data. The synthesis of sea ice data is made possible with the (novel) adjoint of a thermodynamic sea ice model. Model and data are made consistent, in a least-squares sense, by iteratively adjusting several control variables (ocean initial and lateral open boundary conditions and the atmospheric state) to minimize an uncertainty-weighted model-data misfit cost function.

Chapter 2 describes in detail the coupled ocean and sea ice numerical model, adjoint state estimation machinery and method, the first-guess initial, atmospheric, and lateral ocean boundary conditions, the suite of synthesized observations with their uncertainties, and the model control variables.

Chapter 3 is a deeper qualitative review of the current understanding of the evolution and mutual interactions of the coupled sea ice-ocean-atmosphere system during the sea ice annual cycle. The ice annual cycle is chronologically described. Relevant climatological aspects of the ocean and atmosphere are introduced. Emphasis is placed on the sea-ice ocean state during and immediately preceding the seasonal ice maximum; periods when ocean variability is suspected to be important for sea ice variability.

Of the three state estimates, the one-year $1996 - 1997$ reconstruction is analyzed in depth in the chapters that follow. During the $1996 - 1997$ annual cycle, hydrographic data are abundant and the sea ice anomaly pattern is interesting. The main findings of the 1996-1997 analysis apply to the 1992-1993 and 2003-2004 periods.

Chapter 4 is a survey of the consistency of the state estimate made for the annual cycle beginning August 1, 1996. This chapter demonstrates the feasibility of synthesizing sea ice and ocean data into a coupled sea ice-ocean model using the adjoint method. The reproduction of sea ice is compared against ice concentration data (with which the model was synthesized) and ice thickness, freeboard, and motion data (data excluded from the synthesis). The consistency of the ocean in the state estimate is surveyed with a focus on the circulation, transports, and wintertime Labrador Sea mixed layer depths.

In Chapter 5 the state estimate is analyzed to make new quantitative inferences about the mass, energy, and buoyancy budgets of the sea ice-ocean system. Included in the budget calculations is a determination of the predictability of seasonal ice development based solely on local thermodynamic processes. The pattern of the sea ice-ocean surface buoyancy fluxes in the marginal ice zone is studied to determine whether a sea ice-ocean feedbacks play a role in setting the wintertime maximum ice edge position.

In Chapter 6, examination of the $1996 - 1997$ annual cycle continues with a focus on determining the role of hydrographic variability on ocean-sea ice processes which set the position of the wintertime sea ice edge. Emphasis is placed on two areas in the northern Labrador Sea during and immediately preceding the seasonal ice extent maximum. The critical role of the sea ice meltwater mixed layer stability enhancement feedback in setting the

seasonal sea ice edge maximum position is discovered and elaborated upon. Finally, the hydrographic properties of the waters in which this feedback operates (sea ice-preconditioned water) are characterized. The chapter concludes with a discussion of the generality of conclusions by considering the $1992-1993$ and $2003-2004$ one-year state estimates.

Finally, I present the thesis conclusions in Chapter 7. I discuss the implications of the thesis with respect to future interannual seasonal sea ice variability in the Labrador Sea and Baffin Bay and offer some thoughts for future progress in the effort of sea ice-ocean state estimation.

Appendix A provides a more detailed description of the sea ice thermodynamic model and the parameterization of sea ice-ocean coupling.

Chapter 2

Labrador Sea Ocean-Sea Ice State Estimation Setup

2.1 Chapter Overview

This purpose of this chapter is to describe in detail the three components of the state estimation system: the numerical model and its adjoint, the observations and their uncertainties, and the model control variables.

The organization of the chapter is as follows. The coupled sea ice-ocean numerical model and its adjoint are described first (Section 2.2). The model's first-guess initial, lateral ocean open, and atmospheric boundary conditions are then presented (Section 2.3). Next, ocean and sea ice observations (data) to which the coupled model is constrained are described (Section 2.4). The control variables for the optimization problem are then elaborated upon (Section 2.5). The chapter concludes with a summary of the state estimation system, an overview of the size of the optimization problem, and a presentation of the iterative reduction of the model-data misfit for the state estimate (Section 2.6).

2.2 The Coupled Ocean and Sea Ice Model and its Adjoint

In this section, I describe the coupled sea ice and ocean (ocean-ice) model and the automatic differentiation tools used to generate its adjoint. The spatial domain, model grid, and simulation duration are first introduced (Section 2.2.1), followed by a description of the general ocean circulation model (Section 2.2.2), the sea ice model (Section 2.2.3), and,

finally, the adjoint of the coupled model (Section 2.2.4)

In this thesis, a numerical model is used as a tool with which the climate system is simulated in a physically realistic manner thereby permitting plausible inferences about the real system to be made.

Climate models rely on approximations to reality. Some approximations are made willingly, excluding the representation of processes thought to be of marginal importance. Others are made out of necessity due to incomplete knowledge (*e.g.,* turbulence closures) or out of computational expediency (*e.g.,* the filtering of acoustic waves). At present, it is impossible to incorporate the entire range of physical processes constituting the climate system into numerical models. Therefore, model design must revolve around the reproduction of *specific* phenomena. To avoid needlessly complicating the numerical model and the analysis of model output, only aspects of the climate system essential for the reproduction of these phenomena should be included.[1]

The sea ice-ocean model used in this thesis successfully reproduces the observed patterns of large-scale sea ice variability in the Labrador Sea and Baffin Bay. The ultimate determination of a set of sufficient approximations was determined iteratively. As a starting point, I employed the approximations formulated by the Estimating the Circulation and Climate of the Ocean (ECCO) consortium in their global ocean climate model (Wunsch and Heimbach 2007). The ultimate set of approximations differs only modestly, mainly in the inclusion of a new thermodynamic sea ice model, a modification of sea ice-ocean thermodynamic coupling, and an enhancement of spatial resolution.

2.2.1 Model spatial domain, grid, and simulation duration

The horizontal spatial extent of the model is a symmetric four-sided spherical polygon which extends across the Baffin Bay and Labrador Sea. A curvilinear grid is defined within the polygon. The polygon and horizontal grid are shown in Figure 2-1.

The division of the domain into 102 $\times$ 42 cells is convenient for parallel processing and adheres to computational resource and numerical stability requirements (*e.g.,* a maximum aspect ratio of cell edges of 1.5:1 and orthogonality on the sphere). The grid is rotated to prevent the spurious accumulation of grid-scale variance, a consequence of the grid dis-

[1] A caveat to the above: the omission of physical processes from a numerical model obscures their effects. Often, the determination of the minimum set of processes to include in a numerical model involves proceeds iteratively with much trial-and-error.

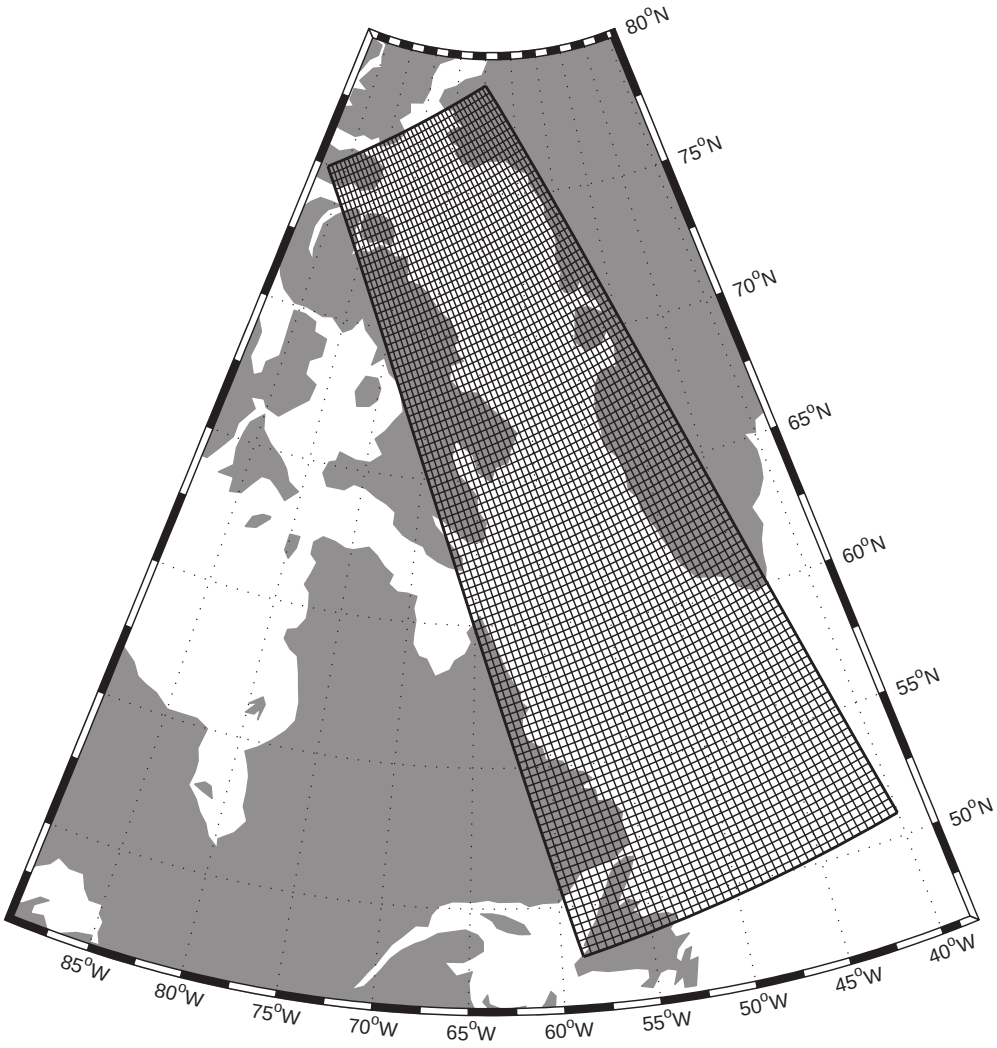

Figure 2-1: The regional model domain and horizontal grid. The model domain boundaries in the longer (predominantly north-south) direction are equal, 3.30×10^3 km. The adjacent boundaries differ in length from 0.73 to 1.42×10^3 km for the northern and southern boundaries, respectively. The horizontal grid is (approximately) defined by equally dividing the domain boundaries into 102 (north-south) and 42 (east-west) cells and then extending their cell edges along great circle arcs from one side to its opposite. Cell edge lengths are (nearly) uniform along the north-south direction, 32.3 km. In the adjacent direction, cell edge lengths vary from 33.8 km (southern boundary) to 17.3 km (northern boundary).

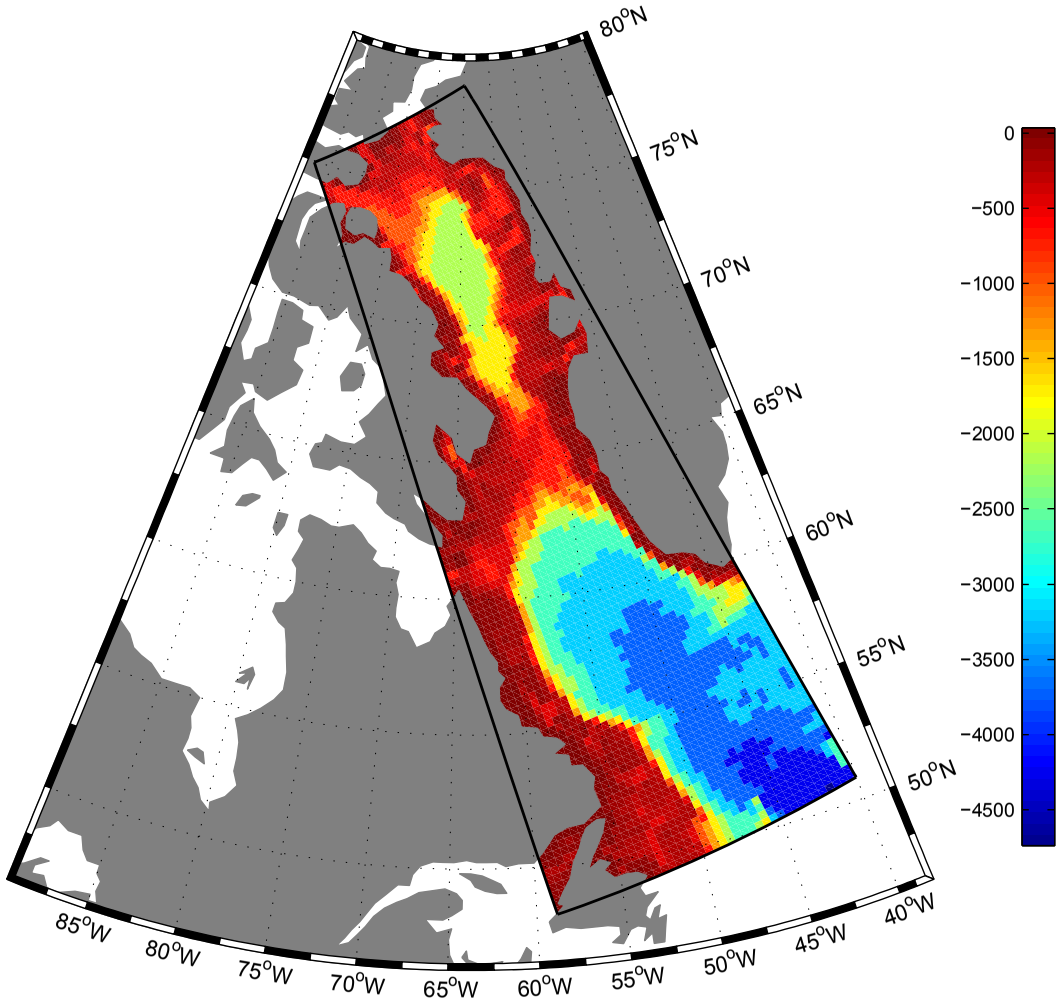

(a)

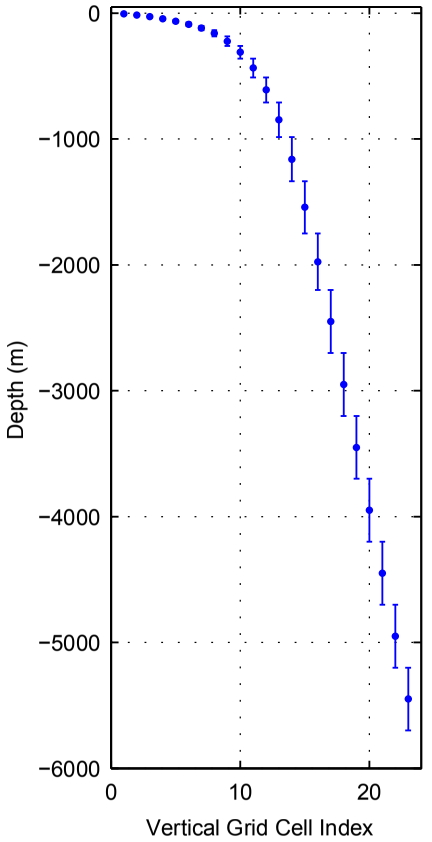

(b)

Figure 2-2: (a) The regional model bathymetry interpolated horizontally and vertically to model grid. (b) Model vertical grid spacing; dots indicate cell centers and horizontal bars indicate bounds. Note enhanced resolution in upper ocean.

cretization method (Arakawa C) and the unresolved, $\sim$ 7 km, Rossy deformation radius (Adcroft et al. 1999; Nechaev and Yaremchuk 2004; Dobricic 2006).

The model grid is divided into 23 unequal vertical levels - a identical configuration identical to that used for the generation of the global state estimates of the ECCO-GODAE consortium. Bathymetry from the 2-minute ETOPO2 of the U.S. Department of Commerce, National Oceanic and Atmospheric Administration, National Geophysical Data Center (2006) global relief model is interpolated onto the curvilinear grid with minor modifications: the opening of the Strait of Belle Isle, the removal of isolated deep ocean points, the broadening of the Greenland Shelf, and the flattening of gradients normal to the open boundaries. The bathymetry is further adjusted to conform to the coarseness of the model's vertical resolution as shown in Figure 2-2.

2.2.2 Ocean model

The ocean model used in this work is the Massachusetts Institute of Technology General Circulation Model (MITgcm) of Marshall et al. (1997a,b). My configuration of the MITgcm solves the Boussinesq and hydrostatic approximations of the Navier-Stokes equations of fluid motion on a sphere. The MITgcm is a z-coordinate model that solves prognostic equations for momentum, potential temperature, and salinity from a set of initial conditions and atmospheric and lateral ocean open boundary conditions.

The model dynamics are described by seven equations - written here in the form used in Gebbie (2004, Appendix A).

$$\frac{D\vec{u}}{Dt} = -\frac{\nabla p}{\rho_0} - 2\vec{\Omega}\hat{k} \times \vec{u} + \frac{1}{\rho_0}\nabla \cdot \tau_h + \nu_h \nabla^4 \vec{u} + \frac{\partial}{\partial z}\nu_z \frac{\partial \vec{u}}{\partial z} \tag{2.1}$$

$$\partial_z p = -g\rho \tag{2.2}$$

$$\partial_z w = -\nabla \cdot \vec{u} \tag{2.3}$$

$$\frac{D\theta}{Dt} = \kappa_h \nabla^4 \theta + \frac{\partial}{\partial z}\kappa_z \frac{\partial \vec{\theta}}{\partial z} + \nabla \cdot H_Q \tag{2.4}$$

$$\frac{DS}{Dt} = \kappa_h \nabla^4 S + \frac{\partial}{\partial z}\kappa_z \frac{\partial \vec{S}}{\partial z} + \nabla \cdot H_S \tag{2.5}$$

$$\rho = \rho(\theta, S, z) \tag{2.6}$$

$$\frac{\partial \eta}{\partial t} = -\nabla \cdot \int_{-H}^{0} \vec{u}\, dz + H_F \tag{2.7}$$

Where $\vec{u}$ is the horizontal velocity, p is the hydrostatic pressure, ρ_0 is a constant reference density, $\vec{\Omega}$ is rotation vector of the Earth, τ_h is the net surface stress from wind and sea ice forcing, and $\nu_{h,z}$ are the biharmonic horizontal and vertical viscosities, respectively. Vertical velocity, w, in the Boussinesq approximation is diagnosed from the divergence of $\vec{u}$. Enthalpy (linearly related to potential temperature, θ) and salinity, S, are subject to (biharmonic) horizontal and vertical diffusion - with diffusivity coefficients of κ_h and κ_z. Heat and salt are conserved absent external heating, H_Q, and freshening, H_F. The nonlinear equation of state of Jackett and Mcdougall (1995) is used for the determination of the three-dimensional seawater density, ρ. The linear free surface, η, is prognostically determined based on the column-integrated horizontal volume divergence and is additionally modified by net surface freshwater fluxes, H_F, due to precipitation, evaporation, and changes in the volume of sea ice and snow. Details on the derivation and numerical techniques for their implementation of these equations can be found in Adcroft (1995); Marshall et al. (1997a,b) and the MITgcm website, *http://mitgcm.org*.

Modeling the Labrador Sea presents special challenges when compared to other regions of the World Ocean. Here, a number of complex and difficult to represent processes interact over a wide range of temporal and spatial scales to give rise to a set of unique oceanographic characteristics (Marshall et al. 1998). Even in state-of-the-art configurations, numerical model solutions inevitably accumulate systematic errors. Simulations of the Labrador Sea reveal serious model drift, especially when simulations span multiple years. One of the more egregious deviations found in these solutions is the development of free convection far deeper and more spatially extensive than observed (Czeschel 2004). Indeed, reproducing the year-to-year observed hydrographic evolution in the central Labrador Sea, where the process of convective overturning is of fundamental importance, is currently beyond our capability (Treguier et al. 2005).

The configuration of the MITgcm for this thesis is intended for simulations of no longer than **one year**. The process of synthesizing model and data is facilitated by limiting the duration of systematic model error accumulation.

The ocean model is further described through its scalar parameters, subgrid scale parameterizations, and treatment of boundary conditions. Each of these aspects will now be described in turn.

Scalar parameters: viscosity and diffusivity

Ocean models are very sensitive to the choice of viscosity parameterization. By determining how momentum is dissipated and diffused, the viscosity parameterization is responsible for shaping major features of the flow field such as its structure, energetics, and transport. Generally speaking, lower viscosities improve the reproduction of observed features of ocean currents. However, numerical stability requirements place bounds on the range of allowable viscosities and therefore on the characteristics of the simulated flow field.

In the model, horizontal viscosity is implemented with both harmonic and biharmonic dissipation terms in the momentum equations. Viscosity magnitudes vary spatially to ameliorate problems stemming from horizontal grid anisotropy. Their numerical values are chosen so as to satisfy the Courant-Friedrichs-Levy, Reynolds number, and Munk Layer criteria and provide a solution which is free from numerical noise. (Griffies 2004, chap. 18). The dissipation of momentum in the vertical is parameterized with a spatially-constant harmonic viscosity.

Despite the choice of lowest permissible horizontal viscosities, the model resolution (with grid cell lengths several times that of the Rossby deformation radius) precludes the explicit reproduction of a mesoscale eddy field.

Interestingly, Jochum et al. (2008) found that sea ice extent in the Labrador Sea is particularly sensitive to the parameterization of viscosity. In their simulations, the source waters from which the East Greenland Current drew differed significantly depending on the magnitude of numerical viscosity. With less viscous flow, the boundary current entrained more warm salty subtropical-origin water from the Irminger Sea. The warmer and saltier the boundary current inflow, the greater the reduction of sea ice downstream in the central Labrador Sea.

In this thesis, inflow boundary conditions are prescribed; the hydrographic properties of boundary current inflow do not depend on the choice of viscosity. However, because of expected inconsistencies of the prescribed open boundaries, open boundary temperature and salinity are control variables.

Unresolved horizontal and vertical mixing is parameterized, in part, with Fickian diffusion. Diffusion coefficients are specified as spatially and temporally constant. The version of the MITgcm model used in this thesis has no parameterization of sub-mesoscale eddy

Horizontal Resolution	32 x 32 km to 32 x 14 km
Vertical Resolution	10 to 500 m
Ocean Grid Points	102 x 42 x 23
Sea Ice Grid Points	102 x 42
Time Step	1 hour
Ocean Lateral Open Boundary Forcing Period	30.5 days
Atmospheric Boundary Forcing Period	6 hours
Horizontal Harmonic Viscosity	6.5×10^3 to 1.5×10^4 m^2s^{-1}
Horizontal Biharmonic Viscosity	2.8×10^{11} to 1.6×10^{12} m^4s^{-1}
Horizontal Tracer Diffusivity	50 m^2s^{-1}
Vertical Viscosity	1.0×10^{-3} m^2s^{-1}
Vertical Tracer Diffusivity	1.0×10^{-5} m^2s^{-1}

Table 2.1: Scalar Model Parameters

fluxes. Hence, Fickian diffusion is included to partially account for unparameterized and unresolved horizontal tracer stirring and mixing by eddies, thought to be important for the restratification of deep convective patches (Marshall et al. 1998).

The relevant scalar parameters chosen for the ocean model component are shown in Table 2.1.

Subgrid scale parameterizations

The unresolved adiabatic stirring and diffusion of tracers and extraction of potential energy from density gradients is treated with the closures of Gent and McWilliams (1990) (GM) and Redi (1982) as implemented by Griffies (1998). The spatially and temporally constant GM coefficient of 1×10^3 m^2s^{-1} was found to be the best compromise between effective restratification of deep convection patches and excessive smoothing of the tracer fields. In the presence of steep isopycnal slopes, cross-isopycnal eddy transport is tapered to zero using the method described by Large et al. (1997).

The KPP nonlocal boundary layer mixing scheme of Large et al. (1994) parameterizes unresolved vertical ocean mixing from buoyancy loss-driven free convection, forced convection from shear instabilities, and double diffusion. Compared to less sophisticated convection schemes, vertical mixing is reasonably well parameterized with KPP when the ocean surface is partially ice-covered and model resolutions are coarse, $\Delta x \geq 15$ km (Losch et al. 2006).

However, KPP was not designed to parameterize vertical redistribution of high salinity

brine parcels released during seawater freezing/ice formation. The vertical redistribution of high salinity brine parcels (salt plumes) is poorly represented using the bulk overturning method of KPP (Duffy et al. 1999; Stössel et al. 2002). Indeed, submodels which parameterize the convective descent of salt plumes as observed (*e.g.,* Morison and McPhee 1998) have been shown to reduce the spurious gradual erosion of the permanent Arctic pycnocline beneath growing sea ice (Holloway et al. 2007; Nguyen et al. 2009). At the time of model development, no salt plume submodel had yet been incorporated into the MITgcm.[2] However, by limiting the simulation duration to one year, near-surface stratifications are probably not significantly degraded by this particular model shortcoming.

Lateral ocean open boundary conditions

Dirichlet boundary conditions of temperature, salinity, and velocity are prescribed at each time step along the lateral open boundaries. Open boundaries are closed with respect to sea ice (Section 2.3.3). Only the component of velocity normal to the open boundary is applied. Non-normal velocities are set as zero.

To reduce spurious along-boundary currents in the model domain proximate to the open boundaries, the component of velocity parallel to the open boundaries, $U_{\parallel}$, is artificially damped by means of a viscous sponge layer. The sponge layer is applied across the first three grid cells (x_1, x_2, x_3) adjacent to the open boundary with a linear damping time scale, τ_i, which increases from the open boundary to the interior from 12 to 96 hours,

$$\frac{\partial}{\partial t} U_{\parallel}(x_i) = -\frac{U_{\parallel}(x_i)}{\tau(x_i)}$$

Imbalances in the prescribed net volume flux are removed by adding a uniform barotropic component to all open boundary columns. In practice, the magnitudes of these adjustments are extremely small, less than 1×10^{-4} m s^{-1}. No meaningful change in the ocean circulation was observed as a consequence of the barotropic adjustments.

Atmospheric surface boundary conditions

Liquid, heat, and momentum exchanges across the air-sea interface are calculated between the evolving ocean surface state and a prescribed atmospheric state using the bulk param-

[2] Although one has since been added.

eterization of Large and Yeager (2004). The atmospheric variables required to calculate these fluxes are: air temperature (2 m), specific humidity (2 m), downwelling long- and shortwave radiation (surface), precipitation rate (surface), and wind vectors (10 m).

The prescribed atmosphere is non-interactive; the specified atmosphere is independent of surface conditions and implied air-sea fluxes.

In the presence of sea ice and open water in the same grid cell, air-sea and air-ice fluxes are separately calculated. The total heat loss to the atmosphere is then determined by adding each term, weighted by their relative areal fraction on the grid.

Sathiyamoorthy and Moore (2002) determined that the loss of ocean enthalpy from the melting of snow precipitated over open water in the Labrador Sea was not trivial. To capture this effect, falling snow (identified as nonzero precipitation in conjunction with surface air temperatures below 0° C) is instantaneously melted upon contact with open water, reducing seawater enthalpy.

2.2.3 Sea ice model

The sea ice model prognostically solves four fundamental equations:

$$\frac{\partial A}{\partial t} = \left(\frac{\partial}{\partial t}\right)_{thermo} - \nabla \cdot (\vec{u}_{ice}\, A) + \Gamma_A \tag{2.8}$$

$$\frac{\partial h}{\partial t} = \left(\frac{\partial h}{\partial t}\right)_{thermo} - \nabla \cdot (\vec{u}_{ice}\, h) + \Gamma_h \tag{2.9}$$

$$\frac{\partial h_s}{\partial t} = \left(\frac{\partial h_s}{\partial t}\right)_{thermo} - \nabla \cdot (\vec{u}_{ice}\, h_s) + \Gamma_{hs} \tag{2.10}$$

$$m\frac{\partial \vec{u}_{ice}}{\partial t} = -m\, f\hat{k} \times \vec{u} + \tau_{air} + \tau_{ocean} - m\nabla\phi(0) + \nabla \cdot \sigma \tag{2.11}$$

Where h is the ice thickness, A is ice concentration (fraction of ice-covered area), h_s is snow depth, $\vec{u}_{ice}$ is the ice velocity, and the Γ terms represent unresolved mechanical redistribution. With respect to sea ice dynamics, snow and ice mass are conserved. The time tendency terms for A, h and h_s are driven by separate thermodynamical and dynamical processes. In the prognostic equation for ice velocity, m is the combined mass of snow and ice per unit area, f is the Coriolis parameter, τ_{air} and τ_{ocean} are the wind and ocean stresses on the ice, respectively, $\nabla\phi(0)$ is the sea surface height gradient, and $\nabla \cdot \sigma$ is the divergence of the internal stress tensor, σ_{ij}. With these equations, sea ice is dynamically

and thermodynamically coupled to the ocean model.

The major assumptions concerning the thermodynamic and dynamic sea ice model components are now summarized. The treatment here is intended for a reader with no knowledge of sea ice models. The thermodynamic sea ice model adept can skip this section and find a more detailed treatment, including a discussion on the parameterization of the turbulent ocean-ice heat fluxes in Appendix A. The fundamental assumptions of the dynamical ice model are described in Hibler (1979) and Hibler (1980). Details of the implementation of the sea ice dynamics model in the MITgcm are thoroughly described in Zhang and Hibler (1997) and Losch et al. (2010).

Sea ice thermodynamics

Sea ice is forms based on considerations of air-sea enthalpy fluxes and ocean temperature. Precipitation falling over ice is considered snow and accumulates. Importantly, ice does not displace liquid volume in the ocean model; the ice "floats" above the sea surface. If the grid cell is not already fully ice covered, new ice growth expands across some fraction of the remaining open water. Ice may expand across an arbitrary fraction of each grid cell's surface.

The thermodynamic ice model is a variation of the classic formulation of Semtner (1976). Vertical heat flux from the ocean to the atmosphere through the ice is treated as a simple one-dimensional heat diffusion problem for a two layer system (ice plus snow if present), each with different conductivity following Parkinson and Washington (1979). Thermal diffusion is assumed to establish a steady state with respect to vertical heat fluxes within the ice on time scales shorter than the model time step (1 hour) - a reasonable assumption (Feltham et al. 2006). Consequently, vertical conductive heat fluxes are assumed constant within each layer.

A schematic of the important components of the sea ice thermodynamic model is provided in Figure 2-3.

The sea ice temperature at the ocean interface is maintained at -1.96° C, the freezing point of seawater at the surface with a salinity of 35.65. Ice and snow enthalpy are assumed to be independent of temperature and salinity. The volume of ice production is determined by relating the net air-sea enthalpy loss with the latent enthalpy of fusion of saline ice. The energy required to melt ice and snow are assumed equal to the energy required to create it.

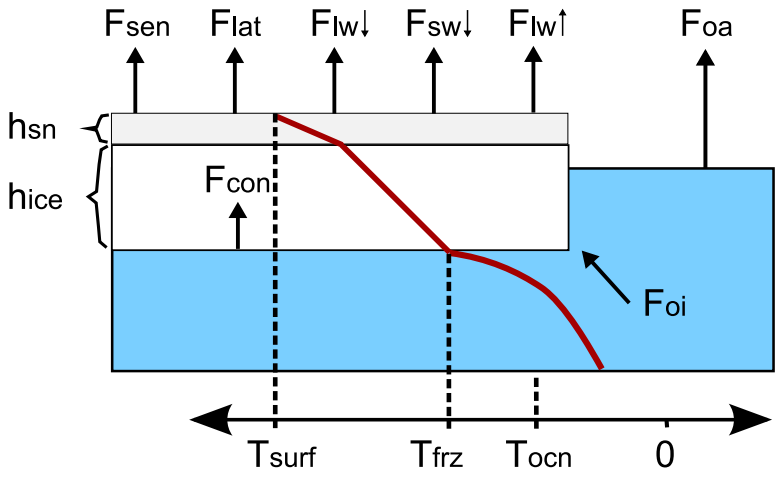

Figure 2-3: Schematic of the ocean (blue), sea ice (white), snow (light gray), and their energy fluxes in a model grid cell. Temperature profiles are shown as red lines going through each of the components above an idealized temperature axis below (Celsius). Fluxes are: F_{sen}: sea ice-atmosphere sensible, F_{lat}: ice-atmosphere latent, F_{lw}: radiative ice-atmosphere longwave (up and downwelling), F_{sw}: downwelling shortwave, F_{oa}: net open water air-sea heat flux, F_{con}: through-ice conductive heat flux, and F_{oi}: turbulent ocean-ice heat flux. Temperature profiles are linear through ice and snow and nonlinear through the upper ocean grid cell. Ice and snow thickness are h_{ice} and h_{sn}, respectively. Ice bottom temperatures are assumed to be at a fixed freezing point ($T_{frz} = -1.96^\circ$ C), which is, by construction, always colder than the mean temperature of the upper ocean grid cell, T_{ocn}. Ice (or snow if present) surface temperatures, T_{surf}, can achieve a maximum of 0° C.

Both ice and snow are modeled as being without heat capacity.

The snow (or bare ice) surface temperature is diagnostically determined such that energy fluxes at air/ice interface are balanced during growth conditions; vertical conductive through-ice heat fluxes are removed by thermal radiation and turbulent fluxes of sensible and latent heat to the atmosphere. Sensible heat extracted from seawater may only conduct from the ice bottom towards the surface; nonzero conduction always implies ice coalescence which thickens the existing ice from below. Unbalanced energy convergence at the snow (or bare ice) surface instantaneously melts snow (if present) then ice.

Snow and ice albedo are treated simply - albedo can take one of four values depending on surface type (ice or snow) and surface condition (melting or frozen). To capture the increased surface albedo associated with standing water in melt ponds, melting ice has the lowest albedo of the four categories. Turbulent air-ice fluxes are calculated using standard bulk aerodynamic formulae without corrections for variations in atmospheric boundary layer stability or air density.

In the model, shortwave radiation may penetrate the surface of snow-free ice. Sea ice-penetrating radiation is attenuated as it is absorbed during transmission. Any remaining radiation at the sea ice-ocean interface continues into the ocean, warming it.

If the weight of accumulated snow implies a snow/ice interface below the waterline in hydrostatic balance, a fraction of the snow pack is flooded - instantaneously converted to an equivalent mass of ice following Winton (2000). After flooding, the ice and sea surface's are parallel.

Finally, a major assumption in the thermodynamic ice model is that ice can form and persist when seawater temperatures in the uppermost model grid cell are above the seawater freezing point. The uppermost ocean temperature is assumed to be the mean within the entire volume. The actual upper ocean temperature profile is unresolved and assumed to be at the seawater freezing point at the sea ice/ocean interface. At each model time step, a fraction of the available seawater enthalpy is used to melt ice - an assumption based on the turbulent ocean-ice heat flux parameterization of McPhee (2008). The melting of sea ice from ocean-ice heat fluxes reduces the sea ice concentration.

Sea ice dynamics

Sea ice dynamics are treated via the popular approximations put forth by Hibler (1979). The ice dynamics equations solve a momentum equation for the ice pack and parameterizes the thickening and thinning of ice due to compressive and tensile stress-induced deformation.

The ice pack is modeled as a two-dimensional compressible non-Newtonian fluid akin to a plastic. Under the plastic assumption, sea ice can resist deformation by external stresses to a point. Sea ice yields (deforms) in stress states which exceed the critical point. The critical stress state is a function of ice thickness, areal fraction within a grid cell, and the orientation of the stresses on its lower (ocean stresses) and upper (wind stresses) surfaces. Field observations of sea ice strength have revealed that deformation is far more likely when subjected to tensile, rather than compressive, stress. This is a crucially important feature incorporated in the model.

Ice that covers less than $\sim 90\%$ of a model grid cell is assumed to have essentially no strength and therefore responds to external stresses without resisting. The implication of this assumption is that sea ice in the marginal ice zone (MIZ), a place of low ice concentrations, is in a state of approximate free drift. In a state of free drift, the sea ice momentum balance equation reduces to one with only terms for air and ocean stresses, dynamic sea surface tilt, the Coriolis term, and inertia.

Wind and ocean current stresses are calculated with constant sea ice-ocean and sea ice-atmosphere drag coefficients. Estimates for these values are highly uncertain and depend sensitively on unresolved small-scale morphological features such as ridges, keels, and ice bottom roughness (Lupkes and Birnbaum 2005; Steiner et al. 1999). The values chosen for the model are based on canonical values taken from the ice modeling literature. Ideally, wind field adjustments in the state estimate will partially compensate for the inevitable errors from this crude coupling. Consistent with the field measurements made by Greenan and Prinsenberg (1998) along the the Labrador Current, a sea ice turning angle is set at 0 degrees. A no-slip condition between ice cover and shoreline is imposed to reduce spurious separations of the ice cover from the Labrador Coast.

Sea ice lateral boundary conditions

Lateral boundaries are impermeable to sea ice. The exclusion of cross-boundary ice flux is justified by noting that the transport from outside the model boundaries ($\sim 200\,\mathrm{km}^3\,\mathrm{yr}^{-1}$) is only $\sim 10-15\%$ of the total ice volume produced within the domain on an annual basis relative to the total volume of ice grown inside the domain over that same time period ($1300-2100\ \mathrm{km}^3\,\mathrm{yr}^{-1}$) (Aagaard and Carmack 1989; Kwok 2005; Prinsenberg and Hamilton 2005).

2.2.4 Adjoint of the ocean-ice model

The MITgcm is particularly well-suited for adjoint state estimation because it has been adapted to processing by automatic differentiation tools through the course of its development. In this thesis, the Transformation of Algorithms in Fortran (TAF) automatic differentiation tool of Giering et al. (2005) was applied to the coupled sea ice-ocean numerical model to efficiently generate its adjoint.

Significant technological achievements are required to make routine the automatic differentiation of as complex a model as the MITgcm. Without these achievements, it is difficult to imagine how observations and their uncertainties could be efficiently synthesized.

The use of the TAF automatic differentiation tool for state estimation with the MITgcm is not new. The interested reader can find examples of its application in Marotzke et al. (1999), Stammer et al. (2002), Heimbach et al. (2005), Gebbie (2007), and Mazloff (2008).

The reader interested in learning more about automatic differentiation (such as alternatives to TAF, non-oceanographic applications, and its theoretical background) is suggested to Griewank and Corliss (1991), Utke et al. (2008), Giering and Kaminski (1998), and references therein.

Recipe for nonlinear optimization

The iterative procedure for synthesizing the model with observations and their uncertainties using the MITgcm and its adjoint (the adjoint method) is now outlined.

1. Starting from a first-guess set of initial (ocean and sea ice state) and boundary conditions (ocean lateral and atmospheric state), run the coupled model forward in time.

2. Quantify the misfit between model and data, weighted by a measure of the uncertainties in each observation, otherwise known as the total model-data misfit or cost function.
3. Run the adjoint model backwards in time, forcing it with the time-varying weighted model-data misfits, while noting the propagation of the the system's Lagrange multipliers.
4. Analyze the Lagrange multipliers, the sensitivities of the model control variables with respect to the cost function and use them to calculate the model control variables.
5. Adjust the first-guess set of initial and boundary conditions using the model control variables and rerun the model in forward mode.
6. Repeat from Step 2, noting a successive reduction in the model-data misfit, until the model-data misfit is acceptably small.

When model-data misfits are acceptably small, one has generated a *state estimate*.

Importantly, the state estimate is a consistent solution to the underlying physical equations embodied in the numerical model. From one time step to the next, the model physics alone propagate the system state forward. Between the first-guess and ultimate solutions, only the initial and boundary conditions differ. No unphysical adjustments or "jumps" are imposed on the system state during the model run. In this sense, the final state estimate is free or free-running.

The absence of unphysical adjustments throughout the simulation distinguishes a state estimate generated using the adjoint method from other model-data synthesis techniques (*e.g.,* sequential filters).

The adjoint method recipe for iterative nonlinear optimization presented above clearly omits many important details, such as the determination of model control adjustments from the Lagrange multipliers. The interested reader is directed to Gebbie (2004, chap. 2) for an excellent discussion of these details.

Nonlinear optimization in this thesis

With the adjoint of the coupled model, the synthesis of observations with the model is rapidly achieved. In the state estimates generated in this thesis, no more than 70 iterations were required to achieve an acceptable level of model-data misfit. Achieving consistency in

so few iterations required regular manual interventions so as to lead the solution trajectory in more fruitful directions.[3]

2.3 First-guess Initial and Boundary Conditions

First-guess initial and boundary conditions (IBC) are of great importance in state estimation. In a sense, the determination of control variable adjustments from the adjoint sensitivities is based on the assumption of a linear system response.[4] A large model-data misfit may require large control variable adjustments which, when applied, may trigger a nonlinear response. A nonlinear system response may cause the model-data misfit to decrease more slowly than expected or even to increase. A carefully chosen (or fortunate) first-guess IBC, may yield a low first-guess model-data misfit, small control variable adjustments, a linear system response and a rapid reduction in the cost function. Therefore, to achieve a low model-data misfit expeditiously, great care should be given to the first-guess IBC.

The first-guess IBC used in this thesis are presented in this section. Ocean initial conditions and lateral open boundary forcing are considered first (Section 2.3.1). The atmospheric forcing fields are then described (Section 2.3.2). The section concludes with a description of the sea ice initial conditions (Section 2.3.3).

2.3.1 Ocean initial and lateral open boundary conditions

To generate a good first-guess ocean IBC for the regional model, I employed a form of the two-level nested multiscale method described by Gebbie et al. (2006). I extract ocean IBC from an existing global ocean state estimate which encompasses the regional domain in both space in time; the regional domain is temporally and spatially *nested* with the global state estimate. The state estimate from which I extract my ocean IBC is the $1^\circ \times 1^\circ$ global ocean state estimate of ECCO project, model version 2 iteration 199 (Wunsch and Heimbach 2007). A sense of the nesting between the thesis domain and that of the encompassing ECCO state estimate is given in Figure 2-4.

[3] In most cases, the manual intervention consisted of adjusting the relative weight given to one dataset over another in the model-data misfit. For example, adjustments to the atmospheric control variables were not included in the cost function for the first several iterations.

[4] In this thesis the system is obviously the coupled sea ice-ocean model.

First-guess ocean open boundary conditions are generated by projecting the ECCO state estimate output to the open boundary grid of the regional model.

The generation of the first-guess ocean initial conditions is as follows. First, the August 1 ECCO ocean state corresponding to the year before the state estimate start date is projected to the regional model grid. Then, to bring the ECCO-based ocean initial conditions into closer consistency with the regional model configuration, the regional model is then run for one year.[5] The ocean state at the end of the spin-up year is used as the first-guess ocean initial condition.

2.3.2 Atmospheric surface boundary conditions

The first-guess atmospheric state is the NCEP/NCAR reanalysis of Kalnay et al. (1996). The atmospheric fields of the NCEP/NCAR reanalysis are 6-hourly averages on a T62 ($\sim$ 209 km) global spectral grid. The reanalysis provides all of the surface and near-surface variables required for the determination of air-sea and air-ice surface fluxes.

To avoid unrealistic gradients in space and time, all reanalysis fields are projected in space and time to the model grid and time steps using bilinear and linear interpolation, respectively.

2.3.3 Sea ice initial and open boundary conditions

The sea ice area cover is initialized with observed sea ice concentrations for the August 1, 1996 model start date. The dataset used for the ice concentration initialization is described in Section 2.4.4.

There is no ice thickness observational dataset from which to initialize the sea ice model. In the absence of data, I initialize ice thickness in an *ad hoc* manner: initial ice thickness is simply the same numerical value as the (dimensionless) initial ice concentration but with units of meters. Initialization of ice thickness using a 1:1 mapping of ice concentration on August 1 is based on the empirical relationship between these two variables found in an unconstrained multi-year model run.

The distribution of sea ice on the $1996 - 1997$ state estimate start date is atypically expansive - a residual ice from the previous sea ice annual cycle. However, this residual

[5] With the corresponding year ECCO ocean open boundary conditions and NCEP/NCAR atmospheric forcing, of course.

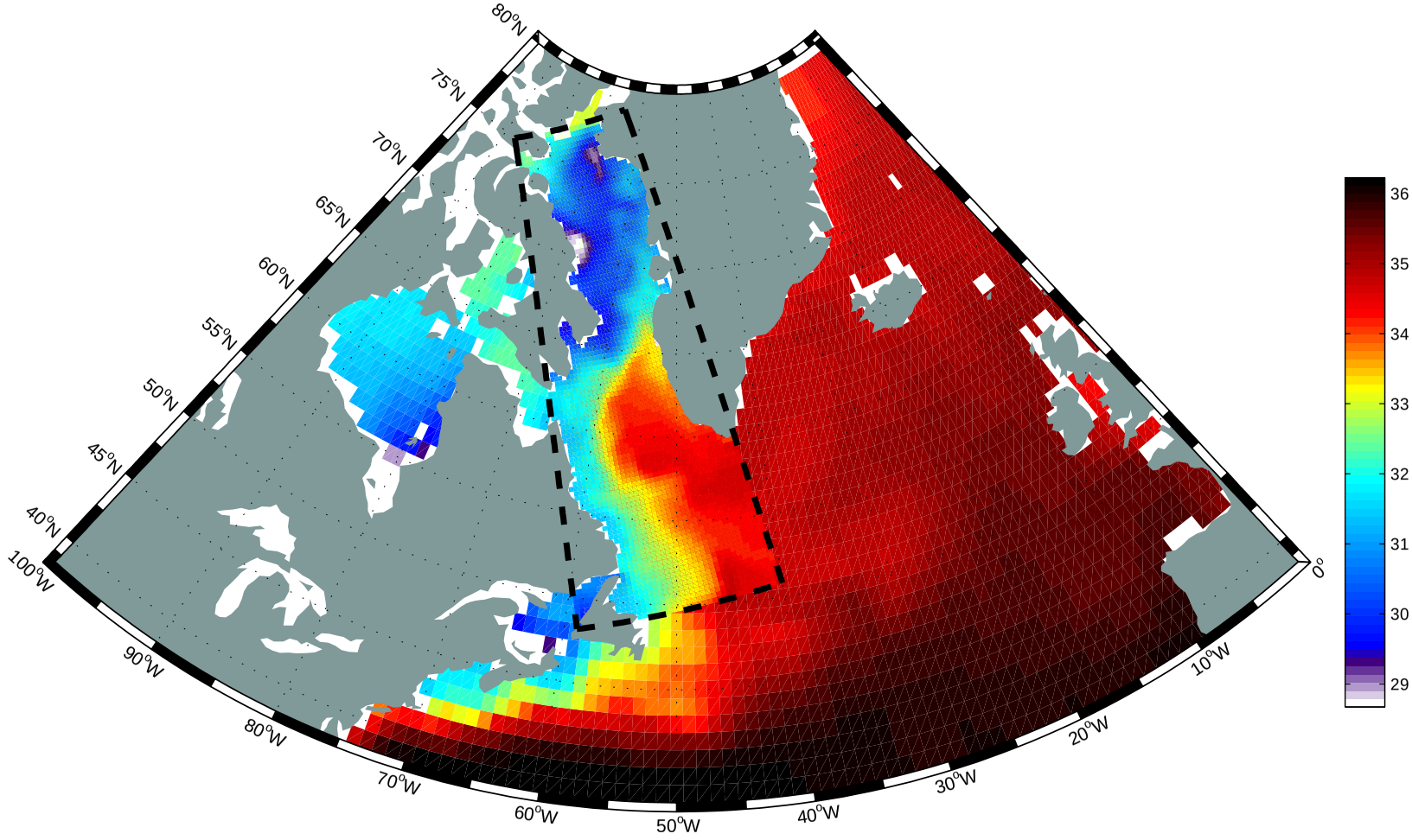

Figure 2-4: Daily-mean 10 m salinity as represented by the $1^\circ \times 1^\circ$ ECCO and the $1/3^\circ$ nested regional state estimate for March 10, 1997. Dashed black lines designate the boundary between the nested and ECCO state estimates.

melts away over the course of the following 1.5 months. Because of this extensive melting, the initial ice thickness significantly influences the upper ocean salinity in the Baffin Bay. It is expected that errors in the upper ocean Baffin Bay salinity stemming from uncertain initial ice thickness will be reduced via adjustments to the model control variables.

2.4 Observation terms of the cost function

In this section, the observations included as terms in the model-data misfit cost function are enumerated along with arguments for the choice of their uncertainties.

2.4.1 Mathematical form of the model-data misfit cost function

The mathematical form of the model-data misfit cost function is simple in the weighted least-squares framework of the adjoint method. Using the terminology and ideas of Wunsch and Heimbach (2007), the model-data misfit cost function, J, can be written,

$$\begin{aligned} J = & \sum_{t=1}^{t_f} [\mathbf{y}(t) - \mathbf{E}(t)\mathbf{x}(t)]^{\mathbf{T}} \mathbf{R}(t)^{-1} [\mathbf{y}(t) - \mathbf{E}(t)\mathbf{x}(t)] \\ & + [\mathbf{x}_0 - \mathbf{x}(0)]^{\mathbf{T}} \mathbf{P}(0)^{-1} [\mathbf{x}_0 - \mathbf{x}(0)] \\ & + \sum_{t=0}^{t_f - 1} \mathbf{u}(t)^T \mathbf{Q}(t)^{-1} \mathbf{u}(t) \end{aligned} \tag{2.12}$$

Where $\mathbf{y}(t)$ is a vector of observations at time t, $\mathbf{x}(t)$ is the model state vector, and $\mathbf{E}(t)$ is a matrix which maps the model state space to the observation space. Model initial conditions, $\mathbf{x_0}$, and control variables, $\mathbf{u}(t)$, are also written in vector form. Finally, $\mathbf{R}(t)$, $\mathbf{P}(t)$, and $\mathbf{Q}(t)$ are the time-dependent error covariance matrices for the observations, initial conditions, and model control variables, respectively.

For the observation terms of the cost function, it is the first term on the RHS of Equation 2.12 which is of interest. As $\mathbf{x}(t)$ is known from the forward model run, $\mathbf{y}(t)$ is the observational data itself, and assuming $\mathbf{E}(t)$ is easily constructed, the central challenge is to interpret and specify $\mathbf{R}(t)$.

One simple interpretation of $\mathbf{R}(t)^{-1}$ is that of a *weight*. For each individual term in the model-data misfit, the corresponding values of $\mathbf{R}(t)^{-1}$ determine the weight of its contribu-

tion to J.

Most data synthesized in this thesis are assigned no error covariance structure, $\mathbf{R}_{i,j}(t) = 0$ if $i \neq j$, allowing the individual error variance elements, σ_i^2, of $\mathbf{R}(t)$ to be written compactly,

$$\mathbf{R}(t) = \text{diag}\left(\sigma(t)_1^2, \sigma(t)_2^2, \ldots, \sigma(t)_n^2\right) \tag{2.13}$$

With $\mathbf{R}(t)$ written in the above form, the relationship between weight and error variance is clear - large error variances correspond to small weights and vice versa.

The error variance specified for a datum need not be based on measurement error. Indeed, most of the error variances specified in this thesis are educated guesses of the minimum model-data misfit achievable given known (and anticipated) numerical model errors and limitations.

To judge the consistency of a state estimate, one must know the observational data error variances and the reasoning motivating their choice; one can only ascertain whether a state estimate is consistent with its synthesized data when one can compare its model-data misfit to the specified error variances. Therefore, knowing the observational error variances is as important as knowing the observational data itself. Throughout the rest of the section, the observational data and arguments for my choice of their error variances are presented side-by-side.

A note concerning terminology. In this thesis, the term "uncertainty" in the context of a observational data takes on a specific meaning: uncertainty is equivalent to the σ of Equation 2.13. The prescription of data uncertainty is the prescription of $\mathbf{R}(t)$.

2.4.2 *In situ* oceanographic data

In situ observations of temperature and salinity (T and S) are drawn from shipboard conductivity, temperature, and depth (CTD) casts, autonomous profiling floats, and expendable bathythermographs (XBT). Excluding XBTs which measure only temperature, most *in situ* oceanographic data in the Labrador Sea come in the form of co-located measurements of T and S at some depth. The set of measurements made during a single descent or ascent of an instrument is referred to as an *in situ* profile or profile. In the model domain, XBTs, autonomous profiling floats, and CTD data are available to 1000 m, 2000 m, and 3500 m, respectively.

Oceanographic *in situ* data are drawn from two repositories, the Hydrobase 2 (HB2)

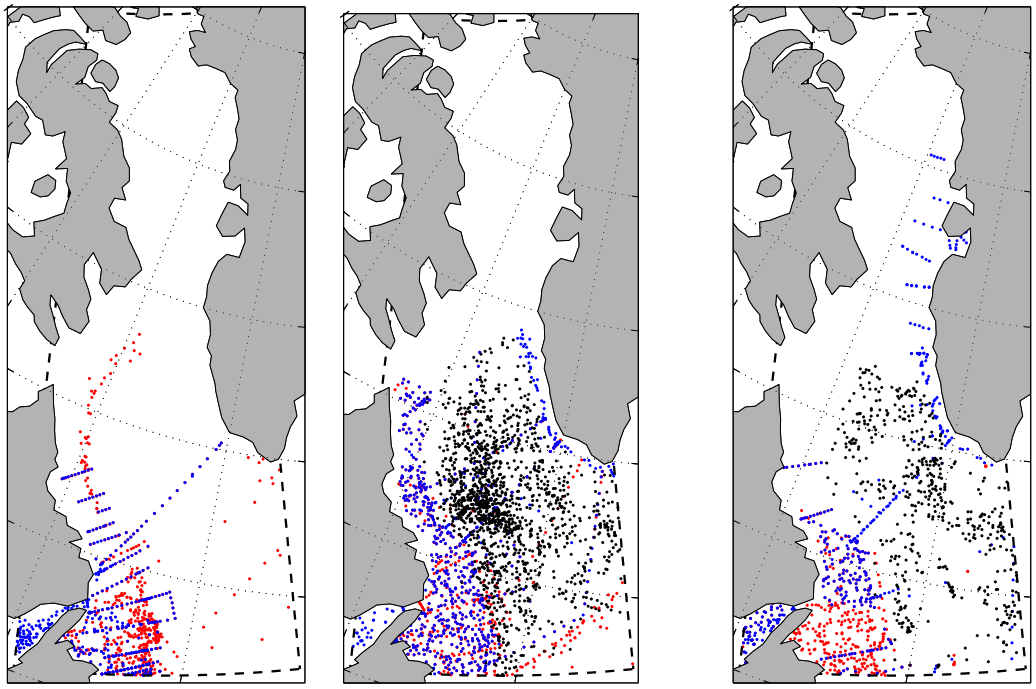

(a) 1992-1993 (b) 1996-1997 (c) 2003-2004

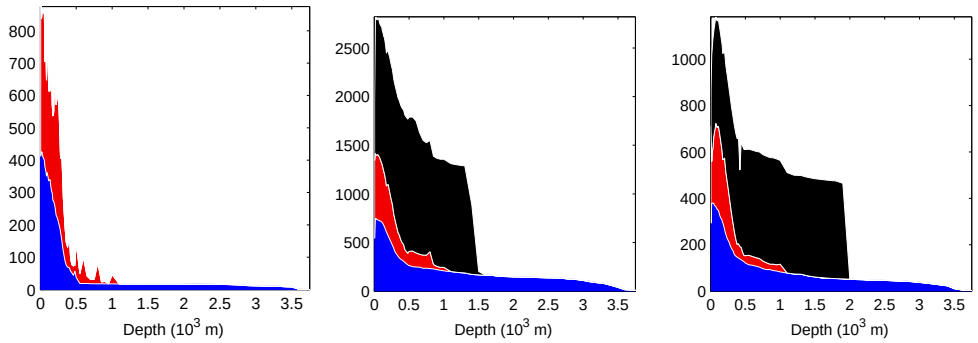

(d) 1992-1993 (e) 1996-1997 (f) 2003-2004

Figure 2-5: Oceanographic *in situ* measurements for each one-year state estimate period (August 1 - July 31) by location (a) and aggregate number as a function of depth (b). Blue - CTD casts, red - XBTs, black - autonomous profiling floats.

of Curry (2001) and the Global Temperature and Salinity Profile Program (GTSPP) from the National Oceanographic Data Center Operational Oceanography Group (2006). Both repositories perform a degree of (mostly undocumented) data quality control. Only those data tagged with the highest quality-control flag are used. Data from both repositories are combined to form a single combined dataset. The combined dataset, while still incomplete, contains profiles from all AR7W WOCE-line cruises and the additional cruises and autonomous profiling floats associated with the $1996-1997$ Labrador Sea Experiment. The distribution of *in situ* oceanographic data as a function of space and depth in the combined dataset is shown in Figure 2-5.

Many *in situ* profiles are stored in both repositories. Duplicate entries are removed to prevent their inordinate contribution to the cost function. Identifying duplicated entries is challenging because of slight differences between each repository's method of recording profile location, time, and identity (float serial number, cruise number, ship code, etc.). Duplicates are identified based on proximity in space (within 25 km) and time (within 24 hours). When a duplicate entry is found, preference is given to the repository storing the profile in the highest vertical resolution, usually GTSPP.

The evaluation of oceanographic *in situ* model-data misfit requires some form of horizontal interpolation as profile locations generally do not coincide with model grid cell centers. The model state at the time step immediately following the recorded profile time is projected to the profile location using bilinear interpolation.[6] When bilinear interpolation is unsuitable (*e.g.,* when a profile is near the coast), the model output from the two nearest alongshore model grid cells is linearly interpolated to the profile location.

In situ oceanographic data uncertainties

In this thesis, *in situ* oceanographic data are given uncertainties which are nearly entirely due to model representation error. Even with perfect initial and boundary forcings, it is likely impossible that this model could reproduce the *in situ* data to within instrument error.

The coarseness of the model grid leads to smooth T and S fields across boundary currents and mesoscale eddies. In contrast, sharp horizontal T and S gradients from mesoscale eddies are commonly observed in the Labrador Sea. For example, eddies originating from the West

[6]The simplest interpolation method for regular structured grids.

Greenland Current can maintain the signature of a warm-salty ring around a cold-fresh core while propagating hundreds of kilometers offshore over a period of weeks (Lilly and Rhines 2002; Lilly et al. 2003; Hátún et al. 2007). Given the longevity and far dispersion of these eddies and the impossibility of their representation in the model, the use of model representation error to inform the choice of *in situ* data uncertainty is justified.

The estimate of ocean model representation error in this thesis is based on a three-dimensional global estimate of T and S variability of Forget and Wunsch (2007). The Forget and Wunsch (2007) T and S variability estimate, hereafter FW2007, is based on the *in situ* T and S data sample variances within $1^\circ \times 1^\circ$ grid cells after removal of the seasonal cycle (where practical). To the extent that small-scale features (*e.g.,* mesoscale eddies) are the predominant source of this T and S variance, FW2007 is an adeqauate estimate of model representation error (Forget and Wunsch 2007).

In effect, the use of FW2007 to inform model representation error is equivalent to stating that an acceptable oceanographic *in situ* model-data misfit is achieved when the statistics of the *in situ* model-data misfit are consistent with the (estimated) *in situ* sample variances.

Before use in the model-data misfit cost function, FW2007 is modified. T and S variances are increased below 500 m to the north of Davis Strait to be of the same order of magnitude as variances estimated in the Labrador Sea. Additionally, to prevent model-data misfits from known model errors in the deep Labrador Sea (> 2000 m) from overwhelming the cost function, T and S error variances are limited to minimum values of $0.01^\circ\,\mathrm{C}^2$ and 3.3×10^{-4}, respectively.

The square root of the modified FW2007 is then used as the *in situ* oceanographic data uncertainty.

A summary of the distribution of *in situ* uncertainties in the domain as a function of depth is provided in Figure 2-6. A sense of the spatial variation of the *in situ* uncertainty field is provided at four model depth levels in Figure 2-7.

It must be noted that few *in situ* oceanographic data are available during the winter months and even fewer within the seasonal sea ice zone. As much of the model domain overlaps the seasonal ice zone in any year, the best choice of model T and S representation error may be quite different than what is used here.

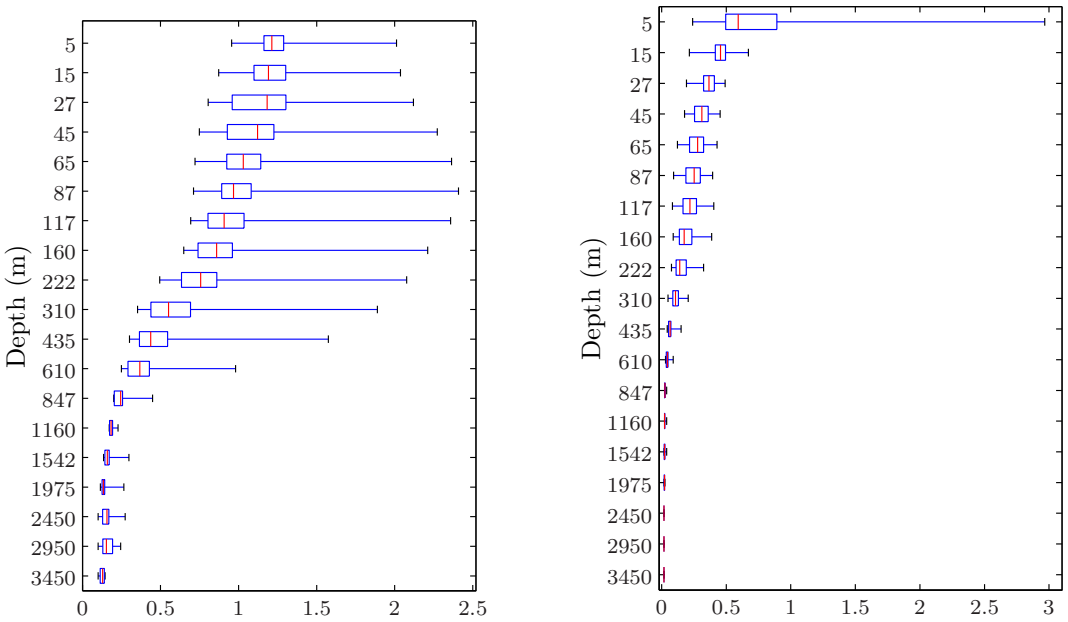

(a) Temperature (Celsius)

(b) Salinity

Figure 2-6: Box-plots of the oceanographic *in situ* data uncertainty used in this thesis at model depth levels: (a) temperature and (b) salinity. The vertial red line in each box indicates the median of the data uncertainty across the model domain at that depth. Boxes extend to uncertainty lower and upper quartiles. Box whiskers extend to data uncertainty minima and maxima. The general decrease of uncertainties with depth reflects diminishing observed variability. Large near-surface salinity uncertainties are due to large surface salinity fluxes associated with ice formation and melt.

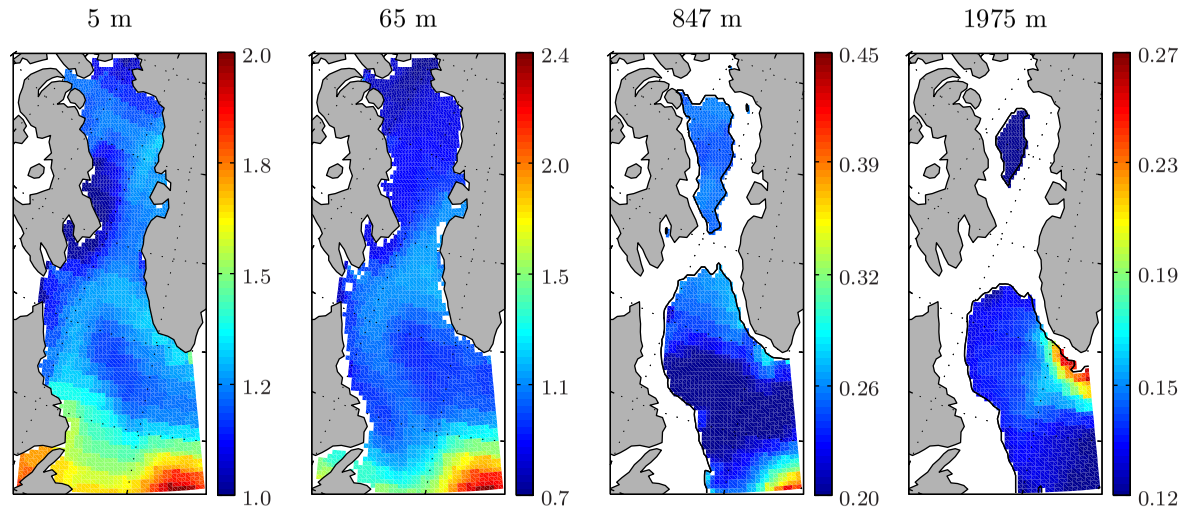

(a) Temperature (Celsius)

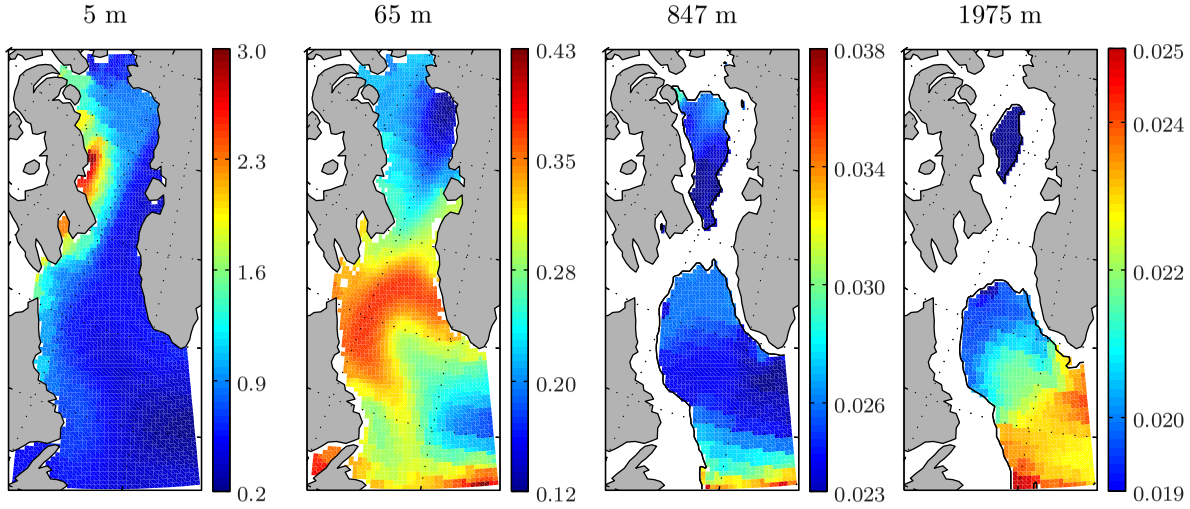

(b) Salinity

Figure 2-7: Plan view of *in situ* oceanographic data uncertainties for (a) temperature and (b) salinity at four model depth levels. Large uncertainties are found in regions with high eddy activity. Large surface salinity uncertainty near Baffin Island is related to large interannual sea ice variability.

2.4.3 Climatology of ocean temperature and salinity

Temperature and salinity (T and S) fields in the state estimates are penalized from deviating from a set of historical *in situ* ocean measurements through the addition of an ocean T and S climatology model-data misfit term in the cost function. The T and S climatology used is a combination of the 1-degree World Ocean Atlas 2001 of Stephens et al. (2001) and Boyer et al. (2001) and the 0.5-degree Gouretski and Koltermann (2004) climatologies. Following Wunsch and Heimbach (2007), the more recently-updated Gouretski and Koltermann climatology is used below 300 m while the World Ocean Atlas 2001 climatology is used above.

Ocean climatology uncertainty

The T and S climatology uncertainties used in the model-data misfit are identical to the uncertainty fields chosen for *in situ* T and S (Section 2.4.2). The use of the *in situ* T and S uncertainty fields is justified because both climatologies are based on *in situ* data. Model representation error is expected to be the limiting factor in the consistency between the model and T and S climatology data.

2.4.4 Sea ice concentration data

Sea ice concentration data for the model-data misfit are taken from the dataset of Comiso (1999, updated 2008), hereafter CM2008, provided by the National Snow and Ice Data Center. CM2008 exclusively utilizes measurements originating from Special Sensor Microwave Imager (SSM/I) passive microwave radiometers on board the F11 and F13 Defense Meteorological Satellite Program (DMSP) satellites. SSM/I measurements are processed with the latest version of the Comiso and Nishio (2008) "bootstrap" geophysical transfer algorithm. CM2008 data are provided on a daily basis on a 25×25 km polar-stereographic grid. .

The choice of CM2008 from the many alternative sea ice concentration datasets was based on five considerations. One, the daily frequency of CM2008 data is sufficient to capture important basin-scale changes to sea ice concentration from synoptic atmospheric variability. Two, the geophysical transfer algorithm used in the generation of the dataset is particularly well-suited for regions with seasonal sea ice, such as Labrador Sea and Baffin Bay (Comiso et al. 1997). Three, the use of measurements from a single instrument design

and the processing of these measurements using a single geophysical transfer algorithm allows for a simple data uncertainty formulation. Four, CM2008 has been quality controlled and is relatively free from artifacts arising from atmospheric and other sources of contamination. Five, both model and data have similar horizontal resolutions thereby mitigating model representation error in the form of missing small-scale features of ice morphology (*e.g.,* individual floes, leads, meanders in the ice edge, and filamentation in the MIZ).

To illustrate the fifth consideration, Figure 2-8 compares the representation of the sea ice field by CM2008 with a higher resolution (4.5 km pixel) product in the southwest Labrador Sea.

Sea ice concentration observation uncertainty

Sea ice concentration measurement error in CM2008 is comparable in magnitude to expected model representation error. Deciding upon appropriate uncertainties for the data therefore requires the consideration of the sources of both error types, the topic of the following sections.

Sea ice concentration measurement errors Regardless of dataset, all ice concentration data are associated with large measurement (instrument + geophysical transfer algorithm) errors. In dimensionless units of ice concentration, estimates of typical uncertainties range between 5-15% (Comiso 1999, updated 2008). Ice concentration errors primarily come from instrument resolution and the limitations of the geophysical transfer algorithms.

In terms of errors associated with instrument resolution, ice concentration datasets based on SSM/I measurements (such as CM2008) systematically overestimate the location of the sea ice edge (15% concentration contour) by 7-10 km when compared to datasets based on higher-resolution AMSR-E measurements (Comiso and Nishio 2008).

The fundamental problem facing sea ice concentration geophysical transfer algorithms which use measurements from passive microwave sensors comes from the difficulty of unambiguously distinguishing between the radiances of open water and sea ice within the sensor footprint. Ambiguities in the radiances of open water and sea ice stem from two sources: their unknown/non-distinct surface emissivities and atmospheric contamination of the open water microwave signal.

Distinguishing the proportion of open water to ice-covered ocean requires knowledge

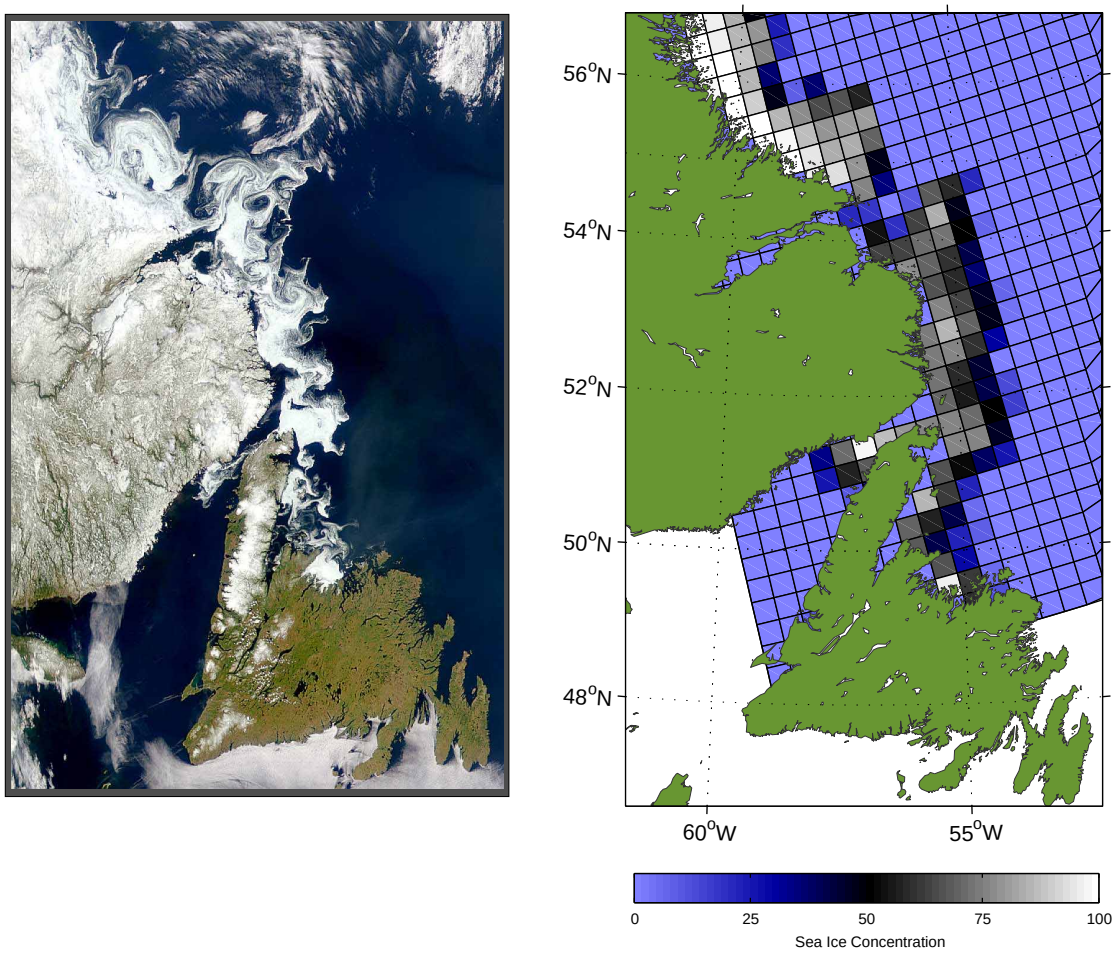

(a) SeaWiFS Quasi-true color

(b) Comiso SSM/I Bootstrap

Figure 2-8: Sea ice on the Labrador Coast and Newfoundland on May 9, 1999 a represented by (a) 4.5 km pixel resolution quasi-true color Sea-viewing Wide Field-of-view Sensor (SeaWiFS) and (b) the CM2008 sea ice concentration dataset. SeaWiFS image provided by the SeaWiFS Project, NASA/Goddard Space Flight Center, and ORBIMAGE

of sea ice emissivity as a function of frequency and polarization (Comiso et al. 1997). Ice emissivity is a complex function of ice brine volume, surface temperature, stage of consolidation, surface melting time, and snow depth - all variables which are highly time-dependent (Hwang et al. 2008). These factors are also difficult to accurately discern from space thereby introducing errors in the form of inconsistencies between the assumed and actual ice emissivities (Tonboe et al. 2006). Indeed, in regions of high concentration ($\sim 100\%$) Arctic sea ice, unknown variations of ice emissivity from precipitation and refreezing events are the single largest source of measurement error (Andersen et al. 2007). The errors associated with unknown sea ice surface emissivity would be less severe if the *range* of ice emissivities was narrow. However, possible ice emissivities span a wide range; during surface melt (or when beneath a surface meltpond) the emissivities of ice and open water can even overlap (Tonboe and Toudal 2005).

Atmospheric contamination, in the form of cloud water, water vapor, and high winds/rough seas, may modify a radiance signal from open water making it appear ice-covered to the geophysical transfer algorithm. The geophysical transfer algorithm used in CM2008 ameliorates the atmospheric contamination problem to some extent by regularly updating the time-evolving radiative properties of open water and sea ice. However, CM2008 is still expected to have large errors during stormy conditions in the MIZ (Andersen et al. 2006).

Sea ice concentration representation errors There are several sources of sea ice concentration representation error stemming from model limitations including: absence of landfast ice, the absence of mesoscale eddies, and the simple subgrid scale ice thickness distribution.

The sea ice model does not represent landfast ice, ice in direct contact with the sea floor via ridges and grounded ice floes. Without a landfast ice parameterization, tensile stresses from offshore winds cause sea ice divergence at the coast rather than at the landfast/pack ice edge which may be many tens of kilometers farther offshore (Tremblay and Hakakian 2006). The spurious divergence of sea ice at the coast in the model causes simulated ice concentrations in the vicinity of the coast to be lower than observed.

The lack of mesoscale ocean eddies is expected to cause systematic errors in simulated ice concentration. Mesoscale eddies in and near the MIZ advect ice out of the MIZ and warmer offshore waters into the MIZ - the combined effect of which is to decrease ice con-

centrations by distributing floes farther afield (thereby expanding MIZ spatial extent) and to induce ice melt (Zhang et al. 1999; Ikeda 1991). Behind the MIZ, mesoscale eddies reduce ice concentrations due to irreversible mechanical convergence (Holland 2001). Therefore, the model is expected to have an erroneously narrow MIZ and higher ice concentrations throughout.

An ideal formulation of the dynamical coupling between the ice pack, atmosphere, and ocean requires a good parameterization of the subgrid scale ice thickness distribution (Steiner et al. 1999; Holland 2001). The sea ice model represents the subgrid scale ice thickness distribution simplistically: ice is treated as a single uniform slab of time-varying thickness distributed equally over a model grid cell with no parameterization of leads, ridges, keels, or individual floes. Consequently, the model introduces errors in large-scale ice motion fields due to errors in the internal ice strength and the sea ice-atmosphere/ocean drag coefficients. As ice motion induced by wind and ocean stresses is critical to the ice cover evolution in Labrador Sea and Baffin Bay, these representation errors may be significant. However, it is difficult to anticipate how errors in the ice motion fields will affect the simulation of ice concentration.

Sea ice concentration data uncertainty specification Taking into account the known measurement and representative errors, concentration uncertainties are defined as follows. The ice concentration data uncertainty, $\sigma_{ic}(x, y)$, is represented as a baseline location-dependent concentration uncertainty, $\lambda(x, y)$, which is modified by a factor, α, a function of the observed ice concentration, $y_{ic}(x, y)$,

$$\sigma_{ic}(x, y, y_{ic}) = \lambda(x, y)\, \alpha(y_{ic}) \tag{2.14}$$

Temporal variability in σ_{ic} is implicit due to the time-dependent nature of y_{ic}.

The baseline location-dependent factor is taken from the estimates of sea ice concentration data errors described above (*e.g.,* Comiso 1999, updated 2008; Comiso and Nishio 2008) and incorporates expected measurement and representation errors in the proximity of a coastline,

$$\lambda(x, y) = \begin{cases} 15\% & \text{if} \leq 50 \text{ km from coastline,} \\ 10\% & \text{if} > 50 \text{ km from coastline.} \end{cases} \tag{2.15}$$

The expectation of higher errors in the low-concentration MIZ and lower errors where no ice is reported is incorporated into the specification of α,

$$\alpha(y_{ic}) = \begin{cases} 0.85 & \text{if } y_{ic} = 0, \\ 1.20 & \text{if } 0 < y_{ic} < 0.15, \\ 1.10 & \text{if } 0.15 \leq y_{ic} \leq 0.25, \\ 1.00 & \text{if } 0.25 < y_{ic}. \end{cases} \tag{2.16}$$

With λ and α thus defined, sea ice uncertainties are spatially and temporally varying, spanning the range 8.5% to 18%.

2.4.5 Sea surface temperature

To constrain the open ocean (ice-free) sea surface temperature (SST), the daily 0.25-degree dataset of Reynolds et al. (2007), hereafter RE2007, is synthesized with the model. RE2007 is based on the combination of retrievals from the Advanced Very High Resolution Radiometer (AVHRR) infrared instrument flown on the NOAA-14 and NOAA-17 satellites and *in situ* buoy and ship-based measurements.

The rationale behind choosing RE2007 closely parallels that used for sea ice concentration: similar resolution to the model, a reasonable observation frequency, and a consistent method and instrument type.

At 0.25-degree resolution, RE2007 SST fields are smoother across the boundary currents and mesoscale eddies than observed. As the model also fails to capture small-scale features in the SST, both model and data are expected to suffer similar representation error. An illustration of the similar spatial representation of SST in RE2007 and the model is provided in Figure 2-9.

Although RE2007 provides SST fields daily, many of the gridded values are not based on daily observations but are in fact temporal and spatial interpolations. To provide a gridded daily product in regions where AVHRR measurements are sparse (*e.g.,* the cloudy Labrador Sea), RE2007 interpolates the few available observations onto a background SST field which is based on observations from a seven-day window. As a result, the RE2007 fields evolve slowly in the domain, on time scales similar to those reproduced in the model. It is therefore expected that RE2007 and the model will both suffer from similar representation

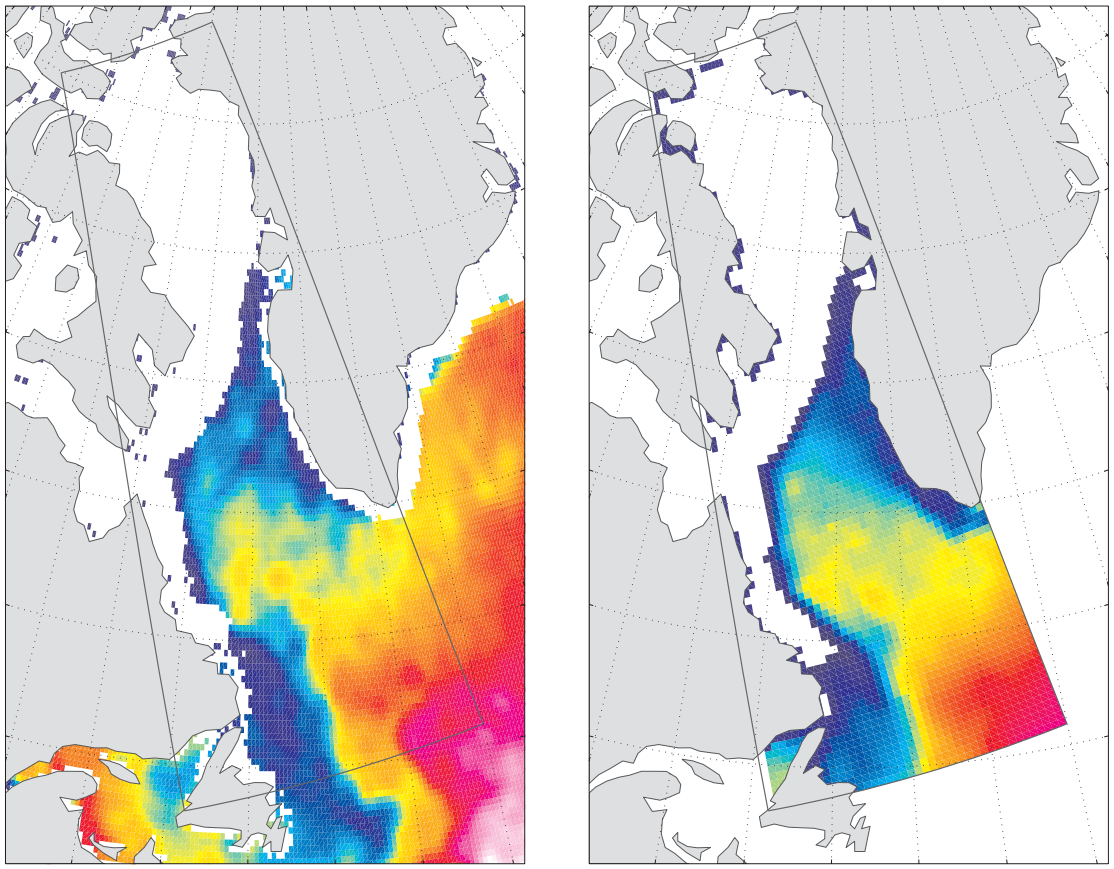

(a) SST from RE2007

(b) SST from state estimate

Figure 2-9: Sea surface temperature (SST) on June 1, 1997 as presented on (a) the 0.25-degree daily RE2007 product and (b) the $1996-1997$ state estimate (one-day mean). Cells with SST $\leq -1^{\circ}\,\mathrm{C}$ or nonzero sea ice concentration in RE2007 and state estimate are masked to facilitate comparison. Boundaries of the regional model are outlined.

errors in the time dimension as well.

The final consideration in the choice of the RE2007 product is its consistent geophysical transfer algorithm and instrument types over the entire study period. Like sea ice concentration data, the use of a consistent geophysical transfer algorithm and instrument types simplifies the specification of SST data uncertainty.

RE2007 provides SST estimates beneath sea ice. These sub-ice SST data are excluded from the cost function because they are not based on observations.[7]

SST uncertainty

In contrast to most other observational datasets synthesized in this thesis, RE2007 is provided with a spatially and temporally varying companion estimate of its uncertainty. It must be emphasized that the RE2007 uncertainty estimates are not used in the model-data misfit cost function.

It is expected that the primary source of error in the model SST fields will be representation error. The RE2007 uncertainty estimates tend to be about $0.3 - 0.8^{\circ}$ C, or $\sim 50\%$ of the magnitude of the *in situ* near-surface uncertainty fields. The model is not expected to reproduce SST data with a higher fidelity than *in situ* near-surface observations. Therefore, the same near-surface (5 m) uncertainty fields used for *in situ* temperature data are used for the RE2007 SST data.

2.5 Model Control Variables

This section is provides detail on the model variables that are adjusted to bring the model into a state of consistency with the observations. Atmospheric terms are described first (Section 2.5.1) followed by initial ocean conditions and the lateral ocean open boundary conditions (Section 2.5.2).

2.5.1 Atmosphere control variables

All the surface or near-surface atmosphere boundary variables described in Section 2.2.2 are model control variables. Collectively, these variables are labeled the atmospheric state.

[7] Sub-ice SST data are included in RE2007 so that the product can be used as a boundary condition for numerical models (Rayner et al. 2003).

The atmospheric state variables are used as control variables by allowing for adjustments to the first-guess atmospheric state, the NCEP/NCAR reanalysis (Section 2.3.2).

The prescription of atmospheric state control variable uncertainties is one of the more important considerations in ocean-sea ice state estimation. Given the direct role of the seasonally-varying atmospheric state in the evolution of the sea ice, one could imagine that with large enough uncertainties, sea ice model-data misfit could be entirely minimized using atmospheric controls. That sea ice is sensitive to atmospheric forcing is well understood. What is perhaps surprising (or troubling) is the wide range of sea ice responses in models forced by various "reasonable" atmospheric datasets (Curry et al. 2002). It is therefore important to take care with the specification of these error uncertainties if the ocean's role in sea ice variability is to be elucidated.

To prevent arbitrary modifications to the reference or first-guess atmospheric state, atmospheric state adjustments are added as penalty terms to the cost function. Recall the control variable component of the cost function from Equation 2.12,

$$J_{controls} = \sum_{t=0}^{t_f-1} \mathbf{u}(t)^{\mathrm{T}}\ \mathbf{Q}(t)^{-1}\ \mathbf{u}(t) \tag{2.17}$$

A component of $\mathbf{u}(t)$ is the spatially-varying atmospheric state control vector, $\mathbf{u}_{\mathrm{a}}(t)$. For the cost function, $\mathbf{u}_{\mathrm{a}}(t)$ is decomposed into two terms: a time-averaged component, $\overline{\mathbf{u}}_{\mathrm{a}}$, and a residual, $\mathbf{u}'_{\mathrm{a}}(t)$,

$$\mathbf{u}_{atm}(t) = \mathbf{u}'_{\mathrm{a}}(t) + \overline{\mathbf{u}}_{\mathrm{a}} \tag{2.18}$$

The interpretation of these terms is straightforward: $\overline{\mathbf{u}}_{\mathrm{a}}$ represents corrections to long-term biases in the first-guess atmospheric state and model, $\mathbf{u}'_{\mathrm{a}}(t)$ represents corrections to time-varying features of the first-guess atmospheric state (*e.g.,* misrepresentation of synoptic events) and transient model errors.

The penalization of both types of control adjustments in the cost function should depend on the uncertainty of the first-guess atmospheric state and the magnitude of adjustments required to compensate for model error. Written symbolically, the atmospheric state control

variable contribution to the model-data misfit is,

$$J_{\text{atm controls}} = \sum_{t=0}^{t_f-1} \mathbf{u}'_{\text{a}}(t)^{\text{T}}\ \mathbf{Q}'_{\text{a}}{}^{-1}\ \mathbf{u}'_{\text{a}}(t) + \sum \overline{\mathbf{u}}_{\text{a}}{}^{\text{T}}\ \overline{\mathbf{Q}}_{\text{a}}{}^{-1}\ \overline{\mathbf{u}}_{\text{a}} \tag{2.19}$$

Where now the control variable adjustment weights (uncertainties) are similarly decomposed.

The problem of choosing sensible weights for Equation 2.19 for ocean and sea ice state estimation is unsolved. The approach taken in this thesis is to choose values of $\mathbf{Q}'_{\text{a}}$ and $\overline{\mathbf{Q}}_{\text{a}}$ such that "consistent" or "acceptable" adjustments to the atmospheric state are comparable in magnitude to estimated errors in NCEP/NCAR reanalysis. In effect, it is assumed that the adjustments needed to correct for reanalysis errors in the Labrador Sea and Baffin Bay are much larger than the adjustments needed to compensate for model error.

The reader who is uninterested in the reasoning behind the choice of atmospheric state uncertainties should advance to **Atmospheric state control variable uncertainties** on page 96 where the uncertainties are presented in Table 2.3. The section concludes with the choice of weights for the atmospheric control variables used in the model-data misfit cost function.

Interpretation of $\overline{\mathbf{Q}}_{\mathbf{a}}$ and $\mathbf{Q}'_{\mathbf{a}}$

Any first-guess atmospheric state from a reanalysis is likely to have spatially-varying time-invariant biases and time-varying random errors. Spatially-varying time-invariant biases can arise from factors such as spurious wind fields in the vicinity of poorly represented orography and the use of turbulent flux parameterizations used outside of the range of meteorological conditions for which it was tuned. Random time-varying errors arise in the representation of synoptic events due to missing or sparse meteorological data and the coarse discretization of the reanalysis model's space and time domain. Adjustments to the atmospheric state need to correct for both types of errors.

A complicating factor to the already difficult task of choosing atmospheric state control uncertainties is that adjustments to the atmospheric state are expected to compensate for errors in the sea ice-ocean model. In other words, atmospheric state adjustments required

to drive the model in accord with observations may be larger than errors within the first-guess atmospheric state itself. For example, as sea ice-ocean and sea ice-atmosphere drag coefficients are poorly known (Kantha and Mellor 1989), even a perfect first-guess wind field would likely need adjustments to drive ice motion in a way consistent with observations.

Of course, it is impossible to know with certainty from the onset whether model or first-guess atmospheric state errors are dominant. All one can do is conduct the state estimate with some specified atmospheric state uncertainties and then determine whether the magnitudes of the adjustments are reasonable. A good starting point is to choose atmospheric control variable uncertainties based on published estimates of the reanalysis errors.

Atmospheric state control variable adjustments are decomposed into time-mean and residual components for the purposes of their penalization in the cost function. By separating the atmospheric state control vector in this way the magnitudes of the adjustments can be appropriately penalized. A small $\overline{\mathbf{Q}}_{\mathrm{a}}$ ($\mathbf{Q}'_{\mathrm{a}}$) allows time-independent adjustments which correct reanalysis biases (random synoptic time scale errors) to be large, and vice versa. The relative magnitudes of $\overline{\mathbf{Q}}_{\mathrm{a}}$ and $\mathbf{Q}'_{\mathrm{a}}$ are likely a function of atmospheric control variable.

In the nonlinear weighted least-squares framework of the adjoint method, no explicit assumption is made on the distribution of time-independent and time-varying adjustments. The distribution of atmospheric state adjustments is not expected to be Gaussian. However, after time-independent biases are removed from $\mathbf{u}_{\mathrm{a}}(t)$, the distribution of $\mathbf{u}'_{\mathrm{a}}(t)$ is expected to be be closer to Gaussian.

Reanalysis errors

There are three main sources of error in the NCEP/NCAR reanalysis. First, meteorological data from remote high-latitude regions, such as the Labrador Sea and Baffin Bay, on which the reanalysis system relies are sparse. Second, the reanalysis model introduces errors through imperfect representation of physics in the numerical model and (inescapable) coding errors.[8] Third, the budgets of the NCEP/NCAR reanalysis state are not closed due to its sequential filtering methodology which introduces unphysical modifications of the atmospheric state from one time step to the next. Finally, the reanalysis suffers from repre-

[8]Consider, for example, corrections to the NCEP/NCAR reanalysis model's turbulent flux parameterization after comparison with ship-based observations revealed serious disagreements (Renfrew et al. 2002; Moore and Renfrew 2002).

sentation errors due to the coarseness of its model grid. Determining acceptable magnitudes of the atmospheric state control variable adjustments should account for the aggregate effect of these errors.

Published estimates of reanalysis errors

Uncertainties for the NCEP/NCAR reanalysis are not provided alongside the atmospheric reconstruction. Nevertheless, progress has been made toward identifying errors and quantifying their magnitudes through various validation programs. Additionally, intercomparisons between the NCEP/NCAR reanalysis and other similar reanalyses, such as the European Centre for Medium-Range Weather Forecasts of Uppala et al. (2005), independent climatologies, and other atmospheric reconstructions provide a source of estimates into the likely magnitudes, distributions, and sources of error.

Over the open ocean and over sea ice, estimates of reanalysis RMS errors and biases are typically made by comparing meteorological measurements from instruments on board research vessels or mounted to buoys. Meteorological instruments are rare in the Labrador Sea and Baffin Bay. No literature was found which directly compared *in situ* meteorological measurements over sea ice in the study region with the NCEP/NCAR reanalysis. To progress, estimates from validation programs outside the study region were reviewed with the assumption that these estimates contained useful information. Only studies which drew from observations in the North Atlantic, North Pacific, and Arctic Oceans are considered.[9]

A summary of published error estimates is presented in Table 2.2.

Reanalysis representation errors

There are several sources of representation error in the reanalysis particular to the model region. These include: poorly represented polar lows (and their associated clouds, precipitation, and winds), distortion of low-level winds by coarsely represented of orography, non-represented atmospheric variance due to its 6-hour time averaging, and, probably the most serious problem for sea ice simulation, incorrectly predicted near-surface air temper-

[9]It is important to note that intercomparisons between the reanalysis and field programs must contend with issues of sampling. In the field, an observed variable is typically available as one or more point measurements while the reanalysis provides 6-hour averages over the entire grid cell. One expects differences between *in situ* meteorological data and the reanalysis to be large during the passing of synoptic weather systems, along the ice edge, in cells which are near the coast or islands, and in cells which span persistent fronts in the ocean or atmosphere.

Variable	**Type**	**Study**							
		Smith (2001)	Ladd and Bond (2002)	Curry et al. (2002)	Serreze et al. (2005)	Betts et al. (2005)	Renfrew et al. (2002)	Bromwich and Wang (2005)	Kolstad (2008)
Wind speed	RMS	3.0	1.9 to 4.4	1.41 to 1.76			4.5	0.48 to 7.07	1.11 to 1.81
($\mathrm{m\,s^{-1}}$)	Bias	-1.0	5%	-1.01 to -0.17			0.4	-1.09 to -0.59	
Air temperature	RMS	4.0		1.95 to 3.62			4.01	2.8	
($^\circ$ C)	Bias	-0.5		-1.67 to 0.69		-4.5 to 3.0	0.04	-3.0 to -2.0	
Specific humidity	RMS	1.1		0.1 to 0.4			0.82	-0.11	
($\mathrm{g\,kg^{-1}}$)	Bias	0.1		-0.02 to 0.3			0.38	-0.11	
Longwave radiation	RMS			22.92 to 41.05					
($\mathrm{W\,m^{-2}}$)	Bias			-37.16 to -14.32		-35 to -15			
Shortwave radiation	RMS			4.2 to 91.64					
($\mathrm{W\,m^{-2}}$)	Bias		22 to 94	3.99 to 78.64		10 to 70			
Precipitation	RMS			0.92 to 3.21					
($\mathrm{mm\,day^{-1}}$)	Bias			-0.04 to 0.45	-75% to +300%	-2.5 to 1.0			

Table 2.2: A summary of published estimates of RMS errors and biases in the surface and near-surface meteorological variables of the NCEP/NCAR reanalysis. Notes: Smith et al. (2001) compare to observations in the North Atlantic ($30 - 70^\circ$ N) including some Labrador Sea observations. Ladd and Bond (2002) compare to data from buoy-mounted instruments in the NE Pacific and Bering Sea. Curry et al. (2002) compare to measurements at the SHEBA ice camp in the Arctic Ocean. Betts et al. (2006) compare NCEP2 to the ERA40 reanalysis. Renfrew et al. (2002) compare to shipboard meteorological observations in the Labrador Sea. Bromwich and Wang (2005) compare to Arctic rawinsonde data. Kolstad (2008) compares reanalysis winds to QuikSCAT data in the Nordic Seas.

atures, humidities, and low-level winds proximate to the ice edge due to the use of a crude sea ice masking algorithm.

Moore et al. (1996) showed that the Labrador Sea is a region which sees the frequent development of small, intense, and short-lived cyclones, known in high-latitudes as polar lows. Polar lows, with length scales of order 200-800 km and time scales of order days, exist at the edge of what can be represented by the NCEP/NCAR reanalysis system. Martin and Moore (2006) predicted that the development and passage of polar lows, with wind speeds of $30\,\mathrm{m\,s^{-1}}$, can trigger intense air-sea heat fluxes, over $600\,\mathrm{W\,m^{-2}}$, and precipitation events. Moreover, the intense winds associated with polar lows alter the distribution and concentration of sea ice, especially in the MIZ where ice is thin and diffuse.

Ladd and Bond (2002) compared NCEP/NCAR wind direction and speed to *in situ* measurements from buoy-mounted wind sensors near the Aleutian archipelago. They found that reanalysis winds were poorly represented within a few hundred kilometers of high topographic features. The influence on topography on reanalysis surface wind quality was also noted by Kolstad (2008). In the Kolstad (2008) study, the largest disagreements between QuikSCAT and NCEP/NCAR reanalysis ocean surface winds in the Nordic Seas were found to be proximate to the high orographic features of Greenland. The thesis study region has high topographic features to the west (Baffin Island) and east (Greenland). Errors in reanalysis low-level flow are therefore expected to be larger proximate to these features.

The NCEP/NCAR reanalysis imposes a sea ice mask as a lower boundary condition to restrict turbulent air-sea fluxes under some circumstances when sea ice is observed. While this approach is sensible in theory, in practice the method used for applying this mask is problematic: a 3 m thick slab of ice with 100% concentration is imposed where average observed ice concentration in a reanalysis grid cell exceeds 55%, otherwise no mask is applied. Ice cover imposed in this manner leads to incorrect estimates of low-level atmospheric conditions in and near the MIZ where the influence of the atmospheric forcing on sea ice development is arguably the greatest.

A sense of the typical significant discrepancies between the reanalysis sea ice mask and the observed sea ice concentrations is presented in Figure 2-10.

In numerical models, air-sea fluxes across a grid cell are functions of the concentration and thickness of ice; ice conductive fluxes are inversely proportional to ice thickness. In the Labrador Sea, ice rarely exceeds 1 m in thickness and is much thinner along its seaward

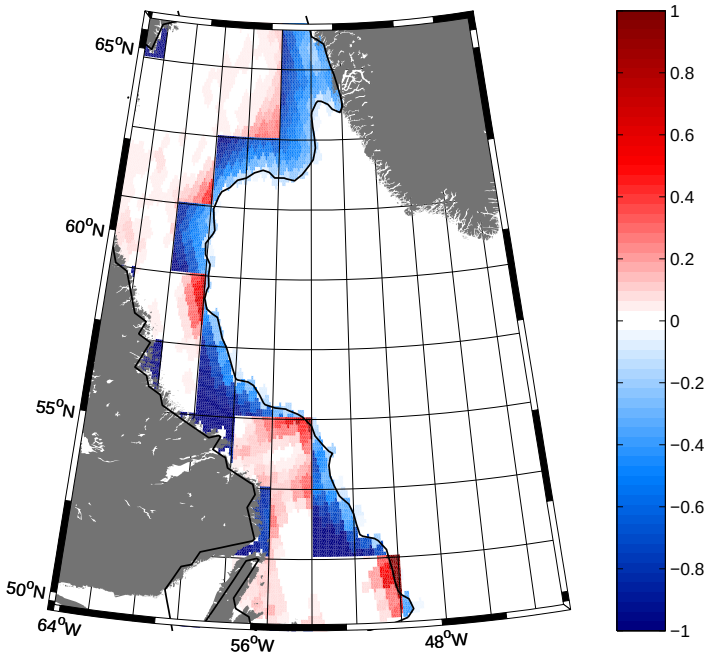

Figure 2-10: Difference between the daily-mean sea ice concentrations as represented in the NCEP/NCAR reanalysis and the CM2008 dataset (see Section 2.4.4 for details) on March 10, 1992. The reanalysis model grid is overlaid. Color indicates ice concentration difference (reanalysis - CM2008). Sea ice is observed farther east over the Labrador Sea than represented by the reanalysis.

margin (Section 4.2.2). Ice concentrations can be high over much of the domain during winter, but the transition zone between consolidated ($\sim$ 100% concentration) ice and open water can span hundreds of kilometers. The use of a 3 m thick, 100% concentration slab of ice for a lower boundary condition, while perhaps sensible for the central Arctic Ocean, is completely inapproprate for the Labrador Sea. Where the reanalysis ice slab is imposed, the atmosphere is spuriously insulated from the warmer ocean/ice below.

Forcing a numerical model with the NCEP/NCAR ice mask is likely to drive simulated ice towards the reanalysis mask. In locations where ice is present in reality but absent in the reanalysis mask, the reanalysis generates spuriously high air-sea fluxes of heat and moisture which cause spuriously high surface air temperatures and humidities. The sea ice growth rates in a sea ice-ocean simulation forced with reanalysis errors of this type will be artificially weak or even absent. Similarly, in locations where ice is absent in reality but covered with the the reanalysis slab, the reanalysis generates spuriously low air-sea fluxes which cause spuriously low surface air temperatures and humidities. The growth of sea ice in a sea ice-ocean simulation forced with reanalysis errors of this type will be artificially high.

An excellent depiction of the influence of ice edge location on the near-surface atmospheric state is found in the remarkable field study of Renfrew et al. (2002) in which dropsondes were deployed perpendicular to the ice edge and parallel to low-level winds at several locations following a cold-air outbreak off the Labrador Coast. Height and along-track profiles of air temperature and specific humidity from dropsonde measurements are shown in Figure 2-11. Remarkably, across only two degrees longitude, approximately the reanalysis grid resolution, the surface air temperature and specific humidity increase by 9° K and $0.5\,\mathrm{g\,kg^{-1}}$, respectively.

Based on the above consideration, the reanalysis surface air temperatures and specific humidities are expected to have errors of this order within a few hundred kilometers on either side of the sea ice edge.

Atmospheric state control variable uncertainties

Ideally, one would like to unambiguously translate the estimates of NCEP/NCAR reanalysis RMS and bias errors and knowledge of probable representation errors into appropriate values of the atmospheric state control variable weights. Unfortunately, no such mapping exists.

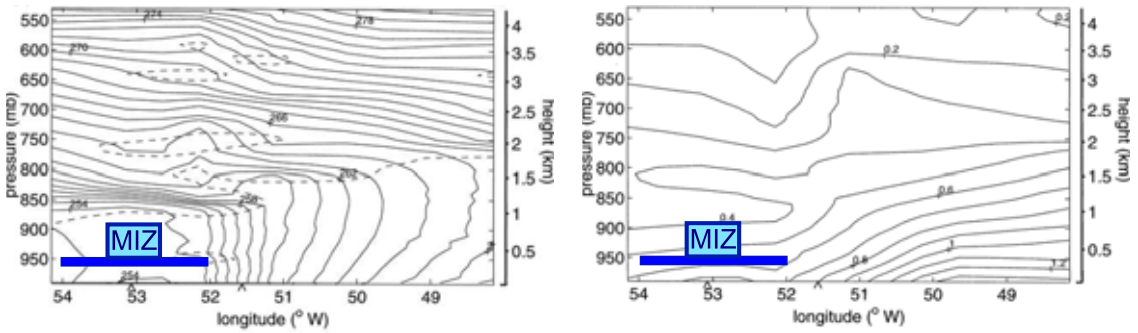

(a) Equivalent potential temperature (° K)

(b) Specific humidity (g kg^{-1})

Figure 2-11: Variation of equivalent potential temperature (a) and specific humidity (b) as a function of height and longitude as measured by dropsondes following a cold-air outbreak in the Labrador Sea. The MIZ extends between 54 and 52° W. Adapted from Renfrew et al. (1999).

However the survey of reanalysis errors permits educated guessing as to the *distribution* of its spatially-varying systematic and random errors. Atmospheric control variable adjustments are considered "consistent" if the adjustment distributions (for both $\mathbf{u}'_{\mathrm{a}}(t)$ and $\overline{\mathbf{u}}_{\mathrm{a}}$) are close to the expected (guessed) error distributions.

The specification of $\mathbf{Q}'_{\mathrm{a}}$ and $\overline{\mathbf{Q}}_{\mathrm{a}}$ assumes time-invariant error covariances with no spatial structure. Recalling Equation 2.13, $\mathbf{Q}'_{\mathrm{a}}$ and $\overline{\mathbf{Q}}_{\mathrm{a}}$ can be written symbolically as,

$$\mathbf{Q}'_{\mathrm{a}} = \mathrm{diag}\left(\sigma'^{\,2}_{\mathrm{u}},\ \sigma'^{\,2}_{\mathrm{t}},\ \sigma'^{\,2}_{\mathrm{q}},\ \sigma'^{\,2}_{lw},\ \sigma'^{\,2}_{sw},\ \sigma'^{\,2}_{\mathrm{p}}\right) \tag{2.20}$$

$$\overline{\mathbf{Q}}_{\mathrm{a}} = \mathrm{diag}\left(\overline{\sigma}^{2}_{\mathrm{u}},\ \overline{\sigma}^{2}_{\mathrm{t}},\ \overline{\sigma}^{2}_{\mathrm{q}},\ \overline{\sigma}^{2}_{lw},\ \overline{\sigma}^{2}_{sw},\ \overline{\sigma}^{2}_{\mathrm{p}}\right) \tag{2.21}$$

With subscripts identifying the individual variables in the atmospheric control vector: u, wind speed (10 m); t, surface air temperature (2 m); q, specific humidity (2 m); lw/sw, long- and shortwave downwelling radiation (surface); p, precipitation rate (surface).

The numerical values of the uncertainties are presented in Table 2.3.

Atmospheric state control variable limits

To prevent adjustments to the atmospheric state control variables that render the forcing unphysical or unacceptably unrealistic, bounds are put on the atmospheric control adjustments and on the final, adjusted atmospheric state.[10]

[10]The model adjustments are not bounded in the global ECCO state estimation framework.

Variable	**Units**	σ_i'	$\overline{\sigma_i}$
Wind speed	$\mathrm{m\,s^{-1}}$	0.5	0.9
Air Temperature	$^\circ\mathrm{C}$	2.5	2.0
Specific Humidity	$\mathrm{g\,kg^{-1}}$	0.25	0.50
Shortwave Radiation	$\mathrm{W\,m^{-2}}$	15	15
Longwave Radiation	$\mathrm{W\,m^{-2}}$	15	15
Precipitation	$\mathrm{mm\,day^{-1}}$	1.5	1.5

Table 2.3: Atmospheric state control variable adjustment uncertainties.

Before the first-guess atmospheric state is adjusted by the control variables, the control variables are bounded by a cut-off of $\pm 2.5\,\sigma'$ - a range which ideally permits $\sim 98.5\%$ of the required control variable adjustments provided the reanalysis errors are truly Gaussian. Hence, all control variable adjustment are restricted to $\pm 2.5\,\sigma'$. Control variable adjustments larger than $\pm 2.5\,\sigma'$ were not required to bring the state estimate into an adequate level of consistency with observations (see Chapter 4). The unbounded atmospheric control adjustments are used to calculate the atmospheric control variable penalty term in the cost function (Equation 2.19).

After applying the cut-off limits on the atmospheric controls and then applying the controls the first-guess atmospheric state, the adjusted atmospheric state is then subjected to another set of bounds. The upper and lower bounds for each of the atmospheric state variables in given in Table 2.4.

Variable	**Units**	**Lower**	**Upper**
Absolute wind speed	$\mathrm{m\,s^{-1}}$	n/a	35
Air Temperature	$^\circ\mathrm{C}$	-74	26
Specific Humidity	$\mathrm{g\,kg^{-1}}$	0	50
Shortwave Radiation	$\mathrm{W\,m^{-2}}$	0	600
Longwave Radiation	$\mathrm{W\,m^{-2}}$	0	500
Precipitation	$\mathrm{mm\,day^{-1}}$	0	35

Table 2.4: Atmospheric state variables' upper and lower permissible bounds.

2.5.2 Ocean initial and lateral open boundary controls

The initial ocean temperature and salinity (T and S) and the open boundary T, S and velocity field are model control variables.

All ocean control variable adjustments are included as penalty terms in the cost function. Adjustments to the initial T and S control variables are penalized using the same uncertainty field as the ocean T and S *in situ* data, described in Section 2.4.2. In the notation of the cost function, Equation 2.12, initial T and S control variable uncertainties are used to construct the $\mathbf{P}(0)$ penalization matrix.

Adjustments to the open boundary controls are penalized differently; T and S uncertainties are functions of depth only, shown in Figure 2-12. The uncertainty associated with open boundary velocity adjustments is defined as a time and space-independent constant, $1.5\ \mathrm{cm\,s^{-1}}$.

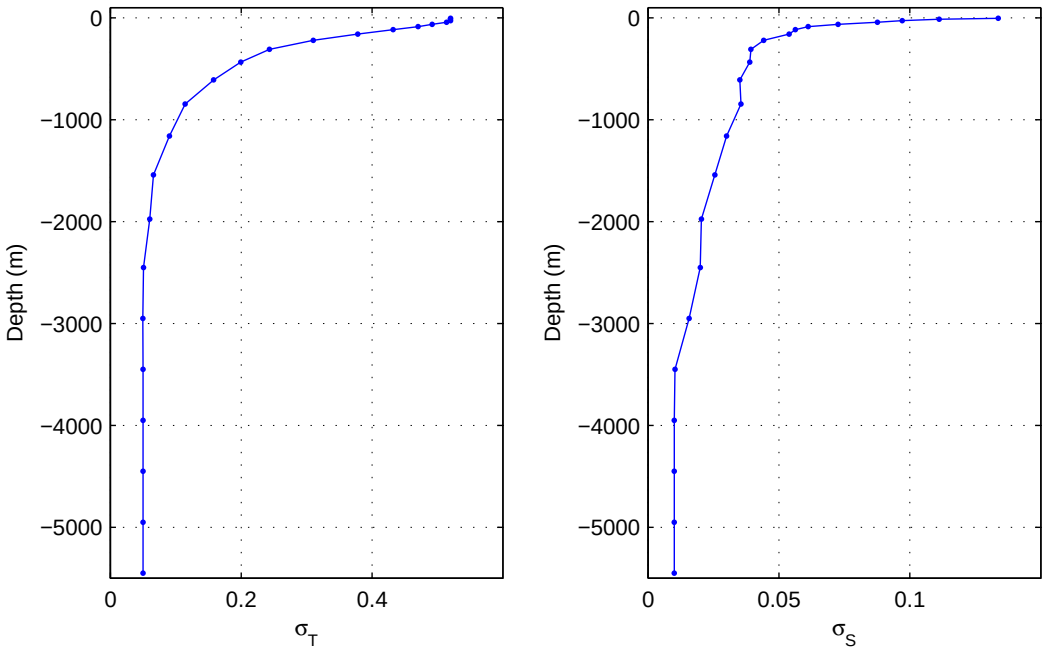

Figure 2-12: Open boundary temperature (left panel) and salinity (right panel) control variable uncertainties as a function of depth.

To prevent unphysical and unrealistic adjustments to the initial conditions, the T and S control variables are subjected to upper and lower bounds that are functions of the T and S *in situ* data uncertainty fields. The T and S initial condition control variable adjustments are bound to within $\pm 5.0\,\sigma_{\mathrm{T,S}}$.

The magnitude of open boundary control adjustments are not bounded. However, the adjusted ocean state is subject to the lower and upper bounds to assure a physically sensible lateral forcing. The bounds for the open boundary state are provided in Table 2.5.

Variable	**Units**	**Lower**	**Upper**
Temperature	$^\circ$C	-1.96	35
Salinity		0	40
Velocity	$\mathrm{cm\,s^{-1}}$	0	50

Table 2.5: Open boundary condition upper and lower permissible bounds after modification by the open boundary control variables.

2.6 Chapter Summary

This section is a summary of the chapter, providing a brief review of the several components which together allow for the generation of the sea ice-ocean state estimate: the numerical model and its adjoint, the first-guess initial and boundary conditions, the data synthesized (with their uncertainties), and the model control variables. The chapter concludes by quantifying the size of the optimization problem and presenting the iteration-to-iteration decrease of the model-data misfit cost function.

2.6.1 Coupled sea ice and ocean model

The ocean model is an approximately $1/3^\circ$ regional configuration of the MITgcm (Marshall et al. 1997a,b). The model domain spans the Labrador Sea and Baffin Bay using a curvilinear grid of $102 \times 42 \times 23$ cells in the north-south, east-west, and vertical dimensions, respectively. Viscosity and resolution limits preclude the explicit generation of a mesoscale eddy field. Free/forced convective mixing and cross/along-isopycnal eddy mixing and stirring is parameterized using the subgrid scale parameterizations of Large et al. (1994) (KPP), Gent and McWilliams (1990), and Redi (1982).

The ocean lateral boundaries are open; Dirichlet boundary conditions of temperature, salinity, and velocity are prescribed at each time step. Exchanges of heat, moisture, and momentum with the atmosphere are modeled using the bulk formulae of Large and Yeager (2004). Atmospheric state variables of surface or near-surface temperature, specific hu-

midity, precipitation, vector winds, and short- and longwave radiation are prescribed and non-interactive.

The sea ice model is a combination of separate thermodynamic and dynamic components. Sea ice thermodynamics are treated with a variation of the classic Semtner (1976) 0-layer model with several extensions including: snow, flooding, multiple albedo categories, and the turbulent ocean-sea ice heat flux parameterization of McPhee (2008). The thermodynamic component solves prognostic equations for ice area fraction within a grid cell (concentration), ice thickness, and the exchanges of salt and heat with the ocean and atmosphere.

Sea ice velocity fields are calculated using the viscous-plastic rheology assumptions of Hibler (1979): ice is given little tensile strength and a variable compressive strength which is dependent on ice thickness and concentration. Dynamical coupling between sea ice-ocean- and atmosphere uses constant drag coefficients. Model boundaries are closed to sea ice.

The adjoint of the coupled model is automatically generated using a source-to-source proprietary commercial program, TAF of Giering et al. (2005). Importantly, the adjoint of the thermodynamic component of the sea ice model is calculated. Optimization is done using a coupled sea ice and ocean adjoint model.

2.6.2 First-guess initial and boundary conditions

The first-guess ocean initial and open boundary conditions are taken from a pre-optimized global 1-degree ocean state estimate of the ECCO group (Wunsch and Heimbach 2007). The ECCO state estimate encompasses the regional domain in both space and time, spanning across each of the 3 one-year thesis state estimate periods: $1992-1993$, $1996-1997$, and $2003-2004$.

The NCEP/NCER reanalysis of Kalnay et al. (1996) is used as the first-guess atmospheric state. Reanalysis surface and near-surface state variables are interpolated in space and time onto the regional model grid.

The initial sea ice concentration field is initialized using observed values from the passive microwave-derived dataset of Comiso (1999, updated 2008). The unobserved ice thickness field is initialized in an *ad hoc* manner.

2.6.3 Synthesized observational data and their uncertainties

Observational data from several sources are synthesized with the model using nonlinear weighted least-squares. These data include: *in situ* ocean observations of temperature and salinity (T and S), a modern ocean climatology of T and S, sea ice concentration, and sea surface temperature.

Uncertainties for all ocean data are assumed to be dominated by representation errors. The magnitudes of these uncertainties is a modified form of an estimate of ocean T and S variability of Forget and Wunsch (2007). Sea ice uncertainty fields are specified using a combination of published estimates of measurement error and expected model representation error.

No other ocean data constrain the state estimate. Notably, these include several data sources used by the ECCO-GODAE consortium such as altimetric sea surface height, scatterometer wind stress, and gravimetric mean dynamic topography. These and other data were excluded from the analysis because of time constraints.

2.6.4 Model control variables

The synthesis of model and data is accomplished solely via the adjustment of model initial and boundary conditions. Specifically, the model control variables are: initial ocean T and S, open boundary T, S, and velocity, and the time-varying atmospheric state.

Adjustments to the first-guess initial and boundary conditions are included as penalty terms in the model-data misfit cost function. Adjustments to the first-guess atmospheric state are permitted within published estimates of the NCEP/NCAR reanalysis errors. Ocean initial and open boundary adjustments are penalized using uncertainties which are similar to those used for *in situ* ocean T and S data.

The final state estimate advances from timestep-to-timestep from the adjusted initial conditions by its own physics encoded in the numerical model and by forcing at its boundaries by an adjusted atmospheric state and lateral open ocean conditions.

2.6.5 Size of control problem and optimization

The complete numerical model state at any given time is represented as a vector, $\mathbf{x}(t)$, consisting of 2.5×10^5 distinct elements representing the ocean and sea ice variables: ocean

temperature and salinity, ocean and sea ice velocity, sea surface height, sea ice concentration, and ice and snow thickness. Each state estimate is run one year, 8684 1-hour time steps, for a total of 2.2×10^9 elements in each state estimate. The model control vector, $\mathbf{u}(t)$, consists of 8.9×10^8 elements. Finally, the data vector, $\mathbf{y}(t)$, contains 2.2×10^6 elements, split approximately equally between ocean and sea ice data.

Once begun, the iterative cost-function reduction advances rapidly, achieving an acceptable degree of consistency before 70 iterations.

It is convenient to compare iteration-to-iteration changes to the model-data misfit and control variable penalty terms of the cost function by examining their normalized costs. The normalized cost, J_{norm} of a set of n model-data misfits or controls, $\boldsymbol{\xi}$, is written,

$$J_{\text{norm}} = \frac{1}{n} \sum_{i=1}^{n} \xi_i \; {\Phi_{i,i}}^{-1} \; \xi_i \tag{2.22}$$

Where $\Phi_{i,i}$ is the model-data misfit or control adjustment penalty weight corresponding to the i^{th} element in the data or control set (assuming no covariance structure in $\boldsymbol{\Phi}$).

The iteration-to-iteration change to the normalized costs of several model-data misfit and control penalty terms for the one-year state estimate is shown in Figure 2-13.

The annual cycle of sea ice in the Labrador Sea and Baffin Bay is more deeply reviewed in the following chapter so as to provide context for the succeeding chapters in which the state estimates are analyzed (Chapters 4, 5, and 6).

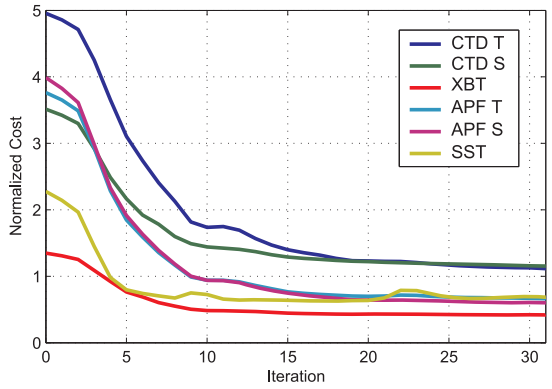

(a) Ocean *in situ* and SST

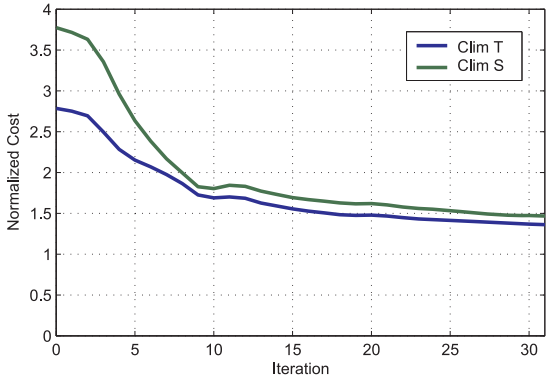

(b) Ocean T and S climatology

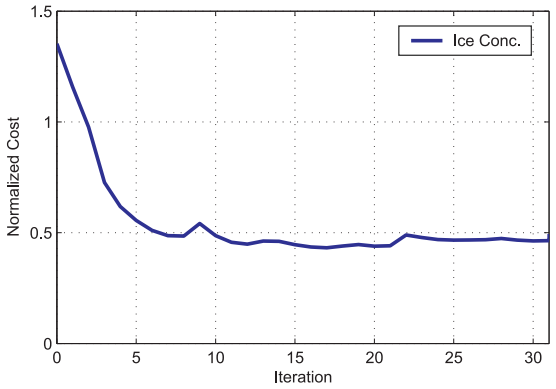

(c) Sea ice concentration

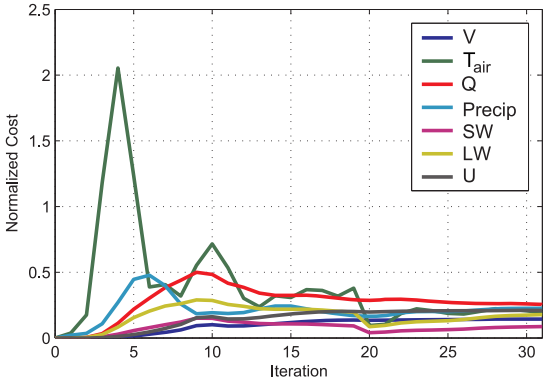

(d) Atmospheric state control: $\overline{\mathbf{u}}_{\mathrm{a}}$

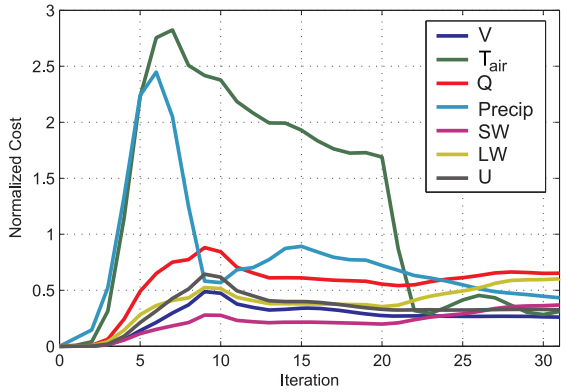

(e) Atmospheric state control: $\mathbf{u}'_{\mathrm{a}}(t)$

Figure 2-13: Descent of normalized cost function terms in the $1996-1997$ state estimate: (a) ocean *in situ* and SST data, (b) ocean T and S climatology data, (c) sea ice concentration data, (d) time-mean atmospheric controls $\overline{\mathbf{u}}_{\mathrm{a}}$, and (e) residual atmospheric controls $\mathbf{u}'_{\mathrm{a}}(t)$. Ocean *in situ* data are divided by instrument type: **CTD, XBT**, and **ABT** - autonomous profiling floats. Atmospheric state controls are separated by variable: **U, V** - 10 m winds, $\mathbf{T}_{air}$ - 2 m air temperature, **Q** - 2 m specific humidity, **Precip** - surface precipitation, and **SW, LW** - short and longwave downwelling radiation at surface.

Chapter 3

The Annual Sea Ice Cycle in the Labrador Sea and Baffin Bay

3.1 Chapter Overview

This chapter provides a review of the phenomenological features and relevant sea ice-atmosphere-ocean interactions associated with the development of the sea ice annual cycle in the Labrador Sea and Baffin Bay.

The review of phenomenological features of the evolution of the annual cycle of ice growth and melt (hereafter referred to as the sea ice annual cycle or annual cycle) significantly expands upon the description of the annual cycle found in the thesis Introduction (see Section 1.4.1). Details on annual cycle are presented chronologically beginning with the seasonal sea ice minimum in September (Section 3.2).

The discussion of ice-atmosphere-ocean interactions focuses on the development and maintenance of the sea ice quasi-equilibrium state - the near steady-state condition of the wintertime ice pack extent, concentrations, and thickness (Sections 3.3). The discussion expands upon the theories of sea ice variability and results from modeling studies and includes a review of relevant supporting observational data.

The reader who is familiar with the sea ice annual cycle and the climatology of the atmosphere and ocean in the study region should advance to the second half of the chapter as many of the concepts introduced therein are invoked throughout the thesis.

The chapter concludes with a summary and a synopsis of some of the open questions

concerning the annual cycle (Section 3.4).

3.2 The Sea Ice Annual Cycle in the Labrador Sea and Baffin Bay

The annual cycle is divided into 5 stages:

1. The initial development in the northern Baffin Bay (Section 3.2.1)
2. The rapid southward expansion of the ice pack through December (Section 3.2.2)
3. The advancement of the seasonal ice across the Thermohaline Front (THF) from December until February (Section 3.2.3)
4. The seasonal ice maximum in March and the subsequent attainment of a sea ice quasi-equilibrium state (Section 3.2.4)
5. The rapid retreat of the ice pack from April until September (Section 3.2.5)

Along with each major stage of ice development, those aspects of the atmosphere and ocean climate necessary to contextualize the ice development are introduced. Importantly, aspects of the atmosphere and ocean climate which are not directly necessary to understand the sea ice annual cycle are not discussed; little is mentioned about ocean hydrography or circulation below 500 m and small-scale atmospheric features.

Many details of the sea ice annual cycle in the Labrador Sea and Baffin Bay vary from cycle to cycle. In light of large interannual variability, summarizing or generalizing the annual cycle is a challenge. An analysis of the mean ice position through time from the entire satellite record would lead the reader to a distorted sense of the spatial variability of ice concentrations within the ice pack. The approach taken in this chapter is to present the major features of a particular realization of the annual cycle, subjectively deemed suitably representative of all annual cycles: September 1994 to August 1995.[1]

Four panels depicting monthly-mean sea ice concentrations during the 1994−1995 annual cycle are provided in Figure 1-5 in the thesis Introduction.

[1]The representativeness criterion was simply a small deviation from the median March ice extent as determined by the three decade long satellite record.

3.2.1 September: Initial Growth and Propagation

The first incursions of sea ice in the study region occur with the entrance of perennial ice remaining within the openings of the northernmost passages of the Baffin Bay, the most northeastern of the Canadian Arctic Archipelago: the Jones and Lancaster Sounds and Nares Strait. Early in the season, sea ice is advected through passages and into Baffin Bay (see Figure 3-2).

Thermodynamic ice growth first occurs in the northwest Baffin Bay due to favorable hydrographic and meteorologic conditions. Besides sea ice, relatively fresh Arctic Ocean surface and near surface waters, otherwise known as Arctic Water (AW) (wintertime $\theta \approx -1.8^\circ$ C, S $\leq$ 34.5), is advected into the domain through Nares Strait, providing Baffin Bay with a well-stratified layer of 100-300 m (Tang et al. 2004). For several months in the summer the near-surface Baffin Bay maintains a shallow fresh cap (S $\leq$ 33.5) of sea ice meltwater-origin. This seasonal fresh AW cap requires little enthalpy loss before the onset of ice growth.[2]

Per the NCEP/NCAR reanalysis, atmospheric temperatures first fall below the salinity-determined freezing point for seawater in the northwest corner of Baffin Bay.

Climatological 10 m winds

It is in the northwest Baffin Bay that cold air of Arctic origin is first advected into the domain. A sense of the large-scale annual-mean climatological wind field in the domain is presented in Figure 3-1.

3.2.2 December: The Thermohaline Front

By December, ice has spread by a combination of wind and ocean forcing and local thermodynamic growth over much of the Baffin Bay.[3] Ice is also found south of Davis Strait, along southern Baffin Island, across the Hudson Strait and closely along the Labrador Coast. Concentrations diminish along the Labrador Coast to the south.

These areas all share similar hydrological properties and meteorological conditions as the Baffin Bay's northwest corner: a shallow buoyant surface layer of AW which is exposed

[2]Indeed, the maximum inferred mixed layer depth throughout most of Baffin Bay is thought to be only of the order 100 m (Tang et al. 2004; Zweng and Muenchow 2006).

[3]The proportion of the initial development of ice in Baffin Bay is due to local thermodynamic growth relative to ice advection is difficult to discern from the available passive microwave satellite data.

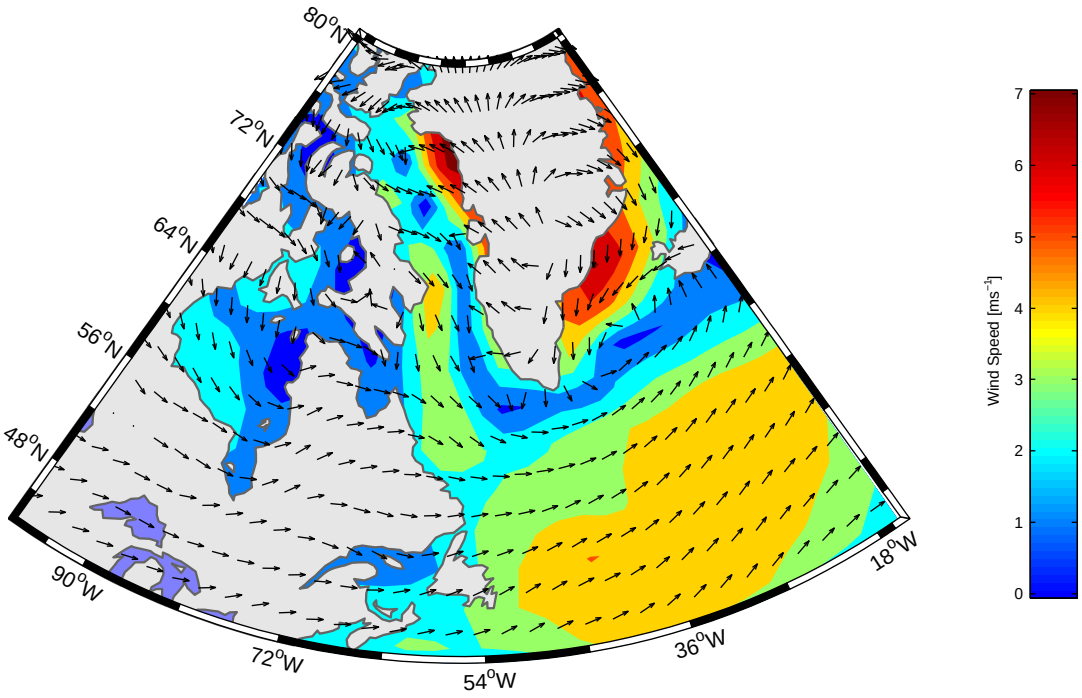

Figure 3-1: Mean 10 m wind field direction (vectors) and speed (colors) from the NCEP/NCAR reanalysis (1948-2008). For the associated reanalysis mean sea level pressure see Figure 4-8.

to extremely cold dry air of continental origin on westerly and northwesterly winds.

Circulation and boundary currents

The distribution of AW across the domain is primarily associated with its southward propagation along the Baffin Island Current (BIC). The BIC is the primary advective pathway on which AW inflow from the northern straits passes through and ultimately out of Baffin Bay at Davis Strait (Cuny et al. 2005). At the Labrador Coast, the BIC becomes the surface component of the shelf-following Labrador Current (LC). The LC continues south along the Labrador Shelf and shelfbreak to Newfoundland and the Grand Banks. The BIC and other major currents in the region are shown schematically in Figure 3-2.

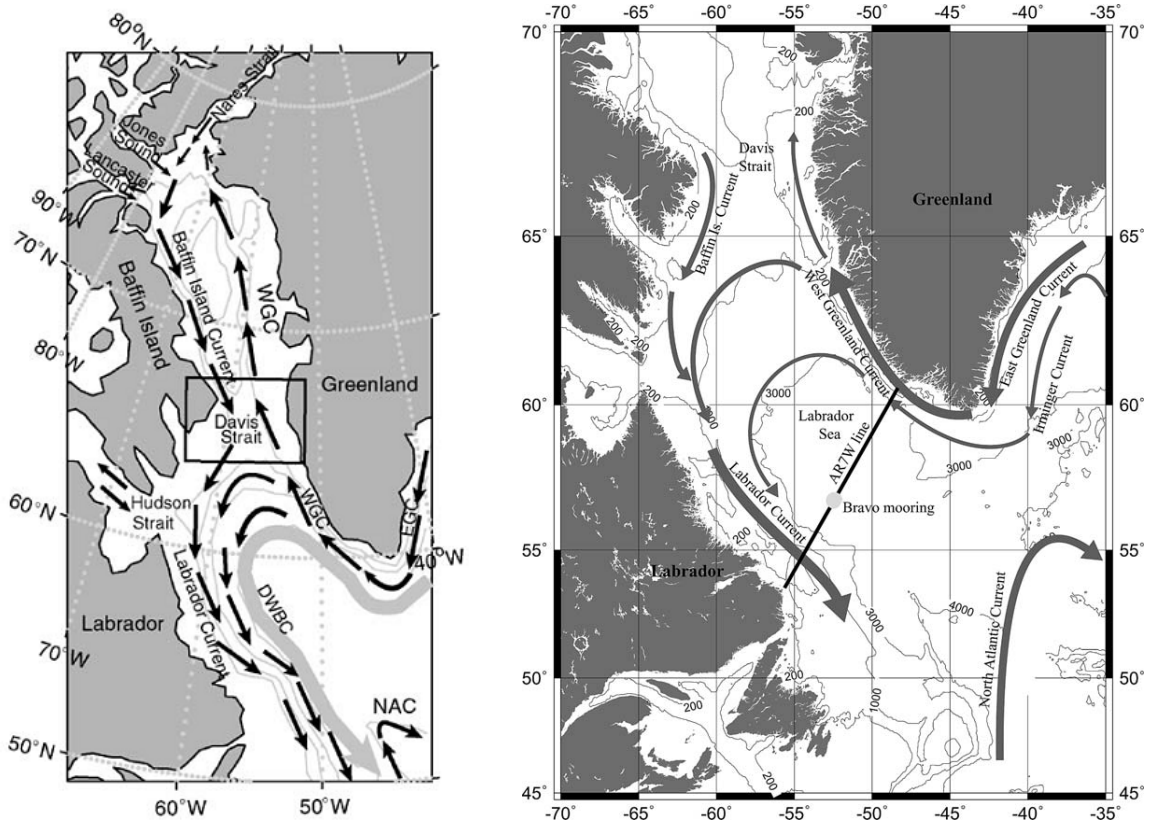

(a) Labrador Sea and Baffin Bay

(b) Labrador Sea

Figure 3-2: Circulation schematic for study region adapted from Cuny et al. (2002) (a) and Lilly and Rhines (2002) (b). (E/W)GC : East/West Greenland Current, NAC : North Atlantic Current branch of North Atlantic Drift, DWBC : Deep western boundary current. Cyclonic looping arrows on the Northern Slope of the Labrador Sea designate the bifurcation of the Arctic and Irminger Water on the WGC starting from the 3000 m isobath.

Climatology of the Thermohaline Front

The extent of sea ice in December is found at the approximate location of the Thermohaline Front (THF) separating cold fresh AW and the warmer and saltier Irminger Sea Water (IW), the predominant water mass of the upper Labrador Sea and eastern Baffin Bay (Cuny et al. 2002). A sense of the location and climatological hydrographic conditions associated with the THF is provided in Figure 3-3. Climatologically speaking, the THF is identified with the location 1026.6 $\mathrm{kg/m^3}$ isopycnal outcropping - which roughly corresponds the December0.75° C isotherm and 33.25 isohaline at 15 m .

3.2.3 December and February: Across the Thermohaline Front

The major developments of the ice pack between December and February involve interactions with waters beyond the THF. Thus, it is necessary to understand the main features of the transport pathways, distribution, and hydrographic properties of IW.

Irminger Sea Water: Pathways and Distribution in the Labrador Sea

IW enters the Labrador Sea on the West Greenland Current (WGC), the continuation of the East Greenland Current (EGC) at Cape Farewell. The WGC, following contours of the shelfbreak, then turns poleward. Interestingly, even though waters from two hydrographically distinct sources are transported along the flow, the waters retain their distinctive hydrographic properties. By the analysis of Cuny et al. (2002), a near-surface component, above 200 m, flows above the shelfbreak, consisting of cold fresh buoyant water (wintertime $\theta \approx -1.8°$ C, S $\leq$ 34.5) of Arctic and Nordic origin. The second component, IW, flows below the surface at depths between 200-500 m. It is warmer and saltier than the surface component, ($\theta \approx 4.5°$ C, S $\approx$ 34.95). At Cape Desolation, a temperature maximum is found between 300-500 m depth (Pickart et al. 2002). The source of IW is warm subtropical water advected north by the North Atlantic Drift which is ultimately advected/mixed into the subpolar gyre until joining the EGC in the Irminger Sea (Bower et al. 2002).

The WGC continues its bathymetry-following course north until reaching the point where the 3000 m isobath diverges from the shelf and turns west. Beginning at the 3000 m isobath and extending to the 1000 m isobath, a fraction of the current bifurcates and, slowing, begins to follow isobaths westward, tracing a broadly cyclonic path (Lavender

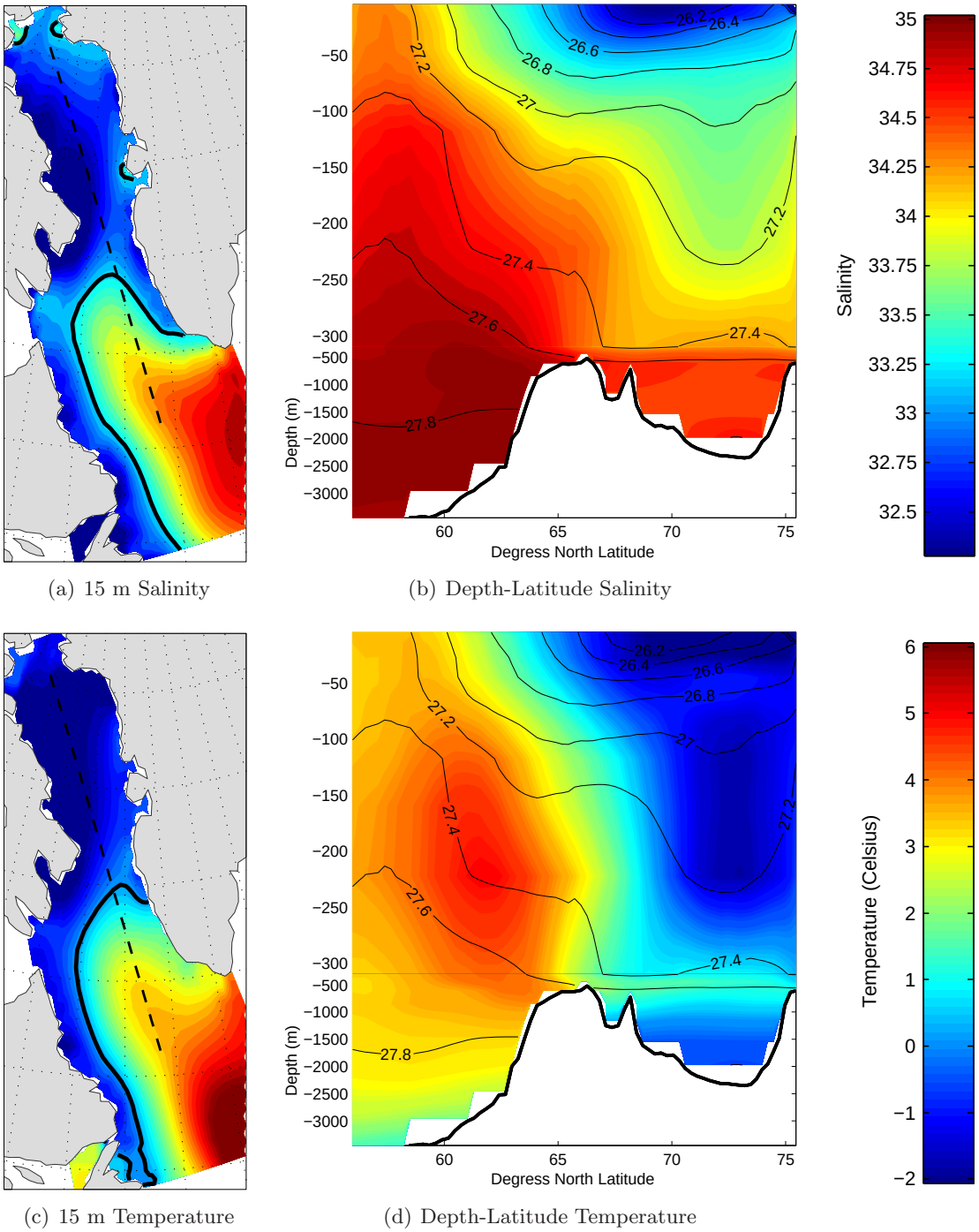

(a) 15 m Salinity

(b) Depth-Latitude Salinity

(c) 15 m Temperature

(d) Depth-Latitude Temperature

Figure 3-3: Climatological position of the December Arctic Water/Irminger Water Labrador Sea Thermohaline Front as depicted by the Levitus-Gourestski-Kolterman climatology (see Section 2.4.3 for details). a) 15 m salinity and 33.25 isohaline (contour). b) latitude-depth cross section of salinity and surface-referenced potential density (contours 1000-kg/m^3). c-d) as (a-b) but temperature and 0.75° C isotherm (contour). Cross-section track location shown as dashed line in (a) and (c). Thermohaline Front is located at approximately the 1026.6 kg/m^3 isopycnal outcropping.

et al. 2000; Cuny et al. 2002). Westward flow across the northern Labrador Sea between these contours, a region referred to by Cuny et al. (2002) as the Northern Slope (NS), ultimately merges with the Baffin Island Current/Labrador Current system. With the arrival of IW, the LC south of the Hudson Strait qualitatively resembles the WGC with fresh cold surface AW above the shelf and warm salty subsurface IW below. As the IW progresses cyclonically around the gyre it is modified, mainly cooled, by lateral and vertical exchanges (Cuny et al. 2002). At the Grand Banks it is scarcely identifiable by its original water mass properties (Fratantoni and Pickart 2007).

Returning to the WGC, the non-bifurcating portion of the flow continues northward on the eastern shelf of the Davis Strait (Cuny et al. 2005). North of Davis Strait *in situ* observations are very scarce. By inferring the circulation from hydrographic measurements and numerical simulations, Tang et al. (2004) suggest a significant weakening of the flow north of Disko Island. The slow-moving IW loses buoyancy as it cools, gradually becomes denser than the surface AW. A cooler denser IW then spreads beneath the surface AW at depths between 400-800 m through pathways that are not well understood (Lobb et al. 2003; Tang et al. 2004).

This classic description of the transport of IW into and through the Labrador Sea and Baffin Bay is a convenient device, historically employed by descriptive oceanographers, but it ignores important features and processes of the real ocean. In a recent reconstruction of WGC velocities from historic CTD sections, Fratantoni and Pickart (2007), showed maximum current velocities confined to a narrow region above the shelfbreak. However, in across-shelf CTD transects in the vicinity of Cape Desolation, warm salty subtropical water is present much farther offshore (≈ 100 km), and substantially deeper (to 2000 m) than the IW velocity core (Pickart et al. 2002; Fratantoni and Pickart 2007).

What accounts for the significant distribution of IW around and away from its subsurface velocity core? How can we reconcile the observed broad distribution of subtropical-origin water with the classical description of well-defined and narrow transport pathways? In reality, the pathways by which IW both enters and is subsequently dispersed throughout the basin are not well known. This uncertainty is mainly due to the extremely complex turbulent mesoscale eddy flow field which dominates the moment-to-moment circulation of the Labrador Sea (Prater 2002).

Mesoscale eddies form along and are shed from the WGC (Eden and Boning 2002). The net effect of these eddies is to laterally disperse the two components of the WGC offshore to the basin interior (Katsman et al. 2004; Straneo 2006; Lilly et al. 2003). The most energetic eddy activity is seen offshore between the 3000-1000 m isobaths, above the NS of the Labrador Sea. In agreement with the classic description, flow on the WGC does bifurcate and turn westward. However, the details of the advective dispersal in the turbulent eddy-rich flow in the northeast Labrador Sea bears little resemblance to the classic picture. A snapshot of the surface temperature signature of the Labrador Sea eddy field is presented in Figure 3-4.

The eddy field in the northern Labrador Sea is observed to extend over an area which includes the southward-penetrating AW from the Baffin Bay. The consequences of the mesoscale eddy mixing of AW and IW on the NS on sea ice development is not well understood at present.

Finally, some portion of the warm salty subtropical-origin waters entering the eastern Labrador Sea may bypass the Irminger Sea altogether. The reconstruction of the mean streamfunction at $\sigma_0 = 27.5\,\mathrm{kg\,m^{-3}}$ of the subpolar gyre from float data by Bower et al. (2002) and output from several high-resolution eddy-resolving ocean models, (*e.g.,* Treguier et al. 2005; Chanut et al. 2008), support the view that some subtropical-origin water from the northwest corner of the North Atlantic Current may reach Cape Farewell from the south.[4]

3.2.4 January-March: Seasonal sea ice maximum extent

By late February, the ice pack extent has expanded to its seasonal maximum. The Baffin Bay reaches near total coverage ($> 95\%$ concentration). Ice is found south across the eastern half of Davis Strait. South of Davis Strait, the Hudson Strait and the full length of the Labrador Shelf shallower than 1000 m are at least partly ice-covered. The combined effects of wind and ocean stresses drive sea ice south to Newfoundland and east across the Grand Banks (Prinsenberg and Peterson 1992). The Grand Banks mark the southernmost extent of the southward flowing AW on the Labrador Current. South of the Grand Banks and north around the Flemish Cap, an anticyclonic branch North Atlantic Current with its warm subtropical-origin waters present a seemingly insurmountable barrier to further southward ice extension. The Grand Banks east of Newfoundland mark the ice pack's

[4]With this caveat in mind, I will refer to all water of subtropical origin as IW.

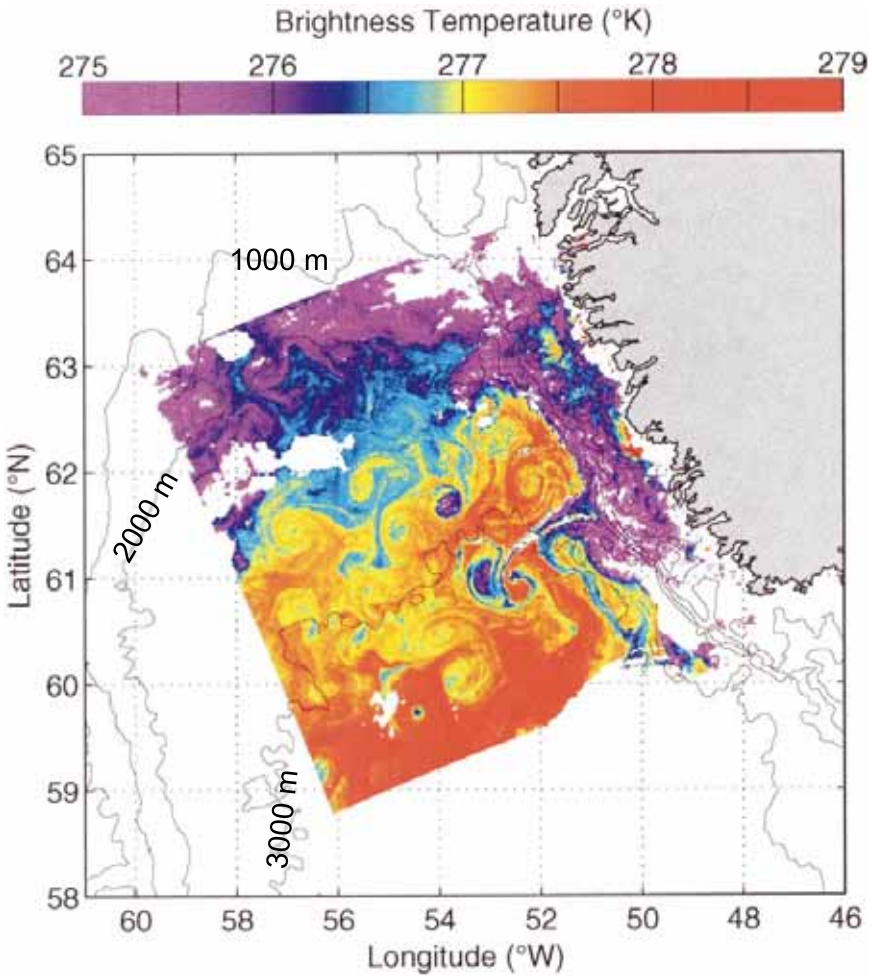

Figure 3-4: Snapshot of sea surface brightness temperature from the Along Track Scanning Radiometer on board the European Remote Sensing Satellite-1. The field shows the stirring and mixing of Arctic and subtropical origin waters in the eddy-rich northeast Labrador Sea. Note that the cold surface waters inner shelf branch of the WGC and north of the 2000 m isobath are easily distinguished from the warmer waters of subtropical origin. Note also eddy abundance between the 1000 and 3000 m isobaths. Figure adapted from Prater (2002).

south-easternmost reach. To the north, the ice edge is seen above the NS, just reaching the 3000 m isobath. Finally, ice is found on the AW on the inner shelf around Greenland's Cape Farewell and Cape Desolation.

3.2.5 April-September: Sea Ice Rout and Retreat

A disorganized ice retreat rapidly progresses once melting is initiated, accelerated by the ice-albedo feedback. By June, mean air temperatures across both the Labrador Sea and Baffin Bay are above typical seawater freezing temperatures, solar insolation reaches its 80% annual maximum, and the Labrador Sea is nearly ice free. The spatial pattern of ice melt resembles the pattern of ice growth but in a temporally reversed sense.

A distinctive feature in the melt pattern is the enlarging of the North Water Polynya at the entrances of the Smith and Jones sounds. A large ice-covered region along the eastern coast of Baffin Island is the final refuge for seasonal ice. It vanishes by September, drawing the annual cycle to a close.

3.3 Sea ice-Atmosphere-Ocean Interactions and the Sea Ice Quasi-Equilibrium State

At some point between January and March, the ice pack achieves an approximate steady state with respect to its spatial extent, concentration, and thickness. The ice edge position effectively ceases its advance and remains at or near the annual cycle's maximum for a period of several weeks. Behind the marginal ice zone (MIZ), the ocean becomes nearly ice-covered while ice thickness growth rates slow logarithmically.

In actuality, the ice pack never ceases to evolve. The location of the MIZ can advance or retreat by several tens of kilometers a day driven by synoptic winds and mesoscale ocean eddies (McPhee et al. 1987; Morison et al. 1987; Greenan and Prinsenberg 1998). In fact, variable wind and ocean forcing is most strongly felt in the MIZ where thin and spatially diffuse smaller ($<$ 10 km radius) pieces of ice (floes) are effectively in a state of free drift.[5] As a consequence, the dynamic response of ice in the MIZ becomes closely coupled to forcing from the highly variable winds from passing polar lows, extratropical cyclones, and

[5]In a state of free drift ice is unable to withstand divergent or convergent forcing through internal ice strength.

ocean eddies which are so prevalent in the Labrador Sea.

The internal ice strength within the consolidated ice pack behind the MIZ alters the large-scale response to forcing variability. Perpetually-changing complex networks of leads, formed when the ice pack mechanically separates, and ridges, formed during mechanical ice convergence, are ubiquitous features throughout the seasonal ice cycle.

With the above caveats in mind, I shall henceforth refer to the state with aforementioned characteristics of approximate steady state as the sea ice quasi-equilibrium state (or the quasi-equilibrium state or simply quasi-equilibrium with the term sea ice implied).[6]

In the following, I review the probable nature of this equilibrium, the locations where it is established, the coupled sea ice-ocean-atmosphere interactions preceding it, and several unique characteristics of the Labrador Sea that are essential for understanding the mechanisms of its maintenance.

3.3.1 Static- and dynamic-thermodynamic equilibria

Conceptually, two classes of equilibrium are hypothesized to be relevant in the Labrador Sea and Baffin Bay: *static-thermodynamic* and *dynamic-thermodynamic*. Ice achieving a static-thermodynamic equilibrium does so because of considerations of local thermodynamical processes alone. Ice achieving dynamic-thermodynamic equilibrium does so through both thermodynamical and dynamical processes.

Feedbacks of static-thermodynamic equilibrium

The defining characteristic of sea ice in static-thermodynamic equilibrium is a thermodynamic growth rate approaching zero. Growth rates approach zero through three negative feedback loops: the ice thickness-insulation, ice area-insulation, and ice-mixed layer buoyancy feedback loops.

In each feedback loop an increase of ice leads to a decrease in the rate of seawater enthalpy loss, phase change, and new ice formation. In the ice thickness-insulation loop, thickening ice becomes an increasingly effective insulator of the seawater. An increase of

[6]In this thesis, individual aspects of the quasi-equilibrium, will be invoked separately in later chapters in phrases such as the quasi-equilibrium ice edge position or the quasi-equilibrium thickness state. The reader is asked to note that the although the attainment of a near steady-state in one aspect of the pack, such as thickness, does not necessarily imply a steady-state in another aspect, such as extent, all of these time-evolving features appear to converge to a steady state at around the same time.

ocean insulation (decrease of vertical conductive heat fluxes) reduces the rate of seawater enthalpy loss, phase change, and new ice formation.

In the ice area-insulation loop, an increase of sea ice concentration decreases (by definition) the open water fraction within some control volume. As ice is an insulator, more expansive ice cover decreases the total area-integrated turbulent ocean-atmosphere heat flux thereby reducing the rate of seawater enthalpy loss, phase change, and new ice formation.

In the ice-boundary layer stabilization feedback, an incursion of sensible heat into the surface boundary layer immediately beneath sea ice (from free or forced convective entrainment of subsurface enthalpy or lateral ocean heat flux convergence) triggers rapid melt at the ice base and a release of relatively fresh ice meltwater which stabilizes the boundary layer (Morison et al. 1987). One possible source of boundary layer destabilization is the increase of boundary layer density resulting from an increase of brine salinity associated with thermodynamic ice growth. Successive episodes of thermodynamic ice growth, boundary layer salinity enhancement/destabilization, boundary layer enthalpy entrainment, and sea ice meltwater release/boundary layer stabilization can maintain ice thicknesses in near steady-state in weakly-stratified upper ocean hydrographic conditions.

Feedbacks of dynamic-thermodynamic equilibrium

In dynamic-thermodynamic equilibrium, that portion of the sea ice pack whose existence requires sustained ice transport ceases to significantly change. Where ice is present in locations of net sea ice mass divergence, a balance condition must hold between the production of new ice and export of existing ice. In steady-state conditions, high ice export rates logically require high thermodynamic production rates. High thermodynamic production rates are only possible in regions of thin ice or high open water fraction or both. Conversely, sustained ice mass convergence implies sustained melt.

Many of the same feedbacks are relevant for dynamic-thermodynamic and static-thermodynamic equilibria. To wit, the ice mass balance attained by thermodynamic growth and dynamic export is linked to the operation of the negative ice thickness and ice area-insulation feedbacks. For example, a positive perturbation to the rate of ice export increases the ice open water fraction and reduces ice thickness thereby driving ice production rates up until these feedbacks re-establish a balance condition.

Observations made during two field campaigns which sought to elucidate the sea ice-

atmosphere-ocean processes in the MIZ, the 1984 Marginal Ice Zone Experiments (MIZEX) (MIZEX Group 1989) and the Labrador Ice Margin Experiment (LIMEX) (Carsey et al. 1989), provide evidence that the ice-boundary layer stabilization feedback may also be relevant in dynamic-thermodynamic equilibrium. The salient findings of these campaigns are now summarized.

In hydrographic measurements across the Labrador Shelf in March/April 1990 in the Newfoundland MIZ made during the LIMEX campaign, Tang (1992) noted that features of the upper ocean hydrography offshore of the Labrador shelfbreak appeared to have been altered via interactions with melting sea ice. The offshore upper ocean water mass properties resembled the fresh, cold and stratified AW on the LC but were limited to a shallower (20 m) boundary layer. The limited depth of these low-salinity waters suggested that they were perhaps not offshore-advected shelf waters but were instead a result of sustained sea ice melt. The author argued that offshore winds of "longer durations" would drive a sustained flux of sea ice offshore of the AW front on the LC and into the warmer offshore waters. Then,

> [sustained ice melt] ... gradually modifies the temperature and salinity of the upper water column until an equilibrium state is reached in which the eastward ice velocity is equal to the rate of ice-edge melt.

In the MIZEX campaign, CTD profilers tethered to drifting ice floes observed essentially the same phenomena speculated upon by Tang (1992) in real time. Sustained winds over a period of several days drove an ice floe from 60 km behind the ice edge towards and eventually across the thermohaline front of the Greenland Sea MIZ. While progressing towards the front, a significant amount of ice ahead of the MIZEX floe crossed the front and subsequently melted. When the MIZEX floe reached the former location of the ice edge, cold fresh surface waters in a very shallow ($\sim$ 20 m) mixed layer were encountered first - remnants of the melted ice which had preceded it. Ice ablation rates in this cold mixed layer were found to be very low (Morison et al. 1987). Eventually, the floe was transported out of the zone of previously melted ice into warmer waters and began to rapidly melt. With the sustained release of ice meltwater, mixed layer salinities fell, shoaling the mixed layer. As the enthalpy of the new shallow ($\leq 20\,\mathrm{m}$) mixed layer was extracted via turbulent ocean-ice heat fluxes, temperatures within the mixed layer fell, slowing ice melt rates.

Based on these data, large positive ocean surface buoyancy fluxes from sea ice meltwater release are associated with mixed layer shoaling and an enhancement of static stability of waters in the mixed layer. Therefore, in the sea ice quasi-equilibrium period, the ice-buoyancy enhancement feedback may operate through the modification of the upper ocean hydrographic conditions in the regions of sustained ice convergence and thermodynamic melt. Specifically, by altering the near-surface stratification, the equilibrium rate of ice melting ocean-ice heat flux may be suppressed.

Both the MIZEX and LIMEX campaigns were conducted during or after the peak of seasonal sea ice extent - well after the sea ice quasi-equilibrium period. Nevertheless, from these campaigns it is possible to hypothesize an additional role of the ice-boundary layer stabilization feedback. The extended distance traversed by the MIZEX floe across the location of the formerly stable ice edge was likely only possible because of the favorable upper ocean hydrographic conditions that preceded it - a shallow layer of cold fresh well-stratified meltwater. In the period preceding the sea ice quasi-equilibrium state, it is conceivable that sustained offshore advection (and subsequent melt) of ice by winds or ocean currents in the warmer offshore waters progressively alters the upper ocean hydrography thereby permitting an incremental seaward advancement of the MIZ. If this is true, the ice-buoyancy enhancement feedback may be fundamental in establishing the characteristics (ice extent, thickness, energy fluxes, etc) of the sea ice quasi-equilibrium state.

In this thesis, the process by which the drifting pack ice is able to progressively advance into and across waters having initially unfavorable hydrographic conditions via the process outlined above is termed the *meltwater stability enhancement mechanism* or MSEM.

Elucidating the role of the MSEM in establishing and maintaining the sea quasi-equilibrium state is a central theme of Chapter 6.

3.3.2 Where is each type of equilibrium likely found?

Probable locations of static-thermodynamic equilibrium

On thermodynamic considerations alone, climatological conditions in the Labrador Sea suggest that static-thermodynamic equilibrium is probably found only in a limited area: the AW side of the THF in the central Baffin Bay. As described earlier, favorable hydrographic conditions on the AW side of the THF are likely responsible for much of the rapid expansion

of ice cover in Baffin Bay by the end of November.

An important caveat for considerations of static-thermodynamic equilibrium is that nearly all sea ice in the domain has a nonzero mean velocity. However, it is conceivable that over large areas of nearly uniform atmospheric conditions and non-divergent winds, a kind of static-thermodynamic equilibrium could be established. In such a state, despite continuous ice advection through a control volume, an absence of net ice convergence would leave the ice thickness unchanged.

Probable locations of dynamic-thermodynamic equilibrium

To identify locations of dynamic-thermodynamic equilibrium we must identify areas of net ice mass convergence and a source of sustained energy to erode the converging ice. Between January and March, the only sources of energy for ice melt are downwelling short- and longwave radiation and sensible heat from seawater above its salinity-determined freezing point. Since sea ice has a high albedo and since shortwave radiative fluxes are comparatively small during these months, one would not expect a significant contribution to melt except for in the low ice concentration MIZ. Longwave downwelling radiative fluxes are greater, logically, in the MIZ and over the open ocean where air temperatures are warmer. Finally, the largest sensible heat reservoir is the surface and subsurface IW south of the THF. Based on the climatological isopycnal gradients in virtual hydrographic cross sections of Figure 3-3(d) and the findings of numerical modeling studies (see Section 1.6.2), IW is likely brought to the MIZ by a combination of vertical and lateral advective transport. Thus, the length of the MIZ satisfies the requirement of sustained energy source.

Where along the MIZ does ice motion lead to net convergence? By the analysis of Kwok (2007), the large-scale wind forcing and ocean currents drive a sustained flux of ice pack out of Baffin Bay, through Davis Strait, and toward the Northern Slope MIZ at rates of $0.02 - 0.23\,\mathrm{ms}^{-1}$. *In situ* and satellite measurements of ice motion on the Labrador Coast give typical values of ice velocity of 1-3% of the wind speed turned to the right at an angle between $0.6{-}30.0^\circ$ (Thorndike and Colony 1982; Greenan and Prinsenberg 1998). Assuming these relations hold in the entire Labrador Sea and using the large-scale climatological wind field to project the trajectory of the ice pack, the entire MIZ in Labrador Sea is likely a place of net ice mass convergence.

The large-scale climatological wind field also suggests that net sea ice mass divergence

likely occurs along the coasts of Baffin Island, Labrador, and Newfoundland.[7] Ice mass divergence results from wind-driven sea ice advection in the direction perpendicular (seaward) to the coasts occurs. Given that some of the coldest air and strongest winds are found near the domain's western coastal boundary, it is expected that sustained ice production is found near its exposed open water. The capabilities of the passive microwave satellite imagers used in the production of ice concentration fields in Figure 1-5 cannot reveal a signature of high open water fraction close to the western boundary. High-resolution (250 m pixel) Moderate Resolution Imaging Spectroradiometer imagery does however, revealing bands of open water along the western edge of the pack ice along Baffin Island and Labrador.

Without a better sense of the actual sea ice flow field and ice thickness gradients, the locations and rates of sustained ice convergence and divergence are uncertain. Indeed, our conclusions regarding ice mass divergence/convergence based on purely climatology data must be regarded as tentative especially in and around the MIZ where ice measurements of any kind are particularly difficult to obtain (Prinsenberg and Peterson 1992).

3.4 Chapter Summary

The main features of the sea ice annual cycle and the sea ice-atmosphere-and ocean interactions are summarized as follows.

- In September, ice first enters the domain after passing through northern Arctic Straits. The combination of cold dry air and reduced incoming solar radiation leads to the initial thermodynamic ice growth in the northwest corner of Baffin Bay.
- Through December, thermodynamic ice growth and lateral advection leads to an expansion across the bay, to the southeast, over the shallow fresh cold buoyant AW. Eventually, the ice pack encounters the thermohaline front separating AW from IW. Ice extends over the AW through western Davis Strait and along the LC.
- Ice-ocean-atmosphere feedbacks likely sustain the advancing ice pack, forced by winds and ocean currents, across a thermohaline front.
- Net sea ice mass fluxes to the Labrador Sea MIZ and away from the eastern coasts of Baffin Island, Labrador, and Newfoundland are implied by observations, model studies, and the climatological wind field.

[7] If landfast ice is found along the coasts, pack ice divergence occurs at the landfast ice/pack ice interface.

- An energy and mass balance condition is implied in the MIZ wherein the advancing ice pack is continuously eroded by ocean-ice or air-ice net energy convergence. The source of the energy required for continual ice melt is uncertain.
- Once initiated, sea ice melt progresses rapidly, generally following the opposite tendencies of growth, until September. Positive feedbacks (*e.g.,* the ice-albedo feedback) accelerate the retreat.

In summary, static-thermodynamic equilibrium, insofar as it even approximately exists, most likely occurs in the Baffin Bay some distance away from the coasts. Dynamic-thermodynamic equilibrium of a convergent-ice nature is theoretically possible along the entire MIZ on the IW side of the THF. Dynamic-thermodynamic equilibrium of a divergent-ice nature is likely along the western coastal boundaries as westerlies and northwesterlies force ice away from the shoreline without replacement.

3.4.1 Open questions

Several open questions concerning the sea ice annual cycle include:

- What is the relative importance of local thermodynamic growth and advective transport in the initial freeze up of AW in Baffin Bay?
- What is the actual nature of the sea ice quasi-equilibrium state? Are there places in which a static-thermodynamic or dynamic-thermodynamic equilibrium actually exist?
- Where are the regions of sustained net ice convergence and divergence? What are the rates associated with each?
- If dynamic-thermodynamic equilibrium exists, what are the pathways and magnitudes of the sea ice energy balance which sustain melt?
- What ocean-ice feedbacks are relevant for establishing the quasi-equilibrium ice state and where and when do they operate?

An attempt to answer these questions motivates the chapters that follow.

Chapter 4

Consistency of the 1996-1997 Sea Ice-Ocean State Estimate

4.1 Chapter Overview

In this chapter, the 1996-1997 one-year sea ice-ocean state estimate is surveyed and analyzed to determine its consistency with respect to observational data. The purpose of the chapter is to demonstrate the accomplishment of a secondary thesis goal. Recall from the Introductory Chapter:

> A secondary goal is to demonstrate the feasibility of the adjoint method, or method of Lagrange multipliers, to simultaneously synthesize observations of sea ice and the ocean into a dynamic coupled numerical model.

The first part of the chapter surveys sea ice in the state estimate and compares aspects of the reproduced sea ice against data (Section 4.2): ice concentration and extent (Section 4.2.1), ice and snow thickness (Section 4.2.2), sea ice plus snow freeboard (Section 4.2.3), and, finally, sea ice velocity (drift) (Section 4.2.4). The second part of the chapter is an evaluation of the ocean reconstruction (Section 4.3). Emphasis is split between ocean circulation/transports (Section 4.3.1) and wintertime mixed layer depths (Section 4.3.2). Finally, the chapter is summarized (Section 4.4) with a review of the sea ice (Section 4.4.1) and ocean consistency (Section 4.4.2). Some thoughts are offered concerning the implications of the outstanding model-data discrepancies.

4.2 Sea Ice Survey

Throughout the sea ice survey, the reader is reminded that the only sea ice data synthesized with the model were sea ice concentration data.

4.2.1 Sea ice concentration survey

Main features of sea ice concentration in the state estimate

Ice concentration in the state estimate fields (model ice concentration) evolves similarly to the $1994 - 1995$ annual cycle - the qualitative details of which have been described in Chapter 3. The time series of total ice area in both years closely follow the median values over the 1979-2008 satellite record. For brevity, only a few notable features of the ice pack development - which is shown in detail Figure 4-1 - are therefore mentioned.

Ice extent at the beginning of the annual cycle in both model and observations is anomalously high. The existence of a large seasonal ice residual in August represents interannual variability in the phase of the annual cycle - the majority of residual seasonal ice melts by the end of September. The second notable feature is the (nearly) stationary Baffin Bay ice edge at the climatological position of the Thermohaline Front (THF) from November until mid-February. During this two month period the ice pack continues to extend south above the Labrador Shelf. Finally, the ice edge rapidly expands between mid-February and mid-March across the THF and over the Northern Slope (NS) in the Labrador Sea.

Sea ice concentrations in the northeastern corner of the Labrador Sea during the peak ice week (week ending March 13) are relatively low ($< 90\%$). Between mid-February and mid-March, the domain-wide ice concentrations are in quasi-equilibrium (Section 3.3).

The time series of daily total sea ice area is compared with observations in Figure 4-2. Total sea ice extent initially decreases from August until mid-September (the melting of the previous annual cycle's residual ice) leaving a small amount of multi-year ice in northern Baffin Bay. The expansion of ice cover proceeds rapidly until December (the initial Baffin Bay freeze-up) and then slows until the end of January (the southward expansion of ice along the Labrador Shelf). A second period of rapid ice cover expansion follows from early February until mid-March (the expansion of ice over the NS).

The sea ice quasi-equilibrium period is identified as the four week period centered in mid-March during which aggregate ice area is within 4% (0.05×10^6 km^2) of its maximum

$(1.31 \times 10^6$ km$^2)$.

Ice area contracts from the basin in a nearly linear fashion after the abrupt loss of sea ice on the NS.

Evaluation of sea ice concentration in the state estimate

Figures 4-1 and 4-2 reveal a very close agreement between the state estimate and data with respect to the time-evolving spatial and temporal patterns of ice concentration. In particular, the timing of ice advance and retreat and the position of the sea ice edge match very well.

The annual cycle of the previous year, $1995 - 1996$, is unusual in that the sea ice area minimum occurs in late September - residual ice is present in the Baffin Bay on August 1. During the first 5 weeks of the state estimate, while this residual ice melts, large discrepancies are found in the ice distribution and ice total area. These discrepancies are not surprising for two reasons: initial ice thickness is only guessed at and is not a model control variable and the low concentrations associated with retreating ice pack are associated with large observational uncertainties. Therefore, the initial model-data misfits are not significant.

With respect to the time series of observed and estimated total sea ice area, the state estimate shows a close agreement with the data in many respects. Disregarding the discrepancies at the very beginning of the simulation, the state estimate recreates the major transitions in the ice pack: initial Baffin Bay freeze-up, extension along the Labrador Coast and NS, and the near linear contraction associated with seasonal melt.

The state estimate's fidelity in reproducing the evolution of ice concentrations exceeds all extant (dynamically-consistent or otherwise) reproductions in the literature for this domain and time period.

The total ice area in the state estimate has less high-frequency (daily) variability than seen in the data. Determining whether the observed high-frequency variability is real or an artifact of unknown errors is difficult to discern from the data and its literature. A cursory examination of the observed (daily) variability reveals that most day-to-day changes in ice concentration occur within the marginal ice zone (MIZ). As the greatest ice concentration data errors are found in the MIZ (See Section 2.4.4), some of the daily variability in the data is likely an artifact of the observational system/geophysical transfer algorithm. Quantifying

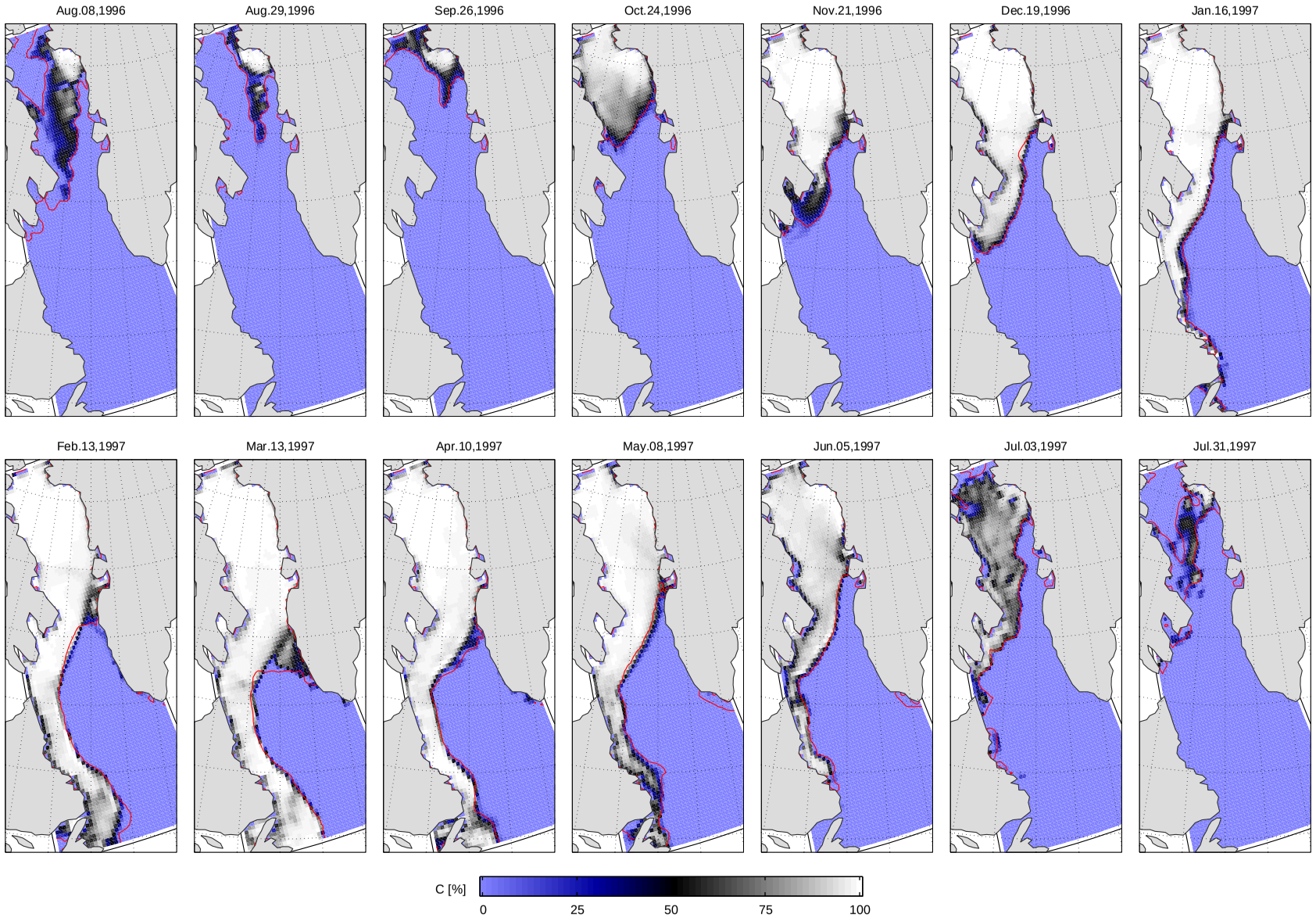
Aug.08,1996
Aug.29,1996
Sep.26,1996
Oct.24,1996
Nov.21,1996
Dec.19,1996
Jan.16,1997
Feb.13,1997
Mar.13,1997
Apr.10,1997
May.08,1997
Jun.05,1997
Jul.03,1997
Jul.31,1997
C [%]
0
25
50
75
100

Figure 4-1 *(previous page)*: Mean sea ice concentration from the state estimate (colors) and ice edge (15% ice concentration) and observations (red line). Dates are last of 7-day averaging period.

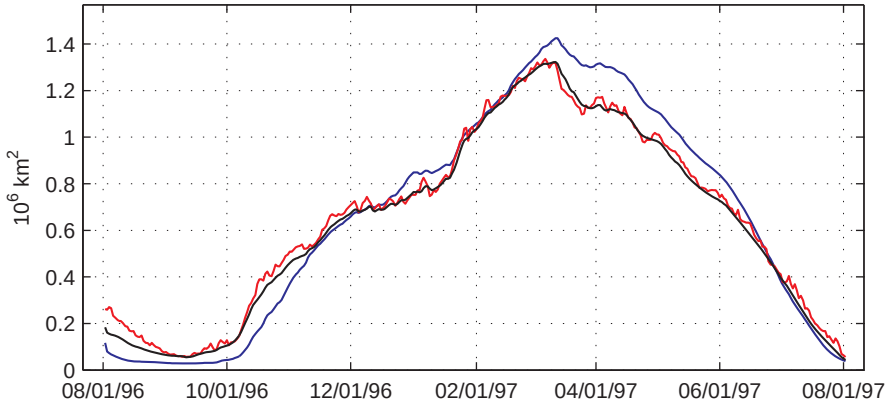

(a) Total sea ice area

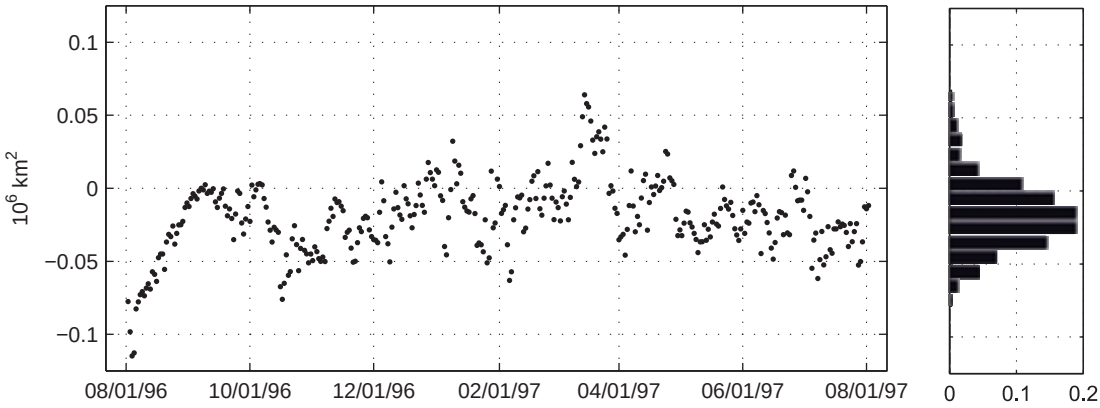

(b) Total sea ice area residuals

Figure 4-2: a) Annual cycle of daily total sea ice area from August 1, 1996 in the study region from observations (red), the state estimate (black), and the first-guess unconstrained forward model (blue). b) Residuals (state estimate - observations) of (a) and the frequency histogram of the residuals (after September 10, 1996 the total area minimum). Note the different vertical scales between (a) and (b). Post-September 10, 1996 residual mean : -0.017×10^6 km^2, standard deviation: 0.022×10^6 km^2.

the measurement error proportion of daily variability in the data is beyond the scope of this thesis.

For the unknown proportion of the observed ice concentration variability which is real, there are several possibilities for its absence in the state estimate: the variability may be related to atmospheric variability which is inadequately represented in the NCEP/NCAR reanalysis (*e.g.,* Section 2.5.1) and representation error from sea ice dynamics and thermodynamics and unrepresented mesoscale ocean variability.

If the consistency state estimate's ice concentration is dominated by model representation errors then the model-data residuals quantify the model representation error. The model-data residuals, which may or may not be dominated by model representation error, are summarized in a frequency histogram in Figure 4-2(b). The magnitude of the residuals are small relative to the total change in ice area over the annual cycle and reveal a slight negative bias in the state estimate. Where is ice missing in the state estimate?

The state estimate fails to recreate sea ice at three locations and times: around the southern tip of Greenland between Cape Farwell and Cape Desolation between May and June, the Labrador Sea's NS region ($62^\circ\,\mathrm{N}, 57^\circ\,\mathrm{W}$) for the week ending March 13, and the south central Labrador Sea east of Newfoundland ($52^\circ\,\mathrm{N}, 52^\circ\,\mathrm{W}$) for the week of February 13.

The absence of simulated ice around southern Greenland is due to the absence of a sea ice inflow open boundary condition. A small amount of ice transport into the Labrador Sea by the East Greenland Current (EGC) and West Greenland Current (WGC) is regularly observed with satellite imagery.

Missing ice to the east of Newfoundland and over the NS are both likely due to inadequate representation of ocean surface currents and missing lateral eddy transport. In MODIS satellite imagery, one observes patterns of sea ice filamentation in the MIZ resulting from interaction with ocean current meanders and eddies. These filaments are, of course, not represented in the model. Examples of how the sea ice front is altered by (unresolved) ocean interaction are provided in Figure 4-3.[1]

[1]No comparable images are available for dates in this case study. Images are chosen for their clarity and proximity to the date in the annual cycle of the state estimate discrepancies.

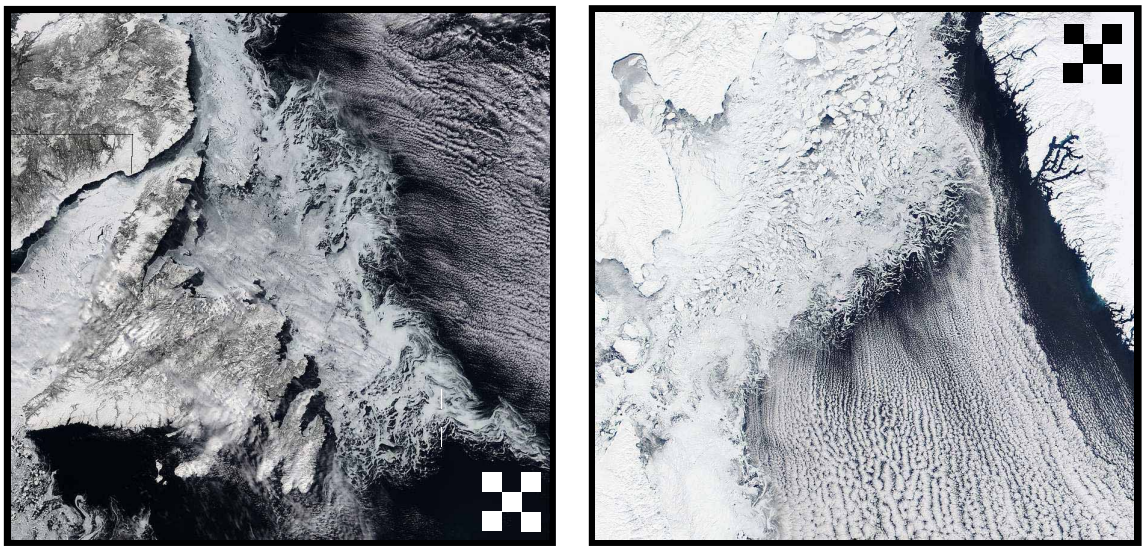

(a) Newfoundland 3/20/2003 (b) Northern Slope 3/29/2002

Figure 4-3: MODIS images indicating sea ice filamentation and lateral redistribution from ocean current meanders and eddies. Images are on same scale. For reference, model grid cells sizes are shown in each figure as five 32×32 km squares. Images owned and provided by NASA.

Sea ice concentration survey conclusions

What does the success in reproducing the $1996 - 1997$ sea ice annual cycle suggest about the difficulties experienced by earlier researchers who attempted to reproduce specific sea ice annual cycles and those who attempted to improve the realism of regional models by increasing sea ice model complexity? This thesis confirms the intuition of earlier researchers who, in efforts to reduce model-data misfit, manually adjusted their initial ocean conditions (*e.g.,* Ikeda et al. 1996), experimented with different ice-ocean-atmosphere coupling schemes (*e.g.,* Zhang et al. 2004), and varied their prescribed atmospheric states (*e.g.,* Yao et al. 2000).

Indeed, this thesis confirms that reasonable adjustments (adjustments which are consistent with the specified uncertainties) to the initial ocean and atmospheric and lateral ocean boundary conditions can be made that lead to sea ice concentration data consistency in the state estimate. A tentative conclusion is therefore that for the goal of reproducing the observed sea ice patterns, more progress is expected through the seeking and using of more accurate ocean initial and atmospheric boundary conditions than through increasing sea ice model complexity. Said in a slightly different way, until model errors can be unambiguously

traced to missing sea ice model physics, the allocation of intellectual resources towards improving the ocean initial and atmospheric boundary conditions would appear to bear more fruit.

One must always keep in mind that complexity is neither a synonym for accuracy nor utility - a distinction which is often lost on modelers. If additional model complexity increases the realism and accuracy of simulated physical processes then the addition of complexity is worthwhile - it just may not be the most useful for the solving of a particular problem.

4.2.2 Sea ice thickness survey

Having established the degree to which sea ice concentration in the state estimate agrees with observations, I now consider sea ice thickness. First, I discuss the main features of the sea ice thickness field. I then compare the sea ice thickness in the state estimate with upward looking sonar and coastal observations.

Main features of sea ice thickness in the state estimate

As shown in Figure 4-4, ice thickens from September through March in Baffin Bay, reaching maximum values between 1.5 - 2.0 m. A zonal gradient in mean ice thickness is observed. Along the west Greenland Coast, ice tends to be $\leq$ 1 m. This is likely due to the local mean cyclonic atmospheric winds which bring comparatively warmer air northward parallel to the steep glacial walls of Greenland before turning westward in northern Baffin Bay.

During the initial period of a shrinking ice pack, from March until June, ice thickness is maintained except in the retreating southeastern periphery.

South of Davis Strait, an unambiguous gradient is also noted at the sea ice edge. For ice along the Labrador Current (LC), the gradient is often confined to a small number of model grid cells. Ice in the LC tends to reach a maximum mean thickness of $\sim$ 1.0 m.

Several interesting small-scale features of very thick ice ($\geq$ 2.5 m) are revealed at points on the coasts of northern Greenland, Baffin Island, and Labrador. These locations of anomalously thick ice are locations of dynamical ice convergence. The streaks which appear to emanate from these points reveal ice trajectories originating from the convergence points (see Sections 4.2.4 and 5.4 for details).

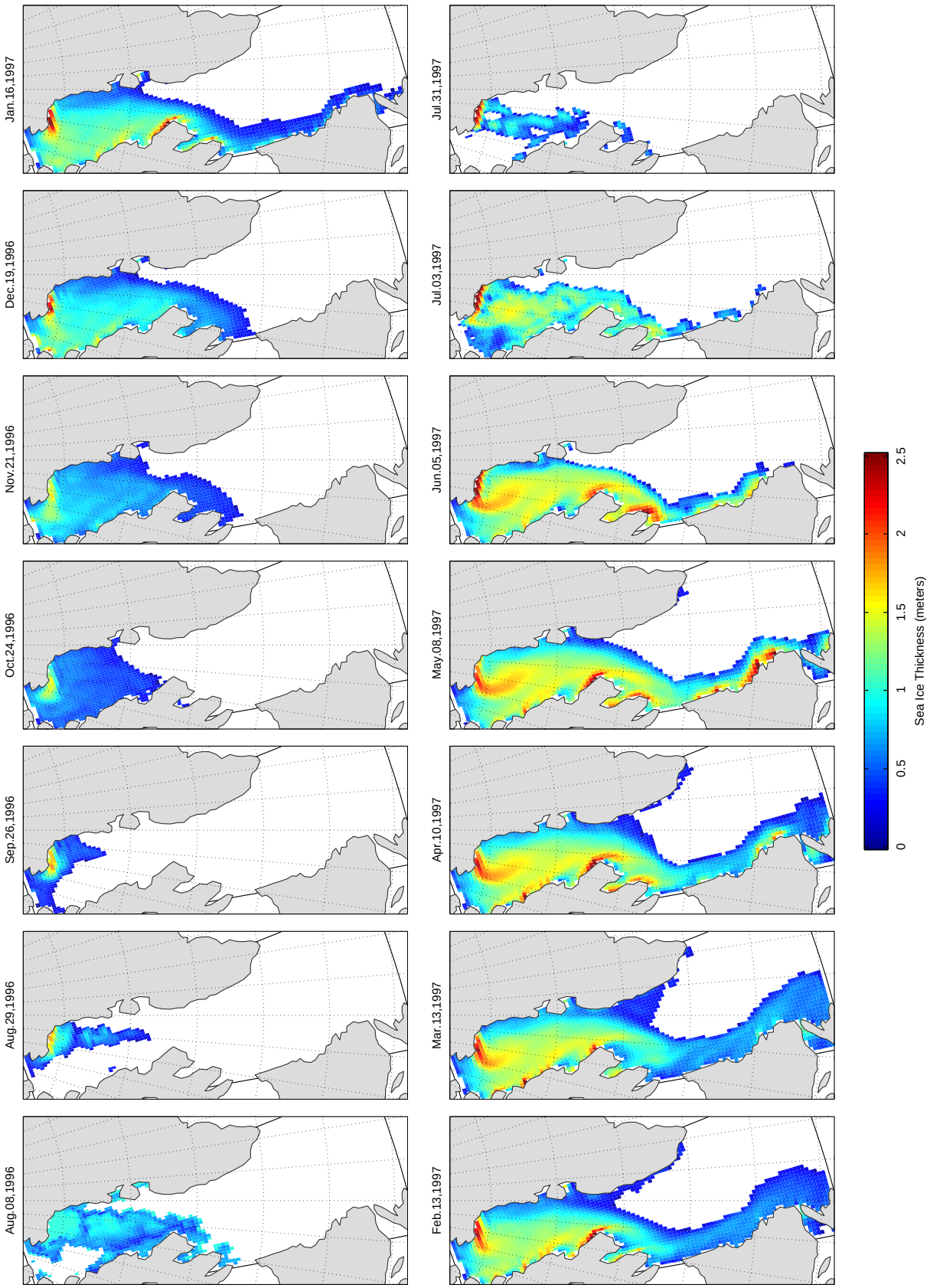
Aug.08,1996
Aug.29,1996
Sep.26,1996
Oct.24,1996
Nov.21,1996
Dec.19,1996
Jan.16,1997
Feb.13,1997
Mar.13,1997
Apr.10,1997
May.08,1997
Jun.05,1997
Jul.03,1997
Jul.31,1997
0
0.5
1
1.5
2
2.5
Sea Ice Thickness (meters)

Figure 4-4 *(previous page)*: Mean ice thickness from the state estimate. Values are thicknesses of the 'thick' ice category of the 2-category ice model (thick ice and thin ice/open water). Dates are last of 7-day averaging period.

Evaluation of sea ice thickness in the state estimate

In the study region, observations of sea ice draft come from upward looking sonar (ULS) on board submarines and direct *in situ* measurements from several coastal stations on the eastern Canadian coast. Ice draft from ULS is considered first, followed by *in situ* coastal measurements.

Establishing uncertainties for each of these datasets presents a serious challenge due to measurement paucity and because most measurements were made outside of the state estimate time period. However, progress can be made by evaluating the state estimate with the range of interannual variability (where available) in the data.

Sea ice draft from upward looking sonar Sea ice draft is the depth of sea ice beneath the ocean surface. Ice draft depends on ice thickness and the weight of overlying snow. Making the assumption of hydrostatic equilibrium, draft, h_{draft}, is given by,

$$h_{\text{draft}} = h_{\text{snow}} \frac{\rho_{\text{snow}}}{\rho_{\text{seawater}}} + h_{\text{ice}} \frac{\rho_{\text{ice}}}{\rho_{\text{seawater}}} \tag{4.1}$$

Where ρ_{snow}, ρ_{ice}, ρ_{seawater}, are densities of snow, ice, and seawater, respectively and h_{ice} and h_{snow} are ice thickness and snow depth, respectively. Ice and snow densities are chosen to be the same as the numerical model, $910\,\text{kg}\,\text{m}^{-3}$ and $330\,\text{kg}\,\text{m}^{-3}$, respectively.

Uncertainties in snow thickness affect the inversion of ice thickness from ice draft. However, given the physical constraints on maximum snow pack depth on sea ice in hydrostatic equilibrium, errors in the ice thickness inversion are typically less than than 12%.

The first measurements of the ice draft by ULS equipped naval submarine were made in February, 1967 and reported nearly two decades later by Wadhams et al. (1985), hereafter WD85. Readings were taken along a looping 669 km track within a region in the Labrador Sea spanning from $61.5 - 64^{\circ}\,\text{N}$ and from $61 - 58^{\circ}\,\text{W}$. The submarine track crossed from open water across the MIZ twice and mainly sampled north and west of the ice edge. Absolute measurement accuracy was estimated at ± 0.15 m. ULS measurements provide

	MIZ			Interior		
	Min	Max	Mean	Min	Max	Mean
Sonar	0.25 m	0.51 m	0.35 m	0.77 m	1.66 m	1.23 m
State Estimate	0.25 m	0.42 m	0.35 m	0.38 m	1.00 m	0.66 m

Table 4.1: Range of mean ice drafts found within each 50 km segment of submarine track.

a more detailed picture the ice draft thickness distribution than is represented in the ice model. The model-data comparison is therefore made with respect to the mean ice draft.

WD85 divided the track into segments $\sim$ 50 km in length and then classified each segment into one of two categories: *MIZ*, measurements within 50 km of the ice edge and *interior*, measurements beyond 50 km of the ice edge. The segment lengths of WD85 are comparable to the model grid edge lengths. Noting this, mean ice drafts from the model grid are treated as WD85 segments and classified using the WD85 criteria. Mean ice drafts from the state estimate "segments" are then compared to the WD85 segments of the same classification. Mean ice drafts from the state estimate are taken from the same measurement dates (February 9-12) and locations.[2]

Draft means and their ranges from the model and data are provided in Table 4.1. Simulated and observed mean drafts agree reasonably well in the MIZ. In fact, the average and minimum of all mean ice drafts in the state estimate are found to be very close to those measured. Drafts from the state estimate are consistent with typical drafts of seasonal sea ice - drafts in excess of several meters would only be expected in regions of multi-year ice, such as the northern Canadian Arctic (Kwok et al. 2007; Kwok and Cunningham 2008). Thus, ice drafts in the state estimate verify that simulated ice growth rates are represented reasonably well.

The greatest model-data discrepancies are found in the ice pack's interior, where simulated drafts are $\sim$ 50% of observations. How should the discrepancy in interior drafts be interpreted? Two explanations are offered: distinct meteorological conditions and unresolved ice physics.

Thermodynamic ice growth rates for thin ice are very sensitive to variations in atmospheric boundary conditions. Therefore, it may simply be the case that air-sea heat fluxes during the September-February period of $1966-1967$ exceeded that of $1996-1997$ leading

[2]Fortunately, the ice edge is in approximately the same location between February 9-12 in 1967 and 1996, greatly simplifying the model-data comparison.

to a deeper thermodynamically-grown February 1967 draft. Given the large uncertainties in the atmospheric state in the region, it is difficult to disprove this hypothesis.

Irreversible mechanical ice convergence by subgrid scale mesoscale eddies and turbulent surface motions are neither resolved nor parameterized by the ice model. By not representing subgrid scale convergence within the ice pack, simulated ice drafts are expected to be erroneously shallow (Holland et al. 2001). Indeed, 17% of drafts recorded by the ULS were mechanically deformed with 12% of those exceeding 2 m. If the same proportion of interior drafts in the state estimate were replaced with ice with a draft of 2.5 m, the mean interior draft would increase to 0.97 m thereby reducing the model-data discrepancy by $\sim 50\%$. Missing model physics is therefore an attractive explanation for the observed discrepancy.

Sea ice thickness from coastal stations Sea ice thickness in the state estimate is compared against ice thickness data compiled against the ice thickness climatology of the Canadian Ice Service (1992), hereafter CIS1992. CIS1992 is a compilation of weekly *in situ* ice and snow thickness from $1961 - 1990$ at several coastal stations, seven of which fall within the study region.

Ice thickness from the state estimate is compared against the mean and interannual ice thickness range provided by CIS1992. Model-data comparison is complicated by representation error: simulated ice thickness is a spatial average over $450 - 1000\,\mathrm{km}^2$ while CIS1992 data are point measurements. Little is known about the ice thickness decorrelation length scales near these stations.

The locations of observation sites are shown in Figure 4-5. Measurements were taken when ice was deemed safe enough to walk upon. Level ice was sampled when ocean depth first exceeded ice draft, presumably within a kilometer of the coastal station [3].

In space, CIS1992 data are compared with the closest non-land non-open boundary model grid cell to each station. In time, CIS1992 data are compared with state estimate one-week means centered in time around the CIS1992 measurement dates. Plots of ice thickness as a function of time for each station (ordered north to south) from CIS1992 and state estimate are presented in Figure 4-6.

Overall, the state estimate and CIS1992 are in fairly good agreement with respect to thickness magnitudes, the dates of ice appearance/disappearance, and ice thickness growth

[3] It is unclear whether measurements were only taken in areas accessible by foot from the coastal station.

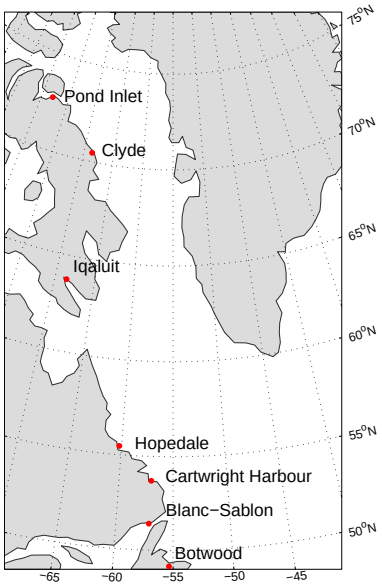

Figure 4-5: Locations of Canadian Ice Service near-coastal sea ice thickness measurement stations

rates (at least in the initial months).

However, two classes of discrepancies are identifiable and require rationalization: state estimate ice thicknesses which are thinner than CIS1992 by more than one standard deviation for several months (Pond Inlet and Iqaluit), and state estimate ice thicknesses which has extreme positive deviations from CIS1992 from mid-March (Hopedale, Cartwright Harbour, and Botwood). These discrepancies are reconcilable by invoking model resolution-related errors.

Compared to the ice at the observed coastal stations, ice in each of the model grid cells identified with a coastal station (simulated coastal station) is exposed to more dynamic interaction with the open ocean and offshore ice pack. In actuality, each coastal station is shielded from the open ocean by either a natural harbor, inlet, or one or more islands. These natural barriers reduce the convergence of offshore ice and the divergence of nearshore ice. In other words, the evolution of ice thickness at each coastal station is probably driven by thermodynamical processes. In contrast, ice at each simulated coastal station has no protective offshore barriers - the evolution of its thickness has both a thermodynamical and dynamical component.

Ice at each simulated coastal station falling into the first discrepancy class is subjected to unrealistic divergence from northwesterlies leading to erroneously thin ice. Ice at each

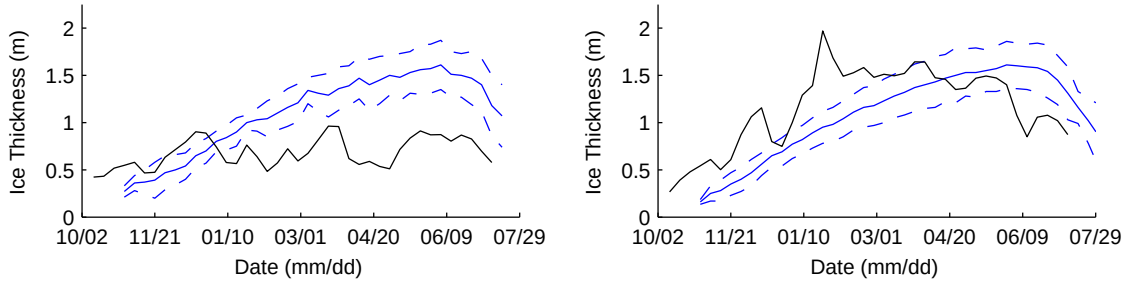

(a) Pond Inlet

(b) Clyde

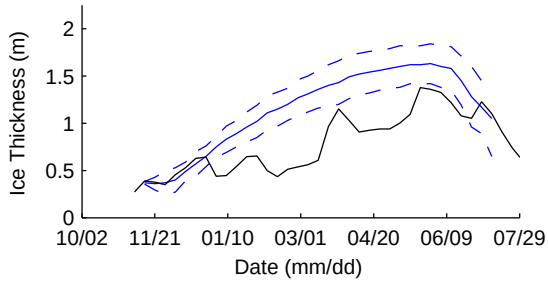

(c) Iqaluit

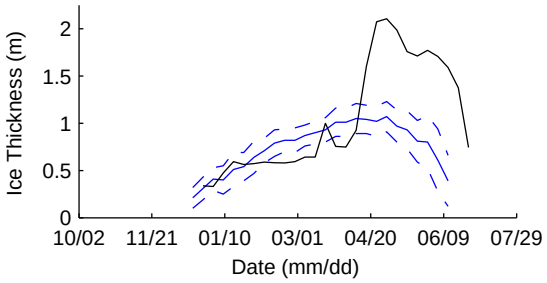

(d) Hopedale

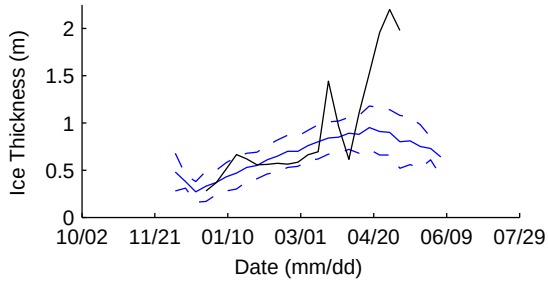

(e) Cartwright Harbour

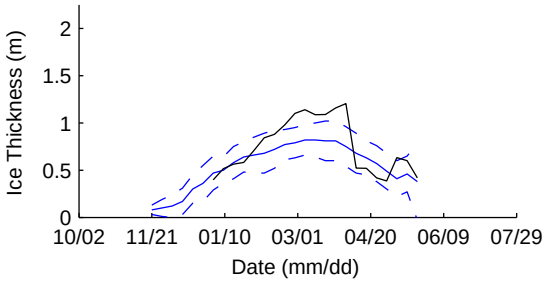

(f) Blanc Sablon

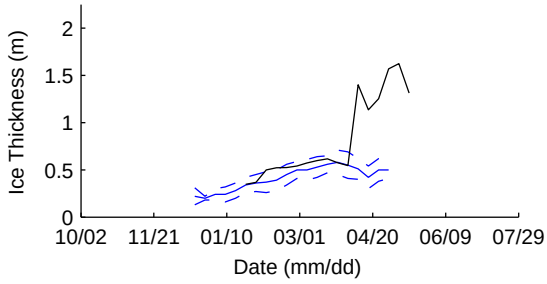

(g) Botwood

Figure 4-6: Sea ice thickness at several coastal stations from the state estimate (black: one-week mean) and Canadian Ice Service climatology (blue solid: climatology mean of weekly measurements, blue dashed: ± one standard deviation of weekly data).

simulated coastal station falling into the second class suffers from unrealistic ice convergence from variable synoptic winds after the widespread springtime thinning of the offshore ice pack.

Support for a these explanations is found from measurements made during a field campaign near Cartwright Harbour in which ice measured within the protective confines of the harbor was observed to be significantly thinner and less deformed than ice 30-50 km offshore (Holladay and Moucha 1994).

A final hypothesis to explain the model-data discrepancies of the second class is sampling bias. The CIS1992 measurement procedure called for the sampling of "level" ice. Ice which had roughened during dynamical convergence would fail this measurement criterion. Therefore, compared with the true spatially-averaged ice thickness, one would expect the CIS1992 to have a negative bias (*e.g.,* Worby et al. 2008).

Sea ice thickness survey conclusions

The reproduction of sea ice thickness in state estimate appears to be sound. Ice thickness gradients are consistent with expectations: thicker ice in the western Baffin Bay, thinner ice along the MIZ, and a cycle of growth and melt which is within the normal expected range of seasonal sea ice. Almost all model-data discrepancies are attributable to either representation error (coarse resolution) or model error (missing physics). Model-data discrepancies do not reveal any large-scale or systematic biases or errors. The extreme paucity of ice thickness data and the absence of reliable estimates of ice volume in the domain prevent additional conclusions to be drawn.

4.2.3 Sea ice plus snow freeboard survey

Following the evaluation of sea ice and sea ice draft thickness in the state estimate, a related variable is now considered: sea ice-plus-snow freeboard. Sea ice-plus-snow freeboard (total freeboard or freeboard) is the combined height of sea ice and snow above the sea surface. Since sea ice thickness contributes to the freeboard depth, an argument can be made that freeboard should be classified as a sea ice thickness measurement. However, in the Labrador Sea and Baffin Bay, the relative contributions of snow and sea ice to freeboard are thought to be of the same order - freeboard is equally a class snow thickness measurement as it is of ice. Furthermore, without accurate knowledge of snow depth, the conversion of freeboard

to ice thickness if prone to extremely large errors (Kwok and Cunningham 2008). Since no accurate snow depth estimates are available for this region and time period, freeboard is considered distinct from ice thickness for the purposes of model-data comparison.

First, the main features of mean state estimate freeboard during two ~ 33 day periods (cycles) are reviewed. State estimate freeboard (model freeboard) is then compared with non-contemporaneous freeboard estimates of Baffin Bay. Model-data differences are then analyzed.

Main features of the snow and ice freeboard in the state estimate

Model freeboard is calculated using the state estimate ice and snow thickness fields and the same densities of ice, snow, and seawater that are used in the model (see Section 4.2.2). The freeboard equation is derived from Equation 4.1. To facilitate later comparison with data, daily-mean model freeboards are averaged over two ~ 33 day cycles, corresponding to dates in October-November (ON) and February-March (FM). Model freeboards for both cycles are presented in Figures 4-7(a) and 4-7(b). ON dates are October 4 to November 19; FM dates are February 17 to March 21.

Model October-November freeboard Mean model freeboards are strikingly uniform (between 10 and 15 cm) across most of the ice-covered Baffin Bay suggesting near-uniform ice growth rates. Thinner freeboards (to 5 cm) are found south of Davis Strait. Thicker freeboards (to 50 cm) are seen in the north, an artifact of residual snow and ice from the previous annual cycle.

Model February-March freeboard Mean model freeboards in the FM cycle have much greater spatial variability and range than ON. A pattern of decreasing freeboards from north (to 75 cm) to south (to 5 cm) is apparent. Freeboard in the western Baffin Bay (to 50 cm) decreases eastward (to 20 cm). Freeboards are thinner south of Davis Strait (to 30 cm). Thinner values tend to be found near the Labrador Coast the northeast Labrador Sea.

In the region of deep freeboard (exceeding 45 cm) in the northern Baffin Bay, snow depth and freeboard depth are equivalent - sea ice is completely submerged by the weight of overlying snow. The very thin freeboards in the northeast Labrador Sea coincide with an area which is ice-covered for only a several-week period in March (see Figures 4-1 and 4-4).

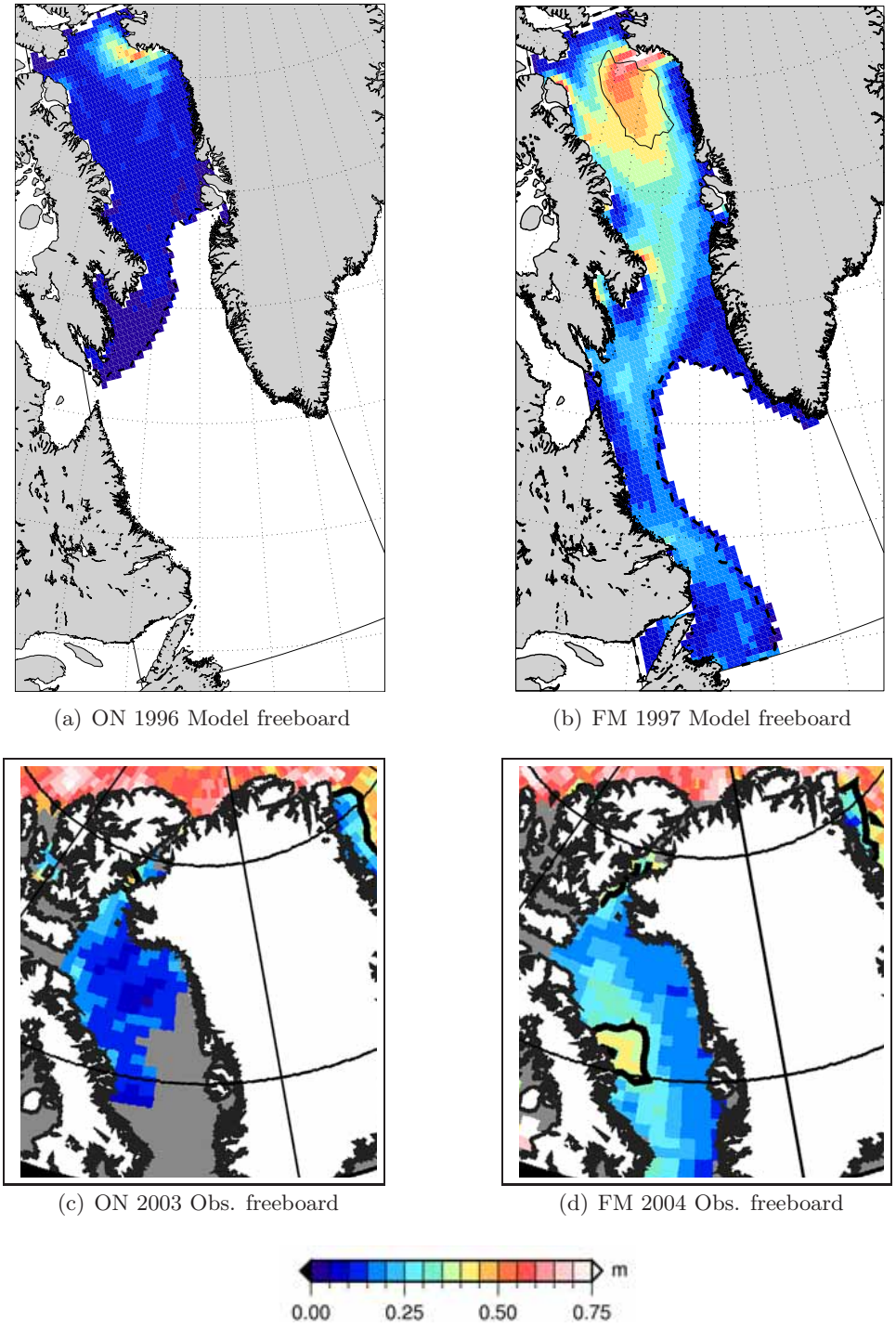

(a) ON 1996 Model freeboard

(b) FM 1997 Model freeboard

(c) ON 2003 Obs. freeboard

(d) FM 2004 Obs. freeboard

Figure 4-7: Total sea ice plus snow freeboard from 1996-1997 state estimate (a-b) and 2003-2004 observations (c-d). Images from (c-d) are adapted from Farrell et al. (2009) (FAR2009). Model freeboards utilize FAR2009 color scheme to facilitate comparison. Black contour in Baffin Bay: (b) area with freeboards of $\geq$ 99% snow, (d) area of multi-year ice estimated by FAR2009.

Evaluation of snow and ice freeboard in the state estimate

Model freeboards are compared to the freeboard reconstruction of Farrell et al. (2009), hereafter FAR2009. FAR2009 is based on measurements from the Geoscience Laser Altimeter System (GLAS) on board the Ice, Cloud and land Elevation Satellite (ICESat) made during the 33-day ON and FM ICESat campaign periods, spanning October 2003 to April 2008.

The FAR2009 method of freeboard reconstruction for each cycle is as follows. After freeboard estimation, measurements are binned into a 50×50 km grid and averaged.[4] The resultant dataset consists of five ON and six FM freeboard reconstructions, each nominally representing the mean freeboard during the cycle.[5] FAR2009 overlaps the model domain north of 65° N.

No FAR2009 data are available for the $1996-1997$ state estimate (being earlier than the ICESat period). Therefore, model freeboard is compared to the median FAR2009 ON and FM cycle freeboards. The range of interannual variability ($\sim 10-20$ cm) plus expected errors ($\sim 5-10$ cm) inform a first-guess model-data misfit uncertainty (Kwok et al. 2007). Note, however, the ICESat record is certainly too short to capture the full range of interannual Baffin Bay freeboard variability.

To simplify a visual model-data comparison, freeboards from the FAR2009 2003 ON and FM 2004 cycles are presented in Figures 4-7(c) and 4-7(d). Freeboard fields during ON 2003 and FM 2004 were subjectively determined to represent each cycle's median conditions.

Model ON freeboards are within FAR2009 uncertainties except in the too-deep (to 50 cm) multi-year sea ice freeboard in the northern Baffin Bay. The deep model freeboard is excessive but understandable as little to no ice remains in Baffin Bay after the summer melt period during the $2003-2008$ ICESat era.

The greatest FAR2009 FM cycle-to-cycle variability is in the western Baffin Bay near Baffin Island where freeboards vary between $\sim 30-60$ cm. Therefore, the FM model freeboard in the western Baffin Bay is within the interannual variability uncertainty.

For all FAR2009 FM cycles, freeboard in the eastern Baffin Bay is exclusively within $10-30$ cm. Therefore, model freeboards in the eastern Baffin Bay are excessive. Model-data discrepancy is greatest northwest of Disko Island where model freeboard exceeds the

[4] A review of the methods of freeboard estimate are beyond the scope of this thesis. The interested reader is directed to the work of Kwok et al. (2004, 2006, 2007)

[5] One winter cycle extended into April.

maximum FAR2009 FM freeboards by $\sim 30 - 50\,\mathrm{cm}$.

As mentioned, FM model freeboards in the excessive freeboard regions in northern Baffin Bay are entirely snow. The spatial patterns of deep snow/freeboards are consistent with a distinct region of high precipitation rates in the NCEP/NCAR reanalysis. High precipitation rates in the northern Baffin Bay are due to a serious uncorrected reanalysis bias. Evidence for a high-precipitation bias in the NCEP/NCAR reanalysis is found in a comparison with the ECMWF reanalysis (Serreze et al. 2005), by comparing the precipitation estimates of the NCEP/NCAR with the North American Regional Reanalysis of Mesinger et al. (2006), and by comparing snow depths implied by the reanalysis precipitation rates with the snow depth estimates of Cavalieri et al. (2004, updated daily). Indeed, the magnitude of the reanalysis precipitation bias implies snow pack depths which are consistent with the magnitude of the model freeboard error.

Snow and ice freeboard survey conclusions

Despite the serious model-data discrepancies in the northern Baffin Bay, the state estimate freeboard reconstruction provide two useful pieces of information. One, the good agreement with the observed freeboard in the autumn cycle suggests well-reproduced thermodynamic ice growth rates during the initial period of Baffin Bay freeze-up. Two, the winter cycle freeboard reconstruction is consistent with the first-guess precipitation fields and the sea ice "flooding" parameterization.

Why were the reanalysis precipitation biases not corrected by the atmospheric state model control variables? The obvious explanation is that freeboard and snow depth were not included in the model-data misfit cost function. It is reasonable to conclude that the negative effects from excessive freeboard on other cost function terms were mitigated by adjustments to other control variables.

4.2.4 Sea ice drift survey

The sea ice motion (ice drift) in the state estimate (model ice drift) is presented and compared with observations in this section. The organization is as follows. The analysis of model ice drift is divided into three parts: the January through March mean drift, statistics of the JFM ice drift at three locations (Baffin Bay, Davis Strait, and LC), and an example of the dynamical response of the ice pack to anomalous synoptic wind forcing. Model-data

comparisons are made separately for each of the three divisions. The section concludes with a summary and overall evaluation of state estimate with respect to ice motion.

For the ice drift model-data comparison, two classes of observations are utilized: data from satellite-tracked ice beacons (beacons) and basin-scale estimates produced using satellite image retrievals. The dataset classes are complimentary in the spatial distribution - ice beacon data are available off the southern Labrador Coast and Newfoundland while the satellite data are more skillful north of Davis Strait.

Main features of the January-March mean ice drift in the state estimate

The model mean January through March (JFM) 1997 ice velocity and mean sea level pressure from the NCEP/NCAR reanalysis is presented in Figure 4-8(a).[6] To clarify the basin-scale sense of drift, velocity vectors are only shown where ice concentration exceeds 35% for at least 10 days thereby filtering out short-lived high-velocity ($\geq 50\,\mathrm{cm\,s^{-1}}$) diffuse ice in the outer MIZ.

The model mean JFM ice drift field indicates a close relationship between surface pressure and mean ice drift. Following isobars, a weak ($\leq 5\,\mathrm{cm\,s^{-1}}$) cyclonic flow in the northern Baffin Bay joins the faster ($7.5\,\mathrm{cm\,s^{-1}}$) south-southeastward flowing pack. Passing through the Davis Strait, the pack accelerates with faster velocities near the center of the Strait ($12.5\,\mathrm{cm\,s^{-1}}$) than to either side ($5\,\mathrm{cm\,s^{-1}}$). Over the NS, the model ice velocities have a nonzero component normal to the ice edge contour.

There is a significant velocity gradient across the Labrador Shelf ranging from $5\,\mathrm{cm\,s^{-1}}$ inshore to greater than $50\,\mathrm{cm\,s^{-1}}$ in the LC MIZ. High model ice velocities over the Labrador shelfbreak indicate a significant momentum transfer from the LC.

This basin-scale mean model ice drift field also reveals that onshore dynamical ice convergence (and subsequent deformation thickening) followed by offshore advective transport is a reasonable explanation for the unusual patterns of ice thickness seen in Figures 4-4 especially northwest Greenland (*e.g.,* 76° N, 65° W) and along the Baffin Island and Labrador Coasts (*e.g.,* 72° N, 70° W and 55.5° N, 60° W).

Comparison of the model JFM mean ice drift is made against two domain-scale satellite imagery-derived ice velocity datasets: the daily-mean 25×25 km gridded estimate of Fowler

[6]Surface pressure is not included a forcing term in the simulation. However, the surface pressure field shown is internally consistent with reanalysis surface wind field and is meant to provide a sense of the mean geostrophic wind stresses imposed on the ice during this period.

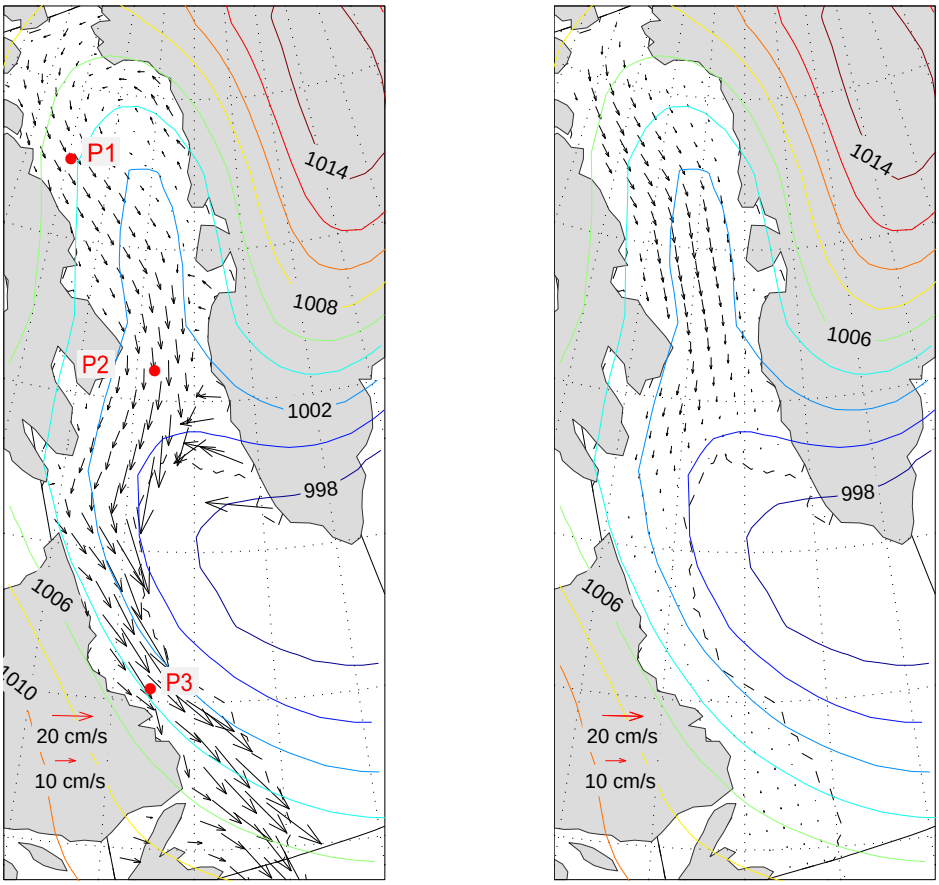

(a) JFM State Estimate

(b) JFM Observations

Figure 4-8: January-March mean sea ice velocity vectors and mean sea level pressure from the NCEP/NCAR reanalysis (hPa) for state estimate (a) and observations (b). Dashed lines in both denote the mid-March pack ice maximum extent (ice concentration $> 35\%$) in state estimate. In both model and data, every fifth vector is shown.

(2003, updated 2007), hereafter FW2003, the monthly-mean mapped estimates of Baffin Bay ice drift by Kwok and Cunningham (2008), hereafter KW2008, and satellite-tracked ice buoy data.

FW2003 is notable for being contemporaneous with the state estimate period utilizing data from AVHRR, SSMR, SSM/I, and the International Arctic Buoy Program. KW2008, in contrast, uses only 2002-2007 AMSR-E data.[7] Additional details on the methodologies of FW2003 and KW2008 can be found in Ikeda and Dobson (1995, chap. 23) and Kwok et al. (1998), respectively.[8] A limited number of buoys were deployed and tracked between $46.5 - 58.0^\circ$ N in association with the 1987-1989 Labrador Ice Margin Experiments field

[7] Although the KW2008 algorithm implicitly uses ice buoy data through its algorithm validation.

[8] However, many of the important methodological details used in FW2003 are apparently unpublished.

campaign off the coasts of Labrador and Newfoundland (Peterson and Prinsenberg 1989; Prinsenberg and Peterson 1992; Tang and Yao 1992).

The methodologies of FW2008 and KW2008 are unreliable under certain conditions and locations: within several tens of kilometers of the shoreline, in regions of active ice deformation, in areas of low ice concentrations, during summer melt, and in periods of high atmospheric water vapor content (associated with synoptic weather systems). Both datasets report RMS errors between $3.4 - 4.2\,\mathrm{cm\,s^{-1}}$. Buoy data are likely more accurate than the satellite imagery-derived products but are far more sparse in space and time.

The JFM 1997 mean ice drift from FW2003 is presented alongside the model ice drift field in Figure 4-8(b). Model and data are agree well in the western Baffin Bay away from the Baffin Island Coast. Cyclonic ice drift in the northeast Baffin Bay is absent in the data, likely a result of the inability of FW2003 to estimate drift in areas of dynamical ice convergence. Strikingly, the data show a dramatic reduction of ice velocity south Davis Strait. This reveals a serious error in the dataset which is discussed in the next section.

The monthly-mean Baffin Bay KW2008 drift fields (not shown) confirm the realism of two features noted in the state estimate: the pattern of accelerating south-southeastward alongshore flow from northern Baffin Island to Davis Strait and the negative west-east velocity gradient. Model ice drift speeds are in excellent agreement with KW2008 with the exception of northwestern Baffin Bay where model ice drift on the northern Baffin Island Current (BIC) is about 50% below the observed multi-year mean. The likely cause of this discrepancy is a weak BIC related to a weak inflow currents through the Canadian Arctic Archipelago in Baffin Bay.

Model mean ice drift agrees with two features seen in beacon data: ice floe trajectories generally follow the path of the LC (even as the current meanders due to bathymetric features and eddies) and the positive gradient in ice drift velocities in the alongshore-direction from the Labrador Coast to the LC shelfbreak. Per the second point, the two-week velocity mean beacons deployed between 51° N and 54° N on the LC at the end of March 1989 increased from from 13 $\mathrm{cm\,s^{-1}}$ on the shelf to over 33 $\mathrm{cm\,s^{-1}}$ on the slope (Prinsenberg and Peterson 1992).

Main features of the January-March daily ice drift in the state estimate

The JFM mean ice drift field obscures features of the ice pack's time-varying directional and speed drift variability. To illustrate model ice drift variability, histograms of daily-mean ice velocity at three locations (identified in Figure 4-8(a) as P1, P2, and P3) are presented in Figure 4-9.

At each location, the time-mean model ice drift speed underestimates the median drift speed because of ice drift directional variability. On the other hand, the mean ice drift directions are consistent with the most frequent daily ice drift directions. For example, in Baffin Bay, the majority of daily ice drift directions are within $\pm 15^\circ$ of its mean but exceed the mean by at least a factor of 2 more than 25% of the time.

In the Davis Strait, the directional variability is even more variable. Incredibly, 25% of daily drifts even have a northward component. On occasions of directly northward flow, model ice drift speeds (15-20 $\mathrm{cm\,s^{-1}}$) exceed the JFM mean in the (mainly) southward direction (12 $\mathrm{cm\,s^{-1}}$).

On the LC, model ice drift directional variability is lower than the Davis Strait, being mostly within $\pm 20^\circ$ of its mean. Interestingly, on occasion model ice drifts are rotated clockwise of its mean alongshore-direction towards the Labrador Coast on occasion - a likely indicator of dynamical ice convergence with the shoreline.

The FW2003 dataset provides daily ice drift at the three locations described above during the period January-March 1997. FW2003 daily ice drift data are presented alongside the state estimate velocity histograms in Figure 4-9.

Overall, model ice drift compares well with FW2003 data north of Davis Strait with respect to both direction and speed distributions. There is somewhat less variability in direction in the FW2003 data which is evident in the more frequent occurrences of drift around the mean direction. Strikingly, the occasional northward model ice drift in the central Davis Strait is almost completely absent in FW2003. The lack of FW2003 directional variability at these locations is likely related to a limitation of the FW2003 methodology - northward ice drift in the Davis Strait is likely undergoing dynamical convergence.

South of Davis Strait, model and data disagree profoundly. On the LC, FW2003 daily ice drift variability has no spatial structure and speeds never exceed 5 $\mathrm{cm\,s^{-1}}$. What is the source of the model-data discrepancy in daily ice drift?

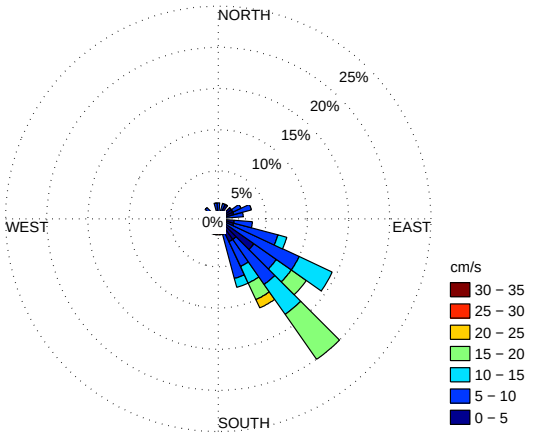

(a) State Est. P1 Baffin Bay

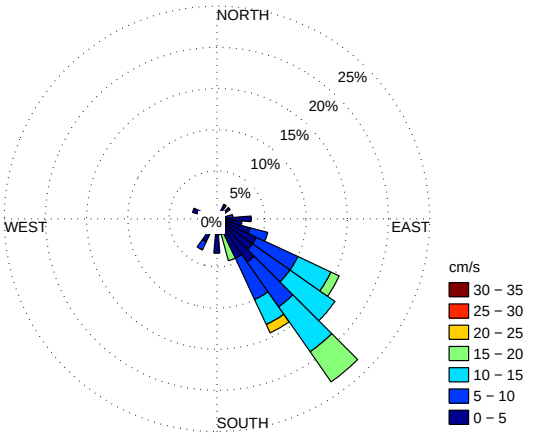

(b) Obs. P1 Baffin Bay

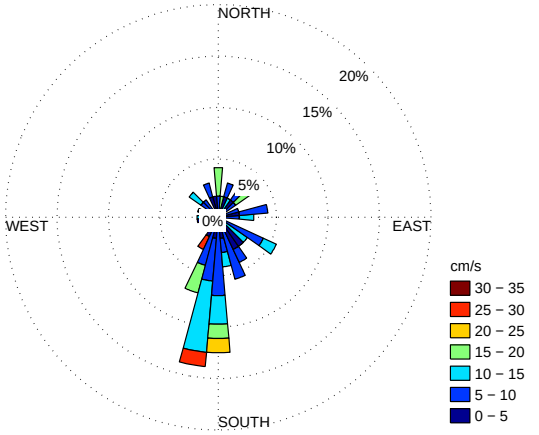

(c) State Est. P2 Davis Strait

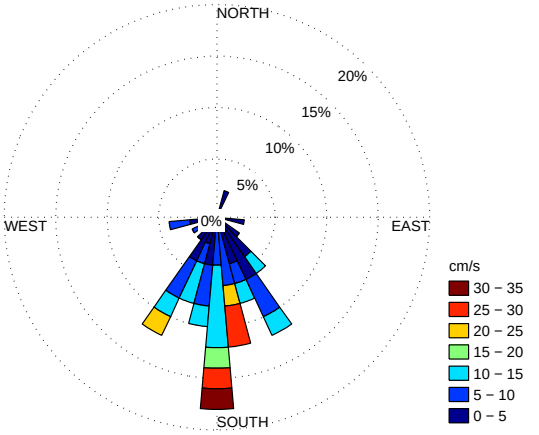

(d) Obs. P2 Davis Strait

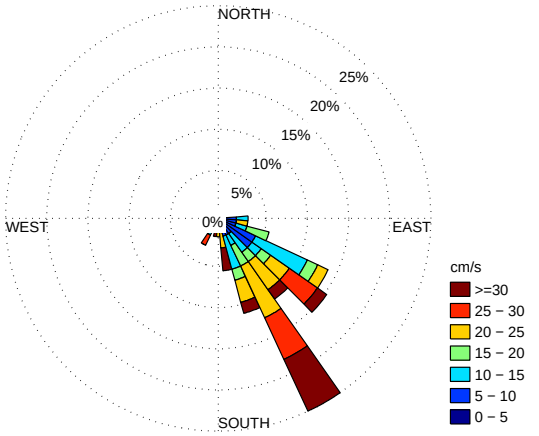

(e) State Est. P3 Labrador Current

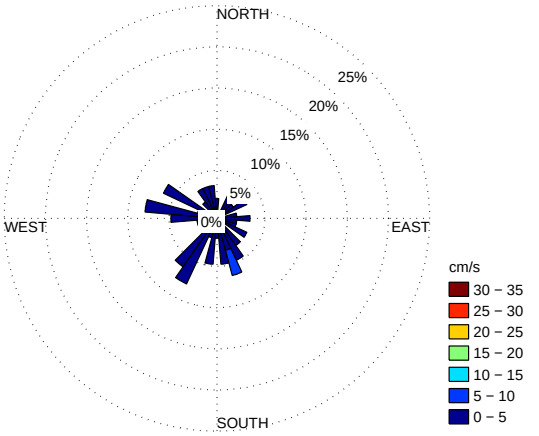

(f) Obs. P3 Labrador Current

Figure 4-9: Velocity rose histograms for daily ice drift direction and velocity at points P1, P2, P3 defined in Figure 4-8(a) from the state estimate (a,c,e) and FW2003 dataset (b,d,f). Colors along the rose segments denote speed (all plots use the same color scheme). Each "wedge" is a histogram bin spanning 10° in direction.

Few observational data south of Davis Strait are incorporated in FW2003 due to previously enumerated methodological limitations (*e.g.,* coastal proximity, cloudiness, rapid deformation, fast ice velocities, etc.). Gaps in the observational data are filled using optimal interpolation with a spatially and temporally fixed decorrelation length scale.[9] The spatial exponentially-decreasing extrapolation can influence points up 1250 km away from an observation - approximately the length from P2 (Davis Strait) to P3 (mid-Labrador Current) - observations from the Baffin Bay are projected to the LC in with exponentially-decreasing magnitudes. The spatial extrapolation method of FW2003 is therefore completely ill-suited for the thesis domain south of Davis Strait.[10]

Abundant satellite data for the entire model region are available for several days during January-March 1997 (on these days little to no spatial extrapolation was required in FW2003 to estimate a basin-scale ice drift field). However, because the number of good satellite coverage days is so small, FW2003 data south of Davis Strait are not suitable for JFM mean or JFM daily model-data comparison.

Main features of ice drift response to anomalous synoptic forcing in the state estimate

The analysis of daily ice drift variability indicated frequent events during which ice drift direction deviated significantly from its mean direction. Events that induce anomalous ice drift are likely associated with synoptic weather systems (*e.g.,* polar lows) passing through the region. A simple way to determine the model's ability to reproduce basin-scale ice drift variability is to compare the dynamical response of the ice pack to anomalous atmospheric forcing in the state estimate and observations.

An interesting synoptic situation occurred on March 11, 1997: a high pressure center over northwest Greenland, a low pressure center several hundred kilometers to the southeast of Newfoundland, and a low pressure center in northern Québec province. Mean sea level pressure and ice drift on this day from the state estimate is shown in Figures 4-10(a).

Relative to the JFM mean, model ice drift on this day is dramatically different. The cyclonic ice drift in the northern Baffin Bay is replaced with northwest ice drift consistent

[9]This length scale is likely derived to optimally fill measurement gaps within broad ice-covered areas (such as the central Arctic Ocean) and not for ice motion on distant boundary currents.

[10]The FW2003 is an unfortunate example of how the blind application of an interpolation scheme, ironically called optimal, can lead to ridiculous and misleading results.

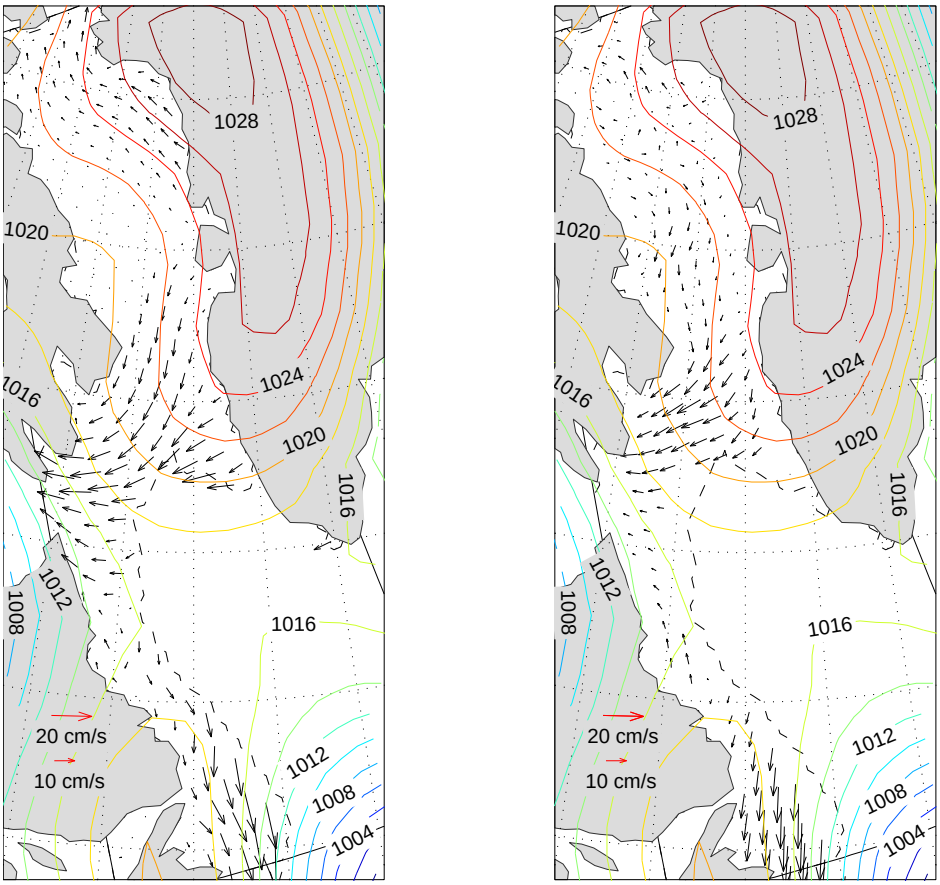

(a) 03/11/97 State Estimate

(b) 03/11/97 Observations

Figure 4-10: Daily mean sea ice velocity vectors sea level pressure (hPa) for March 11, for state estimate (a) and observations (b). Dashed line denotes 35% sea ice edge in state estimate. Every fifth vector of each dataset are shown.

with the anomalous zonal pressure gradient - ice is even driven *into* Smith Sound. Anomalous geostrophic wind stresses in the central Baffin Bay arrest the pack, ceasing its mean southward tendency.

Topographically-steered winds around southern Baffin Island drive the ice anticyclonically into the Hudson Strait. Anomalous geostrophic winds over the north Labrador Shelf reverse the direction of ice drift and deflect ice onshore over the south - phenomena which have been observed during similar synoptic situations (*e.g.,* Peterson and Prinsenberg 1989).

The March 11, 1997 FW2003 ice drift record is derived from abundant satellite data (good coverage across the model domain) and therefore does not suffer significantly from extrapolation-induced errors. The FW2003 ice drift for this day is shown alongside the state estimate in Figure 4-10(b).

The directional and speed tendencies in both model and data show excellent agreement over most of the domain. The smaller quantitative differences, such as the speeds in the northern Baffin Bay, are within the expected uncertainty of the data. Other differences in details, such as the amount of anomalous onshore drift in the southern LC, can be reconciled by invoking arguments about irregular satellite image registration times and errors in the reanalysis forcing fields used to force the model. Overall, the model shows a realistic response to anomalous transient forcing on this day. A more general assessment requires comparison against more data than is currently available.

Ice drift survey conclusions

The analysis of model ice drift reveals good qualitative and quantitative reproduction of basin-scale mean tendencies, daily variability of direction and speed, and realistic response to anomalous atmospheric forcing. It is reasonable to conclude that the dynamical coupling between the atmosphere and sea ice and between the ocean and sea ice is sufficient for the purposes of state estimation in the Labrador Sea.

Even though ice motion data were not included in the model-data misfit cost function, adjustments to the atmospheric state 10 m wind control variable do alter the ice drift trajectories (not shown). Adjusted wind fields/ice drift trajectories alter the ice edge location and improve the ice concentration model-data misfit, especially in the MIZ. From the model-data comparison, it is clear that the impact of wind field adjustments on the basin-scale patterns of ice motion are minor.

4.3 Ocean Survey

A comprehensive survey of the state estimate's representation of ocean hydrography, circulation, and fluxes is not possible within the space confines of this thesis. Instead of an exhaustive review, a few interesting features which provide a succinct overview of the simulated ocean state are presented: integrated barotropic transports, time-mean circulation at several depth levels, and wintertime maximum mixed layer depths.

4.3.1 Ocean Circulation

The circulation and integrated transports of the Labrador Sea and Baffin Bay in the state estimate are presented in this section. In the literature, simulated and estimated motion fields of the subpolar gyre are often presented in the form of a barotropic streamfunction or time-mean (or snapshot) velocities at depth. In high-resolution numerical models, snapshots of the motion field are often presented to demonstrate the simulation of mesoscale eddies (*e.g.,* Chanut et al. 2008). Since mesoscale eddies are absent in this simulation, only the barotropic streamfunction and time-mean fields are presented [11].

With respect to understanding the role of the ocean in setting the evolution of the sea ice pack in the domain, the representation of the large-scale cyclonic tendencies of the flow field in the Labrador Sea is important for several reasons. Across the THF, the advection of heat is hypothesized to be a critical determinant of the sea ice edge location and sea ice-ocean-atmosphere energy fluxes in the MIZ. The advection of buoyant Arctic Water (AW) into the domain from the northern straits and the WGC and its subsequent dispersal across the northern Labrador Sea and LC is also thought to be a zeroth-order factor in the sea ice evolution.

The main features of the barotropic streamfunction in the state estimate are first presented followed by a comparison against transport estimates from other numerical simulations and synoptic transects. The annual-mean velocity fields from the state estimate are then presented at four model depth levels and then compared against estimates from near and subsurface Lagrangian drifters and floats. The section concludes with a short explanation for the model-data discrepancies. For brevity, model-data comparisons are limited to observations and estimates in the Labrador Sea.

Main Features of the barotropic streamfunction in the state estimate

The circulations of both the Labrador Sea and Baffin Bay are baroclinic. Estimates of the mean horizontal velocities indicate that a nearly depth-independent flow direction. It is therefore convenient to present the large-scale motion field in the form of a barotropic

[11] In presenting the time-mean velocities, it is understood that the seasonally-varying aspect of the circulation is obscured.

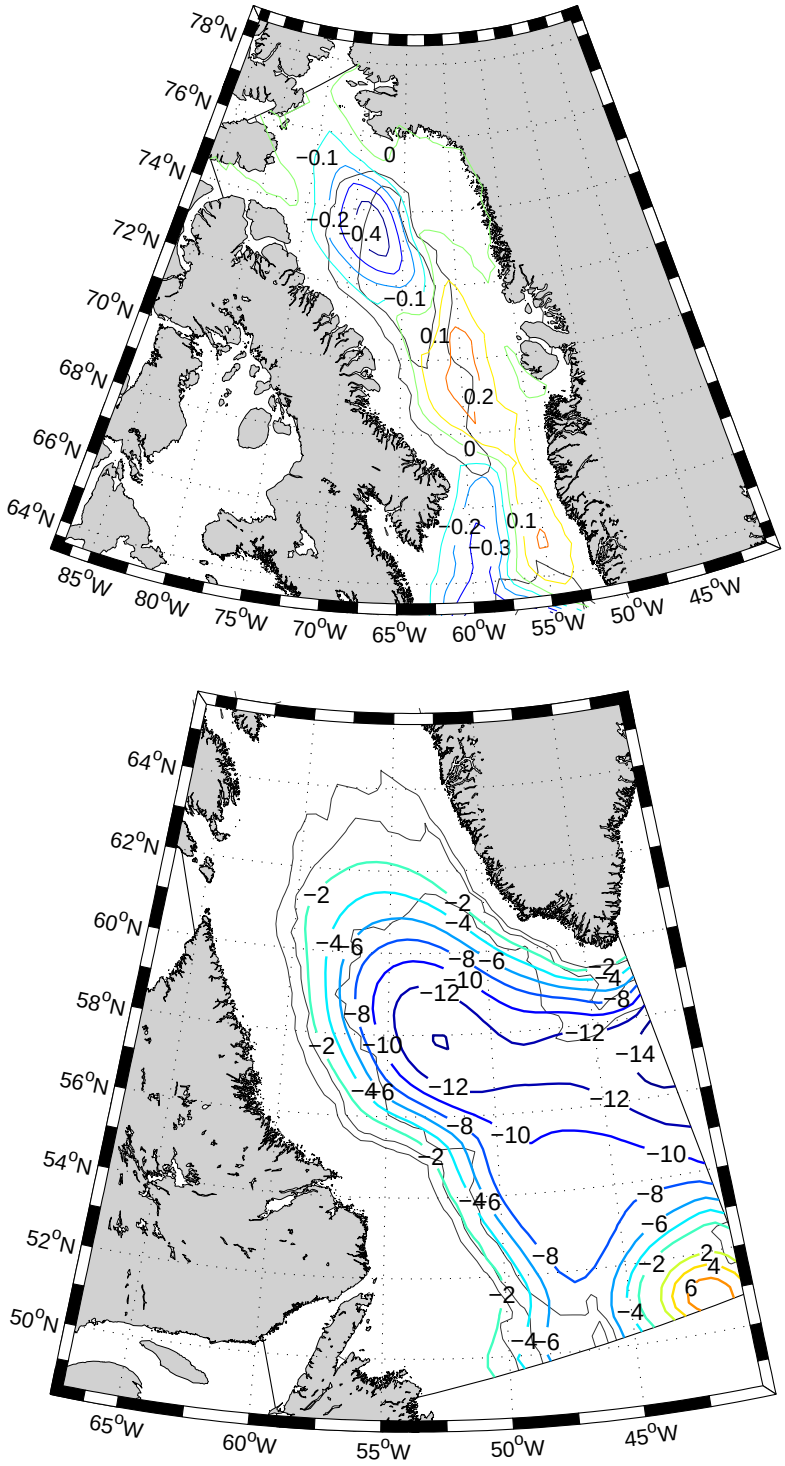

Figure 4-11: Annual mean vertically-integrated transport streamfunction (Sverdrups) averaged (colored contours) and depth contours at 3000, 2000, and 1000 m (gray contours). Transport contour interval 2 Sv in Labrador Sea and 0.1 Sv in Baffin Bay. Maximum cyclonic transport is $\sim$ 14 Sv. The anticyclonic branch of the North Atlantic Drift is noted in the southeast corner.

streamfunction, ψ, which satisfies the following equation:

$$\int_z \vec{u}\, dz = \hat{k} \times \nabla_h \psi \tag{4.2}$$

The calculation of ψ is made using the model flow fields on the rotated curvilinear grid. The vertically-integrated flow in the model's mainly north-south direction is integrated from the model's western edge to its eastern. The result of this calculation, in Sverdrups (Sv, $10^6\,\mathrm{m}^3\,\mathrm{s}^{-1}$) is shown in Figure 4-11.[12]

The volume integrated flow in the state estimate reveals little transport on the boundary current shelves above 1000 m, increased transport with depth in the Labrador Sea and the Northwest Corner of the North Atlantic Drift in the model's southeast corner.

The transport increases with depth monotonically in the Labrador Sea boundary current system. The boundary current system transport is a function of location. Considering total transport from the shoreline to 3000 m, the state estimate gives 13 Sv south of Cape Farewell, 4 Sv south of Cape Desolation, approximately 6 Sv in the northern LC, and 4 Sv south of Hamilton Bank. The transport increases in a nearly linear manner from the southwest of Greenland and Labrador Coast to the streamfunction maximum. Above the shelfbreak the total transport is less than 2 Sv.

In the Baffin Bay, the state estimate shows alternating cyclonic and anticyclonic transports in the northern and southern half of the basin respectively. The net integrated meridional transport in the model across the Baffin Bay is close to zero.

Evaluation of the barotropic streamfunction in the state estimate

Observation-based estimates of vertically integrated transport from observations do not exist in the form of a spatial map for this domain. Instead, hydrographic transects combined with absolute velocity measurements from acoustic Doppler profiles (ADCP) have been used to estimate sea floor to surface transports across several transects within and across the domain. Moreover, basin-scale integrated transports have been estimated using numerical models differing.

The state estimate appears to have between 20 and 38% of the transports indicated by

[12] In this volume conserving Boussinesq model, the integrated lateral volume transport between two points is found by the difference of ψ at those two points. The value of ψ is arbitrary to a constant, in this case, zero. Thus, the transports of the cyclonic boundary currents are given by the nominal value of ψ within the boundary current.

all observation-based transport estimates. Based on synoptic data taken between August-September, 2005, total boundary current transports from Cape Farewell to the 3000 m are estimated to be 29.6 Sv to 3000 m and 53.8 Sv to 3500 m (Holliday et al. 2009).[13] In contrast, the state estimate has approximately 22% and 38% of the observed transport across these two sections, respectively.

Based on a similar combination of ship-based and moored ADCP and hydrographic measurements near 53° N and 56° N made between 1996 and 2005, boundary current transports are estimated to be on the order of 30 Sv from the Labrador shelfbreak to 3000 m (Fischer et al. 2004; Dengler et al. 2006). In contrast, transport in the state estimate at these locations does not exceed 6 Sv.

Finally, cross-basin integrated cyclonic transport estimated with ADCP and hydrographic measurements across three cross-basin transects from the shelfbreaks of Labrador to Greenland during the winter of 1997 are $\sim$ 44 Sv: 33 Sv from the Labrador shelfbreak to the 3000 m isobath on the LC and an 11 Sv in the form of a recirculation gyre in the deeper waters 100 km beyond the 3000 m isobath (Pickart et al. 2002). In the state estimate, maximum cross-basin vertically-integrated cyclonic transport in the vicinity of the three cross-basin transects is 14 Sv.

The comparison of time-mean state estimate transports with published estimates from ship-based oceanographic sections is complicated by issues of sampling - synoptic section data may not be representative of the mean transports. However, observed volume transport seasonal and interannual variability is small (25%) compared to the annual mean (Dengler et al. 2006).

Support for the data-based estimates comes from the output of numerical models simulating the circulation of the subpolar gyre. Maximum vertically-integrated cyclonic transports through the Labrador Sea are found between the range of 25-60 Sv (Treguier et al. 2005; Deshayes and Frankignoul 2008). In general, the greatest cyclonic barotropic transports are found in models with the highest horizontal resolution with an apparent convergence in the 55-60 Sv range.

Given that the state estimate probably underestimates Labrador Sea transports (although to what extent remains an open question), what are the probable reasons? Based

[13]The additional transport in the second transect is due to the addition of a cyclonic recirculation in the boundary current.

on the findings of the numerical simulations, a much higher horizontal resolution, shorter time step, and lower numerical viscosities are probably required to improve simulated transports in the Labrador Sea.

On the other hand, it is possible that the magnitude of the barotropic transports in the state estimate is low simply because open boundary volume inflows are too weak. Indeed, the inflow open boundary volume fluxes taken from the 1-degree ECCO model are much lower than the observation-based estimates of Holliday et al. (2009) but consistent with the transport estimates of the 1-degree models compiled in Treguier et al. (2005).

To test whether a weak inflow was responsible for the low barotropic transport in the state estimate, I conducted an experiment in which I replaced the open boundary volume inflows taken from the 1-degree ECCO model with inflows taken from the 18 km ECCO2 model of Menemenlis et al. (2008). Using the ECCO2 inflows, the maximum Labrador Sea barotropic transport increased to 24 Sv - almost double the original solution - corresponding to 23 Sv of inflow around Greenland and a net 1 Sv of inflow into the Baffin Bay from the Canadian Arctic Archipelago. Consequently, weak inflows in the 1-degree ECCO model appear to be the main reason for the significant model-data discrepancy with respect to vertically-integrated transport.[14]

Main Features of the time-mean circulation in the state estimate

The time-mean horizontal velocities at four depth levels in the upper 1500 m of the Labrador Sea are presented in Figure 4-12. The direction of flow in each of these depth levels (excluding the North Atlantic Current branch) is consistent with the cyclonic pattern seen in the barotropic streamfunction. The simulated flow is intensified over the continental slope and broadly follows bathymetric contours. Diminishing velocities with depth indicate a baroclinic boundary current system. There is evidence of recirculation in the central Labrador Sea at the lowest depths. In the central part of the basin, mean flow speeds are comparatively small.

[14]The use of ECCO2 inflows led to an increase of model-data misfits by $\sim 10\%$. Because of time constraints, no further model control variable adjustments were conducted these misfits (about 10%).

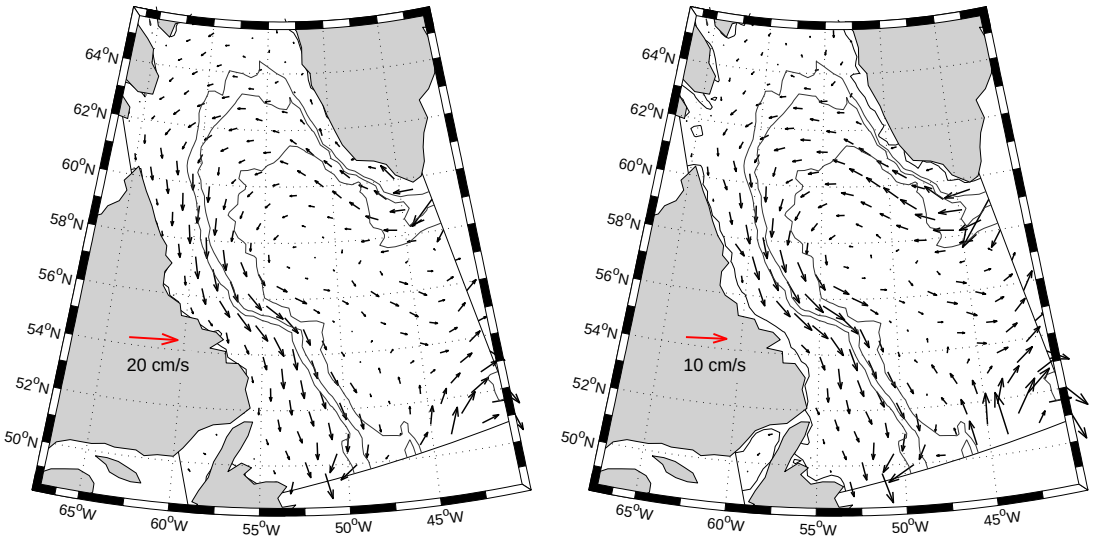

(a) 15 m

(b) 65 m

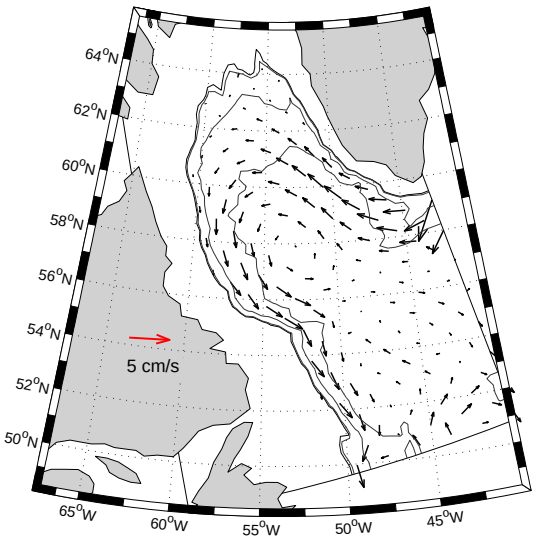

(c) 847.5 m

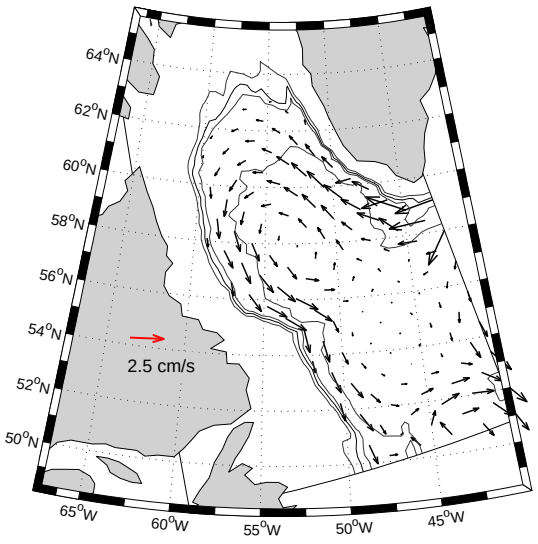

(d) 1542.5 m

Figure 4-12: Annual mean ocean current velocity (arrows) and at four depth levels from the state estimate. 1000, 2000, and 3000 m bathymetric contours are also shown (gray contours).

Evaluation of the time-mean circulation in the state estimate

In light the earlier discussion of model-data discrepancy in transport, time-mean velocities are expected to be significantly slower than observed. This is indeed found to be the case and therefore the model-data comparison is brief.

For each transect in which total volume transport was estimated there, was a corresponding estimate of current speeds in the direction normal to the section. In addition, displacements of surface drifters and subsurface floats have been analyzed to generated estimates of Eulerian mean velocities at the surface and 700 m depth.

One feature which is strikingly absent in the state estimate, besides a vigorous flow, is a significant barotropic component of the flow in the boundary current system. Evidence for largely barotropic flow, at least in first few hundred kilometers off the Labrador and Greenland shelfbreaks, are evident in all of the synoptic sections described in Section 4.3.1.

Average velocities on the Labrador slope and shelfbreak in the transects of Pickart et al. (2002) and the analysis of Dengler et al. (2006) exceed 30 $\mathrm{cm\,s^{-1}}$. Further offshore of the baroclinic shelfbreak jet, nearly depth-independent velocities of 5-10 $\mathrm{cm\,s^{-1}}$ extend to 2500 m up to 125 km away. Similarly, in the synoptic transects of Holliday et al. (2009), nearly barotropic velocities of more than 15 $\mathrm{cm\,s^{-1}}$ extend away from the shelfbreak jet a similar distance offshore.

Also missing in the state estimate are numerous cyclonic recirculation cells, running along the boundary currents at various locations in both the Labrador and West Greenland Currents (Lavender et al. 2000). These recirculation cells, whose origins are a matter of investigation, (*e.g.,* Spall and Pickart 2003), are also detected in the synoptic and mooring sections described above.

Finally, simulated boundary currents at depths below 1500 m (not shown) continue to decay in speed while maintaining a cyclonic tendency. A decaying speed is the reverse of what is observed, especially in the deep western boundary current on the Labrador slope between 2500 and 3000 m, where velocities increase to 15-20 $\mathrm{cm\,s^{-1}}$ (Dengler et al. 2006).

Using surface drifter data, Fratantoni (2001) estimated surface velocities in the North Atlantic. The surface velocity estimate, shown in Figure 4-13(a), shares several qualitative features with the state estimate: a swift shelfbreak current and slower velocities above the NS. However, typical velocities on the shelfbreak jet are significantly slower in the

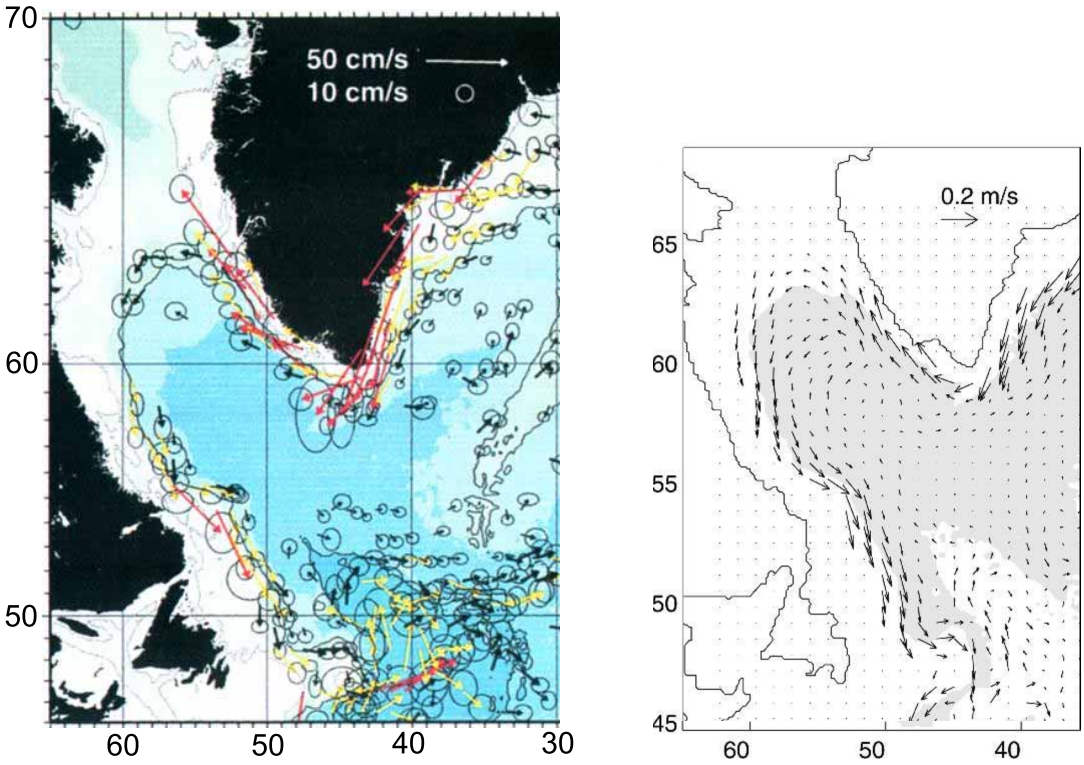

(a) 15 m (b) 700 m

Figure 4-13: Near-surface (a) and mid-depth (b) mean circulation as observed by surface drifters and profiling floats. Near surface circulation figure adapted from Fratantoni (2001). Eclipses provide information on the variability of zonal and meridional drifter velocities. Only those points where the mean velocity exceeds the standard error are included. Red and yellow arrows indicate velocities exceeding 10 and 15 $\mathrm{cm\,s^{-1}}$, respectively. Mid-depth circulation figure adapted from Treguier et al. (2005) which utilizes data from the reconstruction of Lavender et al. (2000).

state estimate.[15] Using profiling float data, Lavender et al. (2000) constructed a similar circulation estimate at 700 m, shown in Figure 4-13(b). Once again, the state estimate represents most of the observed features qualitatively but shows a significantly slower and broader boundary current circulation.

Ocean circulation survey conclusions

Despite the large model-data discrepancies in the magnitude of barotropic ocean transport and current speeds, the large-scale direction of flow in the state estimate is consistent with observations and other numerical models. As no circulation data were included in the model-data misfit cost function, and because of the many known technical challenges of representation the circulation in the Labrador Sea, the model solution is recognized as being about as good as could be expected for its resolution, viscosities, and open boundary inflows. To the extent that ice concentration data have a low model-data misfit in the state estimate, the weak circulation does not appear to have caused irreparable harm to the representation of sea ice-ocean interaction. In any case, ice motion is dominated by wind-forcing over much of the domain.

4.3.2 Mixed layer depth survey

The representation of mixed layer depth (MLD) in the state estimate is important to describe and compare with observational data because well-represented MLDs indicate skill in the state estimate's representation of ocean stratification, heat content, and air-sea heat fluxes. The focus here is on the convective wintertime mixed layer depths because of the important role of convection is thought to play in establishing a pathway through which subsurface enthalpy can ultimately be brought to and interact with sea ice. (Section 1.6.3).

State estimate mixed layer depths are evaluated in two ways. First, state estimate MLDs (model MLDs) are calculated at the location and times of observed *in situ* temperature and salinity profiles from CTD casts and autonomous profiling floats (Section 2.4.2) and then compared against the MLDs calculated on the observed T and S profile. Second, mean model Labrador Sea MLDs during a several week period spanning February and March

[15] Eulerian time-mean circulation in the Labrador Sea interior is small, owning to the numerous mesoscale eddies which dominate the moment-to-moment flow field, (*e.g.,* Chanut et al. 2008) making model-data comparison quite difficult.

1997 are calculated and compared against an estimated MLD field during the same time period based ship-based *in situ* T and S data.

The algorithm used for calculating MLDs in this work was as follows. The surface-referenced potential density at each depth level on the profile is calculated and rounded to the nearest gram per cubic meter (*e.g.,* $1027.0327\,\mathrm{kg\,m^{-3}} \rightarrow 1027.033\,\mathrm{kg\,m^{-3}}$). The lowest potential density below 45 m was identified and labeled the profile minimum. Finally, the mixed layer base is identified with the shallowest depth level with a potential density exceeding the profile minimum by $13\,\mathrm{g\,m^{-3}}$. This procedure for MLD determination is robust for profiles in the Labrador Sea.

Main features of mixed layer depth in the state estimate

MLDs for individual profiles location and mean MLDs for the February-March period for the state estimate are shown in Figures 4-14(a) and 4-14(c), respectively. MLDs in three areas are worthy of consideration in some detail: the site of historically-identified deep convection northeast of Hamilton Bank, a second site of unexpected deep convection south of the 3000 m isobath in the eastern Labrador Sea, and the open ocean within several hundred kilometers seaward of the sea ice edge.

Deep convection near Hamilton Bank in the state estimate reaches a maximum depth of approximately 1400 m. Mixed layers are shallower (400-600 m) to the north before the ice edge while unexpectedly shallow mixed layers (100-200 m) are found to the immediate east.

Far to the east, bordering the eastern open boundary (57° N, 46° W), MLDs are very deep ($\geq$ 800 m). This area is considerably under-sampled by *in situ* profiles relative to the site of traditionally observed deep convection near Hamilton Bank.

MLDs near the sea ice edge have an interesting pattern: shallow near the ice edge (within 30-60 km) and deepening seaward. The shallowest off-ice edge MLDs (100-200 m) are along the western MIZ (60° N, 57° W). Interestingly, these shallowest MLDs are adjacent to much deeper MLDs (300-500 m). The presence of sea ice does appear to significantly modify convective depths in the Labrador Sea.

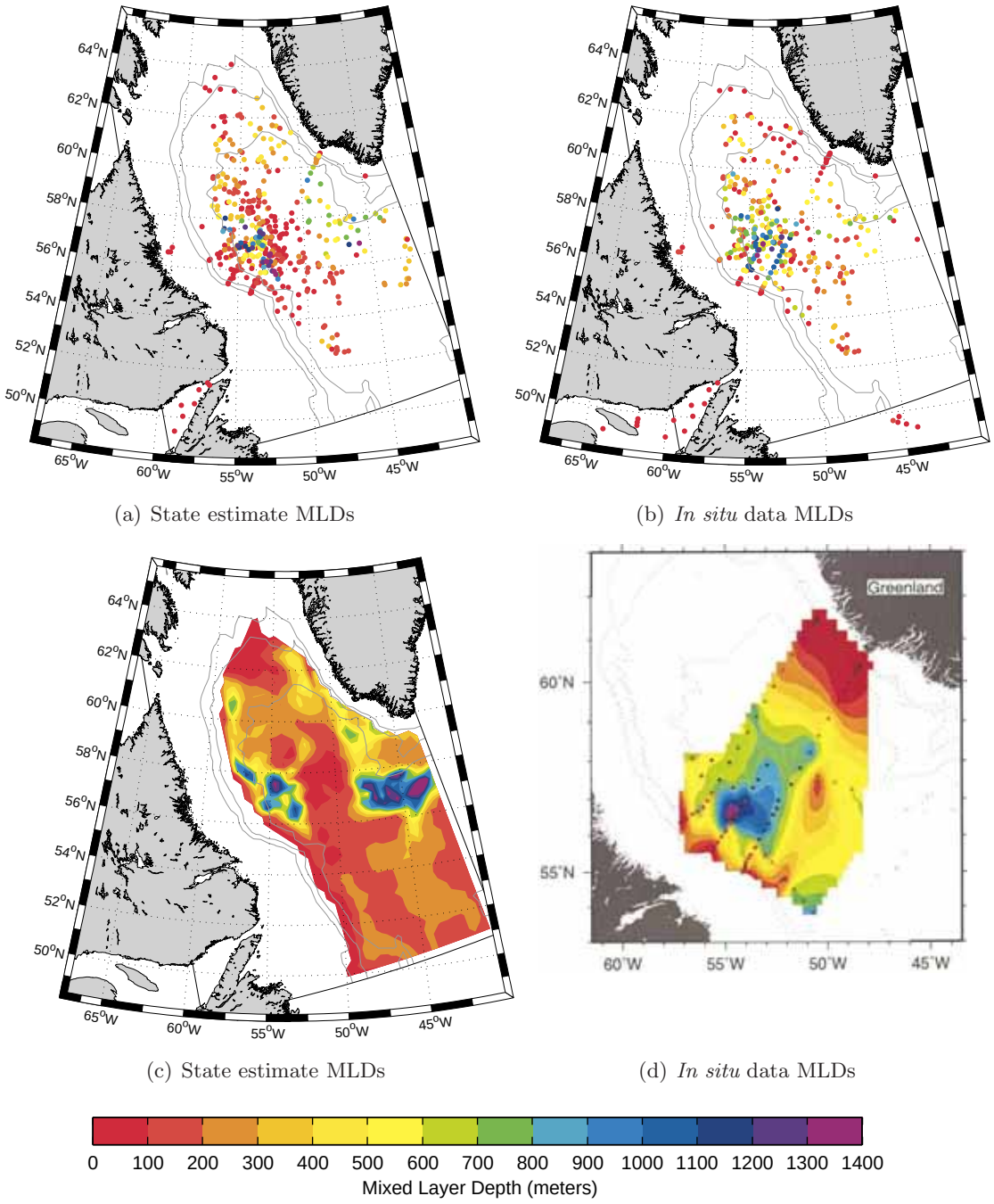

(a) State estimate MLDs

(b) *In situ* data MLDs

(c) State estimate MLDs

(d) *In situ* data MLDs

Figure 4-14: Mixed layer depth (MLD) between February-March 1997 calculated at *in situ* T and S profile locations from (a) the state estimate and (b) *in situ* profile data. MLDs during Labrador Sea Deep Convection Experiment (LSE) cruise dates from (c) state estimate and (d) the analysis of (and adapted from) Pickart et al. (2002)). Points in (d) indicate location of LSE CTD casts and their associated MLDs. Grid cells with nonzero sea ice concentrations in (c) are masked white. 98% of MLDs beneath ice during this period are ≤ 100 m. All figures use the same color-depth shading. Some *in situ* profiles are excluded from (b) due to missing/noisy data.

Evaluation of mixed layer depth in the state estimate

The distribution of observed MLDs is spatially heterogeneous. Moreover, *in situ* measurements provide only a snapshot of MLDs at one point in time at each location. It is important to note that MLDs in the basin are continually evolving over this time period due to large buoyancy losses associated atmosphere heat fluxes. Furthermore, profiles sample within unresolved mesoscale eddy features and therefore model representation errors. The occasional sampling of an eddy whose core hydrographic properties originate from waters on the inner shelves of the WGC or LC are expected far offshore. When sampling of such an eddy occurs, a visual model-data comparison would indicate a significant disagreement. However, because representation errors are built into the *in situ* T and S uncertainties, the model could still be considered consistent with the data.

MLDs calculated for the observed profiles are shown in Figures 4-14(b) and 4-14(c). Overall, MLDs in the state estimate generally agree well with data. This is especially so at the site north of Hamilton Bank and the immediately surrounding waters. There is evidence of shallow mixed layers at the sea ice edge in both the individual profiles and the interpolated map.

The region with the greatest model-data misfit, seen in both the objective map and the individual profiles, is found in a semicircle band to the north, east, and southeast of the Hamilton Bank deep convection site. Along this band, the objective map of Pickart et al. (2002) and profiling floats indicate MLDs of 300-700 m. In comparison, the state estimate MLDs are shallower, generally within the 100-400 m range.

Explanations for MLD model-data discrepancies are now sought. It is probably not coincidental that model MLDs most closely match observations where *in situ* data are abundant - in the adjoint method, the more abundant the data the more information one has about the control variable adjustments required to reduce model-data misfit. However, data scarcity is not the obvious reason for the large model-data discrepancies in the too-shallow MLDs to the east of the traditional deep convection site and the (probably) spurious deep convection near the eastern model boundary.

Why are MLDs shallower than observations to the east of the traditional site of deep convection? The explanation is found in the atmospheric control variable adjustments driven by model-data SST misfits. First-guess wintertime SSTs in the area were too cold.

In the reduction of the SST model-data misfit, the iterative optimization reduced ocean heat loss from air-sea fluxes by increasing surface air temperatures, specific humidity, and downwelling radiation and by reducing wind speeds and precipitation (snowfall) rates. Ultimately, SST misfit was reduced but at the cost of an unrealistically shallow mixed layer.

Model-data misfits would have been reduced if the atmospheric state control variable adjustments had colluded to enhance ocean surface buoyancy losses thereby increasing early winter convectively-driven mixed layer depths. With enhanced buoyancy loss, warmer SSTs would have been achieved through the mixing up of warm subsurface Irminger Water. In retrospect, the optimization trajectory could probably have been guided in a more satisfying direction if more attention had been paid to the iteration-to-iteration atmospheric state control variable adjustments.

Deep convection near the domain's eastern boundary stems from the advection of erroneously weakly-stratified waters into the domain from the open boundaries - an issue related to the ECCO solution from which the open boundary conditions were extracted. Subsequent air-sea interaction/buoyancy loss leads to rapid and spurious mixed layer deepening.

Atmospheric state control variable adjustments led to shallow MLDs in the central Labrador Sea while erroneous open boundary conditions led to deep MLDs in the eastern Labrador Sea.

Model MLDs are clearly sensitive to atmospheric and lateral ocean boundary conditions. However, despite these model-data discrepancies, MLD model-data misfits in the northern and western Labrador Sea near the sea ice edge appear to be well reproduced, lending credibility to the notion that the state estimate is useful for the examination of sea ice-ocean processes.

4.4 Chapter Summary

4.4.1 Summary of the Sea Ice Survey

The state estimate reproduces the basin-scale temporal and spatial sea ice annual cycle as represented in a sea ice concentration dataset within the specified uncertainties. Ice thickness compares favorably with several non-contemporary coastal stations on Baffin Island, Labrador, and Newfoundland. The snow/ice freeboard in the state estimate is in excellent agreement with a data during the initial Baffin Bay freeze-up. Wintertime state

estimate freeboards are contaminated by a spuriously deep snow pack resulting from a positive bias in the NCEP/NCAR reanalysis precipitation fields. The basin-scale mean and synoptic patterns of sea ice drift are in good agreement with reconstructions where data are available.

4.4.2 Summary of the Ocean Survey

State estimate barotropic transports are significantly lower than the (highly uncertain) estimates from synoptic and mooring data. Model time-mean current speeds are also slower than observations and numerical simulations. The model boundary current circulation is more baroclinic from the shelfbreak to the 3000 m isobath than observed. In terms of flow direction, the simulated cyclonic tendencies in the Labrador Sea agree qualitatively with data. Small-scale circulation features, such as recirculation cells adjacent to Labrador Sea boundary currents, are absent - a consequence of model representation limitations.

Simulated mixed layer depths are in excellent agreement north of the Hamilton Bank and in the northern and western Labrador Sea - areas of highest *in situ* observation density. Significant MLD model-data discrepancies are related to adjustments in the atmospheric control variables and to erroneous lateral open ocean boundary conditions. Fortunately, the areas with the greatest model-data misfit were, for the most part, far from the sea ice edge.

4.4.3 Implications of the ocean model-data discrepancies

In what ways do the weak circulation and spurious mixed layer depths in the state estimate affect the utility of the solution? To answer the question properly, one must be very specific as to the aspect of the solution about which one is concerned. If one were interested, for example, in using the state estimate solution to study the seasonal variability of the deep western boundary current or mixed layer development in the central Labrador Sea, one would not be wrong to declare that the solution is so seriously flawed as to warrant its total rejection.[16]

However, 1) the focus of this thesis is the basin-scale sea ice-ocean interaction on seasonal to annual time scales and 2) the importance of simulating the Labrador Sea flow field and its central/eastern basin mixed layer depths with high accuracy for the thesis problem has not

[16] Addition discussion of the implications of the more serious model-data discrepancies is provided in the thesis Conclusions, Section 7.4.

been conclusively established. Indeed, the high-fidelity reproduction of sea ice and ocean data is evidence that the state estimate has skill with respect to the reproduction of the sea ice-ocean state on the temporal and spatial scales of interest. I assert that, despite serious discrepancies with the representation of ocean circulation and some mixed layer depths, the state estimate is consistent and useful for the purposes of making inferences concerning the aforementioned phenomena.

Chapter 5

Mass, Energy, and Buoyancy Budgets of the Ocean-Sea Ice System

5.1 Chapter Overview

Having demonstrated the degree to which the ocean and sea ice in the state estimate are consistent observational data in Chapter 4, the next step is to analyze the $1996 - 1997$ state estimate solution to quantify several important sea ice-related processes. The first is to analyze the importance of the lateral transport of ocean tracers and sea ice for the development of the sea ice quasi-equilibrium state. Following this analysis, new sea ice mass, energy, and buoyancy budgets are constructed and analyzed. Together these two analyses shed light on the important system balances and imbalances which drive the sea ice annual cycle, furthering understanding of the role of hydrographic variability on the development and maintenance of the sea ice quasi-equilibrium state.

The chapter is organized as follows. First, I discuss the importance of determining the role of lateral transport motivation and the analysis of the sea ice-ocean system budgets (Section 5.2). Results of the analyses follow: the potential of seasonal sea ice formation using one-dimensional thermodynamic processes alone (Section 5.3), then budgets of sea ice mass (Section 5.4), energy (Section 5.5), and buoyancy (Section 5.6). The chapter concludes with a summary of the key findings and a discussion of their implications thereby laying

the groundwork for the final chapter (Section 5.7).

Outside of unconstrained numerical simulations, (*e.g.,* Ikeda et al. 1996; Bitz et al. 2005), these budgets have not yet been quantified in the study region. The procedure taken here to construct and analyze the sea ice budgets is largely inspired by (and follows) the method and ideas of Bitz et al. (2005).

5.2 Introduction to the Budgets of the Ocean-Sea Ice System

Why is the value in conducting the analyses which are the focus of this chapter? Understanding the role of sea ice and ocean tracer advection in the development of the sea ice quasi-equilibrium state is necessary to evaluate hypotheses which postulate a link between maximum ice extent and ice drift variability. Ice drift variability is postulated as a main cause of sea ice variability (albeit implicitly at times) in hypotheses which invoke fluctuations in the strength of the westerlies and northwesterlies as determining the seasonal ice maximum extent (see Section 1.5.2). As the $1996-1997$ annual ice cycle is well-reproduced in the state estimate *with* lateral ice and ocean tracer transport, the importance of these transports is ascertained with an experiment which restricts them. Where sea ice remains well-reproduced despite restricted lateral transports, those areas where transports are relatively unimportant are revealed.

The budgets of mass, energy, and buoyancy in the sea ice-ocean system are valuable because they provide insight to critical sea ice-ocean system *balances* and *imbalances*. During the sea ice quasi-equilibrium state, the system is hypothesized to be characterized by several balance conditions with respect to mass, energy, and buoyancy (see Section 3.3). Knowledge of time-evolution of these budgets provides insight into how system imbalances drive the large-scale development of the annual cycle.

As the tendencies of ice mass and concentration are functionally related, determining the ice mass budget allows discrimination of the relative importance of thermodynamic and dynamic processes in establishing sea ice in a given location - complimenting insights gained from the analysis of ice development without lateral transport. The ice mass budget also provides insight into the processes relevant for the development and maintenance of the quasi-equilibrium sea ice state.

To understand the system during the sea ice quasi-equilibrium state, one requires in-

formation concerning the pathways and magnitudes of energy flow which sustain thermodynamic growth and melt. Specifically, with a sea ice energy budget one can understand the source of the sustained enthalpy flux required to melt dynamically converging sea ice in the marginal ice zone (MIZ) - one of the places where a sea ice dynamic-thermodynamic equilibrium is hypothesized to evolve.

Finally, sea ice may substantially modify the upper ocean hydrographic state through the ice-boundary layer stabilization feedback (Section 3.3.1). A first-step in determining whether hydrographic state modifications related to this feedback are relevant for the development of the annual cycle requires a quantification of the contribution of sea ice meltwater release to the total ocean surface buoyancy budget.

5.3 Thermodynamic Ice Growth Potential

A one-dimensional (1-D) thermodynamic mixed layer model is employed to determine the extent to which sea ice cover is reproducible in the Labrador Sea and Baffin Bay without lateral ocean tracer and sea ice transport.

In some ways, the approach taken echoes earlier sea ice-ocean modeling experiments in the Labrador Sea which utilized 1-D mixed layer models (without lateral ocean tracer lateral transport) coupled to thermodynamic and thermodynamic-dynamic sea ice models (*e.g.,* Ikeda et al. 1988).

There are four notable differences between the approach taken here and earlier studies. One, the model domain includes the northern Labrador Sea and Baffin Bay - earlier studies focused on the southwestern Labrador Sea. Two, the predictability calculations are made with an ocean state that is initialized before the appearance of significant Baffin Bay sea ice - earlier studies initialized their models after Baffin Bay freeze-up. Three, the initial ocean state is taken from the state estimate - initial ocean conditions in earlier studies were often derived from climatologies incorporating far fewer *in situ* observations than the state estimate. Four, the air-sea heat fluxes used in the model are the actual open water air-sea heat fluxes from the state estimate - the atmospheric states/fluxes in earlier studies were often *ad-hoc* interpolations of meteorological measurements from coastal stations and ocean-observation platforms.

Based on these four considerations, the results from the 1-D thermodynamic model

experiment are expected to be somewhat more accurate than earlier studies.

5.3.1 Experimental method

The 1-D ocean mixed layer model is a simple parametrization of vertical convective mixing triggered by ocean surface buoyancy loss-driven static instability. The ocean is represented as a series of isolated 1-D columns initialized with individual temperature and salinity (T and S) profiles. Daily-averaged open water air-sea heat fluxes are applied to each column surface. T and S profiles are allowed to evolve based on their time-evolving mixed layer enthalpy and potential density.

Mixed layer static stability is determined at the end of each one-day time step by comparing the surface-referenced potential density of the mixed layer waters with that of the next deepest cell. In the event of instability, the mixed layer instantaneously deepens and mixes its enthalpy and salt with the next deepest cell. When the mixed layer attains a temperature of -1.96° C and is found to be statically stable to a small positive salinity perturbation (representing salt release triggered by 2 cm of ice growth) sea ice is considered to have formed. Mixing of the upper ocean by mechanical processes (wind-induced shear instabilities) are parameterized by initially homogenizing T and S in the upper 45 m.

Each horizontal model grid cell is considered a separate 1-D column and simulated independently. No lateral exchange of any kind (ocean tracers, sea ice, etc.) is permitted between the columns. The 1-D model is run six times from different initial ocean conditions extracted from the sea ice-ocean state estimate from dates between August 1 to December 1, 1996. With minor exceptions, the relevant features are present in each. Therefore, I discuss only the simulation initialized for October 1, 1996.

5.3.2 Analysis

The dates of predicted sea ice formation is compared with the observed sea ice edge locations for three periods is presented in Figure 5-1. The simple mixed layer model is skillful in predicting the date of ice formation over much of the domain during the first several months of the simulation.

In particular, the observed December 1 ice edge closely predicted in Baffin Bay, across Davis Strait, and in the northwestern Labrador Sea around Baffin Island - regions associated with surface Arctic Water (AW). Therefore, on the AW-side of the Thermohaline Front

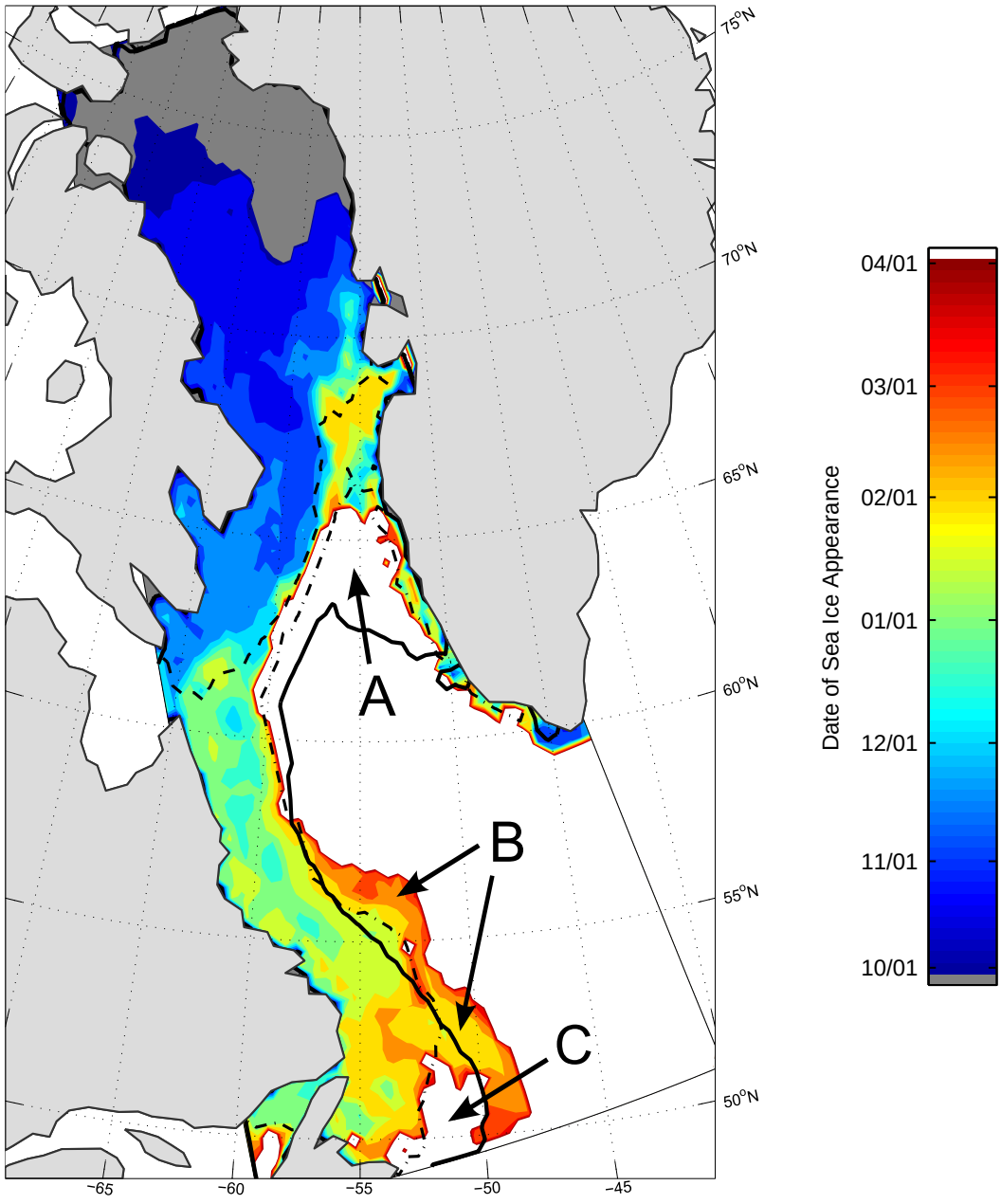

Figure 5-1: Dates of sea ice formation as predicted by a 1-D mixed layer model (colors) and the observed locations of the sea ice edge (contours). 1-D mixed layer model initial temperature and salinity is the October 1 hydrography from the 1996 − 1997 state estimate. Dark gray denotes existing ice on October 1. White denotes no ice formed during the 1-D model simulation. Sea ice edge locations for Dec. 1 − −, Feb. 1 − · −, and Mar. 10. −. Letters (A, B, and C) denote areas of significant discrepancies between the 1-D model and observations.

(THF), the date of sea ice appearance is predictable using one-dimensional processes alone.

Sea ice cover is also well predicted to February 1. In both the 1-D model and observations, the ice edge expands across the eastern half of Davis Strait and south along the Labrador Current (LC) to the shelfbreak and Newfoundland.

After February 1, the 1-D model is unable to predict the further ice cover expansion. Three areas are most notable for their discrepancy, the Northern Slope (NS) of the Labrador Sea (A), a region seaward of the Labrador Shelf south of 57° N (B), and the Newfoundland Shelf south of 53° N (C). Each area of discrepancy (labeled on Figure 5-1) is considered in turn.

On the NS region (A), the 1-D model fails to predict the sea ice on the Irminger Sea Water (IW)-side of the THF between February 1 and mid-March. Two factors are likely responsible for this discrepancy: missing ice dynamics and an inconsistent upper ocean stratification. The analysis of ice drift in Section 4.2.4, confirmed that a nonzero component of ice velocity is perpendicular to the ice edge, suggesting an important role in cross-THF sea ice advection. On the other hand, it is possible that between September 26 and February 1, lateral advective transport of fresh buoyant AW from West Greenland Current (WGC) across the NS modifies the upper ocean hydrography in such a way as to increase the propensity of local thermodynamic ice growth.[1]

In the second area of notable discrepancy (B), a large significant area of sea ice is predicted to form seaward of the Labrador slope where no ice is actually observed. The hydrographic situation in the state estimate on October 1 includes a tongue of residual sea ice meltwater propagating out of the domain in exactly the location of the positive sea ice discrepancy. In the state estimate, the residual meltwater tongue is completely dispersed by February 1. Therefore, excessive ice at (B) is simply an artifact of missing lateral ocean processes.

In the final area of discrepancy (C), the Newfoundland Shelf south of 53° N, we again see a failure of the 1-D model to predict the formation of observed ice. As mentioned in Section 1.6.2, Yao and Ikeda (1990) found that the transport of both sea ice and northern Labrador Shelf waters on the LC to Newfoundland and the Grand Banks were required for sea ice in that area. The failure of the 1-D to predict sea ice in the same area confirms their

[1]Understanding this missing ice discrepancy on the northern Labrador Sea is the focus of the following chapter.

findings.

5.3.3 Conclusions

The simple 1-D mixed layer model is useful because it provides support regarding the importance of ocean tracer transport and sea ice dynamics on the development of the ice pack in two regions of the Labrador Sea: the NS and southern Labrador Shelf. However, the 1-D model is unable to reveal much more. Therefore, the question of how sea ice-ocean processes and ocean tracer and sea ice advection lead to the expansion of sea ice across the THF remains open.

5.4 Sea Ice Mass/Thickness/Volume Budget

The density of sea ice is assumed constant in the sea ice model. Therefore, one may interchangeably speak of the budgets of the ice mass, mean thickness, and volume. Of these, it is convenient to choose the model grid-cell mean ice thickness, h, since model prognostic equations are formulated in terms of this variable.

To distinguish between the thermodynamic and dynamic contributions to the sea ice thickness budget, the ice thickness tendency term is decomposed into contributions from thermodynamic growth/melt and dynamic convergence. The decomposed ice thickness tendency equation is,

$$\frac{\partial h}{\partial t} = \left(\frac{\partial h}{\partial t}\right)_{thermo} - \nabla \cdot (\vec{u}_{ice}\, h) \tag{5.1}$$

Where $\vec{u}_{ice}$ is the ice velocity and the two terms on the RHS describe thermodynamical growth/melt and dynamical convergence/divergence, respectively.[2]

How does considering the mean ice thickness tendencies clarify understanding of the expansion and contraction of the ice pack? Recall that the ice edge is defined as the 15% ice concentration contour in the MIZ. Any process which modifies sea ice concentrations in and around the MIZ must therefore alter the location of the sea ice edge.

The functional relationship between the prognostic sea ice concentration equation and the thermodynamic and dynamic terms in the prognostic mean ice thickness equation is

[2]Convergence and divergence of the ice pack as referred to in the above equation excludes subgrid scale mechanical processes that rearrange ice between thickness categories while leaving the ice mean thickness unchanged.

modeled after the parameterization of Hibler (1979, 1980), hereafter HIB79. In HIB79, thermodynamic ice melt (from basal, lateral, or surface heat flux convergence) thins extant ice and simultaneously diminishes ice concentration. The relationship between thermodynamic ice growth and ice concentration is slightly more complicated. New ice growth in the open water portion of a model grid cell increases ice concentration while the thickening of existing ice does not.

Sea ice dynamical convergence in HIB79 may increase sea ice concentration provided the model grid cell into which ice converges is not already completely ice covered. Logically, dynamical sea ice divergence always increases the open water fraction.

Clearly, relating ice thickness and ice concentration/ice edge tendencies is not straightforward.[3] Fortunately, the analysis of thickness tendencies is greatly simplified by considering periods when the ice edge is relatively stable. Two such periods, one after the initial freeze-up of Baffin Bay, designated Autumn (October 17-November 7), and one during the sea ice quasi-equilibrium state, designated Winter (February 21-March 20), are considered in the analysis.

5.4.1 Autumn period: October 17 - November 1, 1996

In the Autumn period, thermodynamic growth is found over most of Baffin Bay except for a narrow band along the ice pack's southern margin, as shown in Figure 5-2. Growth rates are highest adjacent to the shorelines of Baffin Island (max 3 cm/day) and Greenland (max 12 cm/day). The dynamic tendencies are small in the central basin. Substantial dynamical divergence is present along both coasts. Interestingly, the negative thickness tendencies from dynamical divergence are somewhat offset by the positive tendencies from thermodynamical growth; near-shore ice appears to be approaching a mass-divergence dynamic-thermodynamic equilibrium. Finally, dynamical mass convergence which is not offset by melt is noted near in the southern sea ice MIZ.

Integrated over the entire domain, the sum of thermodynamic and dynamic thickness tendencies indicates a net increase in ice mass nearly everywhere. Integrated over the domain, ice growth exceeds melt by a factor of 48 during the Autumn period.

The interpretation of the Autumn period mass budget is simple. Over most of the central

[3]Such an analysis can be even more difficult with the arbitrarily complex sea ice thickness/concentration parameterizations developed in the decades since HIB79.

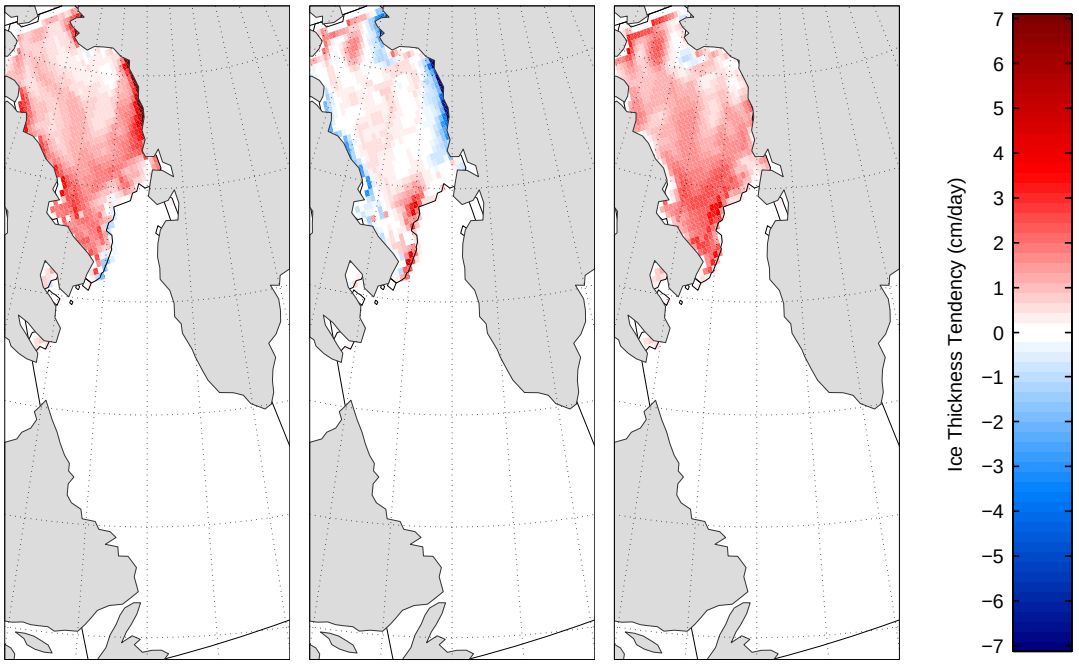

(a) Autumn $\partial_t h$ (Thermo) (b) Autumn $\partial_t h$ (Dynam) (c) Autumn $\partial_t h$ (Total)

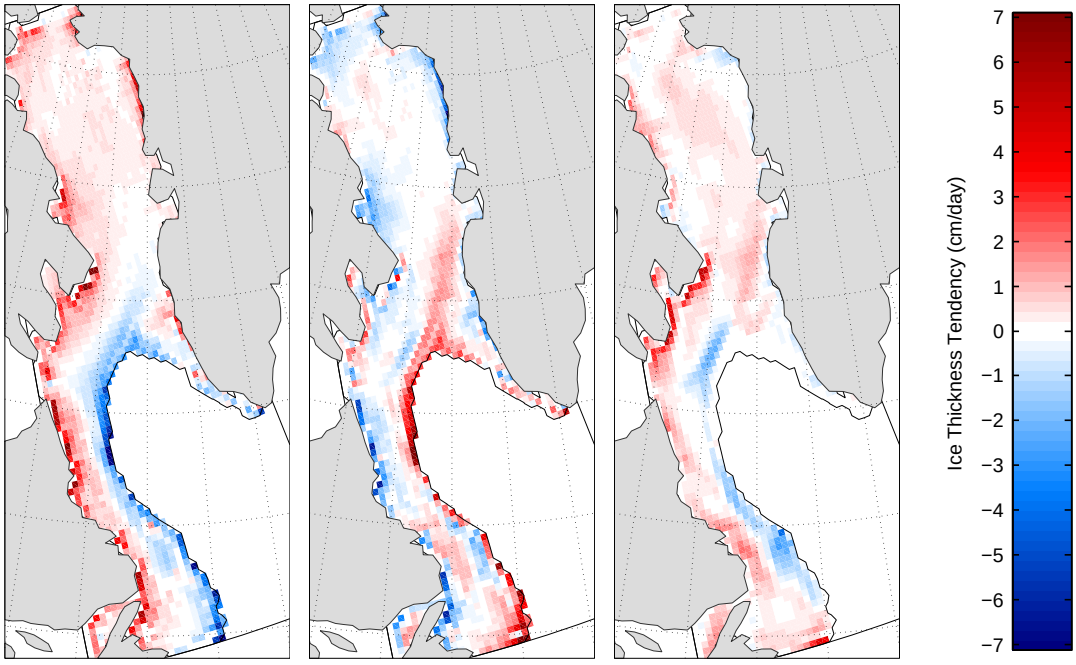

(d) Winter $\partial_t h$ (Thermo) (e) Winter $\partial_t h$ (Dynam) (f) Winter $\partial_t h$ (Total)

Figure 5-2: Sea ice thickness growth rate tendencies averaged over two periods: Autumn (Oct 17-Nov 1) and Winter (Feb 21-Mar 20) 1997. Thickness tendencies are presented as individual thermodynamic and dynamic terms as well as their sum. During both periods the ice edge position is relatively stable. Contour lines denote each the maximum sea ice extent of each period.

Baffin Bay, rapid thermodynamic growth of the still thin ice ($\leq 1\,\mathrm{m}$, see Figure 4-4) is the dominant process affecting sea ice mass. The small dynamical contribution to ice thickness tendencies in the central basin is due to very small spatial gradients of ice thickness. A small ice thickness gradient is not surprising since ice coalesces on the basin's buoyant AW cap with near-simultaneity and subsequently thickens in the presence of similar atmospheric conditions.

The large negative divergences of ice near the coasts is due to mechanical wind and ocean forcing which drive ice seaward. Indeed, divergent ice motion in these locations is consistent with the simulated trajectories of ice drift (Figure 4-8).

The large thermodynamic thickening tendencies of ice in the areas of mechanical divergence is explained by noting that, all else being equal, sea ice thermodynamic thickening and new ice production is greatest in grid cells with thinner ice and a greater open water fraction. Both thin ice and greater open water fraction allow greater air-sea heat fluxes which permit sustained seawater enthalpy loss and phase change.

5.4.2 Winter period: February 21 - March 20, 1997

The thickness tendencies during the Winter period share several similarities with the Autumn period in Baffin Bay: co-located near-coastal high rates of thermodynamic growth and dynamical divergence, net dynamical convergence in the MIZ, and net thermodynamic thickening in the central Baffin Bay.

The pattern of near-coastal co-located thermodynamic growth/dynamical divergence is found extended along the inner Labrador and Newfoundland Shelves and along the southwest Greenland Shelf. As expected, these new high thermodynamic growth areas coincide with regular offshore wind stresses which regularly drive the ice seaward and thereby causing a high near-shore open water fraction.

In the central Baffin Bay, dynamical and thermodynamical ice thickness tendencies approach zero. The state estimate confirms that sea ice the central Baffin Bay attains an approximate state of ice static-thermodynamic equilibrium state (as defined in Section 3.3). Despite nonzero ice drift in the central Baffin Bay, there is no dynamical contribution to ice thickness due to the very small ice thickness gradients in the mean direction of drift (Section 4-8).

In the Labrador Sea MIZ a new pattern is noticed: large areas of thermodynamic melt

(maximum 6 cm/day) which offset dynamic convergence (same maximum). Clearly, separate regions of thermodynamic growth (melt) are co-located with regions of sustained and significant dynamic divergence (convergence) of comparable magnitudes. The regions of sustained significant thermodynamic melt (the MIZ) is distant from the regions of sustained and significant thermodynamic growth (near coastal). Thus, the analysis of the state estimate supports the hypothesis that the sea ice edge position is established and subsequently sustained through a process of distant ice production, transport, and ultimate destruction via thermodynamic melt. In doing so, the MIZ and near-coastal regions of the Labrador Sea are identified as having attained a state of dynamic-thermodynamic equilibrium (also Section 3.3).

Compared to the Autumn period, net thermodynamic and dynamic tendencies are smaller across the entire domain. On the aggregate, ice growth exceeds melt by only a factor of 2 - strong support for the notion of a quasi-equilibrium ice state.

5.5 Sea Ice Energy Budget

The attainment of the sea ice quasi-equilibrium state analyzed in the Winter period of the previous section depends on several factors including the rates of ice production, transport towards the MIZ, and the ice melt in the MIZ.

In the determination of the sea ice-ocean energy budget during the 1984 Marginal Ice Zone Experiment (MIZEX) field campaign, Morison et al. (1987) recognized two important issues which demand consideration here. Point one: to estimate the relative importance of oceanic, radiative, and air-sea turbulent energy fluxes on the ice mass balance, a spatial region must be defined which includes an appropriate fraction of ice-free open water. Point two: the mixed layer beneath sea ice may be quite shallow and highly stratified making it difficult to unambiguously determine the source of oceanic energy between lateral (advective) or vertical (advective and convective) fluxes.

With a numerical model one can easily separate out the vertical and horizontal components of heat flux within a single model grid cell. However, and more importantly, it is not trivial to separate out the horizontal and vertical components of heat flux into the mixed layer (Bitz et al. 2005). The mixed layer depth is not stable even on daily time scales - the complex interaction of turbulent wind-driven mixing, lateral advective exchange, sea

ice interaction (meltwater and salt release), and solar insolation drive mixed layer depth variations that are extremely difficult to track.

These two points must be addressed before the construction of the sea ice energy budget can proceed. With respect to point one, I assert that the spatial extent of each single horizontal model grid cell is sufficiently expansive for the purposes of the energy budget calculation. In all but a very small number of instances, sea ice concentrations in the model are less than unity implying that radiative and turbulent air-sea fluxes contribute appropriately the the sea ice energy/mass balance. With respect to point two, I construct the sea ice-ocean energy budget within a control volume whose base is temporally invariant - it does not track the time-varying mixed layer base - the base of the uppermost ocean grid cell (UOGC) at 10 m. By choosing a control volume in this way, distinguishing between basal and lateral ocean heat fluxes is slightly ambiguous (a lateral advective heat flux convergence into the mixed layer beneath the UOGC might appear as a basal advective heat flux in the UOGC). Therefore, the reader is reminded that it is the sum of the ocean heat flux terms that is relevant for the sea ice-ocean energy budget, not necessarily the direction into which they converge in the UOGC.[4]

5.5.1 Energy flux definitions

The sea ice energy budget is best understood by defining the system to include a volume of sea ice and ocean and defining the system upper boundary to be the surface of the sea ice and open water. The ocean component of the system is the model UOGC and the ice component is any sea ice which floats within and above the UOGC. Furthermore, it is advantageous to speak of the enthalpy fluxes across the open boundaries of the sea ice-ocean system. The system and the various channels through which energy flows are presented in schematic form in Figure 5-3.

The air-ice and air-sea fluxes are written as the average per unit area over the control volume: F_{oa} is the turbulent air-sea heat flux calculated over open water weighted by the open water fraction in the UOGC while F_{ia} is the turbulent air-ice heat flux calculated over the ice/snow surface weighted by the ice concentration.

Nonzero energy fluxes are implied in all non-trivial sea ice quasi-equilibrium states.

[4]Bitz et al. (2005) solved the problem of the time-varying mixed layer depth by drawing the boundaries of the control volume to the sea floor therefore eliminating the basal heat flux component of the energy budget altogether.

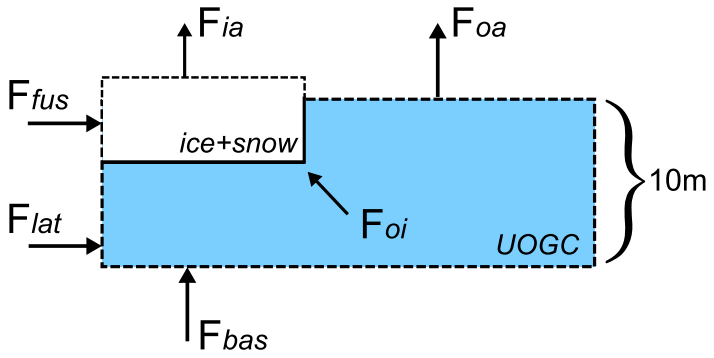

Figure 5-3: Schematic of energy fluxes across and within the boundaries of the sea ice-ocean system (dashed lines). Cross-boundary fluxes: latent heat of fusion from ice advection, F_{fus}; net sensible, latent, and radiative heat flux from ice/snow interface to atmosphere, F_{ia}; net turbulent sensible and latent and radiative heat fluxes from the open water to the atmosphere, F_{oa}; lateral advective heat flux, F_{lat}; and basal advective heat flux, F_{bas}. Intra-boundary ocean to sea ice sensible heat flux, F_{oi}. Cross-boundary flux sign convention is that positive fluxes increase system energy. Intra-boundary ocean flux does not affect system energy

The system enthalpy, E, referenced as zero for an ice-free control volume with seawater at its freezing point, T_{frz}, is approximated by:

$$E(T_{ocn}, h_{ice}) = -\rho_{ice}\, c_{ice}\, h_{ice} + (T_{ocn} - T_{frz})\, h_{ocn}\, \rho_{sw}\, c_{sw} \tag{5.2}$$

Where c_{ice} is the latent heat of fusion for sea ice, h_{ice} is the mean ice thickness in the UOGC, $\rho_{ice,sw}$ are the densities of sea ice and seawater respectively, T_o is the UOGC seawater temperature, c_{sw} is the seawater heat capacity, and h_{ocn}, is the depth of the UOGC (here 10 m). The sea ice enthalpy in the above equation is consistent with the assumption zero-heat capacity ice in the sea ice model.[5]

Assuming the system to be in steady state, the total system energy and sea ice volume is constant - the time derivative of each term in Equation 5.2 must therefore be zero. Postulating no net enthalpy convergence within the system, the sum of energy fluxes must be zero,

$$F_{fus} + F_{ia} + F_{oa} + F_{lat} + F_{bas} = 0 \tag{5.3}$$

A constant ice volume implies a balance of thermodynamic growth (melt) and dynamic

[5]The interested reader should compare the zero-heat capacity assumption against the more sophisticated treatment of internal heat capacity in sea ice models by Bitz and Lipscomb (1999).

divergence (convergence),

$$\frac{\partial h}{\partial t} = \left(\frac{\partial h}{\partial t}\right)_{therm} + \left(\frac{\partial h}{\partial t}\right)_{dyn} = 0 \tag{5.4}$$

From Eq. 5.2, the enthalpy flux associated with dynamical sea ice transport is given by:

$$F_{fus} = -\rho_{ice}\, c_{ice} \left(\frac{\partial h_{ice}}{\partial t}\right)_{dyn} \tag{5.5}$$

The thermodynamic sea ice mass balance can be decomposed into three terms, new ice growth from open water air-ocean (oa) heat fluxes (also referred to as air-sea heat fluxes), thickening/melting of existing ice (ei) via ocean-ice conduction or ice-air heat convergence, and basal melting by turbulent ocean-sea ice (oi) heat fluxes.

$$\left(\frac{\partial h}{\partial t}\right)_{therm} = \left(\frac{\partial h}{\partial t}\right)_{oa} + \left(\frac{\partial h}{\partial t}\right)_{ei} + \left(\frac{\partial h}{\partial t}\right)_{oi} \tag{5.6}$$

The existing (ei) and air-ocean (oa) thickness tendency terms are driven by enthalpy fluxes across the system boundaries,

$$\left(\frac{\partial h}{\partial t}\right)_{oa} = -\,F_{oa}\,(\rho_{ice}\, c_{ice})^{-1} \tag{5.7}$$

$$\left(\frac{\partial h}{\partial t}\right)_{ei} = -\,F_{ia}\,(\rho_{ice}\, c_{ice})^{-1} \tag{5.8}$$

Both F_{oa} and F_{ia} are negative during a sea ice quasi-equilibrium state in the Labrador Sea.

While the basal melting term (oi) is driven by an enthalpy flux, F_{oi}, which is internal to the system - nonzero F_{oi} implies a rearrangement of enthalpy between the liquid (seawater) and solid (ice) components of the system,[6]

$$\left(\frac{\partial h}{\partial t}\right)_{oi} = -\,F_{oi}\,(\rho_{ice}\, c_{ice})^{-1} \tag{5.9}$$

Substitution of Eqs. 5.7-5.9 into Eq. 5.6, equating the net thermodynamic and dynamic growth rates from Eq. 5.4, and making use of Eq. 5.5 to replace mass flux with an equivalent enthalpy flux yields,

$$F_{fus} + F_{oa} + F_{ia} = -F_{oi} \tag{5.10}$$

[6]The details of how F_{oi} is parameterized are unimportant for this development.

The above expression says that the combined (negative) enthalpy fluxes out of the system from sea ice mass convergence and air-sea and air-ice turbulent fluxes is balanced by the turbulent ocean-ice heat flux - to keep sea ice mass constant, ocean heat fluxes must be sufficient to melt all converging ice and offset all turbulent enthalpy loss to the atmosphere.

What about the downwelling radiative fluxes? During the sea ice quasi-equilibrium period, the total incoming radiative fluxes are less than half of the sum of outgoing thermal radiation and turbulent air-sea heat fluxes. Therefore, the downwelling radiative fluxes can be thought of as mitigating the net air-sea/air-ice heat losses, the local thermodynamic ice production, and ultimately the thermodynamic ocean-ice enthalpy fluxes required to maintain sea ice mass balance in the UOGC.

5.5.2 Energy budgets during the quasi-equilibrium state

Spatial maps of the mean energy flux terms of Eq. 5.10 during the sea ice quasi-equilibrium period are presented in Figure 5-4.

The spatial patterns of enthalpy fluxes are qualitatively consistent with the understanding of ice transport and sign of net air-sea and air-ice heat fluxes developed earlier. The dynamical convergence of sea ice mass advected to the MIZ is associated with negative enthalpy fluxes in the range $100 - 200\,\mathrm{W\,m^{-2}}$. Net air-ice fluxes are significantly smaller ($< 50\,\mathrm{W\,m^{-2}}$) and are limited to the near-coastal regions. Interestingly, the air-sea heat fluxes are comparable in magnitude with the fusion convergence fluxes in the western MIZ and exceed fusion convergence fluxes above the NS.

Turbulent ocean-ice fluxes are very nearly equal and opposite in magnitude from the sum of the previous three fluxes (not shown), as expected. The energy balance hypothesized in Equation 5.10 is approximately satisfied - energy fluxes through the sea ice-ocean system during the sea ice quasi-equilibrium state are approximately balanced.

5.5.3 Analysis of energy budgets during the quasi-equilibrium state

The various sources of energy which together permit sustained ocean-ice fluxes are now examined. Because the three terms on the LHS of Eq. 5.10 are negative (net enthalpy divergence) and as F_{oi} represents an internal enthalpy redistribution, a net enthalpy convergence is implied by the remaining terms of Equation 5.3.

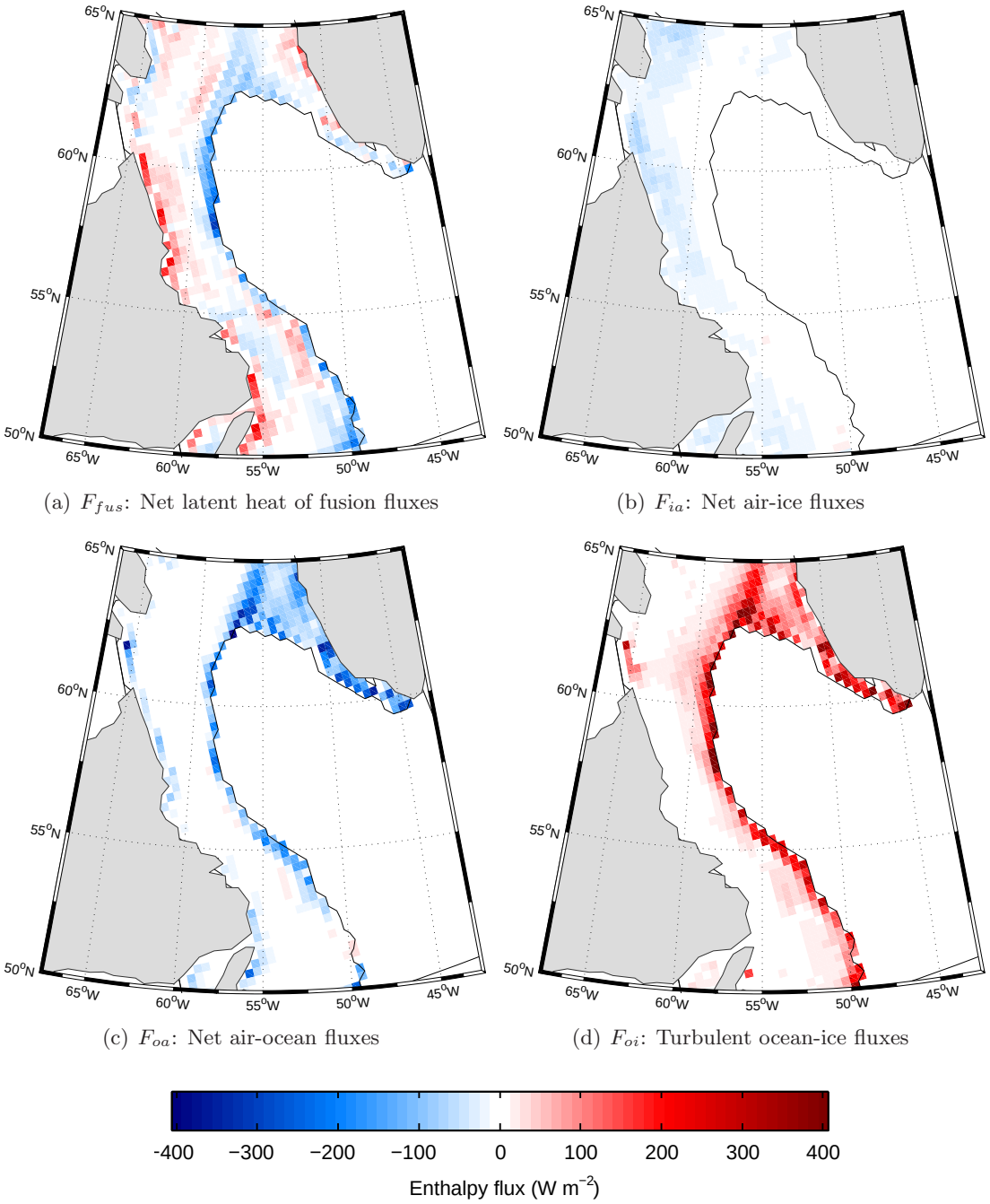

(a) F_{fus}: Net latent heat of fusion fluxes

(b) F_{ia}: Net air-ice fluxes

(c) F_{oa}: Net air-ocean fluxes

(d) F_{oi}: Turbulent ocean-ice fluxes

Figure 5-4: Energy fluxes into the sea ice-ocean system during the sea ice quasi-equilibrium period. Positive turbulent ocean-ice fluxes represent an internal redistribution of enthalpy within the sea ice-ocean system from ocean sensible heat to the sea ice latent heat of fusion (*i.e.*, melting). Net air-ocean and air-ice fluxes include incoming shortwave and outgoing longwave radiation.

Making use of Eq. 5.5, the source of all ice-melting energy must be ocean heat convergence (lateral + basal),

$$F_{oi} = F_{lat} + F_{bas} \tag{5.11}$$

As mentioned, the role of downwelling radiation as an enthalpy source is subsumed by the F_{oi} term. The relative magnitudes of downwelling short- and longwave radiation, basal, and lateral heat fluxes are of the same order. Therefore, it is important to quantify all positive energy contributions to the UOGC. The UOGC lateral and basal advective enthalpy fluxes are presented alongside the short- and longwave radiative fluxes in Figure 5-5.[7]

In the MIZ, all four energy sources contribute to the ablation of converging ice. Positive advective lateral fluxes are spatially limited to grid cells adjacent to the open ocean. Similarly, the contribution from shortwave radiation is nearly zero where ice concentrations are high, and small ($60 - 120\,\mathrm{W\,m^{-2}}$) at their highest in the MIZ where open water fractions are greatest.

The patterns of lateral advective fluxes are easily comprehensible. Behind the MIZ UOGC ocean temperatures are near the seawater freezing point where sea ice is present and therefore have very small horizontal gradients, $\vec{u}\,\nabla\theta \approx 0$. In contrast, large horizontal gradients in temperature are found across the MIZ and adjacent ice-free ocean leading to large lateral advective fluxes.

Vertical advective fluxes are the single largest source of ice-melting enthalpy behind the MIZ in the quasi-equilibrium state. These fluxes, a combination of advection, numerical diffusion, parameterized convection, and parameterized along- and cross isopycnal stirring and mixing, point directly at the importance of subsurface enthalpy reservoir in the maintenance of the position of the sea ice edge.

5.6 Sea Ice Buoyancy Budget

In the previous section the importance of oceanic sensible heat fluxes (lateral and basal) for maintaining the quasi-equilibrium sea ice edge was established. It is now prudent to examine a process which can mitigate these fluxes: surface buoyancy enhancement from sea ice meltwater. The sustained melting of advancing sea ice in the MIZ alters the upper

[7] Under the assumption of a quasi-equilibrium state, lateral advective fluxes are calculated as a residual from Eq.5.11.

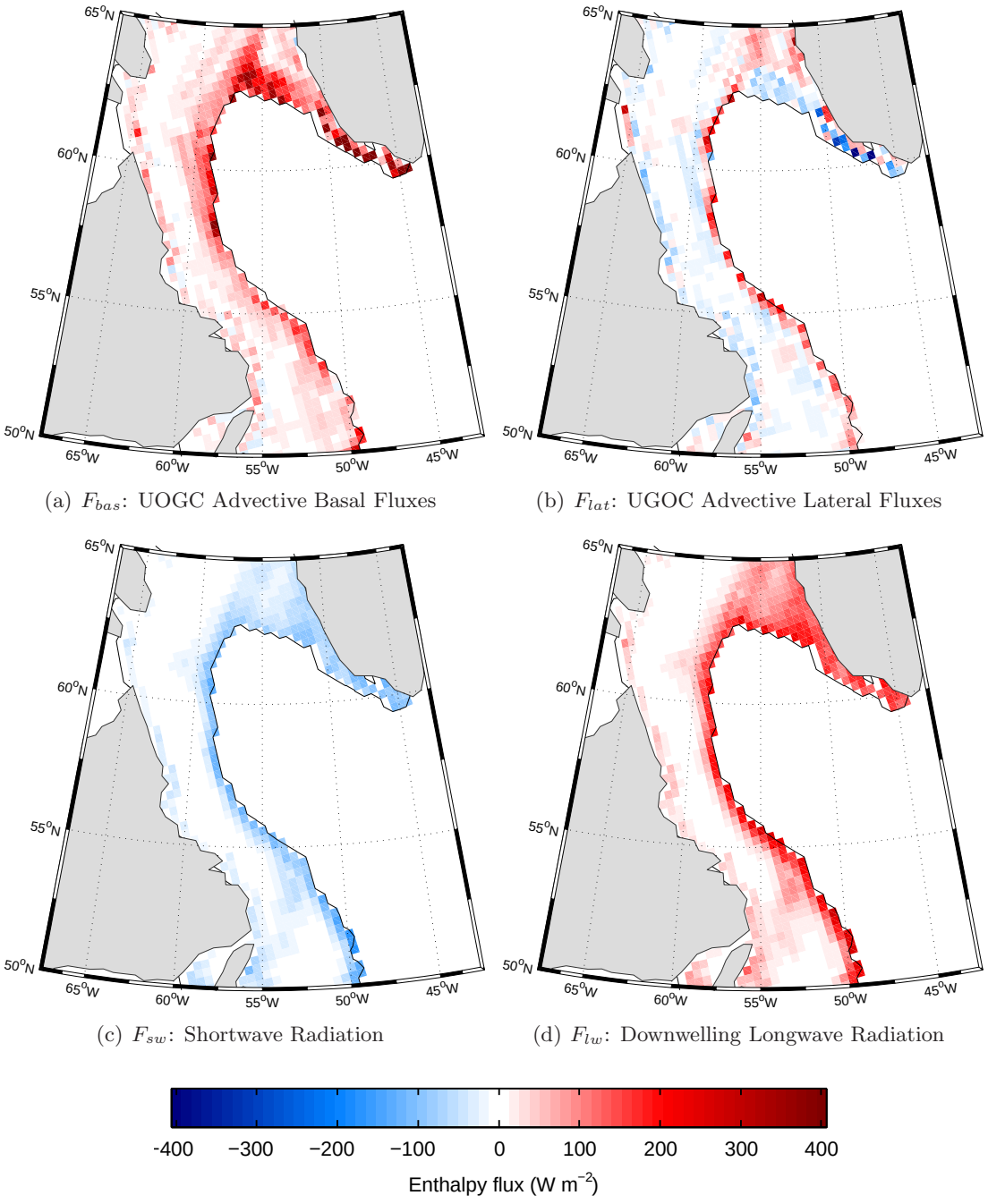

(a) F_{bas}: UOGC Advective Basal Fluxes

(b) F_{lat}: UGOC Advective Lateral Fluxes

(c) F_{sw}: Shortwave Radiation

(d) F_{lw}: Downwelling Longwave Radiation

Figure 5-5: Energy fluxes into the upper ocean during the sea ice quasi-equilibrium period in model grid cells with nonzero ice cover. Positive fluxes signify a flux convergence in the UOGC. The sign of shortwave radiation is reversed.

ocean buoyancy by the release of fresh meltwater and through the removal of enthalpy from sensible heat in seawater during sea ice melt. These terms affect the ocean surface buoyancy in opposite senses, fresh meltwater increases while the loss of sensible heat decreases seawater buoyancy. Similarly, the removal of low-salinity water from the ocean during sea ice growth decreases surface buoyancy. Where sea ice-related changes in the surface buoyancy are sustained, oceanic sensible heat fluxes are altered (McPhee et al. 1987).

The patterns and magnitudes of these buoyancy fluxes are treated in this section. First, buoyancy fluxes associated with sea ice processes are analyzed and compared against the buoyancy fluxes from all processes in the domain. Finally, support for upper ocean buoyancy enhancement from sea ice meltwater as an important process immediately preceding and during the sea ice quasi-equilibrium period is presented.

5.6.1 Buoyancy flux definitions

The time rate of change of seawater surface buoyancy, B, is written,

$$\frac{\partial B}{\partial t} = \frac{g}{\rho_0}\left[\left(\frac{\partial \rho_{sw}}{\partial T}\right)_{T,S} \frac{Q_{flux}}{c_{sw}} - \left(\frac{\partial \rho_{sw}}{\partial S}\right)_{T,S} \rho_0 S_{flux}\right] \tag{5.12}$$

Where ρ_{sw} is seawater density, ρ_0 is a reference seawater density, T is seawater temperature, Q_{flux} is the net surface heat flux that results in a temperature change, S is salinity, c_{sw} is seawater heat capacity, and S_{flux} is the net surface salinity flux.

In the presence of sea ice, the meaning of Q_{flux} is subtle. Net surface heat fluxes can lead to the sea ice growth leaving seawater temperature unchanged and (ignoring for salinity for the moment) implicating no ocean surface buoyancy flux. In some sea ice model formulations, the mere presence of sea ice in a cell implies $Q_{flux} = 0$, the seawater temperature is fixed to the salinity-determined freezing point. In the thesis, sea ice model ocean surface temperature is always above the freezing point (if even only infinitesimally, see Section 2.2.3). Consequently, in the presence of sea ice, net surface heat loss lowers seawater temperatures somewhat and leads to some ice development. Similarly, neat surface heat convergence increases seawater temperatures somewhat and leads to some ice melt. In the formulation of the buoyancy budget, only that fraction of Q_{flux} which affects seawater temperatures is considered in Equation 5.12.

It is useful to decompose the surface buoyancy flux expression into two terms, separating

out the contribution of all sea ice and non-sea ice processes,

$$\left(\frac{\partial B}{\partial t}\right)_{total} = \left(\frac{\partial B}{\partial t}\right)_{ice} + \left(\frac{\partial B}{\partial t}\right)_{non-ice} \tag{5.13}$$

With respect to the sea ice contribution to buoyancy flux, both Q_{flux} and S_{flux} terms are important. Seawater salinity is altered during thermodynamic growth and melt. Where sea ice is present, $Q_{flux} > 0$. As the model is formulated, the ocean-ice flux described in the previous section, F_{oi}, removes enthalpy from the UOGC and melts ice - lowering seawater temperature.

5.6.2 Buoyancy fluxes in the quasi-equilibrium state

Ocean surface buoyancy fluxes during the sea ice quasi-equilibrium period are separated by type (buoyancy changes from changes in ocean enthalpy versus salt) and source (buoyancy fluxes from sea ice-related processes versus all processes) and presented in Figure 5-6.

The contribution of buoyancy fluxes from enthalpy changes due to ocean-sea ice enthalpy fluxes (decreasing seawater buoyancy) is limited to narrow region within the MIZ and NS. This is logical as the MIZ is a region where lateral and basal advective ocean enthalpy flux convergence allows for sustained turbulent ocean-ice fluxes and melt. Deep within the ice pack behind the MIZ, UOGC temperatures eventually approach the seawater freezing point driving ocean-ice heat fluxes and therefore buoyancy fluxes to zero.

In contrast, the contribution of buoyancy fluxes due to sea ice salinity changes are found throughout the entire domain. Sea ice buoyancy fluxes are large and positive in the MIZ due to the large release of meltwater. Large negative buoyancy fluxes are found adjacent to the shorelines - closely following the patterns of thermodynamic ice growth. Small negative buoyancy fluxes are also noted in the central Baffin Bay, indicating sustained (albeit relatively slow) continued thermodynamic ice thickening and salt release. The sum of enthalpy and salt-related sea ice fluxes is dominated by the sea ice salt-related fluxes everywhere in the domain.

When all ocean surface enthalpy fluxes are considered, the intense wintertime open water air-sea heat fluxes in the Labrador Sea are revealed. The relative contribution from ocean-ice enthalpy fluxes to the total enthalpy-related buoyancy fluxes is very small. Conversely, the total ocean surface salt flux is dominated by sea ice-related processes. Small negative ocean

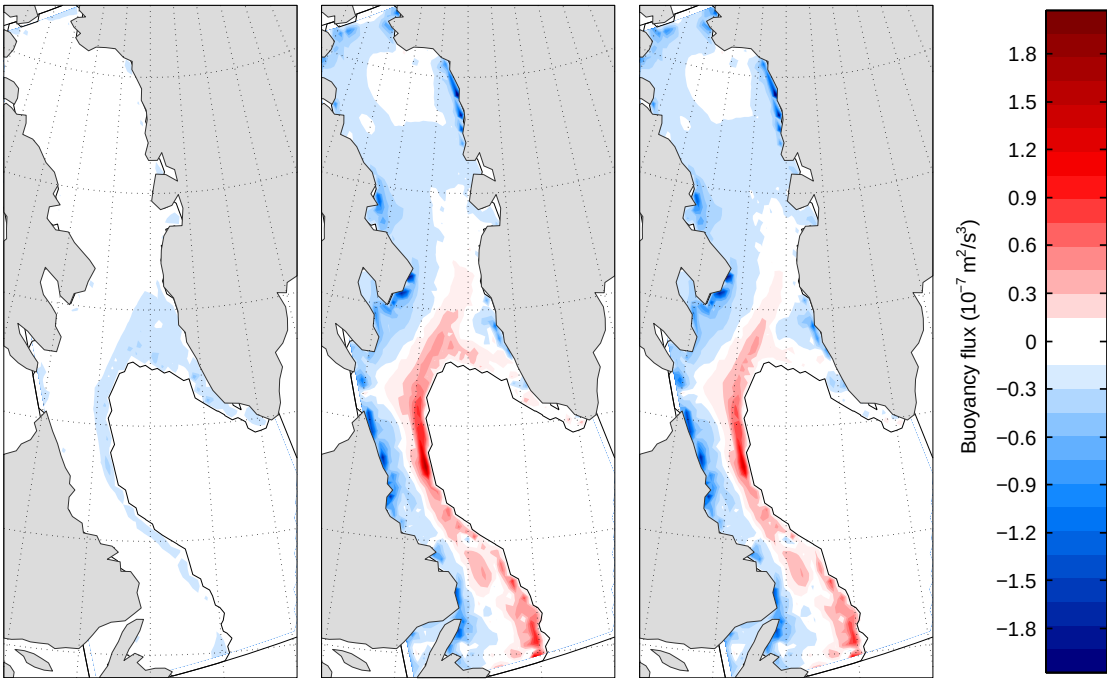

(a) Sea ice: enthalpy (b) Sea ice: salt (c) Sea ice: enthalpy + salt

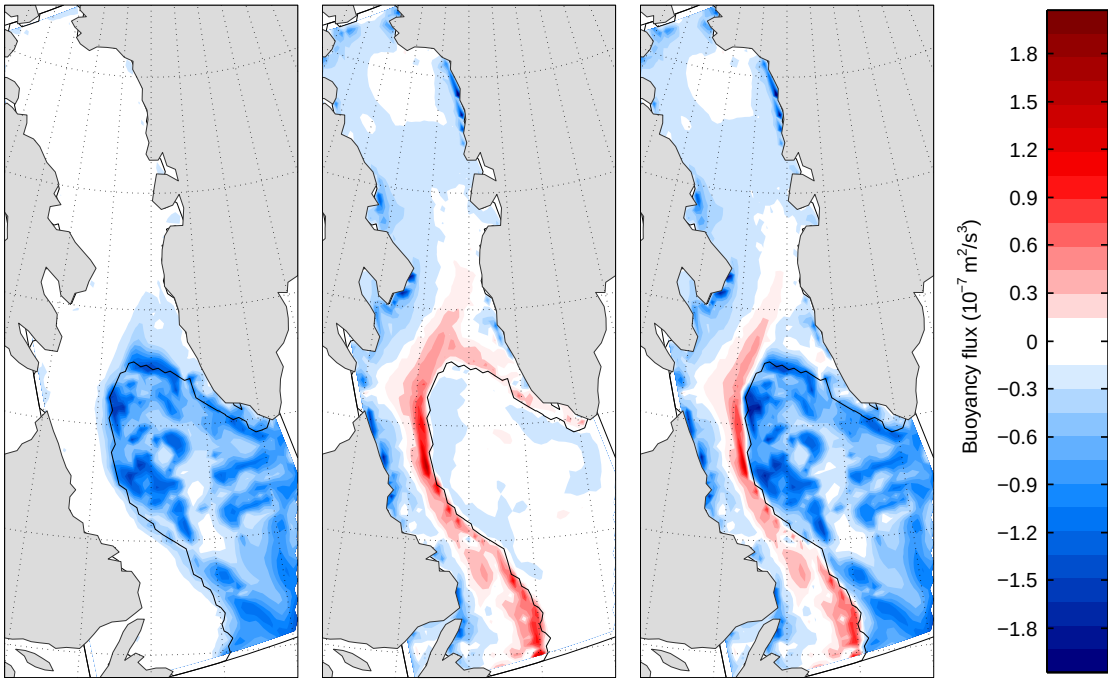

(d) Total: enthalpy (e) Total: salt (f) Total: enthalpy + salt

Figure 5-6: Ocean surface buoyancy fluxes from sea ice and from all ocean surface processes during the quasi-equilibrium state. Buoyancy fluxes from sea ice-related ocean enthalpy (a) and salt (b) fluxes and their sum (c). The total surface buoyancy flux from enthalpy (d) and salt (e) fluxes and their sum (f).

surface salt-related buoyancy fluxes are noted seaward of the MIZ, possibly reflecting the vertical mixing of saltier subsurface waters from convective entrainment from a deepening mixed layer.

The sum of all enthalpy and salinity-related buoyancy fluxes reveals a sharp contrast along the sea ice margin where intense positive buoyancy fluxes (sea ice meltwater release) are found adjacent negative buoyancy fluxes (open water air-sea heat loss) on the same order of magnitude. The MIZ is evidently a location where net ocean surface buoyancy fluxes are approximately balanced during a sea ice quasi-equilibrium state.

5.7 Conclusions

Using a simple 1-D thermodynamic mixed layer model initialized with the state estimate ocean temperature and salinity and driven by reconstructed air-surface heat fluxes, the dates of sea ice formation in the Labrador Sea and Baffin Bay are found to be predicted until mid-January. The initial expansion of ice in Baffin Bay is shown to be driven mainly by thermodynamical processes. The 1-D thermodynamic model fails to predict ice beyond the THF in the northern Labrador Sea- exactly that part of the domain which exhibits the greatest seasonal sea ice maximum extent interannual variability. This result verifies the critical importance of lateral advection of sea ice and/or ocean tracers for the development of ice in the Labrador Sea. However, exactly how lateral advection contributes to the development of the quasi-equilibrium is not further revealed by this analysis - it is, however, the focus of the following chapter.

The sea ice mass balance during the quasi-equilibrium period of $1996 - 1997$ is shown to consist of thermodynamic production/dynamic divergence along the shoreline, transport across Baffin Bay and Labrador Shelf, and ultimately thermodynamic melt/dynamic convergence in the MIZof the Labrador Sea. The ocean-ice heat flux convergence is sufficient to melt all converging and locally produced ice during the quasi-equilibrium period in the MIZ. The dominant energy source which sustains the ocean-ice heat flux convergence is from oceanic heat transport to the mixed layer - a combination of lateral and vertical transports.

Finally, the contribution of ocean surface buoyancy fluxes from ice-related processes was quantified and compared with total surface buoyancy fluxes. Positive buoyancy fluxes

from ice melt are of the same order as negative buoyancy fluxes as air-sea heat fluxes proximate to the MIZ which implies a balance of surface buoyancy fluxes at the ice edge. The extent to which positive buoyancy flux *imbalances* in the period preceding the sea ice quasi-equilibrium period are important for the annual cycle is not determined. On the other hand, model-data discrepancies in the 1-D thermodynamic experiment suggests a possible link between hydrographic changes associated with positive sea ice meltwater buoyancy flux and the crossing of the ice edge beyond the THF.

These findings support some of the existing hypotheses on the role played by sea ice dynamics in the Labrador Sea, mainly that dynamics are essential to some (but not all) of the advancement of the ice edge to its quasi-equilibrium position. To further understanding on the role of ocean-sea ice buoyancy feedbacks further investigation into the time-evolution of the sea quasi-equilibrium state is required - the subject of the final chapter.

Insofar as ocean-ice heat flux convergence rates are a function the distribution of heat within the Labrador Sea, one imagines that interannual variability of Labrador Sea upper ocean heat content might affect the location where a balance is attained between the ice mass latent heat of fusion convergence and ocean-ice sensible heat flux convergence.

Chapter 6

Sea Ice-Ocean Variability in the Labrador Sea and Baffin Bay

6.1 Chapter Overview

The focus of this chapter is to determine the role of hydrographic variability to the development of the sea ice annual cycle in the Labrador Sea and Baffin Bay. The analyses of the mass, energy, and buoyancy budgets of the $1996-1997$ annual cycle conducted in Chapter 4 strongly suggest that the discrepancy between the observed sea ice extent and the ice extent predicted by 1-D thermodynamic processes is likely related to ice advection and ocean-ice interaction. These analyses also established that the release of sea ice meltwater into the upper ocean provides a net positive surface buoyancy forcing of the same order of magnitude as the negative surface buoyancy forcing from turbulent air-sea fluxes. However, the question remains: is this positive buoyancy forcing at the leading ice edge important for the advancement of the pack and the establishment of the quasi-equilibrium position?

In this chapter, the answer to this question is discovered to be yes - the meltwater stability enhancement mechanism (MSEM) is critically important for establishing the position of the seasonal sea ice edge - but only in specific hydrographic conditions.

The chapter is organized into five parts. In the first, I further analyze the state estimate of the $1996-1997$ annual cycle. This analysis provides evidence of the importance of the MSEM under hydrographic conditions where the upper ocean is anomalously fresh and well-stratified - *sea ice-preconditioned* (Section 6.2). In the second, I present the results

from a simple numerical experiment that reveals that the MSEM is required for most of the propagation of sea ice across the Thermohaline Front (THF) in the Labrador Sea (Section 6.3). In the third, I characterize the watermass properties of the sea ice-preconditioned waters in the 1996-1997 annual cycle (Section 6.4). The third section presents evidence that the MSEM suppresses vertical heat fluxes into the upper ocean thereby increasing the persistence of ice across the THF (Section 6.5). In the final piece of analysis, I quantify a potentially serious bias in the state estimate: the partitioning of advective ocean heat fluxes to the marginal ice zone (MIZ) into basal and lateral heat flux components due to missing lateral eddy transport (Section 6.6). The chapter concludes with a summary of the key findings (Section 6.7).

6.2 Buoyancy Fluxes and the Sea Ice Quasi-Equilibrium State

The sea ice quasi-equilibrium period is identified as period of relative sea ice edge stability near the peak of the seasonal sea ice cycle. In the quasi-equilibrium period realized in the $1996-1997$ state estimate, identified as February 21-March 20, the total ice area in the model domain is very stable: $1.3 \pm 0.05 \times 10^6\,\mathrm{km}^2$ (see Figure 4-2). However, while the total ice area may be stable, the location of the sea ice edge is ever changing. To illustrate, consider the 175 km advance of the sea ice edge during the quasi-equilibrium period in the northern Labrador Sea's Northern Slope (NS) region, shown in Figure 6-1(a).

What sea ice-ocean processes are responsible for this advancement? In the weeks preceding it, the basin-scale patterns of ice drift were not appreciably different. Indeed, using the rates of ice drift found by the state estimate, a freely drifting ice pack would have moved many hundreds of kilometers beyond the final sea ice edge position by early February.

As the basin-scale patterns of sea ice thermodynamic growth and subsequent drift in the Labrador Sea and Baffin Bay have shown, a sustained convergence of sea ice is realized in the MIZ. This ice mass convergence and subsequent meltwater release was shown in Section 5.6 to lead to large positive ocean surface buoyancy fluxes at the ice margin. Therefore, one possible explanation for this sea ice edge advancement is the MSEM (introduced in Section 3.3.1).

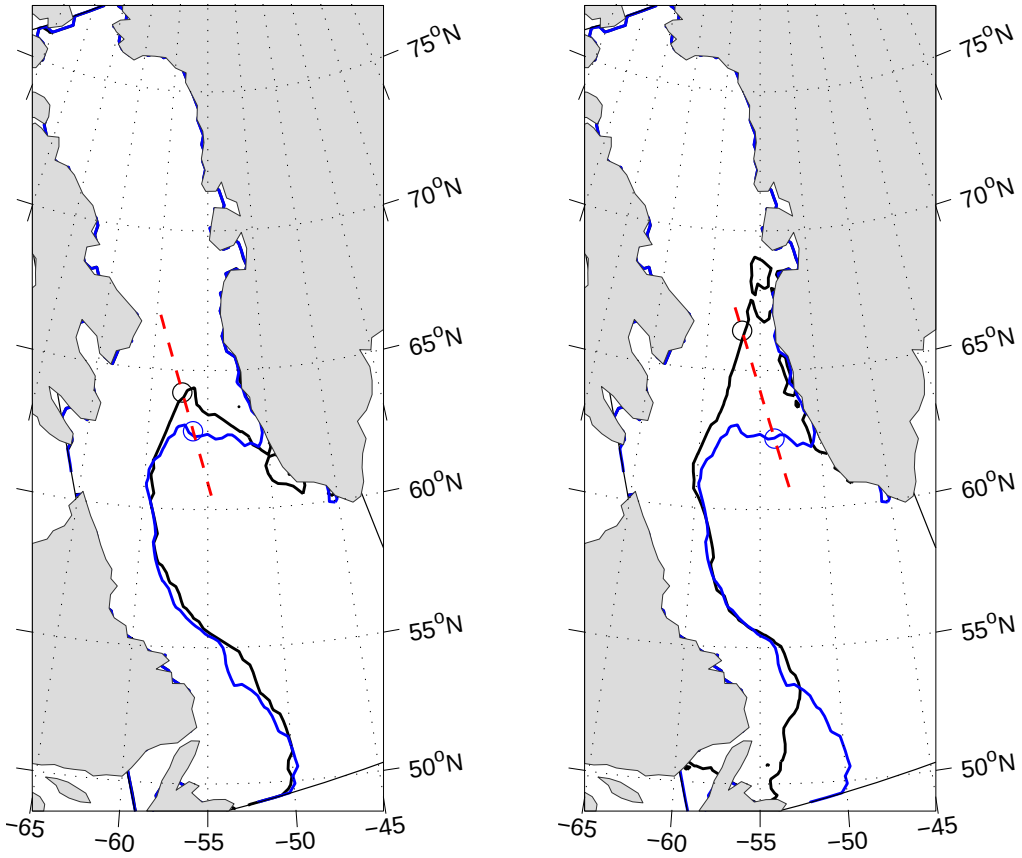

(a) quasi-equilibrium: Feb 21-Mar 20

(b) Pre-quasi-equilibrium: Jan 30-Mar 20

Figure 6-1: Advancement of sea ice edge (15% contours) during two periods: the quasi-equilibrium period (Feb 21-Mar 20) and several weeks preceeding the quasi-equilibrium period (Jan 30-Mar 20). Within quasi-equilibrium period, small ice edge advancement is noted during on the Northern Slope while the ice edge location is approximately stable south of 62° N. The advancement of the ice edge in the weeks preceeding the quasi-equilibrium period is mainly in the northeastern Labrador Sea. Dashed lines indicate location for vertical cross sections in Figures 6-2 and 6-3. Circles indicate sea ice edge locations on these sections for the start and end dates over these periods.

How does the modification of upper ocean hydrographic conditions relate to the progressive advancement of the sea ice edge during the quasi-equilibrium period? In the presence of converging ice mass, the mixed layer stabilization enhancement triggered by ice melt disrupts any ice mass and energy balances which may have been attained, leading to the net accumulation of ice in formerly unfavorable locations. Sustained ice convergence within the MIZ may progressively modify the hydrographic properties of water seaward of the MIZ - initially unfavorable to *in situ* sea ice production - in a way such that the flow of ice across its surface is unabated.

To review, the salient features of the proposed positive-feedback MSEM are:

1. advected ice converges into warmer waters seaward of the MIZ
2. the ice melts and releases low-salinity meltwater
3. the upper ocean buoyancy increases due to freshening
4. the mixed layer shoals and becomes more stratified
5. the rate of advective heat convergence into the mixed layer falls with suppression of convective mixing
6. temperatures in the mixed layer fall from ocean-ice and air-sea heat fluxes
7. the rate of ice convergence exceeds the rate of ice melt
8. sea ice accumulates in the hydrographically-modified upper ocean
9. the MIZ and region of sustained ice convergence moves farther offshore

Recall from Section 3.3.1, that mixed layer shoaling and stabilization enhancement in the MIZ following the introduction of sea ice meltwater has been observed several *in situ* field campaigns. However, because making *in situ* measurements of this sort is so technically challenging, the impact of the contraction of the surface boundary layer from sea ice meltwater-driven stabilizing buoyancy fluxes on the advancement of the sea ice on the basin-scale is not well understood.

Might the MSEM be implicated in establishing the quasi-equilibrium ice edge position in the first place? Consider the prediction of sea ice growth in the Northeast Corner of northern Labrador Sea (NEC) in the 1-D thermodynamic freezing model presented in Section 5-1. In that experiment, it was demonstrated that by forcing the state estimate's October 1 hydrographic conditions with reconstructed atmospheric heat fluxes, ice was unable to thermodynamically develop on the Irminger Sea Water (IW)-side of the THF.

As the discrepancy between the 1-D model and observations is large in the NEC, an

intriguing possibility is that the MSEM is responsible for development of sea ice in that region. Curiously, in the weeks preceding the quasi-equilibrium period, the ice edge advances much farther across the NS in the NEC than it does just a few hundred kilometers to the west, as seen in Figure 6-1(b). What are the relevant differences between the ocean states in each location that lead to such dramatic differences in the observed ice cover expansions in the weeks preceding the sea ice quasi-equilibrium period? If the MSEM is relevant in both cases, why does it lead to such different results?

Determining the role of the MSEM in setting the quasi-equilibrium ice edge position may be important for understanding interannual sea ice variability in the model region. If the MSEM isolates the upper ocean as a function of the rate of seaward ice drift, variability in ocean hydrography may be unimportant in setting the ice edge location. In that case, one might conclude that interannual ice extent variability might be tightly coupled to ice transport variability. If, on the other hand, the MSEM is effective only under very specific *hydrographic* conditions, the role of interannual ice transport variability may be much smaller than currently assumed.

To identify the role of the MSEM, I examine the advancement of the ice edge at two locations and times: the incremental ice edge progression during the quasi-equilibrium over the Northern Slope (Section 6.2.1) and the extensive ice edge progression in the NEC in the lead up to and throughout the quasi-equilibrium period (Section 6.2.2) .

The analysis considers the hydrographic developments near the ice edge during these periods of advancement resulting from buoyancy loss from air-sea heat fluxes and buoyancy enhancement from meltwater release. Developments in the ocean-ice system are conveyed by contrasting depth-latitude hydrographic cross sections, buoyancy fluxes, ice position, and mixed layer development at the beginning and end of each advancement period.

6.2.1 Inching forward on the central Northern Slope

The sea ice and ocean states during two stages of the quasi-equilibrium period (start: week ending February 27, and end: week ending March 20) are presented in Figures 6-2(a) and 6-2(b).

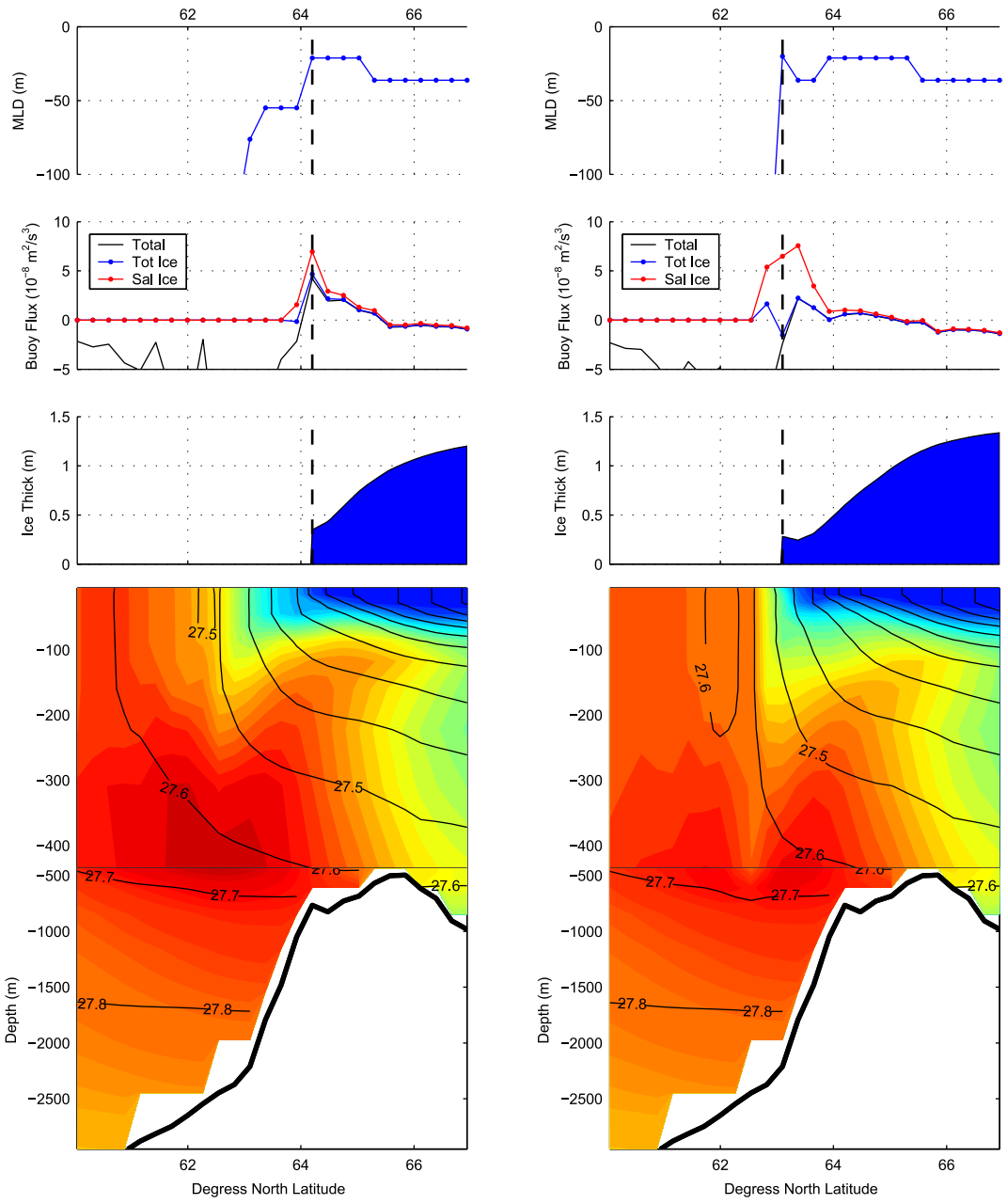

(a) Week ending February 27

(b) Week ending March 20

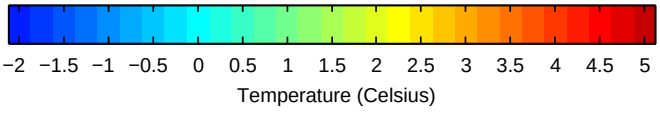

Figure 6-2 *(previous page)*: Panels of weekly-mean mixed layer depth (m), surface buoyancy flux ($10^{-8}\,m^2/s^3$), ice thickness (m), and hydrographic ocean conditions, temperature and potential density (kg/m^3), along the section indicated in Figure 6-1(a) for the week of February 27 (a) and March 20 (b). Displayed mixed layer depths are limited to 100 m and are calculated using the method described in Section 4.3.2. Buoyancy fluxes are decomposed into three terms: the contribution from sea ice processes affecting salinity, the total contribution of all sea ice processes, and the total from all ice + non-ice processes. Actual (not UOGC mean) ice thickness is presented as the shaded area in blue. The ocean hydrography panel indicates temperature (colors) and potential density isopycnals (surface-referenced - 1000 kg/m^3) with 0.1 kg/m^3 contour intervals. The ocean depth spacing intervals are larger below 500 m. Bathymetry is indicated by the heavy black line. The shallow Davis Strait is noted at 66° N. For a more complete sense of the magnitudes of the open water buoyancy fluxes please see Figure 5-6.

Sea ice and hydrographic states: February 27

In the mean state of the ocean-ice system for the week ending February 27 (Figure 6-2(a)), many of the key ocean-ice features and processes discussed in earlier sections are presented from a novel perspective. Hydrographically, one identifies a warm ($2-5°$ C) subsurface IW core at 400 m, the ventilation of subsurface heat through entrainment in convectively-deepened mixed layers, cold highly stratified surface Arctic Water (AW), and the THF. Also evident is a southward extension of anomalous colder, fresher, and more highly stratified waters beyond the sea ice edge overlaying the warmer ($> 2°$ C) IW between $62.5-64°$ N. Exposure to air-sea buoyancy losses have deepened the mixed layer south of 64° N to between 50 and 500 m. Ventilation of IW occurs south of 62.5° N. To the north of 62.5° N and even beneath some of the ice, IW is isolated from the surface at a depth of $\sim$ 100 m.

Ice thickness along this section decreases from north to south from 1.1 to 0.4 m. This is consistent with two factors: an increase of along-section velocities from north to south by approximately 25% (implying ice volume divergence) and additional time for thermodynamic ice thickenening in the northern Baffin Bay. Finally, the ice edge is noted to be within 100 km of a sharp gradient in isopycnal outcropping, 64.5° N, coinciding with waters of S $\sim$ 33.25 or $\sigma_0 = 1027.1\,kg\,m^{-3}$ - the location of the THF in late-February 1997.

The pattern of surface buoyancy forcing indicates two regions where meltwater release and salinity enhancement from ice melt and thermodynamic growth are significant. North of the Davis Strait, negative buoyancy forcing from ice growth/salinity enhancement is evident. Farther south, positive buoyancy forcing from meltwater release is the dominant term in

total surface buoyancy fluxes. At the ice edge, sea ice buoyancy fluxes peak reflecting the high rates of ice melt as the pack encounters warmer offshore waters. Where ice is present, the total surface buoyancy forcing closely follows the total ice surface buoyancy forcing. South of the MIZ, the total surface buoyancy fluxes are large and negative due to the characteristic intense wintertime air-sea heat losses of the Labrador Sea.

Interestingly, positive buoyancy fluxes from sea ice meltwater release are non-zero south of the ice edge; non-zero positive buoyancy fluxes from sea ice meltwater release in the absence of ice cover indicates the complete and near-instantaneous melting of all ice advected out of the MIZ.

Finally, mixed layer depths (MLD) deepen south of the ice edge. The mixed layer is shoaled behind the MIZ between $64 - 65^\circ$ N, an area co-located with the largest net positive surface buoyancy forcing. Importantly, the mixed layer beyond the MIZ is shallower than the subsurface IW, between $63 - 64^\circ$ N.

Sea ice and hydrographic states: March 20

Three weeks later, during the week of March 20 (Figure 6-2(b)), significant changes are evident in ice distribution, hydrographic structure, surface buoyancy forcing patterns, and MLDs. Hydrographically, temperatures in the southern half of the IW core are 1.4° C cooler and upper ocean temperatures beneath the newly expanded ice are cooler by $1.0 - 2.4^\circ$ C. The warm IW core is vertically split with the dividing line falling close to the new ice edge. The isolated IW tongue near 65° N is $\sim 1^\circ$ C cooler in the upper 250 m.

The thickness of the newly extended ice cover is quite thin ($\leq$ 0.25 m), a consequence of incomplete melting of the thicker ice advected southwards. The distance traversed by the ice edge during this time yields an effective mean southward velocity of 7.75 km/day. The actual mean southward velocity at the ice edge is about twice as fast, 15.45 km/day. Erosion of the advancing ice by melting from ocean-ice enthalpy fluxes is the most sensible explanation for the discrepancy between actual and effective ice edge velocities.

The qualitative patterns in the surface buoyancy fluxes are similar but shifted southward. In the vicinity of the earlier MIZ, net ice-related buoyancy fluxes are near zero, indicating that ocean-ice heat fluxes have mainly ceased. At and around the new ice edge, the positive sea ice meltwater buoyancy forcing term is greater in magnitude, evidence of significantly higher melt rates. A potentially significant difference is that total ocean surface buoyancy

fluxes at the ice edge are *negative* - probably due to large open water air-sea heat fluxes in the low ice concentration MIZ.

Finally, the mixed layer depths between the new and old ice edge locations are dramatically shallower. In addition, the horizontal gradients of mixed layer depths between the ice-free and ice-covered regions are sharper.

Interpretation of sea ice and hydrographic evolution

Large positive surface buoyancy forcing at the February 27 edge of the MIZ appears to contribute to the isolation of subsurface IW via mixed layer shoaling and stabilization enhancement. The observation of substantial meltwater release to the south of the actual ice edge supports this interpretation.

However, the state estimate also suggests that the efficacy of the MSEM may be limited to certain regions with special upper ocean hydrographic properties. Consider the evolution of the hydrographic state during this three week period. During the week of February 27, isopycnal slopes indicate IW ventilation in waters denser than 1027.5 kg/m^3 by along-isopycnal stirring and mixing. To the north, between the 1027.0 and 1027.5 kg/m^3 isopycnal outcroppings, the upper ($\sim$ 100 m) of the ocean is comparatively cooler, fresher, and more stratified.

These fresher cooler more stratified waters are certainly a kind of modified IW: fresher than IW and saltier than AW and sea ice meltwater. Moreover, the modified waters are found to the south of the THF and in a region energetic mesoscale eddies.

Consider also the magnitudes of surface buoyancy forcing around the ice edge during both weeks. In the later period, meltwater release is far greater despite nearly identical ice edge velocities (within 5%) and much thicker ice in the MIZ in the former. The tentative conclusion must be that MSEM allows ice edge advancement until the ice edge encounters IW within the mixed layer.

Why would the MSEM fail to allow the advancement of the ice edge across waters with IW in the mixed layer? One possibility is that when the ice edge is adjacent to warm salty surface waters, the net buoyancy fluxes within the upper ocean grid cell approach zero or even remain negative: a decrease of buoyancy from the advection of saltier subsurface waters may offset the increase of buoyancy from ice meltwater release. Another possibility is that the ice begins its melting phase after the vernal equinox and simply does not have enough

time to alter the upper ocean buoyancy after arriving in mid-March. A third possibility is that, proximate to the ventilating IW, sustained lateral heat fluxes provide enough enthalpy to melt any converging ice - regardless of the modification of the upper ocean stratification. In the third scenario, the MSEM feedback would become completely ineffective.

The role of ocean-ice interactions and upper ocean hydrographic conditions in establishing the quasi-equilibrium ice edge position is further explored in the next section.

6.2.2 Rapid advancement above the eastern Northern Slope

Recall the results from the 1-D thermodynamic model presented in Section 5-1. Using the 1-D model the predicted dates of ice appearance agree very well with observations until the end of January. The area of largest discrepancy is the NEC, north of 62.5° N. It is probably not a coincidence that the 1-D model's ice edge is very closely approximated by the location of the THF in late February (as identified in the previous section). What is interesting about this area is that it also coincides with a second source of AW in the model domain, the West Greenland Current (WGC).

Having recognized that the distribution of modified IW may be related to the quasi-equilibrium sea ice location in the previous section, the question now arises: might the upper ocean hydrographic conditions in the NEC share characteristics with waters above the central Northern Slope? If so, as the ice pack extends past the THF does it evolve in similar ways and cease its advancement in similar circumstances?

Ocean-ice cross-sections from the state estimate along the transect shown in Figure 6-1(b) are presented in Figure 6-3. The two selected seven-day mean states correspond to the ice pack's crossing of the THF at January's end and the maximum ice extent realized in mid-March.

Main features of the state estimate

Qualitatively speaking, the ocean-ice states during these two periods share many features with the cross-sections described in Figure 6-2. A warm salty IW core is identified which becomes progressive cooler as it ventilates. An area of low-salinity modified IW is identifiable in the upper 100 m between the initial and final ice edge positions. North of 63.75° N, subsurface IW beneath the low-salinity modified waters remain isolated from the surface. Initially low rates of meltwater buoyancy flux at the ice edge become substantially greater

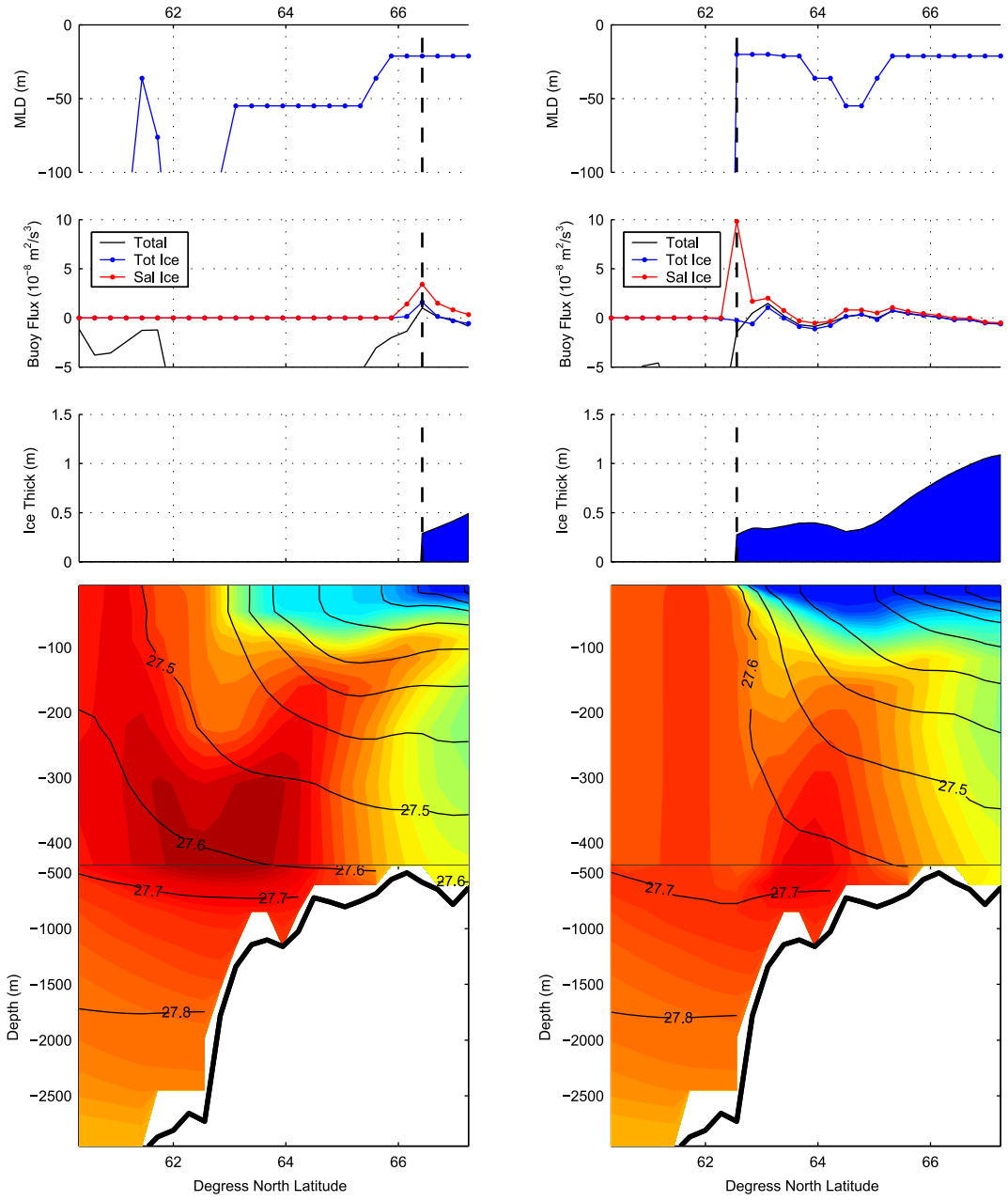

(a) Week ending January 30

(b) Week ending March 20

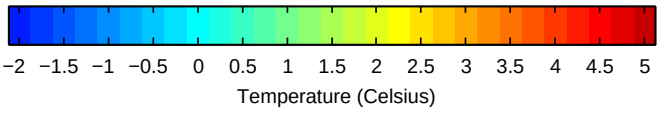

Figure 6-3 *(previous page)*: As Figure 6-2 except different time and hydrographic section. Panels are presented for January 30 (a) and March 20 (b) at the hydrographic section indicated by Figure 6-1(b)

when the ice meets mixed layer-entrained IW at 62.5° N. The mixed layer shoals or remains at the same depth along the entire length of ice advancement.

An additional interesting feature is noted in the ice thickness profiles of Figure 6-3(b): Thin ($\leq$ 0.5 m) ice along the entire length of ice advancement across the THF. What explains the uniformity and thinness of this ice?

At $\sim$ 64° N net ice buoyancy fluxes are negative, the mixed layer is relatively deep, and the ice is somewhat thicker than to the north and south. At this location, negative net sea ice related buoyancy fluxes indicate thermodynamic ice growth. Evidence for thermodynamic ice growth in this location illustrates an important point: while huge amounts of ice may need to melt to stabilize the upper ocean, once stabilized and ice covered, nothing prevents local thermodynamic growth. However, when the stabilization is marginal, as is the case here, seawater buoyancy loss from thermodynamic ice growth may lead to subsurface heat ventilation, enhanced ocean-ice enthalpy fluxes, and subsequent ice thinning - the ice-boundary layer stabilization feedback (See Section 3.3.1).

Operation of this feedback process keeps ice thickness below 0.5 m in the region between $62.5 - 65.0$° N despite large air-sea ice heat fluxes (not shown). Indeed, during the quasi-equilibrium period, net ice-related buoyancy fluxes are near zero in the NEC indicating a cancellation of buoyancy fluxes: negative from ice growth/high-salinity brine release; positive from ice melt/low-salinity brine release (See Figure 5-6).

Therefore, because of the marginal stability of the mixed layer along the entire length of the near-surface modified IW, sea ice thicknesses beyond the THF remain thin.

Interpretation of sea ice and hydrographic evolution

A general interpretation of the sea ice and hydrographic evolution in both regions is now possible. An expanse of modified (fresher, cooler, more stratified) IW overlays some of the warmer subsurface IW south of the THF. Melting of the wind and ocean current-driven ice front progressively shoals the mixed layer in the MIZ before mixed layer deepening entrains subsurface IW. The operation of the MSEM is associated with the translation of the ice

edge in the direction of offshore ice drift.

Once the MIZ is adjacent to waters mixed with ventilated IW, progressive ice drift out of the MIZ leads to extremely high melt rates. However, in the hydrographic regime of surface-mixed IW the MSEM does not operate (the mixed layer does appreciably shoal and the location of the MIZ remains stationary) for reasons which are not entirely obvious.

6.2.3 Section Conclusions

Before drawing the conclusions from the two analyzed transects, I note that similar analyses were conducted for several additional transects across the NS - all of which shared fundamental similarities with the two described above.

This analysis reveals the following:

1. The positive buoyancy forcing associated with the meltwater release in the MIZ shoals the mixed layer.
2. Large expanses of subsurface IW can be isolated from the surface by sea ice.
3. South of the THF, sea ice advance occurs only over waters which are cooler and fresher that the subsurface IW but warmer and saltier than the typical watermass properties of AW found over Baffin Bay.
4. Meltwater buoyancy fluxes are highest when the MIZ is proximate to surface waters with ventilated IW.
5. The sea ice pack does not significantly advance after encountering ventilated IW.

Overall, this section strongly implicates the MSEM for the advancement of ice on the IW side of the THF. As alluded in the section introduction, the MIZ advancement beyond the THF is observed only over specific hydrographic conditions - comparatively cold fresh and stratified waters (to $\sim$ 125 m) overlaying the warm salty weakly stratified IW below.

The above analysis implicates - but not does unambiguously demonstrate - the relevance of the MSEM in the NS of the Labrador Sea. Assuming that the MSEM is indeed relevant and furthermore that its relevance is limited to specific hydrographic conditions, the waters satisfying the specific hydrographic conditions are presently termed *sea ice-preconditioned* or SI-PW.[1]

[1]The use the word *preconditioned* in this thesis should not be confused with a distinct usage pertaining to deep convection proclivity in the Labrador Sea. Examples of the use of the term *preconditioning* or *preconditioned* to refer to a low-salinity ocean state favorable to sea ice can be found in McPhee et al. (1987) and Kitoh et al. (2001).

Before questions about the identification/identifiability of the SI-PW are taken up, the relevance of the MSEM must first be demonstrated more conclusively - a problem which is taken up in the following section.

6.3 Importance of the meltwater stability enhancement mechanism

While indirect evidence of enhanced upper ocean stratification associated with the MSEM has been presented, the importance of this feedback remains speculative. We have seen that under the conditions of the $1996 - 1997$ annual cycle, the quasi-equilibrium ice edge position beyond the THF is limited to an expanse over which IW ventilation is slow to develop.

However, could ice dynamics alone (not the MSEM) account for the quasi-equilibrium ice edge position? Perhaps the 1-D thermodynamic ice-growth model failed to predict ice on the IW side of the THF simply because (missing) lateral transports are required to drive seawater temperatures to the freezing point. To cool upper ocean temperatures to freezing point (or low enough such that ocean-ice heat fluxes are too feeble to erode all converging ice) south of the THF, perhaps additional ocean enthalpy losses associated with melting dynamically-converging ice are necessary. If so, sea ice-related surface buoyancy forcing plays no role in the presence of ice on the IW-side of the THF.

Discerning the regions where the MSEM is relevant for the development of the sea ice quasi-equilibrium state can be determined in a simple numerical experiment. In this experiment, the sea ice model is altered such that the positive buoyancy forcing associated with thermodynamic melt processes is eliminated. The regions where the MSEM ocean-ice feedback is relevant is revealed by examining the differences in ice pack distributions of the state estimate and the experiment.

6.3.1 Experiment setup

To eliminate the MSEM, the sea ice meltwater salinity in the model is instantaneously equated with the salinity of the upper ocean grid cell into which it is released. With this modification, sea ice processes can only provide negative ocean surface buoyancy forcing: salinity increase during thermodynamic growth and temperature decrease during turbulent ocean-ice fluxes.

The numerical model is initialized and forced using the same adjusted fields which generated the consistent state estimate. As the atmosphere is non-interactive, it should be noted that mismatches between the prognostic ocean-ice and the prescribed atmospheric state are inevitable.[2] Therefore, the results of this experiment should not be interpreted as a prediction of the ocean-ice-atmosphere evolution without MSEM, but merely as providing an indication of where MSEM may be important.

6.3.2 Experiment results

The model output from the one-year simulation without the MSEM are collectively referred to as MSEM-OFF while the model output from the original state estimate is referred to as MSEM-ON. Results from MSEM-OFF are compared with MSEM-ON and observations in three ways: 1) time series of total daily ice area over the annual cycle 2) sea ice concentration field during the quasi-equilibrium period, and 3) two sea ice-ocean transects.

MSEM-OFF vs. observations: time series of total ice area

The time series of total sea ice area in the model region with MSEM-OFF compares well qualitatively with observations (and MSEM-ON), as shown in Figure 6-4, but is quantitatively deficient.

During the initial freeze-up of the Baffin Bay and northern Labrador Shelf (until mid-January) the total ice area of MSEM-OFF tracks closely with observations - albeit with a slight negative bias ($\sim 0.1 \times 10^6\,\mathrm{km}^2$). That MSEM-OFF would track observations with so well until mid-January provides further supporting evidence that the 1-D thermodynamic processes are sufficient to explain the location and timing of initial ice expansion on the AW-side of the THF.

The negative bias in MSEM-OFF total area grows from mid-January, a features which is absent in MSEM-ON (see Section 4-2). It is from mid-January that sea ice extends across the THF in the southeastern Baffin Bay (from Disko Island to Davis Strait) and offshore

[2]For example, surface air temperatures over sea ice tend to be lower than over open water (see Section 2.5.1). In the areas of sea ice area discrepancy between the state estimate and the experiment, surface air temperatures may be inconsistent with the ocean state (Griffies et al. 2009). The prescribed surface air temperatures bring with them an imprint of the "true" ice extent (see Section 2.5.1 for details). Consequently, where ice is present in the state estimate (which is the nearly the same as where ice is present in reality) but absent in the experiment, the prescribed air temperatures will still reflect an ice-covered state and therefore be erroneously cold as there is no feedback between the model used in this thesis and the atmospheric state.

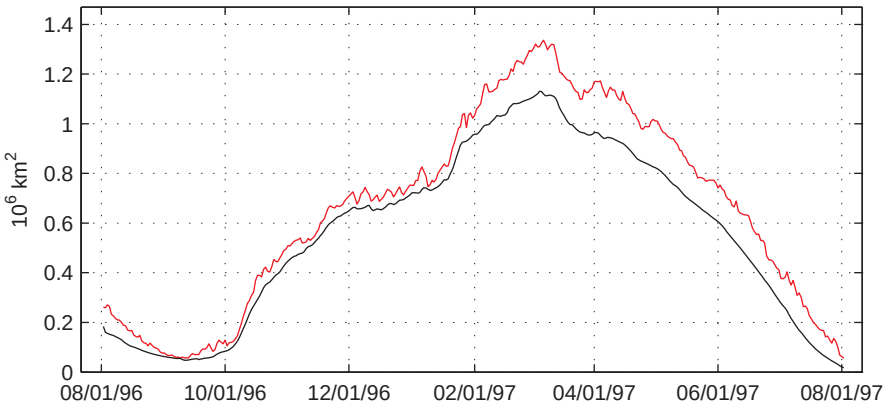

Figure 6-4: Total sea ice area from August 1, 1996 in the study region from observations (red) and the MSEM-OFF experiment (black). The total ice area time series should be compared with MSEM-ON in Figure 4-2.

from the inner Labrador Shelf across the shelfbreak.

From February to mid-March, the expansion of total ice area in MSEM-OFF grows more slowly than observed. Both MSEM-OFF and observations both attain seasonal sea ice maximum extent at approximately the same time. After the peak in total ice area, ice area loss in MSEM-OFF proceeds at a slightly slower rate than observations.

From the above, the MSEM does indeed appear to be important for the development of sea ice across the Labrador Shelf and across the THF in the Northern Labrador Sea, as hypothesized. To determine where the discrepancy between the observed and MSEM-OFF simulated total sea ice area, the spatial patterns of ice concentration in MSEM-OFF are now considered.

MSEM-OFF vs. observations: ice concentrations during quasi-equilibrium

The spatial pattern of the quasi-equilibrium ice concentrations of MSEM-OFF, seen in Figure 6-5 reveals large differences on the IW side of the THF. In MSEM-OFF, ice is absent across the Labrador and Baffin Island shelfbreaks as far north as Davis Strait. Moreover, little ice is found on the Northern Slope.

The absence of ice across the Labrador shelfbreak is a remarkable confirmation of the hypothesis of Tang (1992) which invoked the MSEM to explain hydrographic anomalies across the Labrador shelfbreak in the southwestern Labrador Sea (see Section 3.3.1).

Unexpectedly, a wedge-shaped area of low-concentration ice in the eastern corner of the

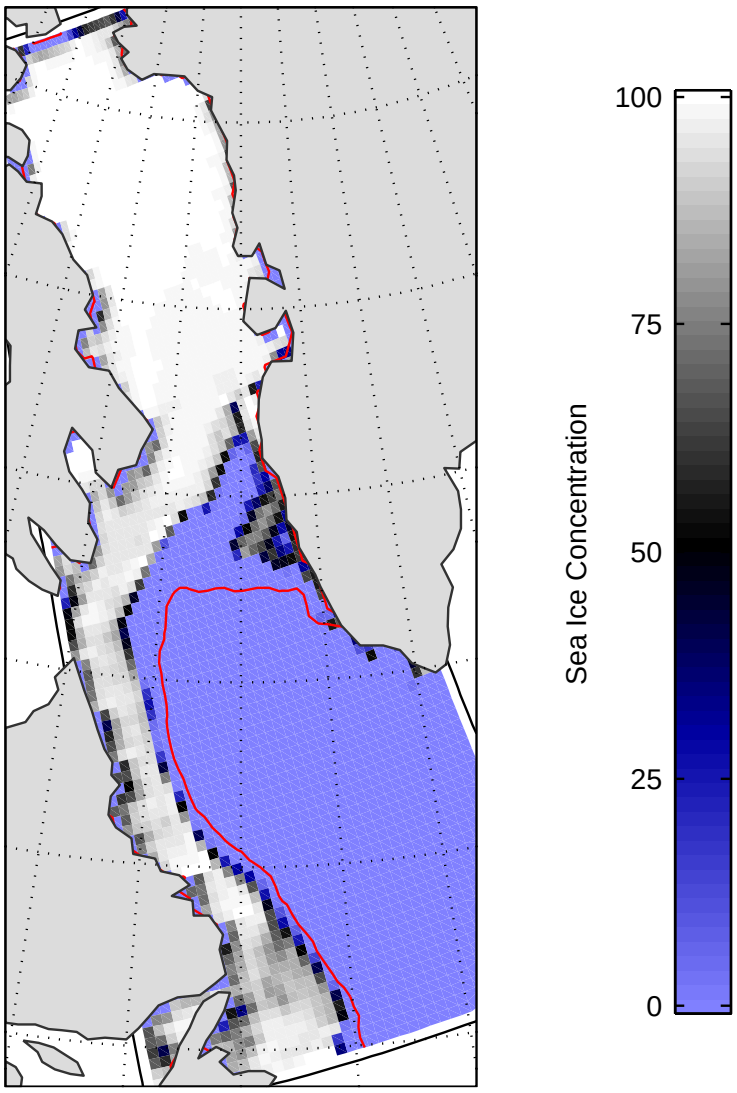

Figure 6-5: MSEM-OFF sea ice concentration during quasi-equilibrium period (week ending March 13) and observed ice edge (red line, 15% concentration cutoff). Compare ice concentration field with MSEM-ON in Figure 4-1.

NS is present despite the lack of the MSEM. One notes that it is here that one branch of the bifurcating WGC transports AW offshore (see Section 3.2.2). Further examination (not shown) reveals that the main source of ice in the wedge-shaped area the inner Greenland Shelf. Therefore, the water mass properties and lateral transport of waters on inner Greenland Shelf are confirmed to be important for sea ice in the NEC of the Labrador Sea.

Only a small fraction of sea ice advected offshelf from southwest Greenland survives on the NS - without the MSEM ocean-ice heat fluxes are large and sustained which leads to very short ice lifetimes.

MSEM-OFF vs. ON: ocean-ice transects during the sea ice quasi-equilibrium period

How does the evolution of the upper ocean and sea ice in the vicinity of the ice edge differ without the MSEM? Is the ice edge in MSEM-OFF limited by IW ventilation as it appeared to be in MSEM-ON? Does the insulating ice cover prevent convective entrainment of subsurface IW across the SI-PW?

To answer these questions, sea ice-ocean cross sections along the same two transects defined in Figures 6-1(a) and (b), are presented during the quasi-equilibrium period in Figure 6-6.

Without the MSEM, the hydrographic and sea ice states along these two transects evolve along slightly different lines when compared with MSEM-ON. The differences between the MSEM-OFF and MSEM-ON cross-sections have several common similarities. The MSEM-OFF MIZ locations are not adjacent sites of IW ventilation. On the contrary, no convective mixing with subsurface IW occurs along the entire span of the SI-PW. Moreover, the region associated with convective mixing of IW to the surface is seen to be nearly independent of MSEM. In both transects, the MIZ is found well within the SI-PW.

A small anomaly is noted in the northeastern Labrador Sea transect: an isolated region of thin ice south of the primary MIZ at 64° N. This ice is of inner Greenland Shelf-origin (referred to in the previous paragraphs) which is advected into the offshore AW from the WGC bifurcation. Net ocean surface buoyancy fluxes in the vicinity of the isolated ice are negative signifying ocean heat loss from ocean-ice heat fluxes/melting.

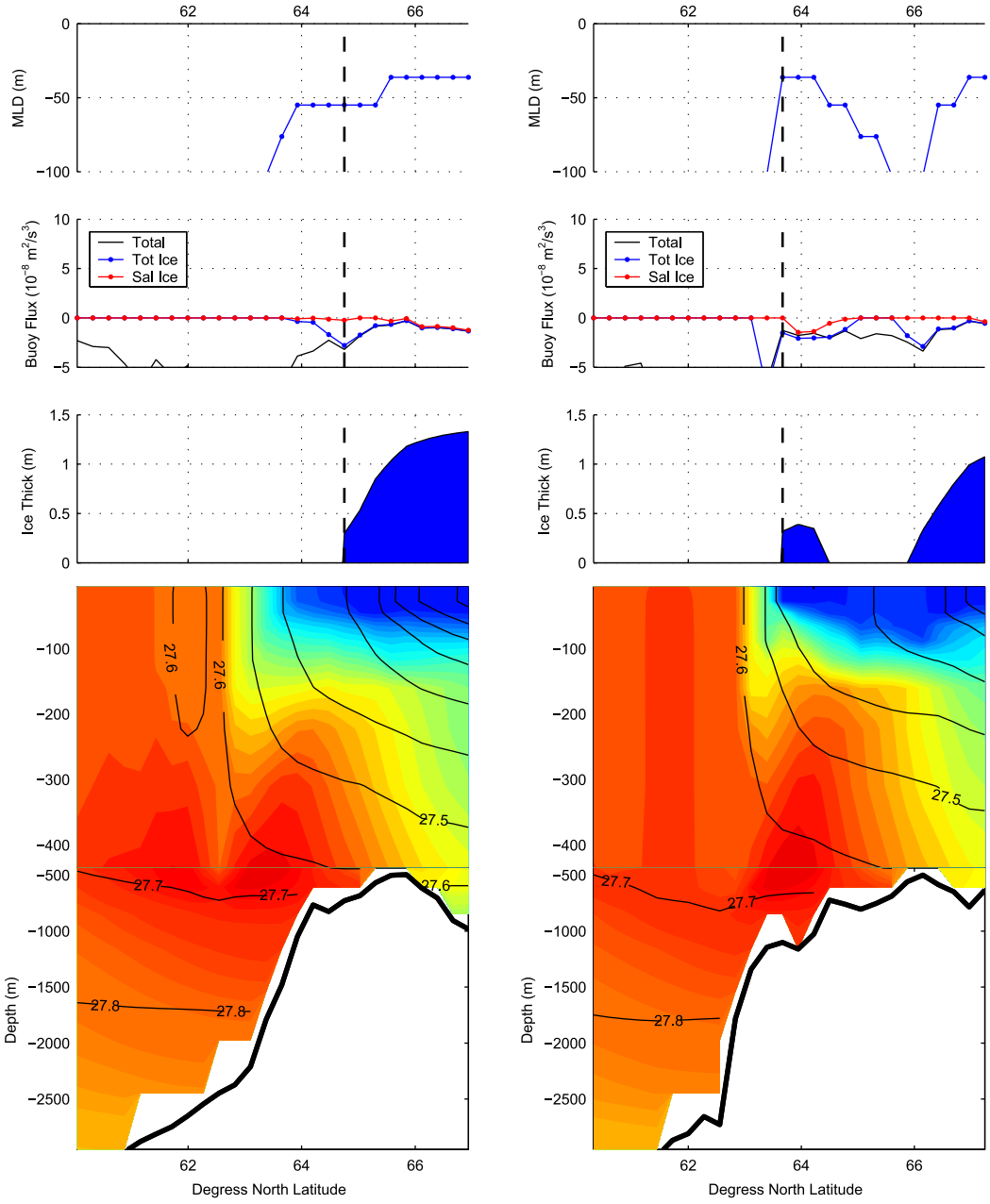

(a) Central Northern Slope transect: Week ending March 20

(b) Northeastern Northern Slope transect: Week ending March 20

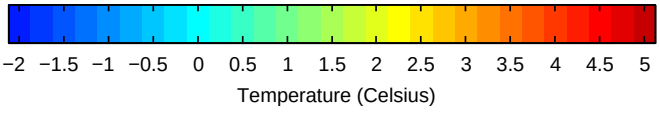

Figure 6-6 *(previous page)*: MSEM-OFF sea ice and ocean state for the week ending March 20 across transects in the central (a) and northeastern (b) Northern Slope of the Labrador Sea. The cross-sections should be compared to the equivalent cross section for MSEM-ON: a) with Figure 6-2(b) and (b) with 6-3(b). Cross-section tracks are location in the same locations as shown in Figures 6-1(a)-(b).

6.3.3 Conclusions

The results of this experiment reveal a great deal about the role of upper ocean hydrographic spatial variability and the MSEM in the development of the sea ice annual cycle and the sea ice quasi-equilibrium state in the Labrador Sea and Baffin Bay. The main findings of this experiment are:

1. The MSEM does indeed operate and is relevant for a significant amount of the seasonal ice in the Labrador Sea and Baffin Bay.
2. One may therefore identify *sea ice-preconditioned* waters: the hydrographic conditions associated with the operation of the MSEM.
3. Most of the seasonal ice cover expansion on the AW-side of the THF does not require upper ocean stratification enhancement.
4. The MSEM is essential for much of the ice cover found across the THF in the northern Labrador Sea and Labrador shelfbreak.
5. Air-sea heat losses are insufficient to trigger convective entrainment of IW beneath the sea-ice preconditioned waters.
6. The enthalpy of the sea ice-preconditioned waters is sufficient to melt the vast majority of ice advected across the front.
7. Offshore transport of AW from the WGC is identified as a possibly important source of upper ocean sea ice-preconditioning.

In the next section, the properties of waters heretofore referred to as *sea ice-preconditioned* are quantified.

6.4 Characterization of Sea Ice-Preconditioned Waters

To what extent are the hydrographic properties of waters amenable to the MSEM characterizable? Is there a well-defined signature to the SI-PW which were shown to be so

important for the maximum sea ice edge position? In this section, an attempt is made at describing the water mass properties of the SI-PW of the Northern Slope of the Labrador Sea.

The section is organized as follows. The criteria for identifying the regions in which SI-PW are found is defined first (Section 6.4.1). To determine whether the water mass properties of the SI-PW are similar on the basin scale, spatial maps of near-surface (20 m) temperature, salinity, and potential density are then shown for two periods in the annual cycle (Section 6.4.2). After confirming broad similarity in these properties, SI-PW then shown to be easily characterizable using temperature/salinity (T/S) diagrams and a heuristic criteria (Section 6.4.3).

6.4.1 Identification

The method I use for the identification of SI-PW is simple. As the sea ice concentration fields from the MSEM-OFF experiment place the MIZ along the approximate location of the THF, I tentatively identify sea-ice preconditioned waters as being near-surface (to 20 m) waters on the IW-side of the THF in the NS on which sea ice develops at some point in the sea ice annual cycle.

The THF position in the $1996 - 1997$ state estimate is defined as the southernmost extent of sea ice during the week of December 4.[3] Other criteria to identify the THF can be used. However, the use of either the early-December ice edge or the 33.25 isohaline at 15 m (the method used in Section 3.2.2) gives a nearly identical result.

6.4.2 Spatial patterns

A sense of the spatial variations in the mean upper 20 m (top two model grid cells) of the water mass properties of the sea ice-preconditioned water mass properties from the state estimate is provided in Figure 6-7.

By the week ending December 4, 1996 the seasonal thermocline has been eroded, clearly revealing the domain's distinct near-surface water mass types: IW in the central Labrador Sea ($S \geq 34.5$) and AW on the Baffin Bay and along the Labrador Shelf ($S \leq 33.25$). The SI-PW have temperatures, salinities, and potential densities of intermediate values between

[3]The reason for choosing the December 4th ice edge location is that after the ice edge reaches this location in mid-November it subsequently remains there over a period of several weeks. It is only after a prolonged period of cooling that the MSEM can advance the ice pack further.

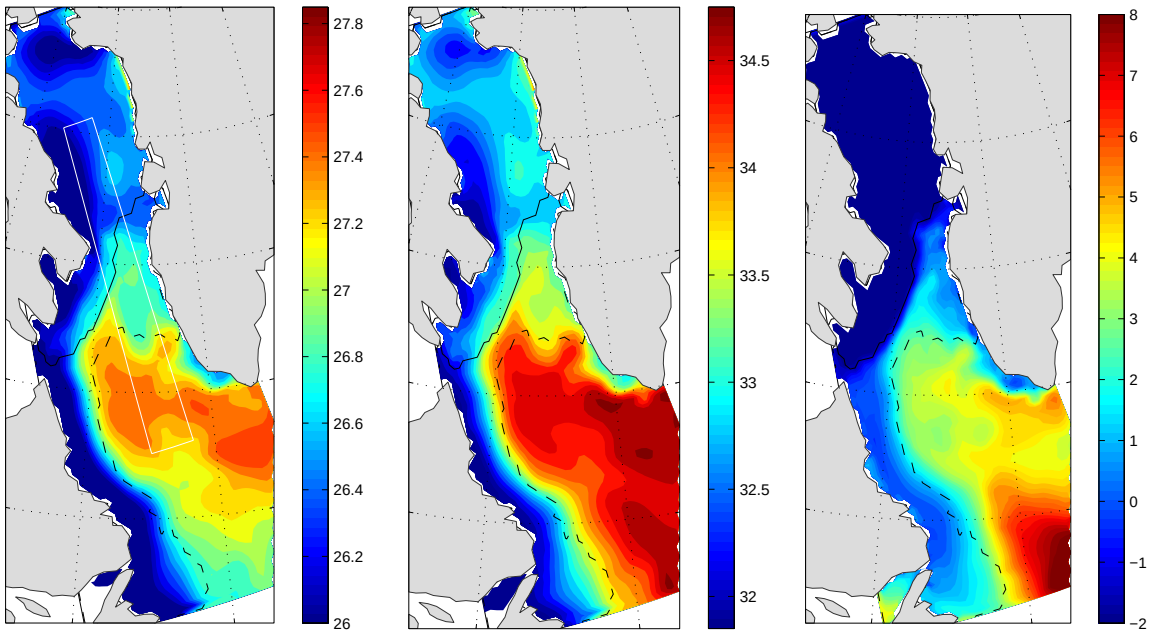

(a) Potential Density : Dec 4 (b) Salinity : Dec 4 (c) Temperature : Dec 4

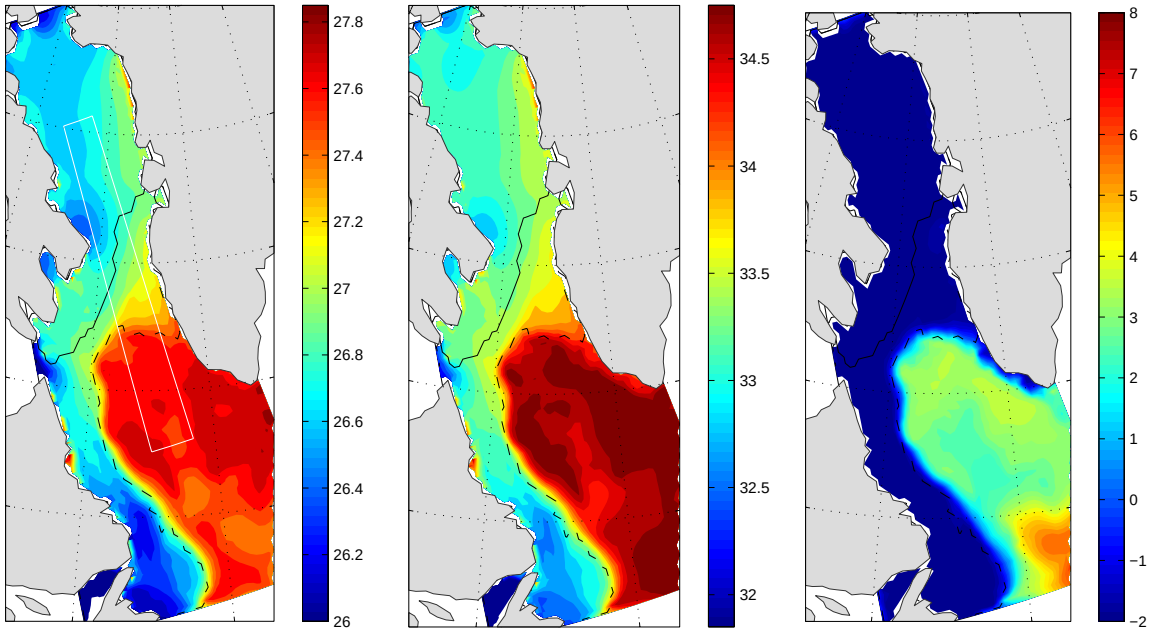

(d) Potential Density : Mar 20 (e) Salinity : Mar 20 (f) Temperature : Mar 20

Figure 6-7: Upper 20 m a) surface-referenced potential density ($\sigma_0 - 1000\,\mathrm{kg\,m^{-3}}$), b) salinity, and c) temperature (degrees Celsius) for week ending Dec 4, 1996. Panels (d-f) same as (a-c) for week ending March 20, 1997. Solid and dashed black lines denotes Dec 4 and March 20 ice edge positions, respectively. Box in (a) denotes region in which water mass properties are characterized in Figure 6-8.

the IW and AW - consistent with what was observed in the analyzed hydrographic cross-sections.

Small-scale details of the hydrographic properties of the SI-PW show spatial variations: salinities are lower to the south of Disko Island than in the vicinity of the maximum ice location on the central Northern Slope. In addition, evidence for some IW already convectively entrained into the mixed layer is noted in the western Northern Slope. Spatial heterogeneity of sea ice-preconditioned water salinity is also found during the quasi-equilibrium sea ice state.

Taken as a whole, the spatial variations of SI-PW water mass properties are small compared to the basin-scale hydrographic variations between IW and AW.

6.4.3 T/S diagrams

The temporal evolution of the weekly-mean water mass properties in the surface (upper 20 m) and subsurface (310 m) within the box defined in Figure 6-14(d) are presented as temperature and salinity (T/S) diagrams during four weeks preceding and during the sea ice quasi-equilibrium state in Figure 6-8.

The 310 m level chosen for the subsurface water mass properties corresponds to the mean depth of the $\sigma_0 = 1027.5\,\mathrm{kg\,m^{-3}}$ isopycnal - a typical outcropping isopycnal along the MIZ at the peak of the ice extent annual cycle - before the erosion of the seasonal thermocline.

T/S pairs are categorized by region within the box: the north of SI-PW region (NPW), SI-PW region (PW), and south of SI-PWregion (SPW). The criteria for identifying these regions is identical to the criteria used in the previous section: the sea ice maximum extent on the week of December 4 delineates NPW and PW regions; the never-ice-covered region within the box is (logically) designated SPW.

To provide a sense of the hydrographic evolution of water mass properties within the box, the first T/S diagram is presented for the week ending October 23.[4] The hydrographic evolution indicated by the T/S diagrams is now described and a heuristic for identifying SI-PW is introduced.

In the October 23 T/S diagram, SI-PW fall along a water mass property continuum between the near-surface waters in NPW and SPW. From north to south, all surface waters

[4]The December 4 ice edge location criteria is used to define the NPW, PW, and SPW regions to classify waters in the October 23 T/S diagram.

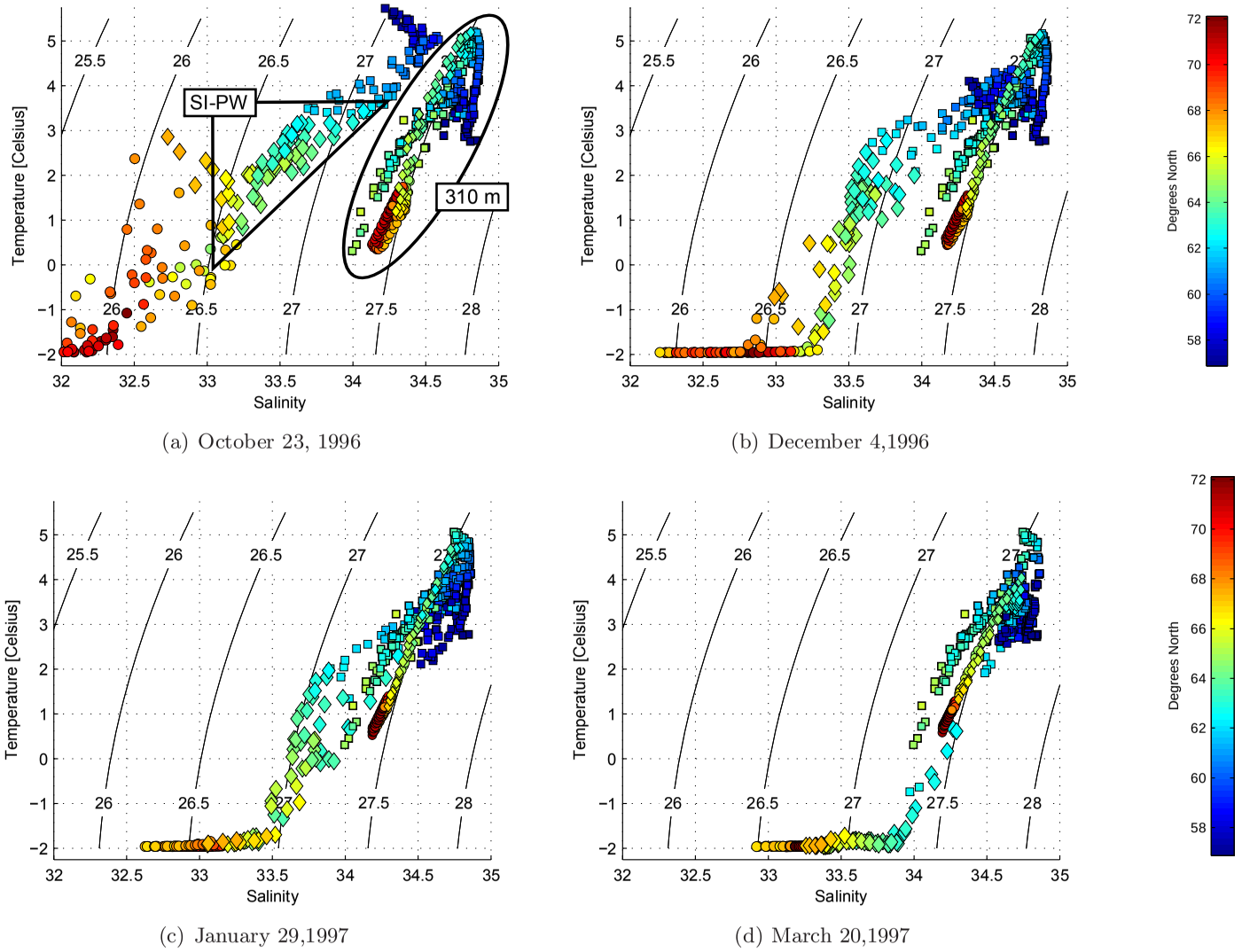

(a) October 23, 1996

(b) December 4,1996

(c) January 29,1997

(d) March 20,1997

Figure 6-8: T/S diagrams for four one-week periods: a) Oct. 23, b) Dec. 4, c) Jan. 29, and d) Mar. 20. T/S points 20 m and 310 m within the domain defined in Figure 6-14(d). Potential density ($\sigma_0 - 1000\,\mathrm{kg\,m^{-3}}$). Colors denote latitude of T/S points. Shapes identify ice-covered state: circles (NPW) ice by Dec. 4; diamonds (PW), between Dec. 4-Mar. 20; squares (SPW), never ice in 96-97 annual cycle. In (a), triangle: sea ice-preconditioned waters, oval: all subsurface waters (also smaller markers).

become warmer and saltier. At the lowest latitudes, SPW T/S points are clustered around 4.5° C and S=34.25, consistent with the values found on the spatial maps (Figure 6-7). At 310 m, the T/S range for all three regions is much narrower ($34 \leq S \leq 35$, $0° C \leq T \leq 5.25° C$) and (by construction) lie along or close to the $\sigma_0 = 1027.5\,kg\,m^{-3}$ isopycnal.

A pattern is immediately evident in the October 23 T/S diagram: the maximum density attainable by all surface NPW and PW waters with an arbitrary decrease of temperature is *less than* the density of the waters immediately beneath them at 310 m. In contrast, the densities attained by surface SPW waters upon arbitrary temperature reduction *exceed (or equal)* the density of the warm subsurface waters below.

From the MSEM-OFF experiments it was observed that the mixed layers in the SI-PW never entrained subsurface IW. However, it is possible that, given a sufficiently long period of buoyancy loss, progressive vertical entrainment with saltier waters below would eventually lead to a penetration into the IW at greater depths.

In contrast, surface waters in the SPW region need not cool by more than a few degrees before warm subsurface IW are incorporated into the mixed layer via convective entrainment.[5]

The evolution of the T/S diagrams throughout the other three periods is a demonstration of the above observations. By December 4, surface NPW waters freeze (by construction), surface PW waters cool from north to south (remaining less dense than their subsurface counterparts), and surface SPW waters begin to take on the T/S values of the waters below as they mix.

By March 20, all SPW surface and subsurface waters are narrowly clustered in T/S space. Surface NPW waters are saltier, owing perhaps to several months of thermodynamically-driven salt release. Finally, all surface T/S pairs of SI-PW are at or near freezing (by construction) while maintaining distinctly lower densities from their subsurface counterparts.

6.4.4 Conclusions

The water mass properties of SI-PW, defined as all near-surface waters (upper 20 m) on the IW-side of the THF on which sea ice eventually develops during the annual cycle, are characterizable.

[5]One should keep in mind that both the MSEM-OFF and 1-D model experiments confirm that SI-PW have enough sensible heat to resist freezing throughout winter and that it is only because of the MSEM that they eventually become ice covered.

With the aid of spatial maps of near-surface waters in early December, it was shown that the hydrographic properties of ice-preconditioned waters are broadly similar across the northern Labrador Sea.

As the temperatures, salinities, and densities of SI-PW evolve through time, their characterization is simplified with the aid of a heuristic. By considering the joint T/S properties of both surface (upper 20 m) and subsurface waters (310 m) in the northern Labrador Sea, a water parcel is identified as sea ice preconditioned by determining whether, after an arbitrary reduction in temperature, its level of neutral buoyancy is within the subsurface IW.

In the $1996-1997$ annual cycle, sea ice preconditioned waters are identified for the week ending December 4 using spatial maps of salinity as being within the range:

$$33.1 \leq \mathrm{S} \leq 34.10$$

If the heuristic method is used, the criteria of SI-PW using surface-reference potential density is within the range:

$$1026.6\,\mathrm{kg\,m^{-3}} \leq \sigma_0(\mathrm{T}{=}{-2^\circ\,\mathrm{C}},\,\mathrm{S}) \leq 1027.3\,\mathrm{kg\,m^{-3}}$$

The range of the potential density identifying SI-PW range is seen to be stable for a period of months leading up to and during the sea ice quasi-equilibrium state.

6.5 Evidence for the Reduction of Vertical Heat Fluxes due to MSEM

Until now, the positive buoyancy forcing associated with the release of sea ice meltwater in the MIZ has been claimed to increase the upper ocean stratification, reducing entrainment of sensible heat available to melt ice from below. The purpose of this section is to provide supporting evidence for this claim by drawing upon the simulated fluxes in the state estimate and the results of the MSEM-OFF experiment described in Section 6.3. The following will be demonstrated:

1. With MSEM-OFF, the depths of the mixed layer (MLD) and planetary boundary

layer (HBLD) are significantly deeper in a band delineated by the ice edge position in MSEM-OFF and the ice edge maximum of MSEM-ON.

2. Deeper MLDs are noted within the band more than 2 months before the ice edge reaches its maximum position.

3. Vertical heat fluxes into the upper ocean grid cells (UOGC), mixed layer, and planetary boundary layer are suppressed in the presence of ice; more heat is brought into the upper ocean where ice is absent in MSEM-OFF but present in MSEM-ON.

6.5.1 Shoaling of the MLD and HBL due to buoyant meltwater release

The MSEM enhances the stratification of the upper ocean - both at the point of the sea ice melt and in the immediate vicinity of the melt location. Following the melting of ice in the MIZ, meltwater can be advected seaward into the open ocean. Mixed layer and planetary boundary layer depths may be shallower where these low-salinity waters are present. A sense of how sea ice meltwater release alters MLDs and HBLDs is provided in Figure 6-9 where MLDs and HBLDs from the state estimate are compared with those from the MSEM-OFF experiment. MLDs are diagnosed using the method described in Section 4.3.2 and HBLDs are calculating as part of the KPP vertical mixing scheme of Large et al. (1994) as implemented in the MITgcm (Section 2.2.2).

The patterns of MLDs and HBLDs with MSEM-ON and MSEM-OFF add a new dimension to the interpretation of how MSEM advances the ice edge across the THF. At the week ending January 9th, the ice edges in MSEM-ON and OFF are nearly coincident. However, layer depths with MSEM-ON are shallower on either sides of the MIZ within ± 70 km. Further examination of this pattern indicates that the offshore signature of shallower layer depths begins when the ice edge reaches the THF in mid-November (See Figure 4-1) and increases over the successive weeks (not shown). Meltwater accumulates within the SI-PW over a period of weeks before the ice-edge advance across the THF. Evidently, SI-PW not only isolate the upper ocean from warm ice-melting subsurface sensible heat, but also permit meltwater to gradually accumulate offshore by inhibiting its dilution with saltier IW.

In the mid-February and mid-March panels, the reduction of layer depths in a band delineated by the ice edge position in MSEM-OFF and the ice edge maximum of MSEM-

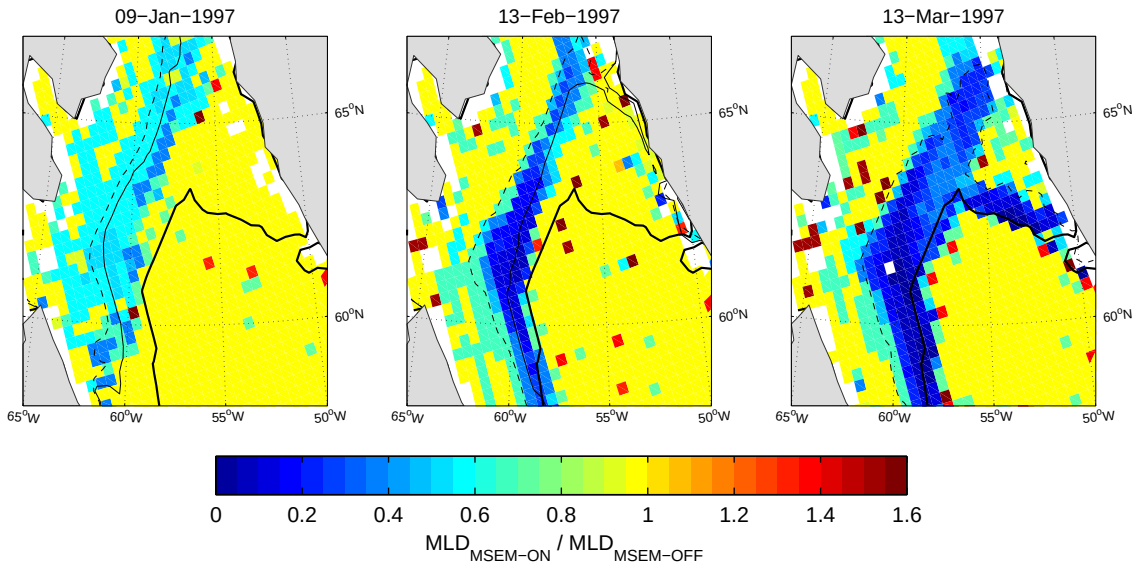

Figure 6-9: Patterns indicating role of buoyant meltwater release on model mixed layer depth (MLDs) during three one-week periods (indicated by end-of-week dates). Colors indicate $\chi = \mathrm{MLD}_{MSEM-ON}/\mathrm{MLD}_{MSEM-OFF}$. Thick black line is the ice edge at March 13, 1997. Thin solid and dashed lines indicate ice edge at the end of each week for MSEM-ON and MSEM-OFF, respectively. Where $\chi < 1$, MLDs are shallower when sea ice meltwater increases ocean buoyancy. Changes to the planetary boundary layer depth are almost identical (not shown).

ON is significant - layer depths with MSEM-ON are often $< 40\%$ of their MSEM-OFF values.

6.5.2 Modification of vertical heat fluxes

The reduction of layer depths due to ice meltwater release and lateral transport when the MSEM is operational implies a reduction of heat fluxes into the upper ocean. To illustrate this reduction, the vertical heat fluxes from the state estimate are compared with the same fluxes generated during the MSEM-OFF experiment. When comparing the magnitudes of vertical fluxes between MSEM-ON and MSEM-OFF one has several choice of the horizontal interface through which the fluxes occur. In this section, fluxes through through the bases of the UOGC, HBL, and ML are shown for three one-week periods in Figure 6-10.

Regardless of the flux interface, a significant increase of vertical flux is indicated in the MSEM-OFF experiment. Spatially, the patterns indicate major differences in a band confined to the areas where ice is present in MSEM-ON but absent in MSEM-OFF. The magnitudes of these fluxes are of the same order as the air-sea heat fluxes (not shown).

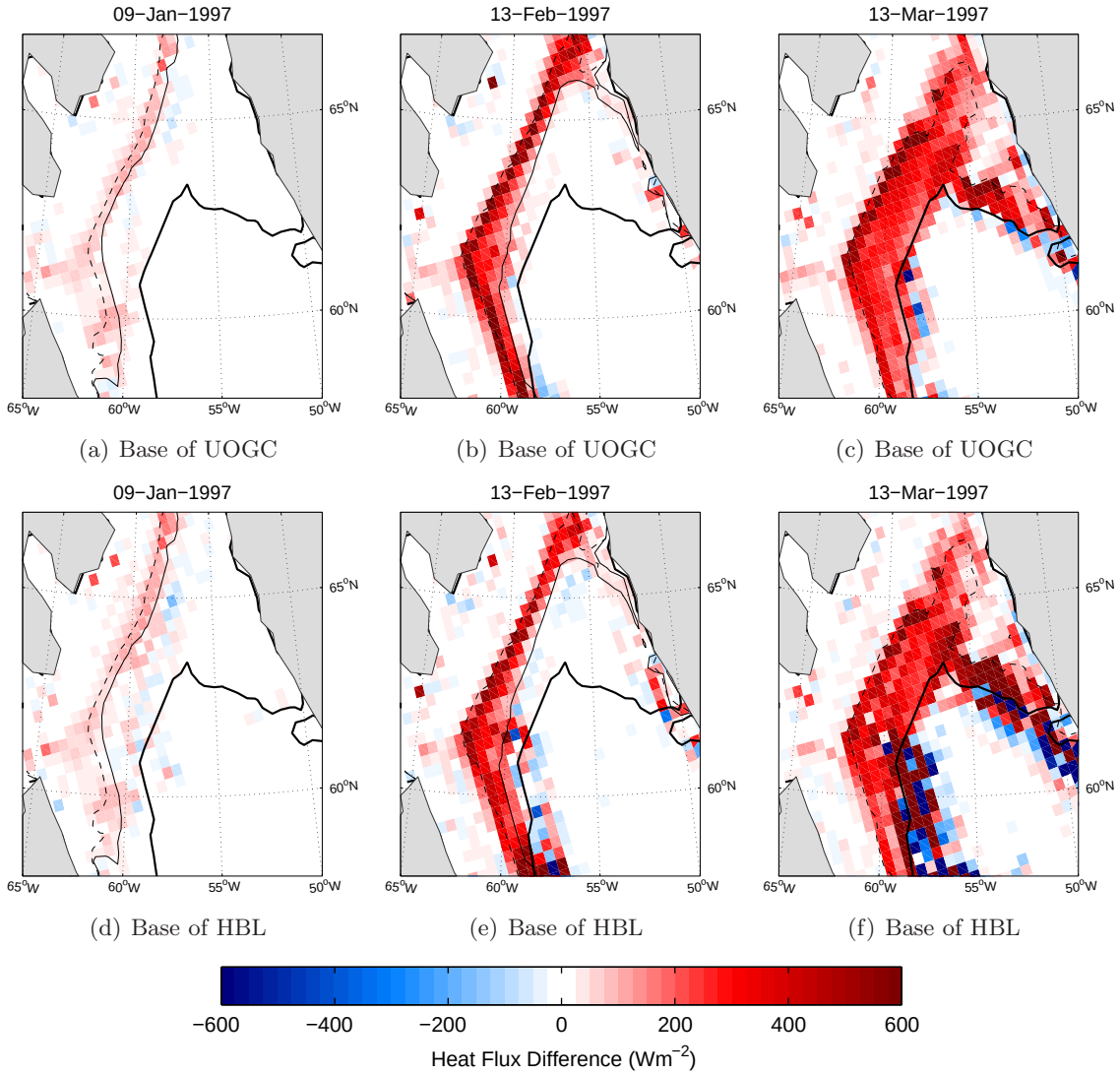

(a) Base of UOGC (b) Base of UOGC (c) Base of UOGC

(d) Base of HBL (e) Base of HBL (f) Base of HBL

Figure 6-10: Difference of vertical heat fluxes between MSEM-OFF and MSEM-ON through several interfaces during three one-week periods (indicated by end-of-week dates): (a-c) the lower boundary of the upper ocean grid cell (UOGC) and (d-f) planetary boundary layer (HBL). Vertical heat flux differences through the base of the mixed layer is nearly identical to those through the planetary boundary layer. Thethick black line denotes the March 13 ice edge. The thin solid and dashed lines show the ice edge at the end of each week for MSEM-ON and MSEM-OFF, respectively.

These plots clearly demonstrate that the MSEM serves to isolate the upper ocean from subsurface heat, even if the subsurface heat is only that which is found in the SI-PW and not the still-warmer IW found at greater depths.

Vertical profiles of heat fluxes

To further illustrate the effect of the MSEM on the modification of vertical fluxes into the upper ocean, a single location is chosen for the analysis of the heat flux vertical structure. The location chosen, shown in Figure 6-11, is useful to examine because 1) it remains ice-free during the entire MSEM-OFF simulation but is ice covered during MSEM-ON, 2) it is proximate to the MSEM-OFF MIZ in the NS (very nearly along the THF), 3) it is subject to a long period of meltwater accumulation during the period of mid-November to early February from when the MSEM-ON ice edge resides along the THF.

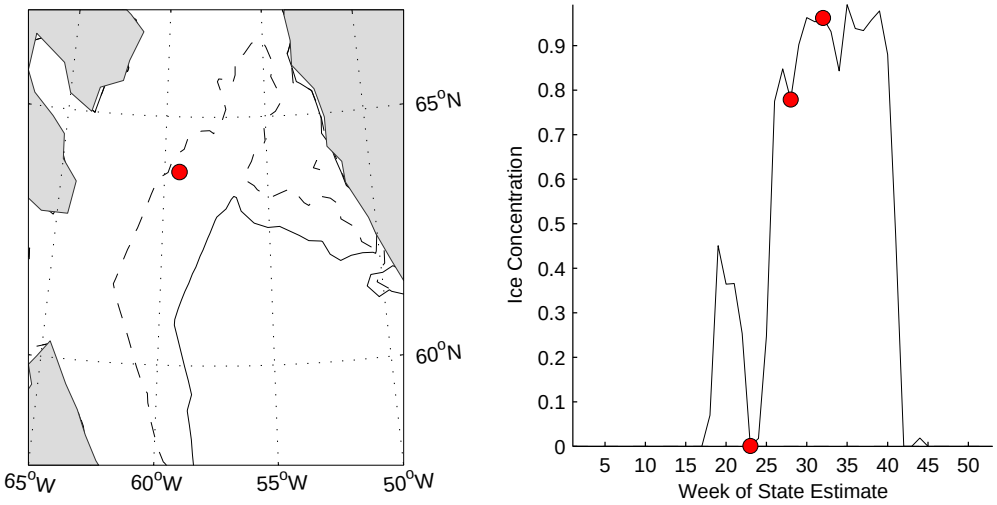

(a) Vertical Profile Location

(b) Location Ice Concentration

Figure 6-11: a) Location of the site chosen for the analysis of the vertical structure of vertical heat fluxes. b) Time history of the sea ice concentration during MSEM-ON at the location of (a). No sea ice is present during the course of the simulation at (a) during the MSEM-OFF experiment. The three points denoted by red circles in (b) mark the analysis periods and are identical to those used in Figures 6-9 and 6-10, the weeks ending January 9, February 13, and March 13. Dashed and solid lines denote the March 13 ice edge location for MSEM-OFF and MSEM-ON, respectively. Importantly, no ice is present at the location in either experiment during the first analyzed week.

The chosen site is not particularly special - other sites satisfying the above criteria reveal essentially the same patterns. The vertical structure of the fluxes, temperature, salinity,

and potential density are shown in Figure 6-12.

The effect of the positive buoyancy forcing associated with ice meltwater release is evident during each of the three one-week periods. In the earliest, the hydrographic differences reveal the effect of the meltwater accumulation: a decrease of upper ocean salinity, enhanced stratification, and lower near-surface temperatures and potential density. That these differences are largely confined to the upper 100 m is not surprising given that, even in the MSEM-OFF experiment, this site is well within the SI-PW region. With respect to the heat fluxes through the various interfaces, the enhanced stratification is associated with a reduction of $\sim 100\,\mathrm{W\,m^{-2}}$ at the bases of the ML and HBL.

As meltwater accumulates through the rest of January, the near-surface waters freshen allowing temperatures to fall without triggering convective overturning. By February 13, sea ice advected into the location in MSEM-ON is able to become established owing to the near complete suppression of turbulent ocean-ice heat fluxes. Conversely, in MSEM-OFF, surface buoyancy losses drive a deepening of the mixed and planetary boundary layers.

Little change is noted in the hydrographic structure of MSEM-ON during the following month save a slight freshening and cooling of the upper 100 m. In addition, the consolidation of the ice cover over the location inhibits nearly all atmospheric heat/buoyancy loss which keeps the upper ocean hydrostatically stable. Hydrostatically stable near-surface waters suppress convective overturning and its associated vertical transport of heat within the column below. The sustained accumulation of meltwater further enhances stratification which drives the HBL and ML towards their shallowest permissible values in the model. As expected, the ML continues to deepen in the MSEM-OFF experiment and large vertical fluxes persist throughout the upper 150 m.

6.5.3 Conclusions

Consistent with the expectations of earlier sections, the enhancement of vertical stratification from the release of sea ice meltwater suppresses vertical heat fluxes. Shoaling of the mixed and planetary boundary layers offshore of the MIZ occurs several weeks before the advancement of ice across the THF. The modification of vertical fluxes and mixed and planetary boundary layer depth is mainly confined to the SI-PW on the IW-side of the THF.

In the state estimate, the vertical fluxes found at the base of these layers were almost

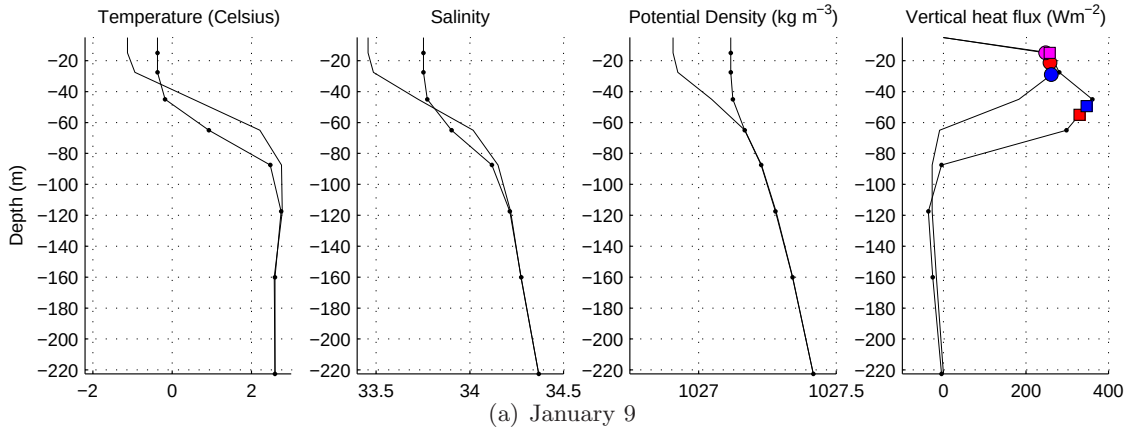

(a) January 9

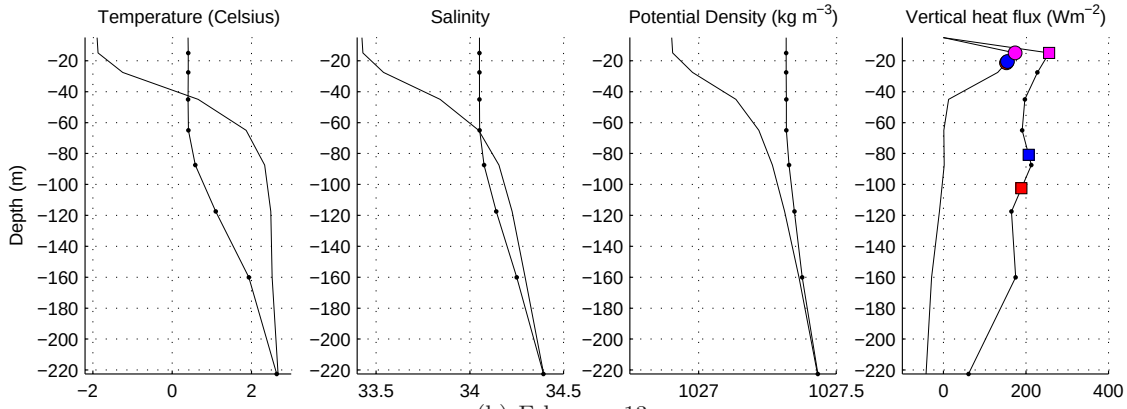

(b) February 13

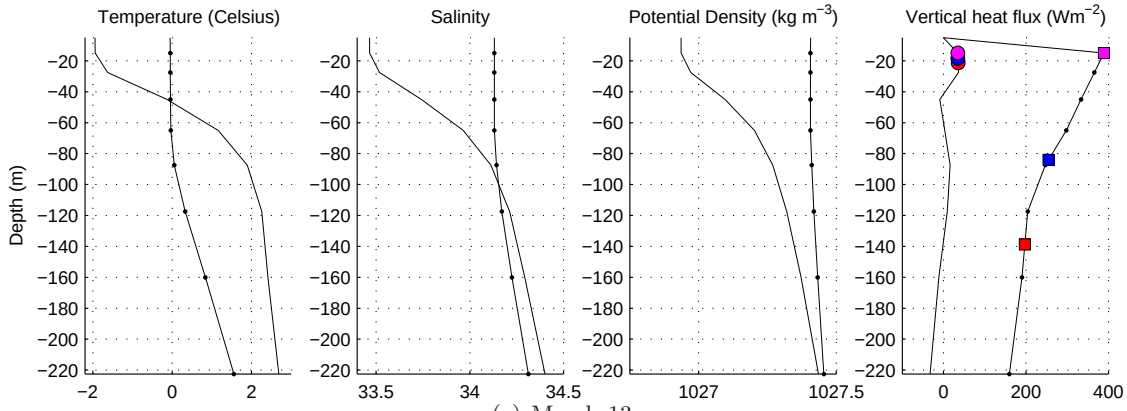

(c) March 13

Figure 6-12: Vertical profiles of hydrography (T, S, and surface-referenced potential density) and vertical heat fluxes for three one-week periods (indicated by end-of-week dates) for the MSEM-OFF (dotted line) and MSEM-ON (solid line). Markers along the vertical heat flux profile are placed at the location of the base of the upper ocean grid cell (magenta), planetary boundary layer (blue), and mixed layer (red) for MSEM-ON (circles) and MSEM-OFF (squares).

always dominated by parameterized convective fluxes. Advective fluxes were proportionally insignificant and fluxes with the Gent-McWilliams-Redi (GM-Redi) parameterization were tapered to zero due steep isopycnal slopes. The tapering of the GM-Redi fluxes suggests that the details of these upper ocean vertical heat fluxes may be quite different in reality than in the model. Determining exactly how they would be different is an important open question.

An unexpected finding of this analysis is that the SI-PW appear to precondition for ice in an additional way: meltwater released into the SI-PW is able to accumulate and spread over a period of weeks as the ice edge remains along the THF. The anomalous stratification found in SI-PW inhibits the dilution of the meltwater with the much saltier subsurface IW. As meltwater is distributed and accumulates in the SI-PW region, seawater temperatures approach the freezing point faster given the same air-heat heat loss.

6.6 Lateral Eddy Heat Transport and the Ice Edge Progression

In Section 5.5.2, the decomposition of advective heat fluxes into the upper ocean in the presence of sea ice during the sea ice quasi-equilibrium period indicated that basal fluxes were proportionally more important than lateral fluxes. Excluding the basin's western ice edge, where lateral and basal fluxes are comparable in the state estimate, behind the MIZ and in the northeast corner of the Labrador Sea, lateral heat fluxes appear to be relatively unimportant. However, the proportion of lateral to basal heat fluxes in ice-covered areas inferred from the state estimate may be biased due to unresolved eddy transport in the model. In reality, there may be areas where lateral eddy heat transports may be as large or larger than basal transports. This short section reviews this issue with the goal of clarifying the expected contribution of eddy heat transport to the ice-covered part of the domain in the real ocean. Emphasis is placed on the expected role of eddy transports during the period of ice edge advancement across the THF and the maintenance of the ice edge during the quasi-equilibrium period.

6.6.1 Estimating the magnitude of lateral eddy transport

The time-tendency of upper ocean potential temperature, T_o, from advection can be decomposed into basal and lateral components,

$$\left(\frac{\partial T_o}{\partial t}\right)_{ocean} = \left(\frac{\partial T_o}{\partial t}\right)_{lateral} + \left(\frac{\partial T_o}{\partial t}\right)_{basal} = \kappa \nabla^2 T_o + \vec{u} \cdot \nabla T_o + \left(\frac{\partial T_o}{\partial t}\right)_{basal} \tag{6.1}$$

Lateral transports are represented in Eq. 6.1 as a combination of a diffusion and advection with κ serving as the lateral eddy mixing coefficient.

Although the numerical model includes a Fickian tracer diffusivity to partially parameterize subgrid scale lateral eddy mixing (See Section 2.2.2), the magnitude of the eddy mixing coefficient is much smaller ($50\,\mathrm{m^2\,s^{-1}}$) than estimates of eddy mixing coefficients in eddy-rich regions ($\sim 1000\,\mathrm{m^2\,s^{-1}}$). The relative importance of missing lateral eddy transports can be estimated by determining the κ required for the lateral eddy and basal transport terms of Eq. 6.1 to be of the same order, the requisite κ or κ_{req}. If the magnitude of κ_{req} is modest, the state estimates partitioning is likely biased. On the other hand, if κ_{req} is larger than the κ appropriate for the region, the state estimate's partitioning bias is probably not severe.

The κ appropriate for the central Labrador Sea based on data from acoustically-tracked floats, Argo float displacements, current meter mooring data, and altimetric eddy kinetic energy (EKE) has been estimated between 721 and $1395\,\mathrm{m^2\,s^{-1}}$ (Funk et al. 2009). In the northern Labrador Sea, where wintertime EKE can be significantly larger than the central part of the basin, a larger κ is expected. A relationship between κ and EKE can be expressed - following Sallee et al. (2008),

$$\kappa = \alpha \sqrt{EKE}\, L_d \tag{6.2}$$

Where α is a empirical factor of order one and L_d is the first baroclinic Rossby radius.

The maximum physically-realizable value of κ, κ_{max}, can be estimated with appropriate estimates of EKE and L_d. Brandt et al. (2004) found EKE values of $\sim 800\,\mathrm{cm^2\,s^{-2}}$ in the northern Labrador Sea near the WGC bifurcation (coinciding with the region's temporal and spatial EKE maximum) during the winter of 1997 from altimeter data. Funk et al. (2009) estimated L_d from Argo data and an ocean climatology to be $\sim 8.8\,\mathrm{km}$. Combining these two values (and assuming $\alpha = 1$) in Eq. 6.2 yields $\kappa_{max} \sim 2500\,\mathrm{m^2\,s^{-1}}$. Missing eddy

transport probably contributes to a bias in the state estimate where lateral eddy and basal transports are of the same order when $\kappa_{req} \leq \kappa_{max}$.

6.6.2 The temporal and spatial variability of lateral transport

The relative importance of lateral heat transport is likely a function of space and time. Far behind the MIZ, upper ocean temperatures are close to the freezing point with little horizontal variation and basal heat fluxes are quite small ($< 50\,\mathrm{W\,m^{-2}}$). Compared to the rest of the ice-covered ocean, both basal heat fluxes and $\nabla^2 T_o$ are largest in the vicinity of the ice edge. The progression of the ice edge therefore implies a large-scale modification of the patterns of basal fluxes and $\nabla^2 T_o$.

To determine whether missing lateral heat transport is important during the evolution of the quasi-equilibrium ice edge position, one must track κ_{req} through time during the weeks preceding the wintertime ice extent maximum. Similarly, to determine whether missing eddy transports are important for the maintenance of the ice edge during quasi-equilibrium, one need only consider κ_{req} during that period.

Much is known about upper ocean hydrographic changes during the period of ice advance from the state estimate. Reflection on the development of the upper ocean hydrography can inform expectations and enhance understanding of the patterns of κ_{req}. First, the advancement of ice across the SI-PW is associated with a progressive cooling of the upper ocean due the large air-sea heat fluxes and the isolation of the upper ocean from the subsurface thermal reservoir. Even before the intrusion of ice, temperatures within the SI-PW fall dramatically; by the end of January, SI-PW temperatures are within $1 - 2^{\circ}\,\mathrm{C}$ of the model freezing point (See Figure 6-3). The release of buoyant ice meltwater progressively increases off-ice edge stratification, enhancing seawater temperature reduction for a given quantity of atmospheric heat loss. Consequently, during the ice edge advance, horizontal temperature variations near the ice edge tend to be small. Upon encountering the seaward edge of the SI-PW and the ventilating IW, $\nabla^2 T_o$ dramatically increases.

From the above, one expects the following. Along the MIZ, κ_{req} will be smaller during the quasi-equilibrium period than during the weeks of ice edge advance owing to the anticipated increase of $\nabla^2 T_o$ at the seaward edge of the SI-PW. Behind the MIZ, basal fluxes are weak and upper ocean temperatures have little horizontal variability. These two factors affect κ_{req} in opposite directions: the magnitude of κ_{req} will be lower where basal fluxes

are weak and higher in regions of little horizontal temperature variability. A lower κ_{req} is also expected in the MIZ wherever ice meltwater stratification enhancement is particularly effective at suppressing basal fluxes.

6.6.3 Requisite κ

To calculate κ_{req}, the eddy mixing (diffusion) and basal flux terms from the RHS of Eq. 6.1 are equated and solved for κ using values of $(\partial_t T_o)_{basal}$ and $\nabla^2 T_o$ from the state estimate for nine one-week intervals preceding and during the sea ice quasi-equilibrium period. The spatial and temporal variability patterns of κ_{req} are shown in non-dimensionalized form as $\log_{10}(\kappa_{req}/\kappa_{max})$ in Figure 6-13.

6.6.4 Interpretation of the patterns of κ_{req}

Several observations are made.

1. During the development of the quasi-equilibrium ice edge position in the northeast Labrador Sea, most κ_{req} is generally much larger than κ_{max}. An exception is noted during the first week of February where basal fluxes in the MIZ are temporarily suppressed in the progressively well-stratified upper ocean due to the sustained release and offshore transport of buoyant sea ice meltwater. During this week, even very small values of κ are sufficient to match the low basal heat fluxes.

2. Once the quasi-equilibrium ice edge position is established (first south of 61° N and on the NS after March 6), κ_{req} falls below κ_{max} along the entire length of the MIZ.

3. Basal ice fluxes on the IW-side of the THF remain large and positive behind the MIZ for several weeks after becoming partially ice covered. No reasonable κ can increase lateral fluxes to the same level as basal fluxes due to the near-uniform upper ocean temperatures beneath the ice.

6.6.5 Conclusions

The above analysis indicates that missing lateral ocean eddy heat transport is probably not crucial during the progression of the ice edge across the THF to its wintertime maximum position. However, once the MIZ reaches the edge of the SI-PW, $\nabla^2 T_o$ increases sufficiently

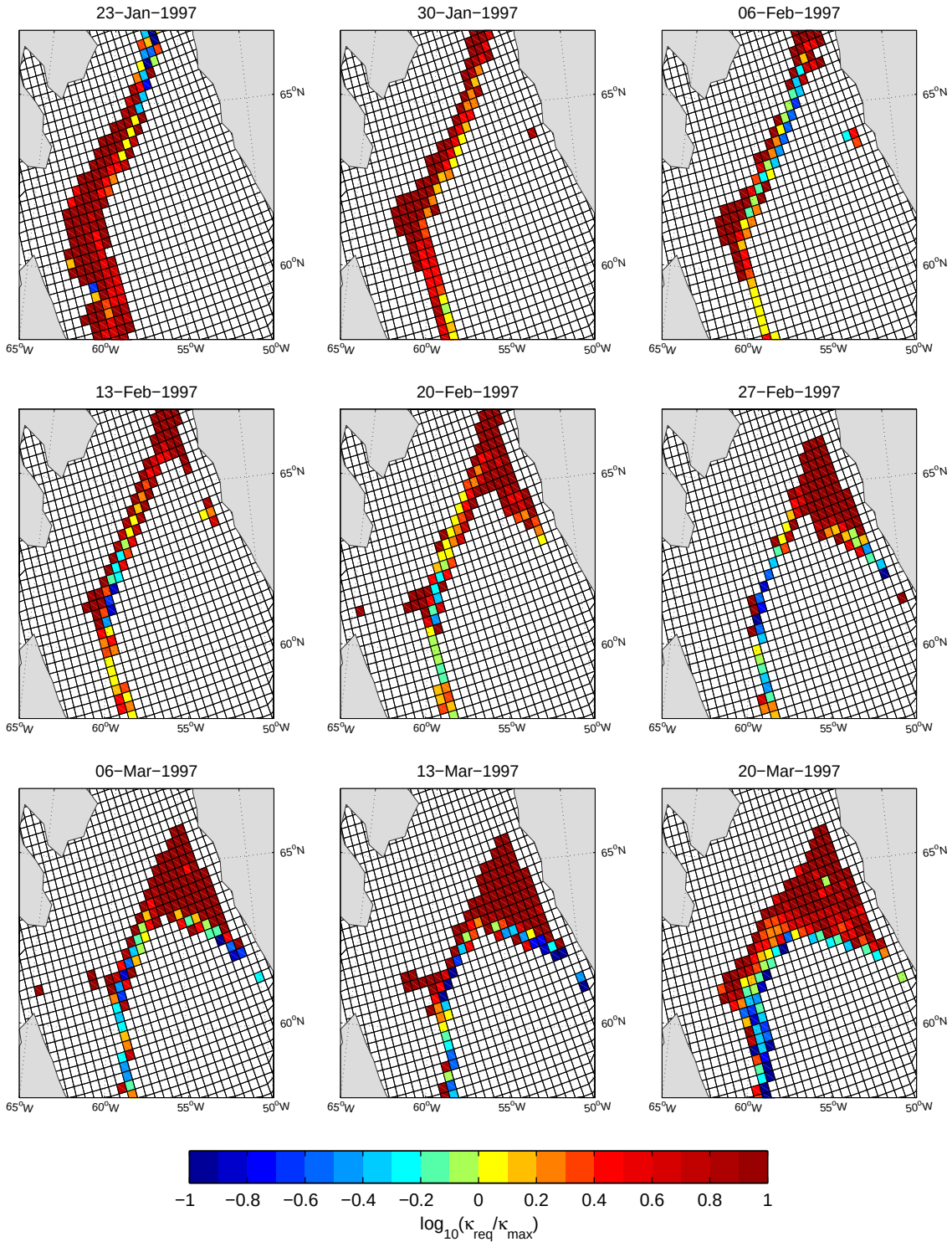

Figure 6-13: Maps of κ_{req} normalized by κ_{max} during nine one-week periods (indicated by end-of-week dates) in model grid cells with nonzero ice concentrations. Shown is $\chi = \log_{10}(\kappa_{req}/\kappa_{max})$. Where $\chi > 0$, unphysically large values of κ are required for lateral and basal heat fluxes to be comparable. Where $\chi \leq 0$, the state estimate's partitioning of basal to lateral heat fluxes may be biased. Only model grid cells with ice concentrations below 90% are shown; generally, $\kappa_{req} \gg \kappa_{max}$ beneath ice of higher concentration.

such that physically-realizable values of κ can bring lateral and basal fluxes to the same order of magnitude. Therefore, the general picture of the process described in this chapter by which the ice edge crosses the THF is not expected to be invalidated with models which explicitly resolve eddies and their associated transports. On the other hand, the state estimate's partitioning of basal and lateral ocean heat transport to the ice-covered regions of the ocean during the quasi-equilibrium period is likely biased - lateral eddy transport is probably more important in the northern Labrador Sea than indicated by the state estimate. To properly quantify the partitioning of these two ocean heat transport components, a state estimate must be generated using a model of much higher spatial resolution.

6.7 Chapter Summary

In this chapter, several links between spatial and temporal hydrographic variability and sea ice variability in the sea ice annual cycle were revealed. The key finding of the chapter is that, under the proper hydrographic conditions, the progression of the wind-driven sea ice pack across the THF in the northern Labrador Sea is self-perpetuating via a positive feedback, the MSEM.

The efficacy of the MSEM in advancing the ice pack is limited to waters which are not actively mixing with warm salty subsurface IW. Why the MSEM would become ineffective in these circumstances remains unclear - especially since the positive surface buoyancy from meltwater release is greatest when the ice edge is rapidly melting in these warmer waters. The most likely reason is dilution: the ventilated IW are so much saltier than the meltwater that, for typical meltwater release rates, the reduction of near-surface densities is too weak to meaningfully enhance the near-surface stratification.

Waters on the IW-side of THF that are slow to entrain subsurface IW via convection into the mixed layer because of anomalous low salinities are designated *sea ice-preconditioned* (SI-PW). On the basin scale, the location of the MIZ is closely correlated with the spatial distribution of SI-PW. The origin of the SI-PW is not taken up in this thesis.

The examination of the distribution of T/S water mass properties in the near surface (20 m) and at depth (310 m) in the Labrador Sea and Baffin Bay reveals a heuristic to identify SI-PW: SI-PW satisfy the following,

1. SI-PW are near-surface anomalies, above $\sim 100\,\mathrm{m}$

2. Sea ice development over SI-PW requires lateral ice transport
3. SI-PW remain more buoyant than the warm salty IW they overlay upon arbitrary temperature reduction.

This heuristic should not be taken to mean that convective mixed layer deepening into IW is impossible in SI-PW - sustained buoyancy loss and progressive convective entrainment could easily cause mixed layer densities to achieve the same levels as the subsurface IW - only that the rate at which mixed layer deepening occurs is significantly reduced due to its anomalously low initial salinity.

The positive buoyancy forcing associated with ice meltwater release into the SI-PW was shown significantly reduce the depths of the ocean mixed and planetary boundary layers. The reduction of these layer depths was noted on the IW-side of the THF well before the advance of ice. This finding raises the possibility of another important feature of SI-PW - they enhance the effect of meltwater release by permitting their gradual *accumulation* ahead of the MIZ by preventing their dilution with the significantly saltier IW.

Vertical heat fluxes in the upper ocean (be it the uppermost ocean model grid cell, or the mixed and planetary boundary layers) were shown to be suppressed with the addition of meltwater and the subsequent development of ice cover. An important caveat to the above is that vertical heat fluxes from the Gent-McWilliams-Redi parameterization are tapered to or near zero at the base of these layers.

A potential bias in the relative importance of lateral heat fluxes to the MIZ by unresolved mesoscale eddies was investigated. It was shown missing lateral heat transport by eddies is probably more important in the maintenance of the sea ice edge in the quasi-equilibrium ice period than during the period of ice advance across the THF. The misrepresentation of both vertical and lateral heat fluxes in the model raises serious questions about the details of ocean heat transport to the MIZ in the real ocean.

Based on the above, the question arises - is there an analogue between SI-PW as realized in the $1996-1997$ annual cycle and other years? Analysis of the other two state estimates $1992-1993$ and $2003-2004$ reveals that sea ice cover variability across the THF is indeed limited to first-order by the distribution of SI-PW. A sense of the spatial distribution of the SI-PW in each state estimate is provided in Figure 6-14. The connection between SI-PW and the maximum seasonal ice edge location appears to be robust.

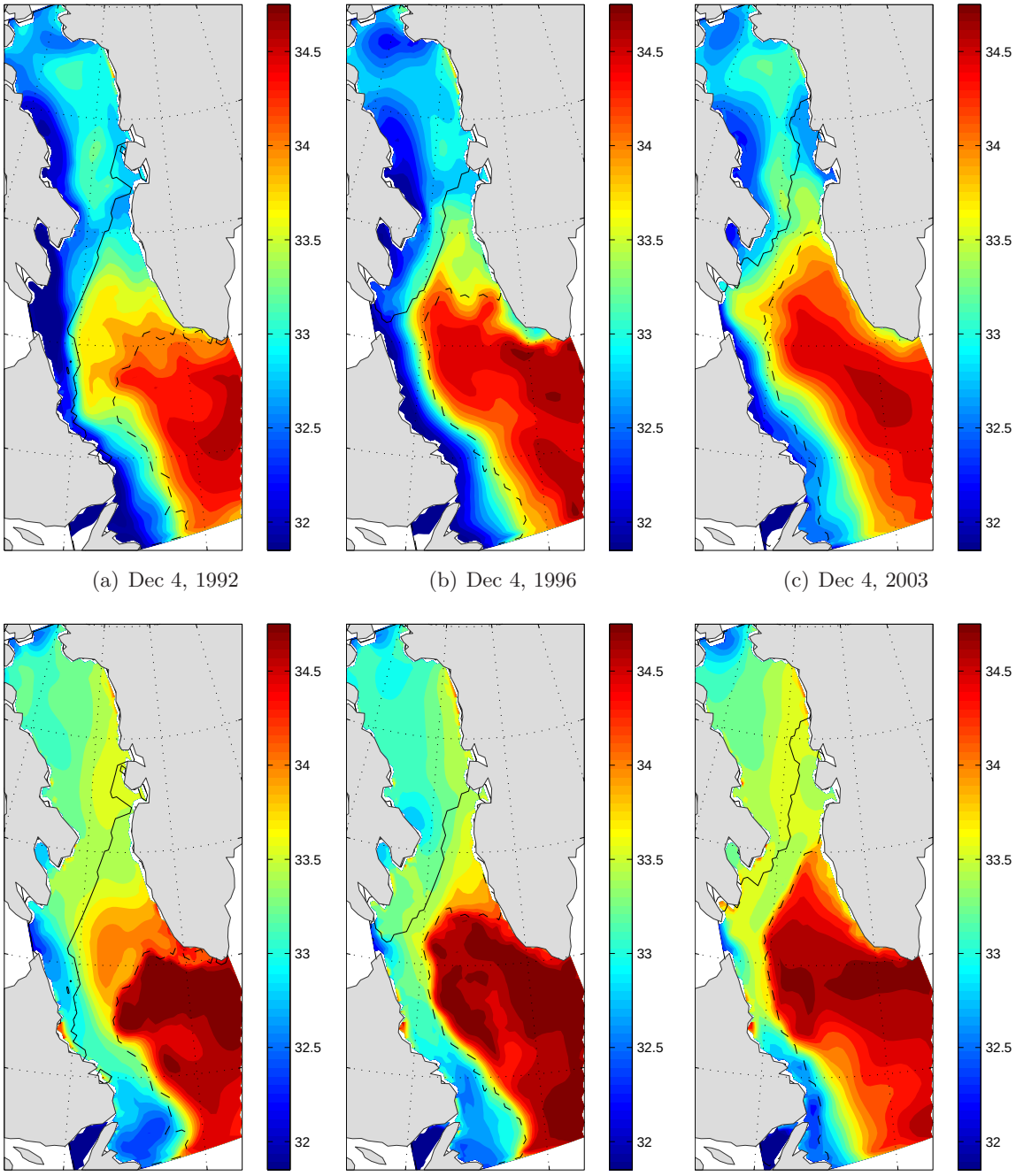

(a) Dec 4, 1992 (b) Dec 4, 1996 (c) Dec 4, 2003

(d) March 20, 1993 (e) March 20, 1997 (f) March 20, 2004

Figure 6-14: Near surface (20 m) salinity for each of the three one-year state estimates December 4, a) 1992, b) 1996, c) 2003 and March 20, d) 1993, e) 1997, f) 2004. Solid and dashed black lines denote the Dec 4 and March 20 ice edge positions, respectively. The pack ice advances across the Thermohaline Front (identifiable by the December 4th ice edge) and is ultimately arrested upon reaching the end of the SI-PW - identified by the S≈34 isohaline in December. Waters with S > 34 are in communication with subsurface Irminger Waters via convectively-driven mixed layer entrainment. Note that the distribution and interannual variability of SI-PW approximately follows the envelope between the Dec 4 and March 19 ice edge locations.

Chapter 7

Conclusions and Future Work

7.1 Restatement of Motivation

To explain the large annual and interannual variability of seasonal sea ice in the Labrador Sea and Baffin Bay, several competing hypotheses have been proposed. While it is rational to postulate underlying oceanic and atmospheric causes, the refutation of these hypotheses - and therefore the advancement of knowledge - is hampered by an incomplete understanding of the ocean state in and around the regions of observed sea ice variability. Without a more detailed picture of the dynamical evolution of the coupled sea ice-ocean system, many of the outstanding hypotheses are untestable and therefore irrefutable.

To advance the state of knowledge with respect to the sea ice annual cycle, I formulated the following primary goal of the thesis:

- Elucidate the ocean's role in setting the variability of seasonal sea ice in the Labrador Sea and Baffin Bay on annual and interannual time scales.

The approach taken to achieve this goal was to create dynamically-consistent three-dimensional time-varying state estimates of the ocean-sea ice system. To generate these reconstructions, I synthesized a suite of *in situ* and satellite-based hydrographic and sea ice data with a modern coupled sea ice-ocean general circulation model using the adjoint method.

Over the past several decades, the number of *in situ* and satellite-based observations of the ocean has significantly increased. In parallel, technical advances have made possible, even routine, the synthesis of ocean measurements with time-varying three-dimensional

ocean general circulation models. However, because the feasibility of synthesizing observations of sea ice with a *coupled* sea ice-ocean model using the adjoint method had yet to be demonstrated, I formulated a secondary thesis goal:

- Demonstrate the feasibility of the adjoint method to simultaneously synthesize sea ice and ocean observations into a dynamic coupled numerical model.

The achievement of the primary goal was made possible with the achievement of the secondary goal. With a sea ice-ocean state estimate the dynamical evolution of the coupled sea ice-ocean system can be analyzed in ways which are simply not possible with a unconstrained model or observations alone.

Based on considerations of data abundance and specific details of the sea ice annual cycle, I decided to generate three one-year state estimates. All three estimates fall within the modern sea ice satellite-era (1979-present) and overlap with the ECCO state estimation period (1992-present). These years are:

- $1992 - 1993$: An unusual year with one of most expansive maximum seasonal ice extents but with few *in situ* hydrographic data.
- $1996 - 1997$: A more "typical" year with respect to the patterns of the seasonal sea ice annual cycle with by far the greatest number of *in situ* hydrographic data.
- $2003 - 2004$: An unusual year with one of least expansive maximum seasonal ice extents but with few *in situ* hydrographic data.

The analysis presented in this thesis focuses on the reconstruction of the $1996 - 1997$ annual cycle because of its abundance of data and "typical" patterns of sea ice cover. The same analyses were conducted for each state estimate. The key findings of the thesis were found to pertain to each.

7.2 Thesis Summary and Key Findings

Chapter 1 introduces the global context of seasonal sea ice variability on annual and interannual time scales in the Labrador Sea and Baffin Bay. A review is made of the competing atmosphere and ocean-centric theories with an emphasis on theories of interannual sea ice variability. To understand the requirements for numerical modeling of the sea ice-ocean

system in the region, a thorough review of the literature concerning the simulation of sea ice in the Labrador Sea and Baffin Bay is included.

Chapter 2 provides the technical basis for the generation of the ocean-sea ice state estimate. The ocean model, a 32 km regional configuration of the MITgcm, and the coupled thermodynamic/dynamic sea ice model are described with the choice of initial, atmospheric, and open boundary conditions. The various sea ice and ocean observations and their uncertainties and the model control variables are then introduced.

Chapter 3 reviews the annual sea ice cycle in the Labrador Sea and Baffin Bay in detail. The climatology of the ocean and atmosphere in the region are described along with speculation on the various roles of ocean-ice and ice-atmosphere interactions in the development of the seasonal cycle.

Chapter 4 demonstrates the achievement of the secondary goal, the successful synthesis of sea ice and ocean observations into a coupled ocean-ice model. Evidence of the state estimate's consistency with respect to several measures of the ice and ocean states is presented.

The survey of the state estimate consistency is summarized as follows:

- Sea ice concentration data are successfully synthesized with the model.
- The annual cycle of sea ice cover in the Labrador Sea and Baffin Bay is reproduced in the model with high fidelity.
- The reproduction of non-synthesized sea ice data - thickness, drift, snow plus ice freeboard - is satisfactory given known and expected model and data errors.
- The simulated ocean circulation reproduces well the basin-scale cyclonic tendency of the Labrador Sea but has a weaker barotropic transport is more baroclinic than observed.
- Simulated mixed layer depths are in excellent agreement in the western Labrador Sea (the location with the most abundant *in situ* temperature and salinity data) but significantly deviate from observations in the central and eastern Labrador Sea.

Some implications of the state estimate's most egregious discrepancies are speculated upon in Section 7.4.

Chapter 5 begins the analysis of the $1996-1997$ state estimate. The role of ice dynamics in the annual cycle is first demonstrated. New budgets of ice mass, energy, and buoyancy

are constructed and analyzed revealing details of the system balances and imbalances which drive the development of seasonal sea ice in the domain.

The key findings of Chapter 5 are:

- A one-dimensional process can predict the dates of the initial appearance of sea ice over much of the Labrador Sea and Baffin Bay - at least on the Arctic Water-side of the Thermohaline Front separating the cold fresh Arctic Waters in Baffin Bay and Labrador Shelf from the warm salty Irminger Waters in the central Labrador Sea.
- At the sea ice/open water interface in the Labrador Sea, an approximate equilibrium state is achieved in mid-March, during which the rate of dynamic ice advection to the ice edge becomes nearly equal to the rate of thermodynamic ice melt, the ice edge ceases to significantly advance, and total ice volume approaches a maximum: the *sea ice quasi-equilibrium state*.
- In the sea ice quasi-equilibrium state, the primary source for the energy required for the sustained melting of ice converging in the Labrador Sea marginal ice zone comes from ocean sensible heat advection drawing from the warm subsurface subtropical-origin Irminger Water.
- At the ice edge, sustained melt provides a sustained positive buoyancy forcing to the upper ocean due to the freshening caused by meltwater release. The sustained positive buoyancy forcing implicates a sea ice-boundary layer stabilization feedback in the setting the quasi-equilibrium ice edge position.

Chapter 6 further extends the analysis of the state estimate by investigating the relationship between positive buoyancy forcing from sea ice meltwater release and the advance of the sea ice edge in the approach to the quasi-equilibrium sea ice edge position.

The key findings of Chapter 6 are:

- A significant proportion of the sea ice cover advance across the Thermohaline Front separating the cold fresh Arctic Waters in the Baffin Bay and warm salty Irminger Waters in the Labrador Sea requires a sea ice-boundary layer stabilization feedback: deemed the *meltwater stability enhancement mechanism*.
- The ultimate restriction on the quasi-equilibrium ice edge appears to be related to the timing and location of the ventilation of warm-salty subsurface Irminger Water.
- The reason for the failure of the meltwater stability enhancement mechanism to ef-

fectively operate across waters where Irminger Waters are entrained into the mixed layer is unclear but is probably related to lateral ocean heat transport.

- The timing and location of Irminger Water ventilation is a function of the spatial distribution of anomalous upper ocean hydrographic conditions - anomalously well-stratified low-salinity waters (termed *sea ice-preconditioned waters*) and not the presence or absence of ice cover.
- Without the meltwater stability enhancement mechanism, the ice edge cannot advance across the Thermohaline Front into the sea ice-preconditioned waters despite the absence of convective entrainment of Irminger Water into the mixed layers of the sea ice-preconditioned water.
- The sea ice-preconditioned waters are characterizable with a heuristic: sea ice-preconditioned waters are near-surface waters on the Irminger Water-side of the Thermohaline Front which - despite arbitrary loss of enthalpy - remain less dense than Irminger Waters at 310 m.
- The abundance and spatial distribution of sea ice-preconditioned waters appears to determine the location of the quasi-equilibrium sea ice edge to first order.
- Missing lateral eddy heat transport in the northern Labrador Sea is unlikely to affect the above description of the ice edge advancement process across the Thermohaline Front. However, during the sea ice quasi-equilibrium state, missing eddy heat transport probably plays a larger role in maintaining the ice edge than is suggested by the state estimate.

7.3 Recounting of Experience

The generation and analysis of a consistent sea ice-ocean state estimate requires time to be spent on many different (but extremely interesting) sub-problems. In this work, the amount of time spent on each sub-problem was approximately:

- 5% : Literature review
- 10% : Devising a suitable configuration of the numerical ocean and ice model
- 10% : Familiarization with the state estimation theory and technology
- 25% : Formulating a sea ice thermodynamic code from which a useful sea ice adjoint could generated

- 20% : Familiarization with observational data and their uncertainties
- 15% : Conducting the model-data synthesis
- 15% : Analyzing of the state estimate

The biggest challenges faced in the thesis were to determine 1) the minimum set of processes requiring representation in a thermodynamic sea ice model to realistically capture the salient features of the sea ice annual cycle and 2) a suitable formulation of these processes in the sea ice model such that its automatically-derived adjoint was amenable for model-data synthesis.

After becoming familiar with the technical details of automatic differentiation and the method through which information about model-data discrepancies are used to adjust the model control variables, accomplishing the latter challenge was a straightforward (yet still somewhat time-consuming) task.

7.4 A Critique of the Conclusions

Many of the inferences drawn from the state estimate about the sea ice-ocean system of the Labrador Sea and Baffin Bay can be challenged. It is conceivable that the failures of model-data synthesis may be serious enough to invalidate many of the thesis findings. Preempting external critiques, I offer my own.

7.4.1 The state estimate is not consistent with observations

The state estimate is not consistent with all data with which a synthesis was attempted nor is it consistent with all available data. Datasets excluded from the synthesis include:

- Ocean and sea ice velocity and volume transports
- Hydrographic data in the northern Baffin Bay
- Mixed layer depth
- Mean and time-varying dynamic ocean surface topography
- Snow/ice skin albedo and temperature
- Snow depth and snow plus ice freeboard
- Turbulent air-sea fluxes of heat, moisture, and momentum

Some of these data were excluded because they are not contemporaneous with each state estimate time period (*e.g.,* snow plus ice freeboard and AMSR-E ice concentration). Some of

these data were excluded because of large expected uncertainties from model representation error (*e.g.,* mean and time-varying dynamic ocean topography, ocean volume transport, and turbulent air-sea fluxes). Others simply were omitted because the numerical code to incorporate the data into the model-data misfit cost function could not be generated in time (*e.g.,* mixed layer depth, snow/ice skin temperature and albedo, and snow depth). Finally, there are datasets for which the required adjoint model components were not ready at the time of the data synthesis (*e.g.,* sea ice motion).[1]

7.4.2 The state estimate has not synthesized sufficient observations in the seasonal ice zone

Even a cursory examination of the spatial distribution of *in situ* hydrographic data (shown in Figure 2-5) reveals that much of the seasonal sea ice zone is not sampled. Arguments for data sufficiency were presented in the Introduction and are not repeated here.

Having generated and analyzed the state estimate and having examined many other unconstrained forward model solutions of the northwest North Atlantic, I can state with a high degree of confidence that - excluding the ocean below 1500 m - the coupled sea ice-ocean reconstructions presented in this thesis are the closest fit to data yet achieved in the region.

7.4.3 Model errors or missing processes invalidate the solution

As described in Chapter 2, modeling the Labrador Sea is associated with a nearly limitless set of technical challenges - many of which remain unsolved and are expected to remain so into the foreseeable future. It is extremely difficult to predict how the state estimate solution would change if the model were able to explicitly resolve important unresolved processes and flow features such as the meso- and sub-mesoscale eddies, convective and sea ice brine plumes, narrow energetic boundary currents and boundary current recirculations. Many details of the state estimate would surely change if data were synthesized into a "perfect" model. However, I do not expect these changes to be fundamental in the regions of seasonal sea ice variability, nor do I expect the main thesis findings concerning the mechanisms of sea ice advance across the Thermohaline Front to be invalidated.

[1]The adjoint of the MITgcm sea ice dynamics model has recently been successfully generated and employed for research (Heimbach et al. 2010).

Many of the model-data discrepancies are described in Chapter 4 and are not repeated here. Discrepancies with respect to ocean circulation and mixed layer depths are significant with implications requiring mention. Circulation and mixed layer depth discrepancies render much of the state estimate solution unsuitable for some kinds of analyses including: 1) budgets of Labrador Sea Water formation (*e.g.,* Khatiwala et al. 2002; Rhein et al. 2007) and export (*e.g.,* Brandt et al. 2007), 2) deep western boundary current transport and variability (*e.g.,* Dengler et al. 2006), 3) details of the mixed layer restratification process (*e.g.,* Chanut et al. 2008), and 4) budgets of boundary current exchange with the central Labrador Sea (*e.g.,* Straneo 2006), among others.

To ascertain whether the evolution of the sea ice-ocean system was sensitive of the model flow field an additional experiment was conducted. Noting that the state estimate's circulation was more baroclinic than observed and that barotropic inflows along the domain's eastern and northern open boundaries were much weaker than observed (see Chapter 4 for details), I replaced the original open boundary volume inflows with more "realistic" values. The more realistic flow field - derived from the 1/8-degree optimized ECCO2 model solution of Menemenlis et al. (2008) - significantly improved the state estimate's circulation relative to data. Barotropic transport in the Labrador Sea nearly doubled to 22 Sv and flows on the Baffin Island, Labrador, and West Greenland Currents were invigorated.

However, the temporal and spatial patterns of the sea ice evolution were nearly unchanged. Stronger northward currents in the northern Labrador Sea slightly enhanced melt rates at the ice edge in mid-March which briefly shifted the marginal ice zone northward by ~ 60 km. A mid-March sensitivity to ocean heat transport is consistent with the findings of Section 6.6 in which I showed that biases in missing lateral heat transport were probably significant during the quasi-equilibrium period when the marginal ice zone reaches the seaward edge of the sea ice-preconditioned waters.

It was not possible within the time frame of the thesis to carefully determine whether the findings of Chapter 6 are sensitive to the mixed layer depth biases in the central and eastern Labrador Sea. Biased mixed layer depths undoubtedly affect the state estimate during the Spring restratification: erroneously shallow (deep) mixed layers have erroneously shallow (steep) horizontal density gradients and therefore less (more) explicit - or parameterized - baroclinic instability/restratifying lateral heat fluxes (Straneo 2006). A potentially serious issue is whether these lateral heat flux biases associated with mixed layer depth biases

affect the energy budgets in the marginal ice zone and therefore the quasi-equilibrium ice edge position. Without a resolution of this issue, it is difficult to anticipate the robustness of the connection between the meltwater stability enhancement mechanism and sea ice-preconditioned waters found in this thesis.

7.5 Next Steps and Outlook

The findings of the thesis raise new scientific questions, hint as the possibility of seasonal sea ice maximum extent predictability, and inform the technical design of a next-generation sea ice-ocean state estimation system. These points are touched upon in turn.

7.5.1 New scientific questions

New questions raised by this thesis include:

- Can the evolution of the distribution of sea ice-preconditioned waters be reconstructed over the sea ice-satellite era?
- What proportion of the sea ice-preconditioning is of *local* origin - anomalies generated due to sea ice-ocean-atmosphere processes internal domain - as hypothesized by Belkin et al. (1998) and what proportion is of *remote* origin - such as the propagation of upper ocean salinity anomalies into the domain from the northern Baffin Bay straits or West Greenland Current- as observed by Marsden et al. (1991)?
- What are the processes which modify the distribution of sea ice-preconditioned waters between one annual cycle to the next?
- How will the explicit representation of currently unresolved small-scale features (such as mesoscale eddies) affect the interpretation of the importance of the meltwater stability enhancement mechanism and sea ice-preconditioning for the advance of ice across the Thermohaline Front?
- Is there an analogue between hydrographic and sea ice extent variability found in in the Labrador Sea and Baffin Bay in other marginal polar and subpolar seas?

7.5.2 Seasonal sea ice predictability

It is possible to predict seasonal sea ice extent, both its annual maximum and minimum, based on foreknowledge of the distribution of sea ice-preconditioned waters? Based on

the findings of this thesis, it may be possible to predict the sea ice edge maximum within ~ 150 kilometers if one had perfect knowledge of the upper ocean hydrographic state several months before the ice edge reaches the Thermohaline Front.

With only a one-dimensional mixed layer model and reasonable (*e.g.,* climatological) assumptions of air-sea heat fluxes, one could easily determine where thermodynamic processes alone lead to local sea ice growth.[2] One could then use the heuristic described in Section 6.4 to identify the spatial distribution of sea ice-preconditioned waters allowing a first-guess of the seasonal sea ice maximum extent. A prediction uncertainty of ~ 150 kilometers is expected stemming from uncertainties associated with the modification of upper ocean salinity anomalies via mixing with Irminger Waters, rates of cross-front ice transport, and air-sea heat fluxes.

Complete foreknowledge of the Labrador Sea late-November/early-December hydrographic state is not expected in the near term. However, it may be possible to observe the spatial distribution of sea ice-preconditioned waters with a combination of satellite-based sea surface salinity and sea surface temperature data. Whether the anticipated sea surface salinity data from SMOS and Aquarius in conjunction with existing data will provide useful for this problem is an interesting open question.

7.5.3 High-resolution sea ice-ocean state estimation of the Arctic and North Atlantic

Having demonstrated the feasibility of synthesizing sea ice and ocean data into a coupled model configured at relatively coarse resolution for the Labrador Sea and Baffin Bay, and having demonstrated the utility of the state estimate for the drawing of new inferences about the evolution of the system, the development of a next-generation state estimation system can proceed. In the new system, to be developed at MIT and in collaboration with colleagues at several other institutions, new data will be synthesized in a substantially expanded model domain into more sophisticated configuration of the MITgcm.

Several new data will be synthesized in the new state estimate beyond the data considered in thesis and the data regularly synthesized as part of the ECCO global state estimation project. These data include: high-resolution (6.25 km) daily gridded sea ice concentration

[2] In the modern climate, 1-D thermodynamic processes are expected to support ice growth only on the Arctic Water-side of the Thermohaline Front, but this remains to be determined.

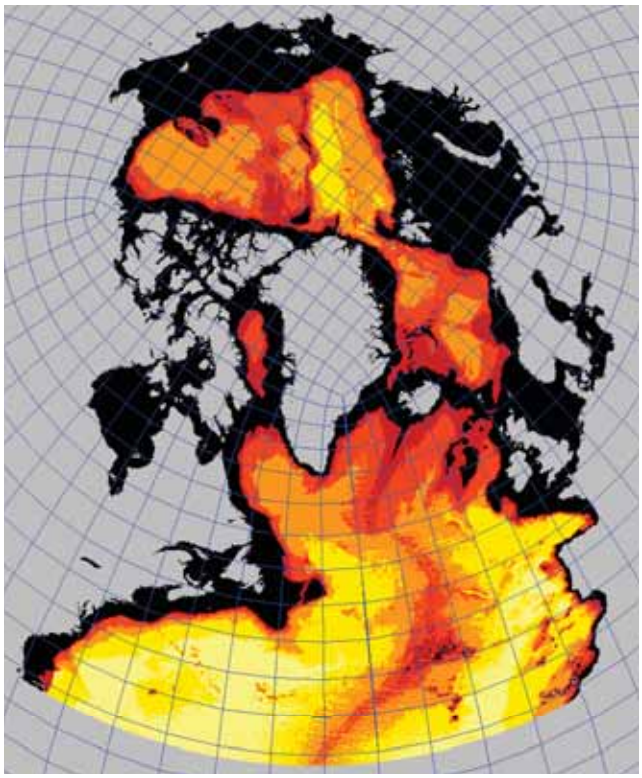

Figure 7-1: Map of the spatial domain and bathymetry for next-generation coupled sea ice-ocean state estimate to be made by the MIT ECCO group.

from AMSR-E, Arctic Ocean ice-tethered CTD profiles, snow plus ice freeboard from the ICESat laser altimeter, sea ice draft (depth below the waterline) from moored upward looking sonar in the Fram Strait and central Arctic, daily gridded 25 km ice motion, and temperature-depth data from instrumented narwhals living in Baffin Bay.

Novel model features include: a much higher horizontal spatial resolution ($\sim 7-11$ km), a longer time window (1992-present), a new sea ice salt plume sub-model, and a model domain which includes the entire Arctic Ocean and North Atlantic to 26° N (shown in Figure 7-1). With the expanded model domain and higher resolution, the new model will more accurately resolve narrow boundary currents and their transports, lateral mixing of tracers by eddies (although the deformation radius and the horizontal grid spacing are of the same order), and mixed layer restratification. This new project is expected to replicate the success of a recent high-resolution adjoint state estimation effort: the Southern Ocean State Estimate (SOSE) of Mazloff (2008).

With the successful synthesis of these new data and model, the new scientific questions raised in this thesis can be investigated. In conclusion, the synthesis of sea ice and ocean data with the new high-resolution coupled sea ice-ocean model is now not only possible, but is expected to be a relatively straightforward exercise. The analysis of the consistent state estimate will certainly yield new insights into the causes of observed climate system variability.

Appendix A

Thermodynamic Sea Ice Model

A.1 Appendix Overview

This appendix describes the thermodynamic component of the sea ice model used in this thesis. The thermodynamic ice model (TIM) prognostically determines rates of sea ice expansion/contraction and thickening/thinning within a model grid cell in response to the local air-ice-ocean state. In addition, the TIM modulates fluxes of heat and water between the ocean and atmosphere.

The major assumptions of the TIM were inherited from an earlier version of the MITgcm - itself an amalgam of still earlier models whose underlying assumptions were drawn from the literature. Among these, arguably the most important was the model entitled "An Even Simpler Model of Sea Ice Thermodynamics" found in the appendix of Semtner (1976) [S76]. Fundamental to the so-called 0-layer model of [S76] was the representation of ice as a single layer without heat capacity. Ice with zero heat capacity has an enthalpy which is always equal to its volumetric latent heat of fusion.

The parameterization relating sea ice area expansion and contraction to thermodynamic thickening and thinning is inspired from Hibler (1979) [H79]. The areal expansion and contraction of ice in [H79] is determined by relating changes of thickness to width through specified aspect ratios.

Major extensions included in the TIM beyond [S76] and [H79] include: 1) the possible submergence of ice beneath the weight of accumulated snow and subsequent conversion of submerged snow into ice, 2) the adaptation of an empirical parameterization of turbulent ocean-ice heat exchange, and 3) a different criterion for new ice formation.

This appendix is organized as follows. First, the TIM's prognostic variables are introduced (Section A.2). A description of the time tendencies of each follow: mean ice thickness (Section A.3), mean snow thickness (Section A.4), and ice concentration (Section A.5). Finally, details of the new ice production procedure are mentioned (Section A.6).

The TIM scalar parameters used in this thesis are provided at the end of the appendix in Table A.2.

A.2 Sea Ice Thermodynamic Model Prognostic Variables

The three main prognostic variables of the sea ice model are: ice concentration (ice-covered fraction of a grid cell), A, mean ice thickness, h, and mean snow thickness h_s.

The time evolution of one of these variables, X, is given by a continuity equation:

$$\frac{\partial X}{\partial t} = \left(\frac{\partial X}{\partial t}\right)_{thermo} - \nabla \cdot (\vec{u}_{ice}\, X) + \Gamma_{dyn} \tag{A.1}$$

Where $\vec{u}_{ice}$ is the ice velocity provided by the sea ice dynamics model. The first term on the RHS describes changes to X from thermodynamical processes while the second and third terms describe changes from sea ice dynamics - mechanical divergence/convergence and unresolved subgrid scale processes. This appendix considers only thermodynamic processes. The fundamental assumptions of the dynamical ice model can be found in [H79] and Hibler (1980). Details of the implementation of the sea ice dynamics package in the MITgcm are thoroughly described in Zhang and Hibler (1997) and Losch et al. (2010) and are not repeated here.

A.3 Mean Sea Ice Thickness Tendency, $\partial h/\partial t$

The conversion of liquid seawater to ice and vice versa involves many different energy fluxes. The time evolution of h is driven by four terms, new ice growth from open water ocean-atmosphere (oa) heat fluxes, thickening/melting of existing ice (ei) via basal thickening and ice-air heat convergence, basal melting by turbulent ocean-ice (oi) heat fluxes, and the

transformation of snow into ice during flooding (fl).[1]

$$\left(\frac{\partial h}{\partial t}\right)_{therm} = \left(\frac{\partial h}{\partial t}\right)_{oa} + \left(\frac{\partial h}{\partial t}\right)_{ei} + \left(\frac{\partial h}{\partial t}\right)_{oi} + \left(\frac{\partial h}{\partial t}\right)_{fl} \tag{A.2}$$

Each of the first three thickness tendency terms on the RHS of (A.2) is driven by an associated energy flux, F_X, operating over some fraction of the cell ξ_X:[2]

$$\left(\frac{\partial h}{\partial t}\right)_X = \xi_X F_X \left(\rho_i L_i\right)^{-1} = \xi_X F_X Q_I \tag{A.3}$$

Where ρ_i and L_i and sea ice density and seawater latent heat of fusion (both assumed constant), respectively, and

$$\xi_X = \begin{cases} 1 - A & X = oa \\ A & X = ei \\ 1 & X = oi \end{cases} \tag{A.4}$$

The energy fluxes driving the first three thickness tendency terms of (A.2) are now described. The snow flooding term is described in Section A.4.3.

A.3.1 Ocean-atmosphere heat fluxes, F_{oa}

Net ocean-atmosphere heat fluxes over open water, F_{oa}, are provided as inputs to the TIM and then weighted by the open water fraction of the grid cell, $1 - A$.

A.3.2 Existing ice heat fluxes, F_{ei}

Existing ice heat fluxes represent fluxes which drive basal thickening and surface thinning based on thermodynamic considerations within the snow and ice layers. The contribution of these fluxes to h is weighted by the ice-covered fraction of the grid cell, A.

During basal thickening, sensible heat is extracted from the ocean and conducted vertically upward through the ice and snow to the snow-ice surface (ice or snow surface if snow overlays ice) and subsequently lost to the atmosphere. At the snow-ice surface, an energy balance condition is assumed whereby conductive heat flux convergence is offset by turbulent and radiative air-sea heat flux divergence.

[1] All energy fluxes are considered in $\mathrm{W\,m^{-2}}$.

[2] Note sign convention for fluxes is opposite that of Chapter 5.

During surface thinning (melting) conditions, net heat flux convergence at the snow-ice surface melts snow (if present) then ice. In this case, the energy for the heat flux convergence is a combination of downwelling radiative and turbulent air-ice heat fluxes.

Thus described, F_{ei} is written:

$$F_{ei} = \begin{cases} F_{con} + F_{ian} & h_s = 0 \\ F_{con} & h_s > 0 \end{cases}$$

Where F_{con} is the upward conductive heat flux at the ice base and F_{ian} is the net ice-atmosphere heat flux divergence at the snow-ice surface. During basal thickening, $F_{con} > 0$ and $F_{ian} = 0$. Provided the ice is free of snow, during surface thinning $F_{con} = 0$ and $F_{ian} < 0$.

Heat conduction through the ice and snow

To determine F_{con}, this model assumes that one-dimensional heat diffusion equations are satisfied within the ice and snow layers. Written explicitly for layer X,

$$\rho_X \, c_X \frac{T_X(z)}{\partial t} = \frac{k_X}{h_x/A} \frac{\partial^2 T(z)}{\partial z^2} - \frac{\partial I(z)}{\partial z} \tag{A.5}$$

Where for each layer, c is the heat capacity, k is thermal conductivity, $T(z)$ is the vertical temperature profile, and $I(z)$ is the shortwave flux penetrating to depth z. The division of h by A converts mean thickness to the "actual" layer thickness (the thickness of the layer within the ice-covered fraction of the grid cell) - as required to calculate conductive fluxes.

Internal temperatures within the ice and snow are assumed to relax to steady-state values on time scales shorter than one model time step (1 hour), a reasonable approximation (Feltham et al. 2006). Temperature profiles yielding vertically uniform conductive fluxes within both the ice and snow layers are therefore implied. For a two-component conducting system (here ice and snow), the steady-state vertically-uniform conductive heat flux is written,

$$F_{con} = -k_{eff}(T_{surf} - T_{frz}) \tag{A.6}$$

Where T_{surf} is the snow-ice surface temperature (See Figure 2-3 for a schematic of the temperature profiles and fluxes in the ice and snow system) and k_{eff} is the effective conductivity of the two-component system. The temperature at the ice base is assumed to be

equal to the seawater freezing point, T_{frz}.

Effective conductivity of the two-component system is given by:

$$k_{eff} = \frac{k_i\, k_s}{k_s\, h/A + k_i\, h_s/A} \tag{A.7}$$

Where k_s and k_i are the thermal conductivities (assumed constant) of snow and ice, respectively.

Net energy divergence at the snow-ice surface

At the snow-ice surface, the net energy divergence is given by:

$$F_{ian} = \mathrm{F_{lw}}\downarrow + \mathrm{F_{lw}}\uparrow + \mathrm{F_{sw}}\downarrow + \mathrm{F_{lat}} + \mathrm{F_{sen}} - \mathrm{F_{con}} \tag{A.8}$$

The names of the variables of (A.8) are described in Table A.3.2.

Symbol	Description
$\mathrm{F_{ian}}$	Net snow-ice surface heat flux divergence
$\mathrm{F_{lw}}\downarrow$	Net downward longwave radiation
$\mathrm{F_{lw}}\uparrow$	Upward longwave radiation
$\mathrm{F_{sw}}\downarrow$	Net downward shortwave radiation
$\mathrm{F_{lat}}$	Latent heat flux
$\mathrm{F_{sen}}$	Sensible heat flux
$\mathrm{F_{con}}$	Upward conductive heat flux

Table A.1: Snow-ice surface ice heat fluxes

The sign convention of (A.8) is such that a positive term removes energy from the snow-ice surface (flux to the atmosphere). Conductive fluxes are signed positive in (A.6) to represent seawater enthalpy divergence and energy convergence at the snow-ice surface. Hence, in (A.8) the sign of F_{con} must be negative.

The determination of these fluxes are now described in more detail.

Short- and Longwave Radiation Surface downwelling short- and longwave radiative fluxes, D_{lw} and D_{sw}, (both negative) are provided as inputs to the ice model. Net longwave

absorption and emission are parameterized:

$$\mathrm{F_{lw}} \downarrow = \epsilon \, D_{lw} \tag{A.9}$$

$$\mathrm{F_{lw}} \uparrow = \epsilon \, \sigma \, T_{surf}^4 \tag{A.10}$$

Where ϵ is the longwave absorptivity/emissivity and σ is the Stefan-Boltzmann constant.

The downwelling shortwave radiation absorbed by ice is reduced by a fraction which is reflected and a fraction which penetrates through the ice without being absorbed,

$$\mathrm{F_{sw}} \downarrow = (1 - \alpha)(1 - i_o) \, D_{sw} \tag{A.11}$$

The attenuated fraction of penetrating radiation passing through the ice base into the ocean after transmission, i_o, is given by,

$$i_o = I_o \exp(-\kappa \, h/A) \tag{A.12}$$

Where I_o is the fraction of shortwave radiation which is not reflected at the surface ($D_{sw}(1-\alpha)$) penetrating the ice interior and κ is the extinction coefficient (Maykut and Untersteiner 1971). It is assumed that shortwave radiation cannot penetrate through snow.

The snow-ice surface albedo takes one of four values depending on surface type (bare ice or snow) and conditions (frozen or melting). Albedo and emissivity values are initially taken from observations (*e.g.,* Grenfell and Perovich 1984, 2004) and take their final values after subsequent manual tuning.

Sensible heat flux Turbulent air-sea sensible heat flux is parameterized using a bulk formula,

$$\mathrm{F_{sen}} = C_D \, |\vec{U}| \, (T_{surf} - T_{air}) \tag{A.13}$$

Where C_D is the sensible heat bulk transfer coefficient, T_{air} is the air temperature at 2 m, and $\vec{U}$ is the vector wind at 10 m. The latter two variables are ice model inputs.

Latent heat flux The latent heat flux is also parameterized with a bulk formula,

$$\mathrm{F_{lat}} = C_E \, |\vec{U}| \, (q_{ice} - q_{atm}) \tag{A.14}$$

Where C_E is the latent heat bulk transfer coefficient, and q_{ice} and q_{atm} are the specific humidities at the snow-ice surface and of the air at 2 m, respectively. Atmospheric specific humidity is an ice model input.

The vapor phase of water adjacent to the snow-ice surface is considered to be in equilibrium with its solid phase. The specific humidity of this saturated air is:

$$q_{ice} = \frac{\delta\, e}{P_{atm} - (1-\delta)\, e} \tag{A.15}$$

Where $\delta = 0.622$ (the ratio of the molecular weights of water vapor to dry air), P_{atm} is the surface pressure (Pascals), and e is the saturation vapor pressure adjacent to the snow-ice surface (Pascals).

The saturation vapor pressure parameterization is taken from the empirical expression of Marti and Mauersberger (1993):[3]

$$e = 10^{\left(\frac{a_1}{T_{surf}} + a_2\right)} \tag{A.16}$$

With $a_1 = -2663.5$ and $a_2 = 12.537$.

Determination of T_{surf}

The determination of T_{surf} is a major component of the TIM. The Newton-Rhapson (NR) method - suggested in [S76] - is employed to solve for the T_{surf} which is consistent with the assumed snow-ice surface energy balance.

NR is a suitable methodology for this particular problem because, for a wide range of physically realistic atmospheric conditions, the snow-ice surface energy divergence as a function of T_{surf} has neither local extrema, nor does it exhibit asymptotic behavior, nor does it have multiple zero crossings.

The NR method is an iterative search method requiring a function (in our case $F_{ian}(T_{surf})$, its derivative with respect to the variable being sought (T_{surf}), and a first-guess of the solution at iteration 0. The first-guess solution is chosen to be the T_{surf} from the previous time step - provided it exists - otherwise 0° C.

[3]This expression is preferable over polynomial forms as it is monotonically increases with temperature - a requirement for determining T_{surf} using the Newton-Rhapson method (described in the following section).

During the search, T_{surf} at iteration $n+1$ is given by,

$$T_{surf}^{n+1} = T_{surf}^{n} - F_{ian}(T_{surf}) \left[\frac{\partial F_{ian}(T_{surf}^{n})}{\partial T_{surf}} \right]^{-1} \tag{A.17}$$

For the vast majority of atmospheric conditions realized in the Labrador Sea and Baffin Bay, convergence of (A.17) is found to machine precision within ~ 6 iterations.

There are three possible cases associated with the T_{surf} found from the NR search - two of which require special treatment. These cases are described below.

Case 1 $T_{surf} > 0^{\circ}\,\mathrm{C}$

The only T_{surf} consistent with a surface energy balance may exceed the melting point of snow and ice. In such a case, T_{surf} is reduced to $0^{\circ}\,\mathrm{C}$ thus rendering the surface energy flux divergence nonzero.

When the snow-ice surface is warmer than the ice base ($T_{surf} > T_{frz}$) downward conductive heat fluxes are implied. To simplify accounting, F_{con} is permitted to be nonzero when conductive fluxes are upward. Therefore, in this case F_{con} is set to $0\,\mathrm{W\,m^{-2}}$ and F_{ian} is re-evaluated at $T_{surf} = 0^{\circ}\,\mathrm{C}$.

Case 2: $T_{frz} < T_{surf} \leq 0^{\circ}\,\mathrm{C}$

As in Case 1, downward heat conduction is implied - although in this case an energy balance condition is achieved. To determine surface energy convergence, F_{con} is set to $0\,\mathrm{W\,m^{-2}}$ and F_{ian} is re-evaluated at the T_{surf} found in the NR search.

Case 3: $T_{surf} < T_{frz}$

When $T_{surf} < T_{frz}$, an energy balance solution is found ($F_{ian} = 0$), with nonzero upward conductive fluxes ($F_{con} \geq 0$). No special treatment of T_{surf} or F_{con} is required.

A.3.3 Ocean-ice heat fluxes, F_{oi}

The parameterization of the enthalpy flux from seawater sensible heat across the ice-ocean interface is a major factor determining the spatial extent of sea ice cover in a model. Where sea ice is routinely advected out of the marginal ice zone into warmer offshore waters (such as the Labrador Sea), this parameterization can strongly influence the distance ice floes

can travel before completely melting. If parameterized melt is too rapid, the meanders of the ice edge out across warmer waters will be artificially damped. On the other hand, if parameterized melt is too slow, the ice edge may extend unrealistically seaward.

The mean turbulent ocean-ice heat flux convergence at the ice-ocean interface is written:

$$F_{oi} = -c_p \, \rho_{sw} \, \overline{w'T'} \tag{A.18}$$

Subgrid scale turbulent heat fluxes in (A.18) can be parameterized using a local closure for $\overline{w'T'}$.

In early sea ice models, such as Häkkinen (1987) and earlier versions of the MITgcm, seawater temperatures in grid cells containing ice were maintained at a constant or salinity-determined freezing point. Any heat entering this volume was immediately extracted (bringing the seawater temperature back to its freezing point) and used to melt ice (the so-called ice bath formulation).

In the ice bath formulation, $\overline{w'T'}$ is written:

$$\overline{w'T'} = \frac{\Delta z}{\Delta t} \, (T_{ocn} - T_{frz}) \tag{A.19}$$

Where T_{ocn} and T_{frz} are the model and freezing point temperatures for the uppermost grid cell. Δz is the depth of the grid cell, and Δt is the time step.

The ice bath formulation is a limiting case which generates unrealistically high rates of ocean-ice heat flux (Schmidt et al. 2004).

The closure used in this thesis is based on the empirical parameterization of McPhee (1992). In it, the far-field ocean temperature, T, the friction velocity beneath ice, u_*, and an observationally-inferred constant the Stanton number, St, are used. To wit,

$$\overline{w'T'} = St \, u_* \, (T - T_{frz}) \tag{A.20}$$

In this TIM, fluxes are parameterized with the additional following assumptions:

1. Model seawater temperature in the upper ocean grid cell is approximately the far field, $T_{ocn} \approx T$.
2. $T_{ocn} \geq T_{frz}$ in the presence of ice.
3. The far-field freezing point and friction velocities beneath ice are approximately con-

stant.

The constant friction velocity is chosen to be a typical value found beneath ice as observed by Uusikivi et al. (2006) and Hayes and Morison (2008). Note that ocean-ice heat fluxes calculated with (A.20) are ~ 50 times smaller than those given by (A.19).

In the future, progress is expected in providing a feedback between the sea ice melt rate and the Stanton number. The modeling study of Notz (2005, Chap 10), observational work of Sirevaag (2009), and theoretical considerations (*e.g.,* McPhee 2008, Chap 6.5) suggest that during periods of rapid ice melt, the freshening of seawater at the ice base will modify the Stanton number. However, at present the sign of the modification is a matter of debate (*McPhee*, personal communication, 2009).

A.4 Mean Snow Thickness Tendency, $\partial h_s/\partial t$

Mean snow depth changes in three ways: accumulation of new snow via precipitation, melting from net energy flux convergence, and conversion of snow to ice via flooding. Symbolically written:

$$\left(\frac{\partial h_s}{\partial t}\right)_{therm} = \left(\frac{\partial h_s}{\partial t}\right)_{P} + \left(\frac{\partial h_s}{\partial t}\right)_{ei} + \left(\frac{\partial h_s}{\partial t}\right)_{fl} \tag{A.21}$$

These three terms are described below.

A.4.1 Snow accumulation

Precipitation falling over a grid cell accumulates over ice as snow. The accumulation of mean snow thickness is given by:

$$\left(\frac{\partial h_s}{\partial t}\right)_{P} = A\,P\,\frac{\rho_w}{\rho_s} \tag{A.22}$$

Where ρ_w is the density of freshwater and P is the precipitation rate - a prescribed model input.

A.4.2 Snow melt

Net energy convergence at the snow surface is entirely directed towards melting snow (while it exists),

$$\left(\frac{\partial h_s}{\partial t}\right)_{ei} = F_{ian}\left(\rho_s L_i\right)^{-1} \tag{A.23}$$

Where ρ_s is the density of snow.

A.4.3 Snow flooding

Following Winton (2000), if the weight of accumulated snow over ice is such that in hydrostatic equilibrium the interface between the snow and ice layers is beneath the waterline, some fraction of the snow beneath the waterline is flooded - *i.e.,* converted to ice while conserving mass. Flooded snow is assumed to completely accrete with the ice below.

The adjustments to mean snow thickness, δh_s, and mean ice thickness, δh, are applied at the end of each model time step:

$$\delta h_s = -A \max\left[\left(\frac{h_s}{A} - \left(\frac{\rho_s - \rho_i}{\rho_s}\right)\frac{h}{A}\right)\frac{\rho_i}{\rho_w}, 0\right] \tag{A.24}$$

$$\delta h = A \max\left[\left(\frac{h_s}{A} - \left(\frac{\rho_s - \rho_i}{\rho_s}\right)\frac{h}{A}\right)\frac{\rho_s}{\rho_w}, 0\right] \tag{A.25}$$

With the above adjustments, the snow and ice layer interface is found parallel to the waterline.

A.4.4 Redistribution

The volume of snow in a grid cell is assumed unchanged by the contraction or expansion of ice cover - provided the ice cover does not entirely vanish. Snow over a contracting (expanding) ice cover is assumed to converge (spread out) leaving mean snow depth unchanged. Any snow remaining on ice when all ice area is lost is assumed to melt.

A.5 Mean Ice Concentration Tendency, $\partial A/\partial t$

Thermodynamic changes to the ice concentration from thermodynamic processes are linked to changes in mean ice thickness. As changes to h are themselves driven by various energy

fluxes, so it is that energy fluxes drive changes to A.

Three terms contribute to changes to A: 1) expansion/contraction from ocean-atmosphere heat fluxes (F_{oa}), contraction from net ice-atmosphere snow-ice surface heat convergence (F_{ian}), and contraction from turbulent ocean-ice heat fluxes (F_{oi}). It is assumed that basal ice thickening ($F_{con} > 0$) does not A.

$$\left(\frac{\partial A}{\partial t}\right)_{therm} = \left(\frac{\partial A}{\partial t}\right)_{oa} + \left(\frac{\partial A}{\partial t}\right)_{ian} + \left(\frac{\partial A}{\partial t}\right)_{oi} \tag{A.26}$$

In a way analogous to (A.3), each of the tendency terms on the RHS of (A.26) can be written in terms of associated energy fluxes operating over some fraction of the cell, ξ_X.

$$\left(\frac{\partial A}{\partial t}\right)_{X} = \xi_X \, F_X \, Q_I \, \psi_X \tag{A.27}$$

Where ξ_X is a term which mitigates the effect of the energy fluxes (setting them proportional to the areal fraction of the cell to which they pertain) and ψ_X is a term which specifies the ratio of changes to h to A. ξ_X and ψ_X take the following values,

$$\xi_X = \begin{cases} 1 - A & X = oa \\ A & X = ian \\ 1 & X = oi \end{cases} \tag{A.28}$$

$$\psi_X = \begin{cases} h_o^{-1} & X = oa, \mathrm{sgn}(F_{oa}) = 1 \\ A(2h)^{-1} & \mathrm{sgn}(F_X) = -1 \end{cases} \tag{A.29}$$

Where $\mathrm{sgn}(x) = 1, x > 0$ and $\mathrm{sgn}(x) = -1, x < 0$. If and only if $F_{oa} > 0$ (net open water energy flux divergence) does ice concentration increase. Net open water energy flux convergence reduces ice area. Based on the specifications of F_{ian} and F_{oi} in (A.8) and (A.20), the second and third terms in (A.26) can only reduce ice area:

$$\left(\frac{\partial A}{\partial t}\right)_{ian}, \quad \left(\frac{\partial A}{\partial t}\right)_{oi} \leq 0 \tag{A.30}$$

Addition explanation for the form of ψ in (A.29) is now provided.

A.5.1 Ice cover expansion

In the TIM, only net open water energy flux divergence, $F_{oa} > 0$ leads to the formation of new ice cover. The parameterization used by [H79] gives new ice a fixed "actual" thickness of h_0, thereby associating new ice with an area. Written symbolically,

$$\left(\frac{\partial A}{\partial t}\right)_{oa} = \xi_{oa}\,\psi_{oa}\,F_{oa}\,Q_I = (1-A)\,h_o^{-1}\,F_{oa}\,Q_I \tag{A.31}$$

Illustrating with an example: an initially ice-free grid cell undergoes ocean-air heat loss consistent with the creation of new ice with a mean thickness of 0.1 m. Using $h_0 = 0.5$ m in (A.31) yields $A = 0.20$. The actual thickness of the new ice, h_a, is 0.5 m ($h_a = hA^{-1}$, extending across 20% of the domain. As the open water fraction in the cell decreases, this parameterization continues to set the actual thickness of new ice in the ice-free region to h_o.

A.5.2 Ice cover contraction

The relationship between ice thinning and ice concentration reduction is also taken from [H79]. The salient features of this parameterization are as follows:

1. For the purposes of ice area loss only, the actual thickness of ice within the ice-covered fraction of the grid cell is considered to be equally distributed between thickness 0 and $2\,h\,A^{-1}$.

2. Over some finite time interval, the loss of mean ice thickness uniformly reduces actual ice thickness.

3. Because of the assumed distribution of h_a, a nonzero fraction of the ice-covered area is associated with all nonzero actual ice thickness loss.

Given the above assumptions, the choice of $\psi = A\,(2\,h)^{-1}$ is easily derived (a derivation which is not repeated here). To illustrate this process, the loss of mean ice and actual ice thickness and the subsequent loss of ice-covered area are presented schematically in Figure A-1.

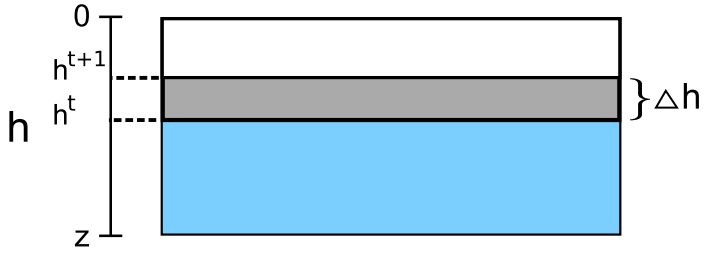

(a) Loss of h

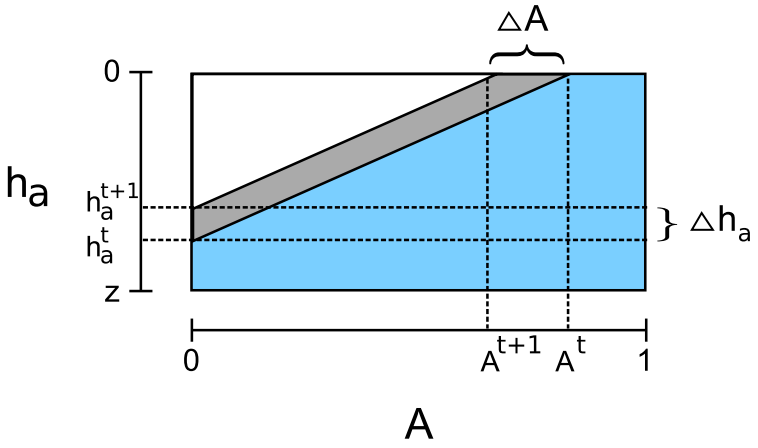

(b) Loss of h_a and contraction of A

Figure A-1: a) The loss of mean ice thickness, Δh, over time interval $(t \rightarrow t+1)$. b) the loss of actual ice thickness, Δh_a, over the same time interval and the associated contraction of ice-covered area, ΔA. In b), h_a is initially distributed equally between 0 and $2\,h\,A^{-1}$. Over the ice-covered region of the grid cell, the reduction of h_a is assumed to eliminate all ice with $h_a \leq \Delta h_a$, thereby contracting A.

A.6 Sea Ice Production

Two aspects of ice production in this TIM are treated differently than many other models: 1) the criterion for new ice coalescence - the conditions under which ice is first permitted to form in an initially ice-free grid cell - and 2) the distribution of ocean-atmosphere enthalpy loss between ice production and ocean temperature reduction. Details of both processes are described.

A.6.1 New ice coalescence criterion

In the real ocean, there is three-dimensional structure in temperature and salinity within volumes on the order of the size of this model's uppermost grid cells (32 km x 32 km x 10 m). The structures generated by the diurnal cycle of solar insolation, mesoscale eddies, and meandering boundary current fronts are unresolved yet may play in role in the determining the new ice formation. The assumption that the uppermost model grid cell temperature must attain its freezing point before the initial formation of ice is equivalent to the assumption that there is no meaningful unresolved vertical structure in temperature and stratification.

In this model, the assumption of a structureless upper ocean grid cell is relaxed. As a consequence, ice is allowed to form in grid cells with seawater temperatures above their nominal freezing point. The new ice coalescence criterion is simple: the rate of thermodynamic ice production from air-sea heat loss must exceed the rate of thermodynamic ice melt from ice-ocean turbulent fluxes.

In each time step, a virtual quantity of ice with enthalpy equivalent to the total air-sea heat loss is produced. This virtual quantity is then subjected to virtual turbulent ocean-ice heat fluxes which melts some or all of the virtual ice. When nonzero virtual ice remains after virtual ocean-ice heat fluxes, new ice is formed.

Written symbolically, from (A.2) and (A.3),

$$\left(\frac{\partial h}{\partial t}\right)_{therm} = \left(\frac{\partial h}{\partial t}\right)_{oa} + \left(\frac{\partial h}{\partial t}\right)_{oi} \tag{A.32}$$

$$\left(\frac{\partial h}{\partial t}\right)_{therm} = Q_I \left(F_{oa} + F_{oi}\right) \tag{A.33}$$

Employing the same ocean-ice turbulent heat flux parameterization as (A.20),

$$\left(\frac{\partial h}{\partial t}\right)_{therm} = Q_I\Big(F_{oa} - c_p\,\rho_{sw}\,St\,u_*\,(T_o - T_{frz})\Big) \tag{A.34}$$

It is further assumed that the open water friction velocity is 3-5 times larger in ice-free conditions than when ice is present - $u_* \approx 3{-}5\,\mathrm{cm\,s^{-1}}$ vs. $u_* \approx 1\,\mathrm{cm\,s^{-1}}$ (Klinger et al. 2006). Using typical values for the parameters in (A.34), atmospheric heat losses of $500\,\mathrm{W\,m^{-2}}$ will lead to new ice production when the ocean temperature reaches 0.058° C above its nominal freezing point.

A.6.2 Ice production with nonzero turbulent ocean-ice heat fluxes

Once the criterion for new ice coalescence is met, ocean heat losses both increase ice volume and decrease the temperature of the uppermost ocean grid cell. Determining the proportions of new ice volume and ocean temperature reduction is explained as a two-stage process occurring during one model time step.

In the first stage, the total energy extracted from the ocean to the atmosphere creates a volume of ice, determined by equating the extracted enthalpy with seawater's latent fusion energy. In the second stage, the ocean-ice heat flux parameterized by (A.20) transfers energy to the ice, melting a fraction its volume. It is this ocean-ice energy transfer which reduces the seawater temperature.

A graphical illustration of these two stages is shown in Fig. A-2.

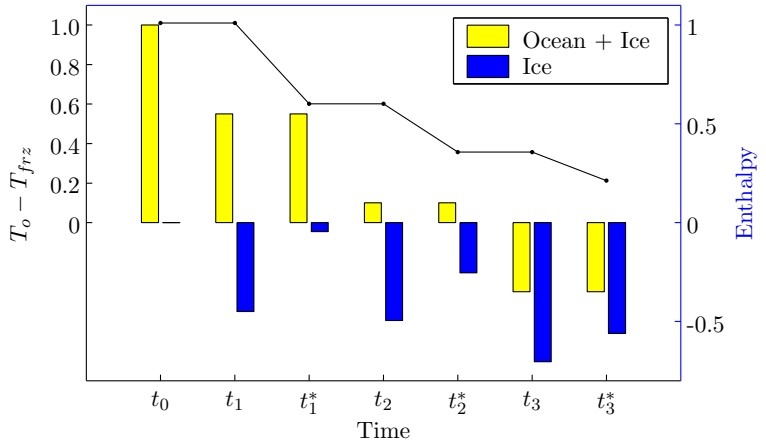

Figure A-2: The progression of enthalpy (referenced to seawater at its freezing point, T_{frz}) in the sea ice + ocean (yellow bars) and sea ice alone (blue bars), and the difference between the temperature of the ocean, T_o, and T_{frz} (dotted black line) during three time steps of ocean-atmosphere heat divergence. The reduction of T_o and the formation of ice develops as a two–stage process occurring each time step. At the initial time, t_0, no ice is present and $T_o - T_{frz} = 1$ unit. At the first stage of the next time step, t_1, ocean heat loss produces ice with a volumetric enthalpy equal to the ocean enthalpy loss. In the second stage, t_1^*, turbulent ocean-ice fluxes cause some of the new ice to melt, reducing its volume and volumetric enthalpy. It is this thermal energy transfer which reduces the ocean enthalpy thereby lowering its temperature. As $T_o \rightarrow T_f$, the amount of thermal energy transferred from the ocean to the ice is progressively reduced.

Seawater heat capacity	c_p	$4.01 \times 10^3\,\mathrm{J\,kg^{-1}\,K^{-1}}$	
Thermal conductivity (snow, ice)	k_s, k_i	$0.31\,\mathrm{W\,m^{-1}\,K^{-1}}$	$2.17\,\mathrm{W\,m^{-1}\,K^{-1}}$
Seawater Latent heat of fusion	L_i	$3.34 \times 10^5\,\mathrm{J\,kg^{-1}}$	
Density (ice, snow)	ρ_i, ρ_s	$910\,\mathrm{k\,m^{-3}}$	$330\,\mathrm{kg\,m^{-3}}$
Seawater freezing temperature	T_{frz}	$-1.96^\circ\,\mathrm{C}$	
Ice albedo (dry, wet)	α	0.75	0.66
Snow albedo (dry, wet)	α	0.85	0.70
Longwave emissivity	ϵ	0.97	
Shortwave extinction coefficient	κ	5.0	
Shortwave penetration coefficient (ice,snow)	I_o	0.30	0
Sensible heat transfer coefficient	C_D	2.28	
Latent heat transfer coefficient	C_E	6.45	
Friction velocity (ice/no ice)	u_*	$1\,\mathrm{cm\,s^{-1}}$	$5\,\mathrm{cm\,s^{-1}}$
Stanton number	St	5.6×10^{-3}	
Ice bulk salinity	S_{ice}	5.0	
New ice thickness parameter	h_0	0.5 m	
Drag (ice-ocean, ice-air)		$8.5{\times}10^{-3}$	1.0×10^{-3}
Ice strength parameter	P^*		$5.0 \times 10^3\,\mathrm{Nm^{-2}}$
Ice strength parameter	C		20
Yield curve eccentricity ratio	e	2	

Table A.2: Sea ice model parameters

Glossary

Arctic Water (AW)

The term used for cold fresh water of Arctic Ocean and Nordic Sea origin in the Labrador Sea and Baffin Bay. Some of these waters enter the domain through the straits of the Canadian Arctic Archipelago which connect the Arctic Ocean and Baffin Bay while some is transported along the East/West Greenland Current system around Cape Farewell into the Labrador Sea.

Baffin Island Current (BIC)

A southward flowing boundary current found along eastern Baffin Island transporting Arctic Water advected into Baffin Bay through the straits of the Canadian Arctic Archipelago.

East Greenland Current (EGC)

A southward flowing current found along the eastern coast of Greenland. The composition of waters in the EGC are a composite of Arctic Water outflow and subtropical-origin Irminger Water cyclonically advected by the Irminger Current within the North Atlantic subpolar gyre. When the current reaches the southern tip of Greenland it becomes the West Greenland Current

Irminger Sea Water (IW)

The term used for warm salty water of subtropical origin in the Labrador Sea and Baffin Bay. Most waters of subtropical origin are advected through the Irminger Sea before being entering the Labrador Sea via the West Greenland Current

Labrador Current (LC)

A southward flowing boundary current found along the eastern coast of Labrador. An on-shelf component consists of Arctic Water from the Baffin Island and West Greenland Currents. An off-shelf component consists of (modified) Irminger Water brought from the West Greenland Current.

marginal ice zone (MIZ)

The boundary between ice-free open water and the consolidated pack ice. Within the region, large ice floes break apart from ocean-wave interaction leaving a diffusely scattered field of variously sized floes.

mixed layer depth (MLD)

The depth of the ocean mixed layer.

meltwater stability enhancement mechanism (MSEM)

The process by which sustained ice convergence into warmer waters beyond the ice edge leads to 1) sustained ice meltwater release into the upper ocean, 2) an increase of the mixed layer stratification, 3) mixed layer shoaling, 4) a reduction of oceanic vertical advective heat flux convergence, 5) a cooling of the mixed layer, 6) a reduction in ocean-ice heat fluxes/ice melt rates, and 7) a net accumulation of ice into regions initially unfavorable to ice.

Northeast Corner of northern Labrador Sea (NEC)

The area in the northeast Labrador Sea within the Northern Slope adjacent to southwest Greenland. The Northeast Corner of the Labrador Sea is identified with the a maximum in eddy kinetic energy in the domain.

Northern Slope (NS)

A region in the northern Labrador Sea between the 1000 m and 3000 m isobaths. The West Greenland Current bifurcates into the eddy-rich Northern Slope. The Northern Slope is also a region of high interannual sea ice variability.

sea ice quasi-equilibrium state

The several week long period around mid-March during which the ice thicknesses, concentrations, total area and extent, and marginal ice zone location reach an approximate steady-state.

sea ice-preconditioned waters (SI-PW)

Upper ocean (< 100 m) waters on the Irminger Water side of the Thermohaline Front in the Labrador Sea on which sea ice eventually develops via the *meltwater stability enhancement mechanism* over the course of the annual cycle. The cold, fresh, and well stratified sea ice-preconditioned waters tend to overlay warm, salty, and less stratified Irminger Waters.

sea surface temperature (SST)

The ocean surface skin temperature

Thermohaline Front (THF)

A region of where cold fresh Arctic Water meets warm salty Irminger Sea Water in the Labrador Sea. The location of the front is temporally variable but generally is found near the 1000 m isobath of the Labrador Sea.

West Greenland Current (WGC)

A northward flowing current found along the western coast of Greenland. The WGC transports a composite of cold-fresh Arctic Water (originating in the Arctic Ocean) found above the Greenland Shelf and warm-salty subtropical-origin Irminger Water (originating in the Irminger Sea) beyond the shelfbreak.

Bibliography

Aagaard, K. and E. C. Carmack, 1989: The role of sea ice and other fresh water in the Arctic circulation. *Journal of Geophysical Research*, **94**, 14485–14498.

Adcroft, A. J., 1995: *Numerical Algorithms for use in a Dynamical Model of the Ocean*. Ph.D. thesis, University of London and the University of London.

Adcroft, A. J., C. N. Hill, and J. C. Marshall, 1999: A new treatment of the coriolis terms in C-grid models at both high and low resolutions. *Monthly Weather Review*, **127**, 1928–1936.

Andersen, S., R. Tonboe, L. Kaleschke, G. Heygster, and L. T. Pedersen, 2007: Intercomparison of passive microwave sea ice concentration retrievals over the high-concentration Arctic sea ice. *Journal of Geophysical Research – Oceans*, **112**.

Andersen, S., R. Tonboe, S. Kern, and H. Schyberg, 2006: Improved retrieval of sea ice total concentration from spaceborne passive microwave observations using numerical weather prediction model fields: An intercomparison of nine algorithms. *Remote Sensing Of Environment*, **104**, 374–392.

Belkin, I., S. Levitus, J. Antonov, and S. Malmberg, 1998: "Great Salinity Anomalies" in the North Atlantic. *Progress in Oceanography*, **41**, 1–68.

Betts, A. K., M. Zhao, P. A. Dirmeyer, and A. C. M. Beljaars, 2006: Comparison of ERA40 and NCEP/DOE near-surface data sets with other ISLSCP-II data sets. *Journal of Geophysical Research – Atmospheres*, **111**, D22S04.

Bitz, C., M. Holland, E. Hunke, and R. Moritz, 2005: Maintenance of the sea-ice edge. *Journal of Climate*, **18**, 2903–2921.

Bitz, C. and W. Lipscomb, 1999: An energy-conserving thermodynamic model of sea ice. *Journal of Geophysical Research – Oceans*, **104**, 15669–15677.

Bower, A. S., B. Le Cann, T. Rossby, W. Zenk, J. Gould, K. Speer, P. L. Richardson, M. D. Prater, and H. M. Zhang, 2002: Directly measured mid-depth circulation in the northeastern North Atlantic Ocean. *Nature*, **419**, 603–607.

Boyer, T. P., C. Stephens, J. I. Antonov, M. E. Conkright, M. E. Locarnini, T. D. O'Brien, and H. E. Garcia, 2001: World Ocean Atlas 2001. *Salinity*, S. Levitus, ed., U.S. Government Printing Office, Washington, D.C., volume 2 of *NOAA Atlas NESDIS 50*, 165 pp.

Brandt, P., A. Funk, L. Czeschel, C. Eden, and C. W. Boening, 2007: Ventilation and transformation of Labrador Sea Water and its rapid export in the deep Labrador Current. *Journal of Physical Oceanography*, **37**, 946–961.

Brandt, P., F. Schott, A. Funk, and C. Martins, 2004: Seasonal to interannual variability of the eddy field in the Labrador Sea from satellite altimetry. *Journal of Geophysical Research – Oceans*, **109**.

Brauch, J. and R. Gerdes, 2005: Response of the northern North Atlantic and Arctic oceans to a sudden change of the North Atlantic Oscillation. *Journal of Geophysical Research*, **110**, 1–16.

Bromwich, D. H. and S. H. Wang, 2005: Evaluation of the NCEP-NCAR and ECMWF 15- and 40-Yr Reanalyses using rawinsonde data from two independent Arctic field experiments. *Monthly Weather Review*, **133**, 3562–3578.

Canadian Ice Service, 1992: *Ice Thickness Climatology, 1961-1990 Normals*. Number En57-28, Canada Communication Group Publishing, Ottawa, Canada, K1A 0S9, 277 pp.

Carsey, F. D., B. Holt, S. A. D. Argus, M. J. Collins, C. E. Livingstone, and C. Tang, 1989: Overview of LIMEX'87 ice observations. *IEEE Transactions on Geoscience and Remote Sensing*, **27**, 468–482.

Cavalieri, D., T. Markus, and J. Comiso, 2004, updated daily: AMSR-E/Aqua Daily L3 12.5 km Brightness Temperature, Sea Ice Conentration, & Snow Depth Polar Grids V002, [2002-2009]. Technical report, National Snow and Ice Data Center, Boulder, Colorado USA, digital media.

Cavalieri, D. J., C. L. Parkinson, and K. Y. Vinnikov, 2003: 30-Year satellite record reveals contrasting Arctic and Antarctic decadal sea ice variability. *Geophysical Research Letters*, **30**.

Chanut, J., B. Barnier, W. Large, L. Debreu, T. Penduff, J. M. Molines, and P. Mathiot, 2008: Mesoscale eddies in the Labrador Sea and their contribution to convection and restratification. *Journal of Physical Oceanography*, **38**, 1617–1643.

Comiso, J., 1999, updated 2008: Bootstrap sea ice concentrations from NIMBUS-7 SMMR and DMSP SSM/I, [1992-2004]. Technical report, National Snow and Ice Data Center, Boulder, Colorado USA, digital Media.

Comiso, J., D. Cavalieri, C. Parkinson, and P. Gloersen, 1997: Passive microwave algorithms for sea ice concentration: A comparison of two techniques. *Remote Sensing Of Environment*, **60**, 357–384.

Comiso, J. C. and F. Nishio, 2008: Trends in the sea ice cover using enhanced and compatible AMSR-E, SSM/I, and SMMR data. *Journal of Geophysical Research – Oceans*, **113**, C02S07.

Crane, R., 1978: Seasonal Variations of Sea Ice Extent in the Davis Strait-Labrador Sea Area and Relationships with Synoptic-Scale Atmospheric Circulation. *Arctic*, **31**, 434–447.

Cuny, J., P. Rhines, and R. Kwok, 2005: Davis Strait volume, freshwater and heat fluxes. *Deep Sea Research Part I: Oceanographic Research Papers*, **52**, 519–542.

Cuny, J., P. Rhines, P. Niiler, and S. Bacon, 2002: Labrador sea boundary currents and the fate of the Irminger Sea Water. *Journal of Physical Oceanography*, **32**, 627–647.

Curry, J. A., J. L. Schramm, A. Alam, R. Reeder, T. E. Arbetter, and P. Guest, 2002: Evaluation of data sets used to force sea ice models in the Arctic Ocean. *Journal of Geophysical Research – Oceans*, **107**, 3102.

Curry, R., 2001: Hydrobase 2 - a database of hydrographic profiles and tools for climatological analysis. Technical reference, Woods Hole Oceanographic Institution, Woods Hole, USA, preliminary Draft.

Czeschel, L., 2004: *The Role of Eddies for the Deep Water Formation in the Labrador Sea*. Ph.D. thesis, University of Kiel.

DeGrandpre, M. D., A. Koertzinger, U. Send, D. W. R. Wallace, and R. G. J. Bellerby, 2006: Uptake and sequestration of atmospheric CO2 in the Labrador Sea deep convection region. *Geophysical Research Letters*, **33**.

Dengler, M., J. Fischer, F. A. Schott, and R. Zantopp, 2006: Deep Labrador Current and its variability in 1996-2005. *Geophysical Research Letters*, **33**.

Deser, C., M. Holland, G. Reverdin, and M. Timlin, 2002: Decadal variations in Labrador Sea ice cover and North Atlantic sea surface temperatures. *Journal of Geophysical Research – Oceans*, **107**, 3035.

Deser, C., G. Magnusdottir, R. Saravanan, and A. Phillips, 2004: The Effects of North Atlantic SST and Sea Ice Anomalies on the Winter Circulation in CCM3. Part II: Direct and Indirect Components of the Response. *Journal of Climate*, **17**, 877–889.

Deser, C. and H. Teng, 2008: Evolution of Arctic sea ice concentration trends and the role of atmospheric circulation forcing, 1979-2007. *Geophysical Research Letters*, **35**.

Deser, C., J. Walsh, and M. Timlin, 2000: Arctic sea ice variability in the context of recent atmospheric circulation trends. *Journal of Climate*, **13**, 617–633.

Deshayes, J. and C. Frankignoul, 2008: Simulated variability of the circulation in the North Atlantic from 1953 to 2003. *Journal of Climate*, **21**, 4919–4933.

Dobricic, S., 2006: An improved calculation of Coriolis terms on the C grid. *Monthly Weather Review*, **134**, 3764–3773.

Duffy, P., M. Eby, and A. J. Weaver, 1999: Effects of sinking of salt rejected during formation of sea ice on results of an ocean-atmosphere-sea ice climate model. *Geophysical Research Letters*, **26**, 1739–1742.

Eden, C. and C. Boning, 2002: Sources of eddy kinetic energy in the Labrador Sea. *Journal of Physical Oceanography*, **32**, 3346–3363.

Farrell, S. L., S. W. Laxon, D. C. McAdoo, D. Yi, and H. J. Zwally, 2009: Five years of Arctic sea ice freeboard measurements from the Ice, Cloud and land Elevation Satellite. *Journal of Geophysical Research – Oceans*, **114**.

Feltham, D. L., N. Untersteiner, J. S. Wettlaufer, and M. G. Worster, 2006: Sea ice is a mushy layer. *Geophysical Research Letters*, **33**, doi:10.1029/2006GL026290.

Fischer, J., F. Schott, and M. Dengler, 2004: Boundary circulation at the exit of the Labrador Sea. *Journal of Physical Oceanography*, **34**, 1548–1570.

Forget, G. and C. Wunsch, 2007: Estimated Global Hydrographic Variability. *Journal of Physical Oceanography*, **37**, 1997–2008.

Fowler, C., 2003, updated 2007: Polar Pathfinder Daily 25 km EASE-Grid Sea Ice Motion Vectors. Digital media, National Snow and Ice Data Center, Boulder, CO, USA.

Fratantoni, D., 2001: North Atlantic surface circulation during the 1990's observed with satellite-tracked drifters. *Journal of Geophysical Research – Oceans*, **106**, 22067–22093.

Fratantoni, P. S. and R. S. Pickart, 2007: The western North Atlantic shelfbreak current system in summer. *Journal of Physical Oceanography*, **37**, 2509–2533.

Funk, A., P. Brandt, and T. Fischer, 2009: Eddy diffusivities estimated from observations in the Labrador Sea. *Journal of Geophysical Research – Oceans*, **114**, doi:10.1029/2008JC005098.

Gebbie, G., 2007: Does eddy subduction matter in the northeast Atlantic Ocean? *Journal of Geophysical Research*, **112**, C06007.

Gebbie, G., P. Heimbach, and C. Wunsch, 2006: Strategies for nested and eddy-permitting state estimation. *Journal of Geophysical Research – Oceans*, **111**, C10073.

Gebbie, G. A., 2004: *Subduction in an Eddy-Resolving State Estimate of the Northeast Atlantic Ocean*. Ph.D. thesis, Massachusetts Institute of Technology and the Woods Hole Oceanographic Institution.

Gent, P. R. and J. C. McWilliams, 1990: Isopycnal mixing in ocean circulation models. *Journal of Physical Oceanography*, **20**, 150–155.

Giering, R. and T. Kaminski, 1998: Recipes for adjoint code construction. *ACM Transactions on Mathematical Software (TOMS)*, **24**, 437–474.

Giering, R., T. Kaminski, and T. Slawig, 2005: Generating Efficient Derivative Code with TAF: Adjoint and Tangent Linear Euler Flow Around an Airfoil. *Future Generation Computer Systems*, **21**, 1345–1355.

Gouretski, V. and K. Koltermann, 2004: *WOCE Global Hydrographic Climatology*. Berichte des Bundesamtes fur Seeschifffahrt und Hydrographie, 35/2004 edition, 52 pp.

Greenan, B. J. W. and S. J. Prinsenberg, 1998: Wind forcing of ice cover in the Labrador shelf marginal ice zone. *Atmosphere – Ocean*, **36**, 71–93.

Grenfell, T. C. and D. K. Perovich, 1984: Spectral Albedos of Sea Ice and Incident Solar Irradiance in the Southern Beaufort Sea. *Journal of Geophysical Research – Oceans*, **89**, 3573–3580.

— 2004: Seasonal and spatial evolution of albedo in a snow-ice-land-ocean environment. *Journal of Geophysical Research – Oceans*, **109**, C01001.

Griewank, A. and G. F. Corliss, eds., 1991: *Automatic Differentiation of Algorithms: Theory, Implementation, and Application*. Society for Industrial & Applied Mathematics, Philadelphia, Pennsylvania.

Griffies, S., 1998: The Gent-McWilliams skew flux. *Journal of Physical Oceanography*, **28**, 831–841.

Griffies, S. M., 2004: *Fundamentals of Ocean-Climate Models*. Princeton University Press.

Griffies, S. M., A. Biastoch, C. Bning, F. Bryan, G. Danabasoglu, E. P. Chassignet, M. H. England, R. Gerdes, H. Haak, R. W. Hallberg, W. Hazeleger, J. Jungclaus, W. G. Large, G. Madec, A. Pirani, B. L. Samuels, M. Scheinert, A. S. Gupta, C. A. Severijns, H. L. Simmons, A. M. Treguier, M. Winton, S. Yeager, and J. Yin, 2009: Coordinated Ocean-ice Reference Experiments (COREs). *Ocean Modelling*, **26**, 1–46.

Gruber, N., M. Gloor, S. E. M. Fletcher, S. C. Doney, S. Dutkiewicz, M. J. Follows, M. Gerber, A. R. Jacobson, F. Joos, K. Lindsay, D. Menemenlis, A. Mouchet, S. A. Mueller, J. L. Sarmiento, and T. Takahashi, 2009: Oceanic sources, sinks, and transport of atmospheric CO2. *Global Biogeochemical Cycles*, **23**.

Häkkinen, S., 1987: A coupled Dynamic-Thermodynamic Model of an Ice-Ocean System in the Marginal Ice-Zone. *Journal of Geophysical Research – Oceans*, **92**, 9469–9478.

Hakkinen, S. and P. Rhines, 2004: Decline of subpolar North Atlantic circulation during the 1990s. *Science*, **304**, 555–559.

Hátún, H., C. C. Eriksen, and P. B. Rhines, 2007: Buoyant Eddies Entering the Labrador Sea Observed with Gliders and Altimetry. *Journal of Physical Oceanography*, **37**, 2838–2854.

Hayes, D. R. and J. Morison, 2008: Ice-ocean turbulent exchange in the Arctic summer measured by an autonomous underwater vehicle. *Limnology and oceanography*, **53**, 2287–2308.

Heimbach, P., C. Hill, and R. Giering, 2005: An efficient exact adjoint of the parallel MIT General Circulation Model, generated via automatic differentiation. *Future Generation Computer Systems*, **21**, 1356–1371.

Heimbach, P., D. Menemenlis, M. Losch, J.-M. Campin, , and C. Hill, 2010: On the formulation of sea-ice models. Part 2: Lessons from multi-year adjoint sea ice export sensitivities through the Canadian Arctic Archipelago. *Ocean Modelling*, **33**, 145–158.

Hewitt, C. D., A. J. Broccoli, M. Crucifix, J. M. Gregory, J. F. B. Mitchell, and R. J. Stouffer, 2006: The effect of a large freshwater perturbation on the glacial north Atlantic Ocean using a coupled general circulation model. *Journal of Climate*, **19**, 4436–4447.

Hibler, W. D., 1979: A Dynamic Thermodynamic Sea Ice Model. *Journal of Physical Oceanography*, **9**, 815–846.

— 1980: Modeling a variable thickness sea ice cover. *Monthly Weather Review*, **108**, 1943–1973.

Hibler, W. D. and K. Bryan, 1984: Ocean Circulation - Its Effects on Seasonal Sea-Ice Simulations. *Science*, **224**, 489–492.

Hilber, W. D. and J. E. Walsh, 1982: On Modeling Seasonal and Interannual Fluctuations of Arctic Sea Ice. *Journal of Physical Oceanography*, **12**, 1514–1523.

Holladay, J. S. and R. Moucha, 1994: Electromagnetic/Laser Ice Thickness Data From the Labrador Shelf, 1994. Canadian Contractor Report of Hydrography and Ocean Sciences No. XXX, Bedford Institute of Oceanography, P.O. Box 1006 Dartmouth, Nova Scotia Canada, B2Y 4A2.

Holland, D. M., 2001: An Impact of Subgrid-Scale Ice-Ocean Dynamics on Sea-Ice Cover. *Journal of Climate*, **14**, 1585–1601.

Holland, M. M., C. M. Bitz, and B. Tremblay, 2006: Future abrupt reductions in the summer Arctic sea ice. *Geophysical Research Letters*, **33**.

Holland, M. M., C. M. Bitz, and A. J. Weaver, 2001: The influence of sea ice physics on simulations of climate change. *Journal of Geophysical Research – Oceans*, **106**, 19639–19655.

Holliday, N. P., S. Bacon, J. Allen, and E. L. McDonagh, 2009: Circulation and Transport in the Western Boundary Currents at Cape Farewell, Greenland. *Journal of Physical Oceanography*, **39**, 1854–1870.

Holloway, G., F. Dupont, E. Golubeva, S. Haekkinen, E. Hunke, M. Jin, M. Karcher, F. Kauker, M. Maltrud, M. A. M. Maqueda, W. Maslowski, G. Platov, D. Stark, M. Steele, T. Suzuki, J. Wang, and J. Zhang, 2007: Water properties and circulation in Arctic Ocean models. *Journal of Geophysical Research – Oceans*, **112**.

Houghton, R. and M. Visbeck, 2002: Quasi-decadal salinity fluctuations in the Labrador Sea. *Journal of Physical Oceanography*, **32**, 687–701.

Hwang, B. J., J. K. Ehn, and D. G. Barber, 2008: Impact of ice temperature on microwave emissivity of thin newly formed sea ice. *Journal of Geophysical Research – Oceans*, **113**, C02021.

Ikeda, M., 1991: Numerical Modeling Of Ocean Circulation And Ice Cover Over The Continental-Shelf. *Journal of Physical Oceanography*, **21**, 97–117.

Ikeda, M. and F. W. Dobson, eds., 1995: *Satellite remote sensing of ice motion, in Oceanographic Applications of Remote Sensing*. CRC Press, Boca Raton.

Ikeda, M., G. Symonds, and T. Yao, 1988: Simulated Fluctuations in Annual Labrador Sea-Ice Cover. *Atmosphere – Ocean*, **26**, 16–39.

Ikeda, M., T. Yao, and Q. Yao, 1996: Seasonal evolution of sea ice cover and shelf water off Labrador simulated in a coupled ice-ocean model. *Journal of Geophysical Research – Oceans*, **101**, 16465–16489.

Jackett, D. R. and T. J. Mcdougall, 1995: Minimal Adjustment of Hydrographic Profiles to Achieve Static Stability. *Journal of Atmospheric and Oceanic Technology*, **12**, 381–389.

Jochum, M., G. Danabasoglu, M. Holland, Y. O. Kwon, and W. G. Large, 2008: Ocean viscosity and climate. *Journal of Geophysical Research – Oceans*, **113**.

Jones, H. and J. Marshall, 1993: Convection with Rotation in a Neutral Ocean: A Study of Open-Ocean Deep Convection. *Journal of Physical Oceanography*, **23**, 1009–1039, doi:10.1175/1520-0485(1993)023¡1009:CWRIAN¿2.0.CO;2.
URL `http://journals.ametsoc.org/doi/abs/10.1175/1520-0485%281993%29023%3C1009%3ACWRIAN%3E2.0.CO%3B2`

Kalnay, E., M. Kanamitsu, R. Kistler, W. Collins, D. Deaven, L. Gandin, M. Iredell, S. Saha, G. White, J. Woollen, Y. Zhu, M. Chelliah, W. Ebisuzaki, W. Higgins, J. Janowiak, K. C. Mo, C. Ropelewski, J. Wang, A. Leetmaa, R. Reynolds, R. Jenne, and D. Joseph, 1996: The NCEP/NCAR 40-year reanalysis project. *Bulletin of the American Meteorological Society*, **77**, 437–471.

Kantha, L. H. and G. L. Mellor, 1989: A Two-Dimensional Coupled Ice-Ocean Model Of The Bering Sea Marginal Ice-Zone. *Journal of Geophysical Research – Oceans*, **94**, 10921–10935.

Katsman, C. A., M. A. Spall, and R. S. Pickart, 2004: Boundary Current Eddies and Their Role in the Restratification of the Labrador Sea. *Journal of Physical Oceanography*, **34**, 1967–1983.

Khatiwala, S., P. Schlosser, and M. Visbeck, 2002: Rates and mechanisms of water mass transformation in the Labrador Sea as inferred from tracer observations. *Journal of Physical Oceanography*, **32**, 666–686.

Kitoh, A., S. Murakami, and H. Koide, 2001: A simulation of the last glacial maximum with a coupled atmosphere-ocean GCM. *Geophysical Research Letters*, **28**, 2221–2224.

Klinger, B. A., B. Huang, B. Kirtman, P. Schopf, and J. Wang, 2006: Monthly climatologies of oceanic friction velocity cubed. *Journal of Climate*, **19**, 5700–5708.

Kolstad, E. W., 2008: A QuikSCAT climatology of ocean surface winds in the Nordic seas: Identification of features and comparison with the NCEP/NCAR reanalysis. *Journal of Geophysical Research – Atmospheres*, **113**.

Krahmann, G. and M. Visbeck, 2003: Arctic Ocean sea ice response to Northern Annular Mode-like wind forcing. *Geophysical Research Letters*, **30**.

Kwok, R., 2005: Variability of Nares Strait ice flux. *Geophysical Research Letters*, **32**, doi:10.1029/2005GL024768.

— 2007: Baffin Bay ice drift and export: 2002-2007. *Geophysical Research Letters*, **34**.

Kwok, R., G. Cunningham, H. Zwally, and D. Yi, 2006: ICESat over Arctic sea ice: Interpretation of altimetric and reflectivity profiles. *Journal of Geophysical Research – Oceans*, **111**.

Kwok, R. and G. F. Cunningham, 2008: ICESat over Arctic sea ice: Estimation of snow depth and ice thickness. *Journal of Geophysical Research – Oceans*, **113**.

Kwok, R., G. F. Cunningham, H. J. Zwally, and D. Yi, 2007: Ice, Cloud, and land Elevation Satellite (ICESat) over Arctic seaice: Retrieval of freeboard. *Journal of Geophysical Research – Oceans*, **112**.

Kwok, R., A. Schweiger, D. Rothrock, S. Pang, and C. Kottmeier, 1998: Sea ice motion from satellite passive microwave imagery assessed with ERS SAR and buoy motions. *Journal of Geophysical Research – Oceans*, **103**, 8191–8214.

Kwok, R., H. J. Zwally, and D. H. Yi, 2004: ICESat observations of Arctic sea ice: A first look. *Geophysical Research Letters*, **31**.

Ladd, C. and N. A. Bond, 2002: Evaluation of the NCEP/NCAR reanalysis in the NE Pacific and the Bering Sea. *Journal of Geophysical Research – Oceans*, **107**, 3158.

Large, W. and S. Yeager, 2004: Diurnal to decadal global forcing for ocean and sea-ice models: thedata sets and flux climatologies. NCAR Technical Note: NCAR/TN-460+STR, CGD Division of the National Center for Atmospheric Research.

Large, W. G., G. Danabasoglu, S. C. Doney, and J. C. McWilliams, 1997: Sensitivity to surface forcing and boundary layer mixing in a global ocean model: Annual-mean climatology. *Journal of Physical Oceanography*, **27**, 2418–2447.

Large, W. G., J. C. McWilliams, and S. C. Doney, 1994: Oceanic Vertical Mixing: A Review and a Model with a Nonlocal Boundary Layer Parameterization. *Reviews of Geophysics*, **32**, 363–403.

Lavender, K., R. Davis, and W. Owens, 2000: Mid-depth recirculation observed in the interior Labrador and Irminger seas by direct velocity measurements. *Nature*, **407**, 66–69.

Lazier, J., R. Hendry, A. Clarke, I. Yashayaev, and P. Rhines, 2002: Convection and restratification in the Labrador Sea, 1990-2000. *Deep Sea Research Part I: Oceanographic Research Papers*, **49**, 1819–1835.

Lilly, J. M. and P. B. Rhines, 2002: Coherent Eddies in the Labrador Sea Observed from a Mooring. *Journal of Physical Oceanography*, **32**, 585–598.

Lilly, J. M., P. B. Rhines, F. Schott, K. Lavender, J. Lazier, U. Send, and E. D'Asaro, 2003: Observations of the Labrador Sea eddy field. *Progress in Oceanography*, **59**, 75–176.

Lobb, J., A. Weaver, E. Carmack, and R. Ingram, 2003: Structure and mixing across an Arctic/Atlantic front in northern Baffin Bay. *Geophysical Research Letters*, **30**.

Losch, M., S. Herlufsen, and R. Timmermann, 2006: Effects of heterogeneous surface boundary conditions on parameterized oceanic deep convection. *Ocean Modelling*, **13**, 156–165.

Losch, M., D. Menemenlis, J.-M. Campin, P. Heimbach, and C. Hill, 2010: On the formulation of sea-ice models. Part 1: Effects of different solver implementations and parameterizations. *Ocean Modelling*, **33**, 129 – 144.

Lu, Y., D. G. Wright, and I. Yashayaev, 2007: Modelling hydrographic changes in the Labrador Sea over the past five decades. *Progress in Oceanography*, **73**, 406–426.

Lupkes, C. and G. Birnbaum, 2005: Surface drag in the arctic marginal sea-ice zone: A comparison of different parameterisation concepts. *Boundary-Layer Meteorology*, **117**, 179–211.

Magnusdottir, G., C. Deser, and R. Saravanan, 2004: The Effects of North Atlantic SST and Sea Ice Anomalies on the Winter Circulation in CCM3. Part I: Main Features and Strom Track Characteristics of the Response. *Journal of Climate*, **17**, 857–876.

Manabe, S. and R. F. Strickler, 1964: Thermal Equilibrium of the Atmosphere with a Convective Adjustment. *Journal of the Atmospheric Sciences*, **21**, 361–385.

Marotzke, J., R. Giering, K. Q. Zhang, D. Stammer, C. Hill, and T. Lee, 1999: Construction of the adjoint MIT ocean general circulation model and application to Atlantic heat transport sensitivity. *Journal of Geophysical Research – Oceans*, **104**, 29529–29547.

Marsden, R., L. MYSAK, and R. MYERS, 1991: Evidence for Stability Enhancement of Sea-Ice in the Greenland and Labrador Seas. *Journal of Geophysical Research – Oceans*, **96**, 4783–4789.

Marshall, J., A. Adcroft, C. Hill, L. Perelman, and C. Heisey, 1997a: A finite-volume, incompressible Navier Stokes model for studies of the ocean on parallel computers. *Journal of Geophysical Research – Oceans*, **102**, 5753–5766.

Marshall, J., F. Dobson, K. Moore, P. Rhines, M. Visbeck, E. d'Asaro, K. Bumke, S. Chang, R. Davis, K. Fischer, R. Garwood, P. Guest, R. Harcourt, C. Herbaut, T. Holt, J. Lazier, S. Legg, J. McWilliams, R. Pickart, M. Prater, I. Renfrew, F. Schott, U. Send, W. Smethie, and G. Lab Sea, 1998: The Labrador Sea deep convection experiment. *Bulletin of the American Meteorological Society*, **79**, 2033–2058.

Marshall, J., C. Hill, L. Perelman, and A. Adcroft, 1997b: Hydrostatic, quasi-hydrostatic, and nonhydrostatic ocean modeling. *Journal of Geophysical Research – Oceans*, **102**, 5733–5752.

Marti, J. and K. Mauersberger, 1993: A Survey and New Measurements of Ice Vapor-Pressure at Temperatures Between 170 and 250K. *Geophysical Research Letters*, **20**, 363–366.

Martin, R. and G. Moore, 2006: Transition of a synoptic system to a polar low via interaction with the orography of Greenland. *Tellus Series A – Dynamic Meteorology And Oceanography*, **58**, 236–253.

Maykut, G. and N. Untersteiner, 1971: Some Results from a Time-Dependent Thermodynamic Model of Sea Ice. *Journal of Geophysical Research*, **76**, 15501575.

Mazloff, M. R., 2008: *The Southern Ocean Meridional Overturning Circulation as Diagnosed from an Eddy Permitting State Estimate*. Ph.D. thesis, Massachusetts Institute of Technology and Woods Hole Oceanographic Institution.

McPhee, M., 1992: Turbulent Heat Flux in the Upper Ocean Under Sea Ice. *Journal of Geophysical Research – Oceans*, **97**, 5365–5379.

McPhee, M., G. Maykut, and J. Morison, 1987: Dynamics and Thermodynamics of the Ice-Upper Ocean system in the Marginal Ice Zone of the Greenland Sea. *Journal of Geophysical Research – Oceans*, **92**, 7017–7031.

McPhee, M. G., 2008: *Air-Ice-Ocean Interaction: Turbulent Boundary Layer Exchange Processes*. Springer, New York, 215 pp.

Menemenlis, D., J. Campin, P. Heimbach, C. Hill, T. Lee, A. Nguygen, M. Schodlock, and H. Zhang, 2008: ECCO2: High resolution global ocean and sea ice data synthesis. *Mercator Ocean Quarterly Newsletter.*, **31**, 13–21.

Mesinger, F., G. DiMego, E. Kalnay, K. Mitchell, P. C. Shafran, W. Ebisuzaki, D. Jovic, J. Woollen, E. Rogers, E. H. Berbery, M. B. Ek, Y. Fan, R. Grumbine, W. Higgins, H. Li, Y. Lin, G. Manikin, D. Parrish, and W. Shi, 2006: North American Regional Reanalysis. *Bulletin of the American Meteorological Society*, **87**, 343–360.

MIZEX Group, 1989: MIZEX East 1987. Winter marginal ice zone program in the Fram Strait and Greenland Sea. *EOS, Transactions of the American Geophysical Union*, **70**, 545–555.

Moore, G., M. Reader, J. York, and S. Sathiyamoorthy, 1996: Polar lows in the Labrador Sea - A case study. *Tellus Series A – Dynamic Meteorology And Oceanography*, **48**, 17–40.

Moore, G. and I. Renfrew, 2002: An assessment of the surface turbulent heat fluxes from the NCEP-NCAR reanalysis over the western boundary currents. *Journal of Climate*, **15**, 2020–2037.

Morison, J. and M. McPhee, 1998: Lead convection measured with an autonomous underwater vehicle. *Journal of Geophysical Research – Oceans*, **103**, 3257–3281.

Morison, J. H., M. G. McPhee, and G. A. Maykut, 1987: Boundary Layer, Upper Ocean, and Ice Observations in the Greenland Sea Marginal Ice Zone. *Journal of Geophysical Research – Oceans*, **92**, 6987–7011.

Mysak, L., S. Peng, and R. Wood, 1991: Application of a coupled ice-ocean model to the Labrador Sea. *Atmosphere – Ocean*, **29**, 232–255.

Mysak, L. A., R. Ingram, J. Wang, and A. van der Baaren, 1996: The anomalous sea-ice extent in Hudson Bay, Baffin Bay and the Labrador Sea during three simultaneous NAO and ENSO episodes. *Atmosphere – Ocean*, **34**, 313–343.

Mysak, L. A. and D. K. Manak, 1989: Arctic Sea-Ice Extent and Anomalies, 1953-1984. *Atmosphere – Ocean*, **27**, 376–405.

National Oceanographic Data Center Operational Oceanography Group, 2006: Global Temperature–Salinity Profile Program. Accessed: July 2008.

Nechaev, D. and M. Yaremchuk, 2004: On the approximation of the Coriolis terms in C-grid models. *Monthly Weather Review*, **132**, 2283–2289.

Nguyen, A. T., D. Menemenlis, and R. Kwok, 2009: Improved modeling of the Arctic halocline with a subgrid-scale brine rejection parameterization. *Journal of Geophysical Research – Oceans*, **114**, C11014.

Notz, D., 2005: *Thermodynamic and Fluid-Dynamical Processes in Sea Ice*. Ph.D. thesis, Trinity College.

Parkinson, C. L. and W. M. Washington, 1979: Large-Scale Numerical-Model of Sea Ice. *Journal of Geophysical Research – Oceans and Atmospheres*, **84**, 311–337.

Perovich, D. K., C. S. Roesler, and W. S. Pegau, 1998: Variability in Arctic sea ice optical properties. *Journal of Geophysical Research – Oceans*, **103**, 1193–1208.

Peterson, I. and S. Prinsenberg, 1989: Observations Of Sea Ice Drift Off Newfoundland Using Satellite Imagery And Ice Beacons. *IEEE Transactions on Geoscience and Remote Sensing*, **4**, 2359–2362.

Pickart, R. S., D. J. Torres, and R. A. Clarke, 2002: Hydrography of the Labrador Sea during active convection. *Journal of Physical Oceanography*, **32**, 428–457.

Prater, M. D., 2002: Eddies in the Labrador Sea as Observed by Profiling RAFOS Floats and Remote Sensing. *Journal of Physical Oceanography*, **32**, 411–427.

Prinsenberg, S. and J. Hamilton, 2005: Monitoring the volume, freshwater and heat fluxes passing through Lancaster Sound in the Canadian Arctic Archipelago. *Atmosphere – Ocean*, **43**, 1–22.

Prinsenberg, S. and I. Peterson, 1992: Sea-Ice Properties Off Labrador And Newfoundland During Limex-89. *Atmosphere – Ocean*, **30**, 207–222.

Prinsenberg, S. J., I. K. Peterson, S. Narayanan, and J. U. Umoh, 1997: Interaction between atmosphere, ice cover, and ocean off Labrador and Newfoundland from 1962-1992. *Canadian Journal of Fisheries and Aquatic Sciences*, **54**, 30–39.

Rayner, N. A., D. E. Parker, E. B. Horton, C. K. Folland, L. V. Alexander, D. P. Rowell, E. C. Kent, and A. Kaplan, 2003: Global analyses of sea surface temperature, sea ice, and night marine air temperature since the late nineteenth century. *Journal of Geophysical Research – Atmospheres*, **108**, 4407.

Redi, M. H., 1982: Oceanic isopycnal mixing by coordinate rotation. *Journal of Physical Oceanography*, **12**, 1154–1158.

Renfrew, I. A., G. W. K. Moore, P. S. Guest, and K. Bumke, 2002: A Comparison of Surface Layer and Surface Turbulent Flux Observations over the Labrador Sea with ECMWF Analyses and NCEP Reanalyses. *Journal of Physical Oceanography*, **32**, 383–400.

Renfrew, I. A., G. W. K. Moore, T. R. Holt, S. W. Chang, and P. Guest, 1999: Mesoscale forecasting during a field program: Meteorological support of the Labrador Sea Deep Convection Experiment. *Bulletin of the American Meteorological Society*, **80**, 605–620.

Reverdin, G., D. Cayan, and Y. Kushnir, 1997: Decadal variability of hydrography in the upper northern North Atlantic in 1948-1990. *Journal of Geophysical Research – Oceans*, **102**, 8505–8531.

Reynolds, R. W., T. M. Smith, C. Liu, D. B. Chelton, K. S. Casey, and M. G. Schlax, 2007: Daily high-resolution-blended analyses for sea surface temperature. *Journal of Climate*, **20**, 5473–5496.

Rhein, M., D. Kieke, and R. Steinfeldt, 2007: Ventilation of the Upper Labrador Sea Water, 2003-2005. *Geophysical Research Letters*, **34**.

Rogers, J. C. and H. Van Loon, 1979: The Seesaw in Winter Temperatures between Greenland and Northern Europe. Part II: Some Oceanic and Atmospheric Effects in Middle and High Latitudes. *Monthly Weather Review*, **107**, 509–519.

Sallee, J. B., K. Speer, R. Morrow, and R. Lumpkin, 2008: An estimate of Lagrangian eddy statistics and diffusion in the mixed layer of the Southern Ocean. *J. Mar. Res.*, **66**, 441–463.

Sathiyamoorthy, S. and G. Moore, 2002: Buoyancy flux at Ocean Weather Station Bravo. *Journal of Physical Oceanography*, **32**, 458–474.

Schmidt, G., C. Bitz, U. Mikolajewicz, and L. Tremblay, 2004: Ice-ocean boundary conditions for coupled models. *Ocean Modelling*, **7**, 59–74.

Semtner, A. J., 1976: Model For Thermodynamic Growth of Sea Ice In Numerical Investigations of Climate. *Journal of Physical Oceanography*, **6**, 379–389.

Serreze, M., J. Maslanik, T. Scambos, F. Fetterer, J. Stroeve, K. Knowles, C. Fowler, S. Drobot, R. Barry, and T. Haran, 2003: A record minimum arctic sea ice extent and area in 2002. *Geophysical Research Letters*, **30**.

Serreze, M. C., A. P. Barrett, and F. Lo, 2005: Northern high-latitude precipitation as depicted by atmospheric reanalyses and satellite retrievals. *Monthly Weather Review*, **133**, 3407–3430.

Serreze, M. C., M. M. Holland, and J. Stroeve, 2007: Perspectives on the Arctic's Shrinking Sea-Ice Cover. *Science*, **315**, 1533–1536.

Sirevaag, A., 2009: Turbulent exchange coefficients for the ice/ocean interface in case of rapid melting. *Geophysical Research Letters*, **36**, L04606.

Smith, S. R., D. M. Legler, and K. V. Verzone, 2001: Quantifying uncertainties in NCEP reanalyses using high-quality research vessel observations. *Journal of Climate*, **14**, 4062–4072.

Spall, M. and R. Pickart, 2003: Wind-driven recirculations and exchange in the Labrador and Irminger Seas. *Journal of Physical Oceanography*, **33**, 1829–1845.

Stammer, D., C. Wunsch, R. Giering, C. Eckert, P. Heimbach, J. Marotzke, A. Adcroft, C. Hill, and J. Marshall, 2002: Global ocean circulation during 1992-1997, estimated from ocean observations and a general circulation model. *Journal of Geophysical Research – Oceans*, **107**.

Steiner, N., M. Harder, and P. Lemke, 1999: Sea-ice roughness and drag coefficients in a dynamic-thermodynamic sea-ice model for the Arctic. *Tellus Series A – Dynamic Meteorology And Oceanography*, **51**, 964–978.

Stephens, C., J. I. Antonov, T. P. Boyer, M. E. Conkright, M. E. Locarnini, T. D. O'Brien, and H. E. Garcia, 2001: World Ocean Atlas 2001. *Temperature*, S. Levitus, ed., U.S. Government Printing Office, Washington, D.C., volume 1 of *NOAA Atlas NESDIS 49*, 167 pp.

Stone, P. H., 1978: Constraints on Dynamical Transports of Energy on a Spherical Planet. *Dynamics of Atmospheres and Oceans*, **2**, 123–139.

Stössel, A., K. Yang, and S.-J. Kim, 2002: On the Role of Sea Ice and Convection in a Global Ocean Model. *Journal of Physical Oceanography*, **32**, 1194–1208.

Straneo, F., 2006: Heat and freshwater transport through the central Labrador Sea. *Journal of Physical Oceanography*, **36**, 606–628.

Stroeve, J., M. M. Holland, W. Meier, T. Scambos, and M. Serreze, 2007: Arctic sea ice decline: Faster than forecast. *Geophysical Research Letters*, **34**.

Stroeve, J., M. Serreze, F. Fetterer, T. Arbetter, W. Meier, J. Maslanik, and K. Knowles, 2005: Tracking the Arctic's shrinking ice cover: Another extreme September minimum in 2004. *Geophysical Research Letters*, **32**.

Symonds, G., 1986: Seasonal Ice Extent on the Northeast Newfoundland Shelf. *Journal of Geophysical Research – Oceans*, **91**, 718–724.

Tang, C., 1991: A Two-Dimensional Thermodynamic Model for Sea Ice Advance and Retreat in the Newfoundland Marginal Ice Zone. *Journal of Geophysical Research – Oceans*, **96**, 4723–4737.

— 1992: Oceanographic Features in the Newfoundland Marginal Ice-Zone, March April 1990. *Atmosphere – Ocean*, **30**, 151–172.

Tang, C. and Q. Gui, 1996: A dynamical model for wind-driven ice motion: Application to ice drift on the Labrador Shelf. *Journal of Geophysical Research – Oceans*, **101**, 28343–28364.

Tang, C., C. Ross, T. Yao, B. Petrie, B. DeTracey, and E. Dunlap, 2004: The circulation, water masses and sea-ice of Baffin Bay. *Progress in Oceanography*, **63**, 183–228.

Tang, C. and T. Yao, 1992: A Simulation Of Sea-Ice Motion And Distribution Off Newfoundland During Limex, March 1987. *Atmosphere – Ocean*, **30**, 270–296.

Tang, C. L. and B. M. DeTracey, 1998: Space-time variation of mixed-layer properties, heat and salt fluxes, and ice melt in the Newfoundland marginal ice zone. *Journal of Geophysical Research – Oceans*, **103**, 1177–1191.

Tang, C. L., Q. Gui, and B. M. DeTracey, 1999: A modeling study of upper ocean winter processes in the Labrador Sea. *Journal of Geophysical Research – Oceans*, **104**, 23411–23425.

Thorndike, A. and R. Colony, 1982: Sea Ice Motion in Response to Geostrophic Winds. *Journal of Geophysical Research – Oceans and Atmospheres*, **87**, 5845–5852.

Tonboe, R., S. Andersen, L. Toudal, and G. Heygster, 2006: *Thermal Microwave Radiation - Applications for Remote Sensing*, Institution of Engineering and Technology, London, U.K., chapter Sea ice emission modelling applications. Number 52 in IET Electromagnetic Waves Series, 382–400.

Tonboe, R. and L. Toudal, 2005: Classification of new-ice in the Greenland Sea using Satellite SSM/I radiometer and SeaWinds scatterometer data and comparison with ice model. *Remote Sensing Of Environment*, **97**, 277–287.

Treguier, A. M., S. Theetten, E. P. Chassignet, T. Penduff, R. Smith, L. Talley, J. O. Beismann, and C. Boning, 2005: The North Atlantic subpolar gyre in four high-resolution models. *Journal of Physical Oceanography*, **35**, 757–774.

Tremblay, L. B. and M. Hakakian, 2006: Estimating the sea ice compressive strength from satellite-derived sea ice drift and NCEP reanalysis data. *Journal of Physical Oceanography*, **36**, 2165–2172.

Uppala, S. M., P. W. Kallberg, A. J. Simmons, U. Andrae, V. D. Bechtold, M. Fiorino, J. K. Gibson, J. Haseler, A. Hernandez, G. A. Kelly, X. Li, K. Onogi, S. Saarinen, N. Sokka, R. P. Allan, E. Andersson, K. Arpe, M. A. Balmaseda, A. C. M. Beljaars, L. Van De Berg, J. Bidlot, N. Bormann, S. Caires, F. Chevallier, A. Dethof, M. Dragosavac, M. Fisher, M. Fuentes, S. Hagemann, E. Holm, B. J. Hoskins, L. Isaksen, P. A. E. M. Janssen, R. Jenne, A. P. McNally, J. F. Mahfouf, J. J. Morcrette, N. A. Rayner, R. W. Saunders, P. Simon, A. Sterl, K. E. Trenberth, A. Untch, D. Vasiljevic, P. Viterbo, and J. Woollen, 2005: The ERA-40 re-analysis. *Quarterly Journal of the Royal Meteorological Society*, **131**, 2961–3012.

U.S. Department of Commerce, National Oceanic and Atmospheric Administration, National Geophysical Data Center, 2006: *2-minute Gridded Global Relief Data (ETOPO2v2)*. http://www.ngdc.noaa.gov/mgg/fliers/06mgg01.html.

Utke, J., U. Naumann, M. Fagan, N. Tallent, M. Strout, P. Heimbach, C. Hill, and C. Wunsch, 2008: OpenAD/F: A modular open-source tool for automatic differentiation of Fortran codes. *ACM Transactions on Mathematical Software (TOMS)*, **34**.

Uusikivi, J., J. Ehn, and M. A. Granskog, 2006: Direct measurements of turbulent momentum, heat and salt fluxes under landfast ice in the Baltic Sea. *Annals of Glaciology*, **44**, 42–46.

van Loon, H. and J. C. Rogers, 1978: The Seesaw in Winter Temperatures between Greenland and NorthernEurope. Part I: General Description. *Monthly Weather Review*, **106**, 296–310.

Visbeck, M., J. Fischer, and F. Schott, 1995: Preconditioning the Greenland Sea for deep convection : ice formation and ice drift. *Journal of Geophysical Research – Oceans*, **100**, 18489–18502.

Wadhams, P., 2000: *Ice in the Ocean*. Gordon and Breach Science Publishers, London, 351 pp.

Wadhams, P., A. Mclaren, and R. Weintraub, 1985: Ice thickness distribution in Davis Strait in February from submarine sonar profiles. *Journal of Geophysical Research – Oceans*, **90**, 1069–1077.

Walsh, J., W. Hilber, and B. Ross, 1985: Numerical-simulation of northern hemisphere sea ice variability, 1951-1980. *Journal of Geophysical Research – Oceans*, **90**, 4847–4865.

Walsh, J. E. and C. M. Johnson, 1979: An Analysis of Arctic Sea Ice Fluctuations, 1953-77. *Journal of Physical Oceanography*, **9**, 580–591.

Winton, M., 2000: A Reformulated Three-Layer Sea Ice Model. *Journal of Atmospheric and Oceanic Technology*, **17**, 525–531.

Worby, A. P., T. Markus, A. D. Steer, V. I. Lytle, and R. A. Massom, 2008: Evaluation of AMSR-E snow depth product over East Antarctic sea ice using in situ measurements and aerial photography. *Journal of Geophysical Research – Oceans*, **113**.

Wunsch, C. and P. Heimbach, 2006: Estimated decadal changes in the North Atlantic meridional overturning circulation and heat flux 1993-2004. *Journal of Physical Oceanography*, **36**, 2012–2024.

— 2007: Practical global oceanic state estimation. *Physica D-Nonlinear Phenomena*, **230**, 197–208.

Yao, T. and M. Ikeda, 1990: A Model Of Sea Ice And The Upper Ocean Mixed Layer Off Labrador. *Journal of Geophysical Research – Oceans*, **95**, 11603–11612.

Yao, T., C. L. Tang, and I. K. Peterson, 2000: Modeling the seasonal variation of sea ice in the Labrador Sea with a coupled multicategory ice model and the Princeton ocean model. *Journal of Geophysical Research – Oceans*, **105**, 1153–1165.

Yashayaev, I., 2007: Hydrographic changes in the Labrador Sea, 19602005. *Progress in Oceanography*, **73**, 242276.

Zhang, J. and W. D. Hibler, 1997: On an efficient numerical method for modeling sea ice dynamics. *Journal of Geophysical Research*, **102**, 8691–8702.

Zhang, S., J. Y. Sheng, and R. J. Greatbatch, 2004: A coupled ice-ocean modeling study of the northwest Atlantic Ocean. *Journal of Geophysical Research – Oceans*, **109**, C04009.

Zhang, Y. X., W. Maslowski, and A. J. Semtner, 1999: Impact of mesoscale ocean currents on sea ice in high-resolution Arctic ice and ocean simulations. *Journal of Geophysical Research – Oceans*, **104**, 18409–18429.

Zweng, M. M. and A. Muenchow, 2006: Warming and freshening of Baffin Bay, 1916-2003. *Journal of Geophysical Research – Oceans*, **111**.